ULSAN NATIONAL INSTITUTE OF SCIENCE AND TECHNOLOGY

Master's Thesis

Synthesis of Single-Crystalline Tungsten Ditelluride (WTe_2) Nanostructures Using Eutectic Metal Alloys

Jong Hwa Lee

Department of Materials Science and Engineering

Graduate School of UNIST

2017

ULSAN NATIONAL INSTITUTE OF SCIENCE AND TECHNOLOGY

Synthesis of Single-Crystalline Tungsten Ditelluride (WTe_2) Nanostructures Using Eutectic Metal Alloys

Jong Hwa Lee

Department of Materials Science and Engineering

Graduate School of UNIST

ULSAN NATIONAL INSTITUTE OF SCIENCE AND TECHNOLOGY

Synthesis of Single-Crystalline Tungsten Ditelluride (WTe_2) Nanostructures Using Eutectic Metal Alloys

A thesis/dissertation
submitted to the Graduate School of UNIST
in partial fulfillment of the
requirements for the degree of
Master of Science

Jong Hwa Lee

01. 19. 2017.

Approved by

Advisor
Soon-Yong Kwon

ULSAN NATIONAL INSTITUTE OF SCIENCE AND TECHNOLOGY

Synthesis of Single-Crystalline Tungsten Ditelluride (WTe_2) Nanostructures Using Eutectic Metal Alloys

Jong Hwa Lee

This certifies that the dissertation of Jong Hwa Lee is approved.

01. 19. 2017

Adviser: Soon-Yong Kwon

Zonghoon Lee : Thesis Committee Member #1

Sung Youb Kim : Thesis Committee Member #2

Abstract

Beyond graphene, group-VI transition metal dichalcogenides (TMDs) which is compound of transition metal and chalcogen have recently attracted much attention and mechanically exfoliated flakes of two-dimensional TMDs hold great promise due to their rich variety of properties. As a member of the TMDs family, tungsten ditelluride (WTe_2), which has a stable distorted octahedral phase (1T') among several polymorphs, are appealing because of their unique properties such as an unusual magnetoresistance and quantum spin Hall effect. In an effort to synthesize WTe_2 nanostructures, researchers have tried to develop many growth techniques. Nonetheless, there remains considerable difficulty in obtaining high-quality WTe_2 nanostructures due to a high equilibrium vapor pressure of tellurium at growth temperatures and a weak binding energy of W-Te than other chalcogens.

Here, we suggest a novel facile method to realize the synthesis of single-crystalline WTe_2 nanostructures using eutectic metal alloys. In our work, we studied on the role of eutectic metal alloys and its behavior on synthesis parameters and more details will be presented. In addition, the as-synthesized WTe_2 nanostructures can be easily transferred to different substrates and/or solutions as well as successfully formed on desired substrate without the needs for a further transfer process. The transfer-free formation of WTe_2 nanostructures can be adopted to research the novel properties of WTe_2 nanostructure without any degradation of the intrinsic characteristics. Moreover, feasibility of synthesis for $MoTe_2$ nanostructure as a member of the layered TMDs family was evaluated through our methods. We expect that the emergence of new type of transition metal telluride nanostructures will create exciting prospects for further technical devices and applications in nano-electronics, catalysts and other fields.

Keywords : Transition Metal Dichalcogenides (TMDs), Tungsten ditelluride (WTe_2), Eutectic metal alloys, Nanostructures, Molibdenum ditellruide ($MoTe_2$)

Contents

List of Figures

List of tables

Chapter 1. Overviews

1.1 Transition Metal Dichalcogenides (TMDs)

1.1.1 Introduction of TMDs

Beyond 2D Graphene, scientific interest has been extended to low-dimensional materials because of the wealth of unusual and unique properties that occur when scaled down from bulk to nanoscale dimensions[1]. Recent progress suggests that such truly atomically-thin low-dimensional materials could be one pathway for future electronic devices. The advantages of low-dimensional (2D) materials compared with 3D materials for FETs are demonstrated by the differences that occur in the charge transport between the bulk and the single layer[2]. In 2D materials, charge carriers are confined in atomically thin channels because of the vdW materials' low density of dangling bonds and minimal surface roughness, resulting in excellent gate electrostatics (see figure 1-1). These features make them promising candidates for the revolutionary applications, such as truly atomically-thin field-effect transistors (FET)[3-6], stacked vdW layered hetero-junctions[7-9], and flexible and transparent electronic devices[10-11].

Layered group-VI transition metal dichalcogenides (TMDs) which is compound of transition metal and chalcogen have a chemical formula of MX_2, where M is the transition metal (i.e. Mo or W in group VI metal) and X stands for chalcogen atoms. (i.e. S, Se or Te). Since layered TMDs have a layered stacked structure with weak van der Waals (vdW) force along out-of-plane and strong covalent bonding along in-plane, it could be mechanically and chemically exfoliated into single and/or few layers. Each layer typically has a thickness of 7~9 Å, which consists of a hexagonally packed layer of metal atoms sandwiched between chalcogen atoms.

The layered TMDs exhibit a variety of polymorphs, which are 1T, 2H where the letters stand for trigonal, hexagonal and the digit indicates the number of X–M–X units in the unit cell respectively, as displayed in figure 1-2 (single-layer TMDs exhibit two polymorphs: trigonal prismatic and octahedral phases.)[12].

For most TMDs, the crystal coordination and combination of metal and chalcogen atoms have effects on the material's electrical properties. The bandgap decreases as the atomic number (atomic mass) of the chalcogen atom increases (from S to Se to Te). For example, the bandgap of 2H-MoS_2, 2H-$MoSe_2$ and 2H-$MoTe_2$ decreases gradually from 1.3 to 1.0 eV. The tungsten (or molybdenum) sulfides and selenides shows the semiconducting behavior, but the tellurides are known as semimetal. The group-VI TMDs' electrical properties are summarized in table 1-1.

Among the group-VI TMDs, Mo (or W) sulfides and selenides are semiconductors and possess bandgaps in the range of 1-2 eV with the unit cell of trigonal prismatic (2H-phase, in figure 1-2b). Since the material has discrete band gap level, high carrier mobility and the absence of dangling bonds, they have a possibility for the novel applications of electronics. Since semiconducting TMDs have sizable bandgap, they are a promising optical materials having the energy spectrum ranged from visible to near infrared wavelength. The observation of indirect-to-direct bandgap transition at the monolayer regime[13], strong light-matter interactions[14], and large exciton binding energies[15] can be used for the potential platform for investigation of unusual physical properties as well as the application of the photonic devices in the next-generation.

On the other hand, semi-metallic group-VI metal tellurides display the semi-metallic properties when it has a distorted 1T-phase (1T' or Td, also called distorted orthorhombic, see figure 1-2c)[16-17]. In addition, the tellurides have low energy barriers for the phase transition, so phase transition can be controlled by growth temperature, pressure, or strain[18-19].

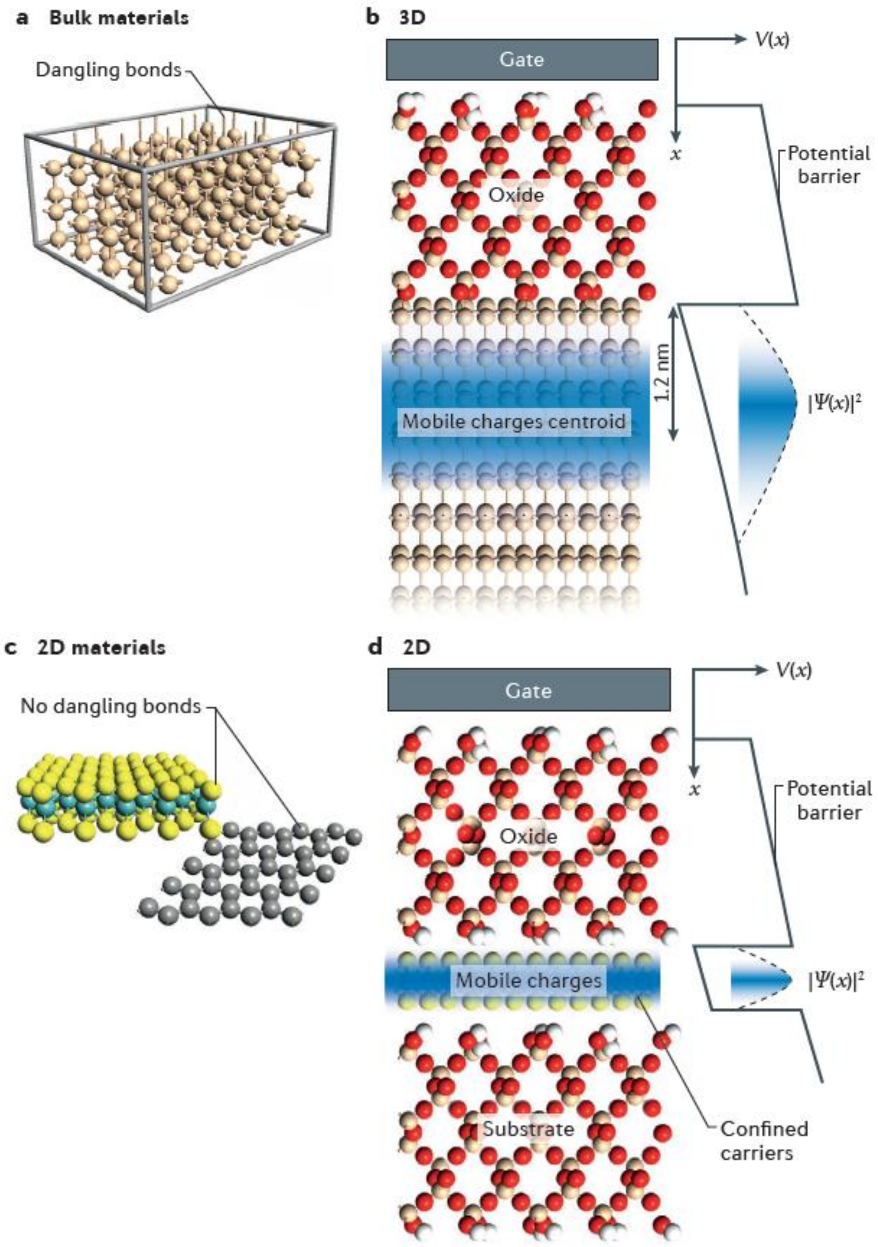

Figure 1-1. Advantage of 2D materials compared with 3D materials. (a) 3D (bulk) semiconductors reduce the performance of field-effect transistors (FETs) due to its dangling bonds that form traps for carriers. (b) Mobile charge distribution in 3D semiconductors and gate electrostatics. (c) 2D materials exhibit pristine surfaces. (d) In atomically thin materials, charge carriers are confined, resulting in a narrower mobile charge distribution. The confinement of charge carriers allows the mobile electrons to be easily controlled by the gate voltage[2].

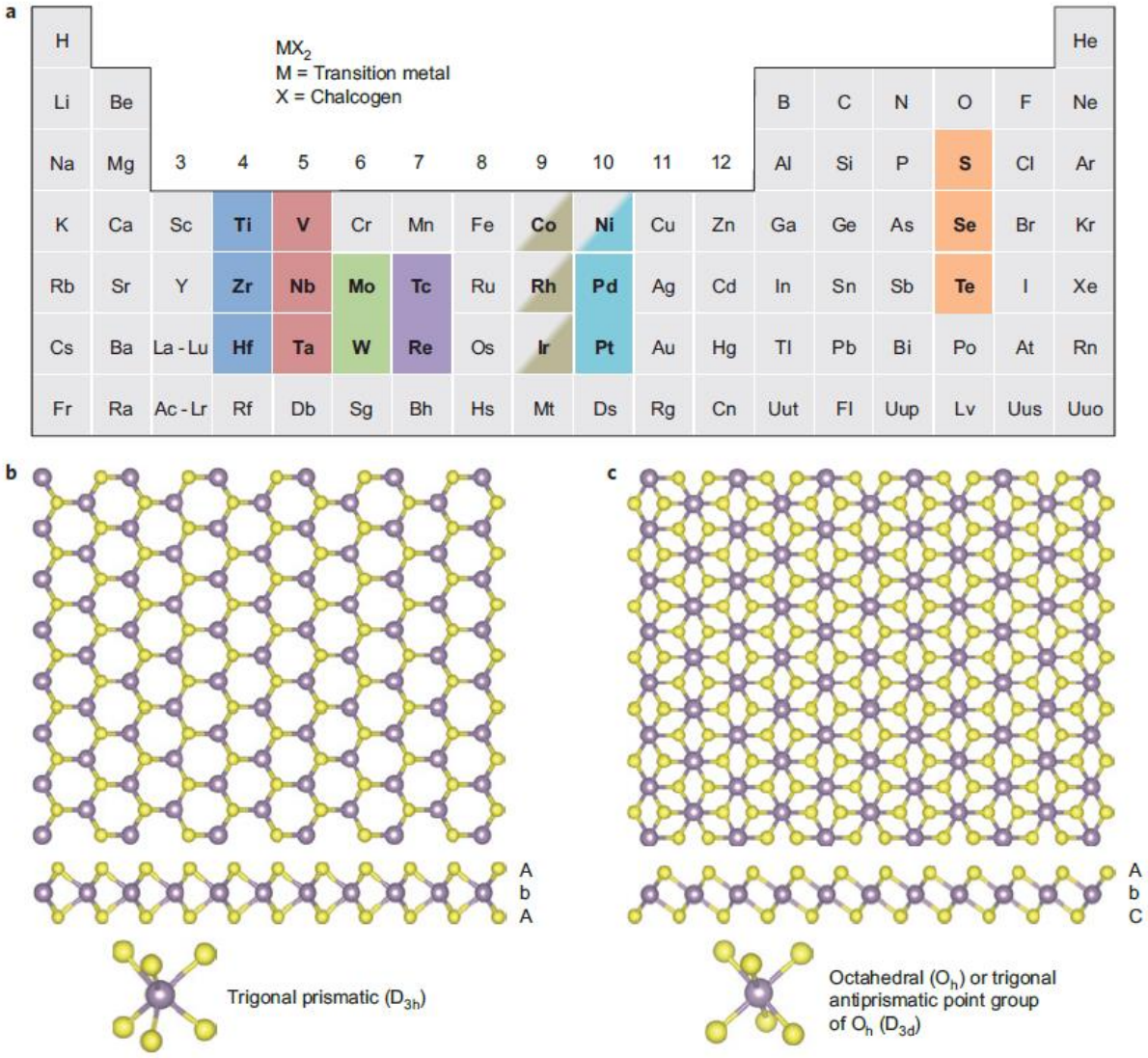

Figure 1-2. Structure of single-layered TMDs. (a) In the periodic table, the transition metals (M) and three chalcogen (X) elements that predominantly crystallize in those layered structure are highlighted. (b,c) c-axis and section view of monolayer TMDs with (b) trigonal prismatic and (c) octahedral coordinations (Atom colour code: purple- metal, yellow- chalcogen)[12].

Table 1-1. Comparison of the group-VI layered TMDs.

	Semiconducting TMDs					Semimetal TMDs	
Materials	**MoS_2**	**$MoSe_2$**	**$MoTe_2$**	**WS_2**	**WSe_2**	**$MoTe_2$**	**WTe_2**
Phase	2H (trigonal prismatic)					1T' (octahedral)	
Band gap	1.80	1.38	1.07	2.1	1.75	-0.20	-0.21
Mobility [$cm^2V^{-1}S^{-1}$]	0.01-200	0.01-23	5-12	12	7.3	10^3-10^4	
Spectral range	Visible, UV		NIR, Visible, UV	Visible, UV		THz, FIR, MIR, NIR, visible, UV	

1.1.2 Synthesis of TMDs

Low-dimensional TMDs have attracted significant attention due to their exotic properties associated with their defined dimensionalities. Due to unique electronic properties and high specific surface areas of low-dimensional TMDs, it has been seen as a promising and ideal candidates in various fields including optoelectronics, catalysis, flexible and wearable electronic devices. To achieve the practical applications mentioned above, developing controllable and scalable synthesis method of atomically thin or few-layer TMDs with layer controllability and large-area uniformity must be an essential requirement.

So far, lots of different ways have been developed[20-23], as presented in table 1-2. Until now, both *top-down* exfoliation and *bottom-up* synthesis methods are developed for preparation of atomically thin or few-layer TMDs.

Top-down exfoliation methods, such as mechanical exfoliation and chemical exfoliations, are method to separate single- or few- layers TMDs from their corresponding bulk TMDs. The individual layers of the 3D bulk material can be successfully separated from each other. This common top-down method have been studied widely, but there are some problems in obtaining reproducibility for large-area thin layers and difficulty to scale up.

Bottom-up methods may present alternative approaches. The chemical vapor deposition technique (CVD) has shown great promise to gain high-quality TMDs layers with a scalable size, controllable thickness. But they still need to be developed further to attain high-quality and large-area TMDs on the desired substrates. The large area and uniform synthesis of low-dimensional TMDs has remained a challenge for a long time. Table 1-2 also shows the conventionally used bottom-up synthesis methods and advantages/disadvantages of them. The synthesis methods include solid-precursor based vapor phase deposition, vapor phase chalcogenization, vapor-precursor based chemical vapor deposition. These scalable synthesis techniques enable to produce highly-crystalline large-area 2D TMDs crystals for wafer-scale and have tremendous potential for manufacturing in future nano-electronics.

Currently, most promising scalable synthesis technique is vapor phase deposition. In general, vapor phase deposition methods relies on physical transport (usually with inert carrier gases) and chemical reaction of vaporized precursors to deposit TMDs onto the desired substrate.

In terms of the initial precursor state, vapor phase deposition technique can be classified into solid- and gas-precursor based vapor phase technique. Firstly, there are two classes of solid-precursor based vapor phase deposition technique: (1) chemical vapor deposition (CVD) based on the reaction of solid-metal and chalcogen precursors, where both solid- metal precursors and chalcogen powders are heated into the vapor phase, and then transported to form TMDs layers; (2) chalcogenization of pre-deposited film based precursor, where the metal (or metal oxide) thin films are firstly deposited onto the substrates, then chalcogen powders are heated to be vapors and transported to the substrates to produce TMDs

films by conversion of the pre-deposited metal(metal oxide) film into TMDs films at the atmosphere of chalcogen vapors[24], as shown in figure 1-3a.

In addition, recent studies have also employed gas-precursors to improve the controllability during vapor phase growth. The reaction of gaseous metal and chalcogen feedstocks is illustrated in figure 1-3a. Here, the H_2 gas can be used for promoting the reduction of precursors. The desired substrates including SiO_2, quartz, mica and sapphire can be used (figure 1-3b) due to their high thermal stability and chemical inertness. The hexagonal crystal structure of quartz, mica and sapphire also helps to arrange the absorbed TMDs molecules.

Table 1-2. Table showing the different growth methods for layered TMDs.[1, 12, 19-24]

Technique		Schematics showing each technique	TMDs available to date	Achievements	Challenges
Top-down	Mechanical exfoliation	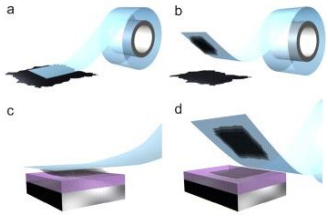	**Single phase TMDs** (MoX_2, WX_2, etc.)	High crystallinity	Thickness control, Yield, Not scalable
	Liquid exfoliation	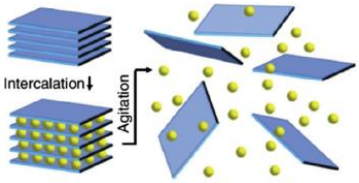		High productivity	Small crystallites, Thickness control, Yield
Bottom-up	Solid-precursor vapor phase deposition	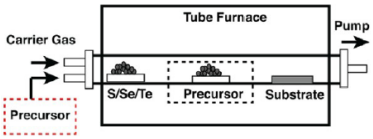	**Single phase TMDs** (MoS_2,$MoSe_2$,WS_2,WSe_2) **TMDs alloy** ($Mo_xW_{1-x}S_2$) **Doped TMDs** (Mn-, Co-doped MoS_2) **Hetero-structures** (MoS_2-WS_2,WS_2-BN MoS_2-graphene etc.)	High scalability, Hetero-structure availability	Defects, Stoichiometry control, Crystal quality
	Vapor phase chalcogen-ization	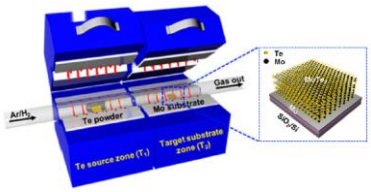	**Single phase TMDs** (MoS_2, $MoTe_2$,WSe_2 etc.) **Hetero-structures** (MoS_2-WSe_2-graphene)		Defects, Stoichiometry control, Crystal quality
	Gas-precursor vapor phase deposition	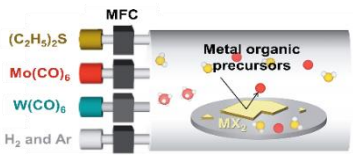	**Single phase TMDs** ($MoSe_2$,WSe_2)		Defects, Crystal quality

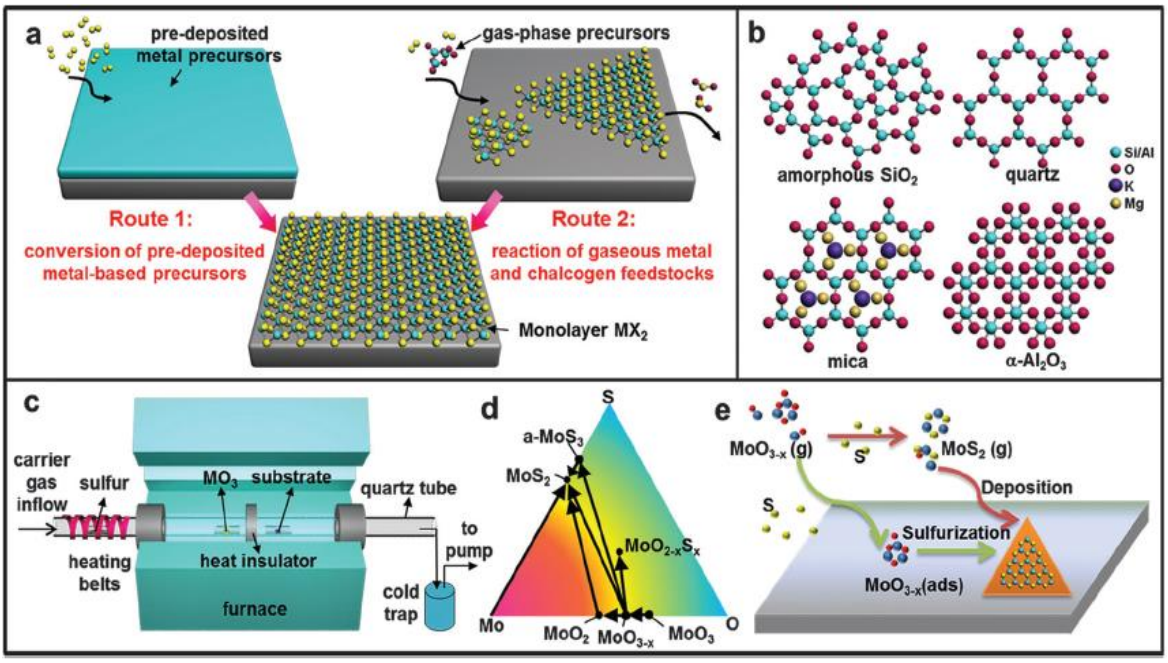

Figure 1-3. Introduction to the CVD synthesis of MX_2 thin layers. (a) Two routes for synthesis of MX_2. (b) Commonly used the insulating desired substrates for MX_2 growth. (c) Typical setup of a LP-CVD system. (d) Mo–S–O ternary phase diagram, in which the labelled arrows indicate reaction pathways for the CVD growth of MoS_2 from MoO_3 precursors. (e) Possible growth processes of MoS_2 by the reaction of S and MoO_{3-x}[24].

1.2 Tungsten ditelluride (WTe_2)

1.2.1 Introduction of WTe_2

Layered group-VI TMDs have been investigated widely because of its noticeable unique characteristics when thinned down from bulk to nanoscale. However, the semi-metallic TMDs such as tungsten ditelluride (WTe_2) and molybdenum ditelluride ($MoTe_2$) have not been examined relatively compared to the semiconducting TMDs. As shown in figure 1-4, the semi-metallic WTe_2 crystal exhibit a distortion of the octahedral 1T structure[25]. The tungsten atoms in the Td crystal structure are octahedrally coordinated by tellurium with alternating long and short distances between tungsten atoms due to strong intermetallic bonding. Even though $MoTe_2$ can have either 1T'- or 2H - phases and show the reversible structural phase transition by external stimulation such as strain and temperature[26-27], WTe_2 only crystallizes in distorted octahedral phase (1T' or Td) in nature among several polymorphs, regardless of growth condition and external strain.

It is found that WTe_2 has its stable energy in a distorted 1T (Td) structure and semi-metallic electronic characteristics[17, 28-29]. Figure. 1-5 shows the calculated band structure of 2H- and 1T'- WTe_2. While the 2H-phase WTe_2 has an indirect 0.702 eV bandgap, 1T'-WTe_2 has small overlap of electron and hole pockets at the Fermi energy along the Γ direction (corresponding to the a-axis, along the tungsten chains in crystal), indicating its semi-metallic properties. Figure. 1-6 shows the representative x-ray diffraction (XRD) patterns of WTe_2 experimentally grown by chemical vapor transport method, with the theoretical XRD patterns of 1T'- and 2H- phase WTe_2.

The semi-metallic properties of WTe_2 can be confirmed directly by using temperature-dependent resistance measurements. In general, the resistivity of a metal decreases linearly as the temperature decrease. Regarding the resistivity of metal at zero kelvin, there are only scattered electrons caused by crystal defects such as grain boundaries, impurities, etc. In semiconductor, the resistivity decreases at the elevated temperature induced by excitation of carriers. Therefore, characterization of temperature-dependent resistivity allows us to recognize whether the materials is a semiconductor or metal. Figure. 1-7 exhibits the typical temperature-dependent resistivity of layered WTe_2 crystal with different thickness, showing a well-metallic behavior of WTe_2 on temperature dependence. Moreover, extraction of residual-resistivity ratio (RRR=ρ_{300K}/ρ_{oK}) is a good indicator of crystal quality, the relationship between the electrical mobility and RRR is indicated[30], in figure 1-8.

The vibrational behavior of WTe_2 can be explored by using the incident photon energy via Raman spectroscopy[31]. Raman spectroscopy measurements is an useful technique as the fingerprint recognition

for confirming the existence of the material and assuming its thickness of WTe_2, already commonly used in the research of graphene and other 2D materials. Figure 1-9 (a) shows the representative Raman spectra of WTe_2, as a function of its thickness. The Raman spectrum of WTe_2 shows four main peaks approximately at 118, 134, 164, and 212cm^{-1}, and they are noted as the A_1^3, A_1^4, A_1^7 and A_1^9, respectively. The simulated lattice vibration of the Raman modes in bulk WTe_2 is illustrated in figure 1-9b, as well.

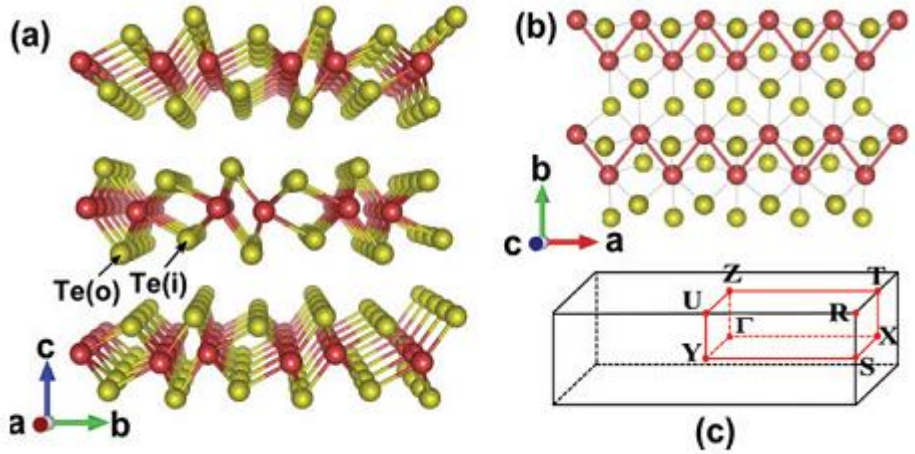

Figure 1-4. Crystal structure of WTe_2 viewed along (a) the a-axis (parallel to the zigzag W-W chains) and (b) the c-axis (perpendicular to the stacked layers); (c) the corresponding Brillouin zone. The red and yellow balls represent W and Te atoms, respectively[25].

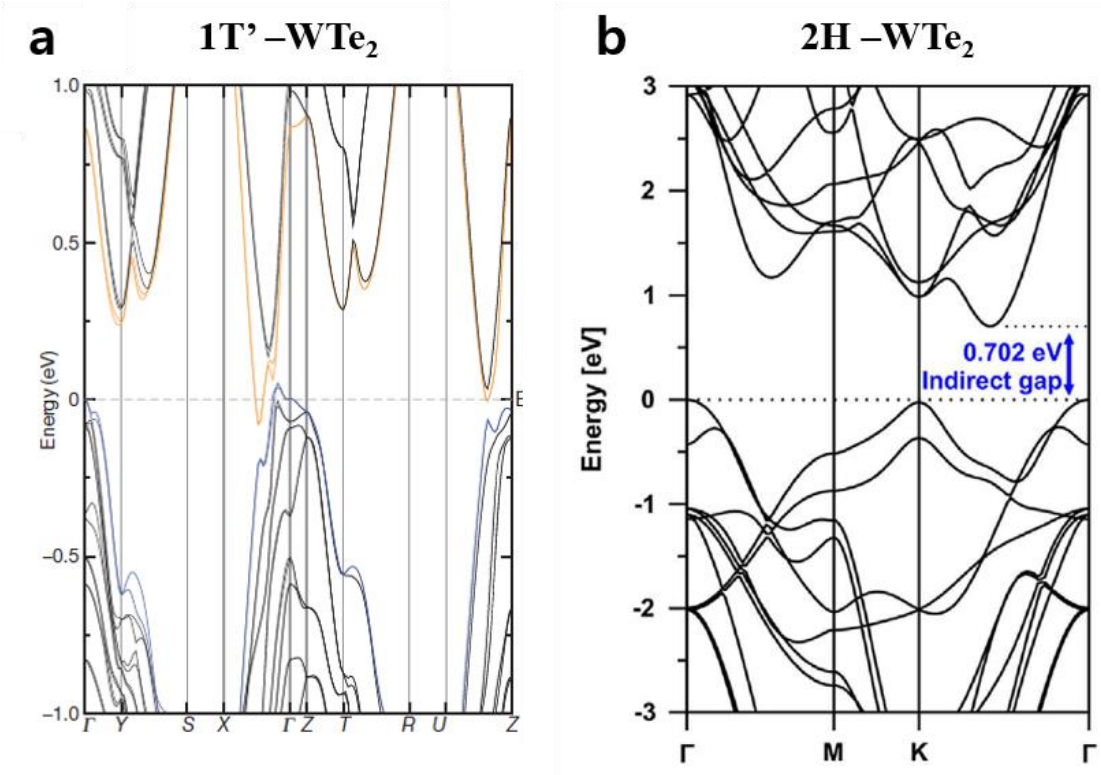

Figure 1-5. The electronic band structures indicate that bulk WTe_2 (a) in the 1T' phase has a 0.21 eV band overlap and (b) in the 2H structure has an indirect 0.702 eV bandgap[17, 28].

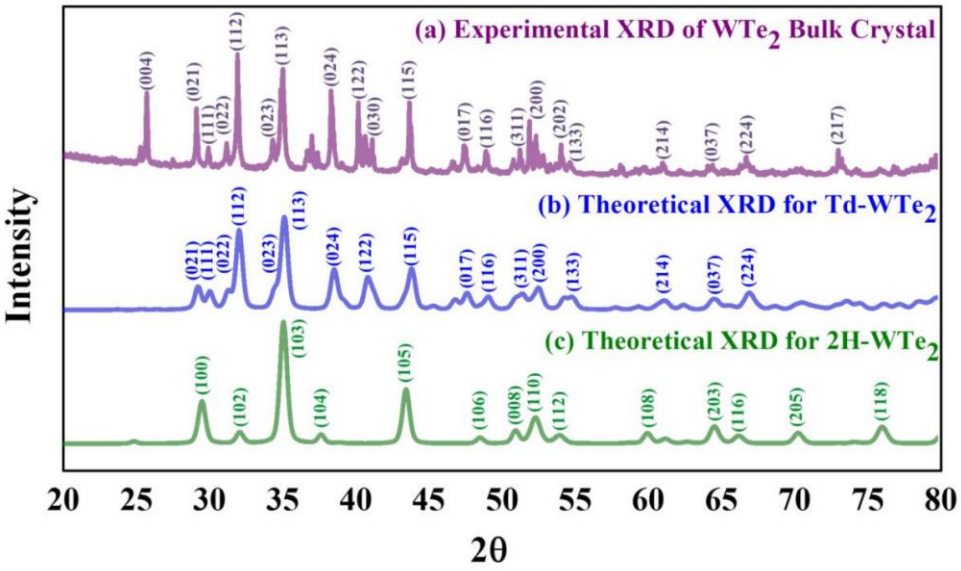

Figure 1-6. The representative X-ray Diffraction Patterns (XRD) for (a) experimental WTe_2 bulk crystal; (b) theoretical 1T' (or Td) WTe_2; (c) theoretical 2H-WTe_2[28].

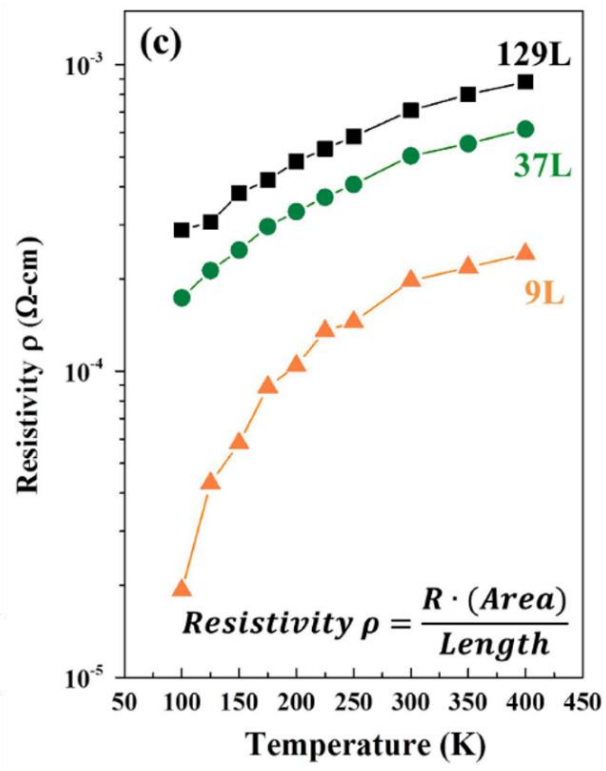

Figure 1-7. The temperature-dependent resistivity depending on the WTe_2 layer thickness, showing the WTe_2 is metallic in nature (resistivity proportional to temperature) rather than the semiconducting behavior[28].

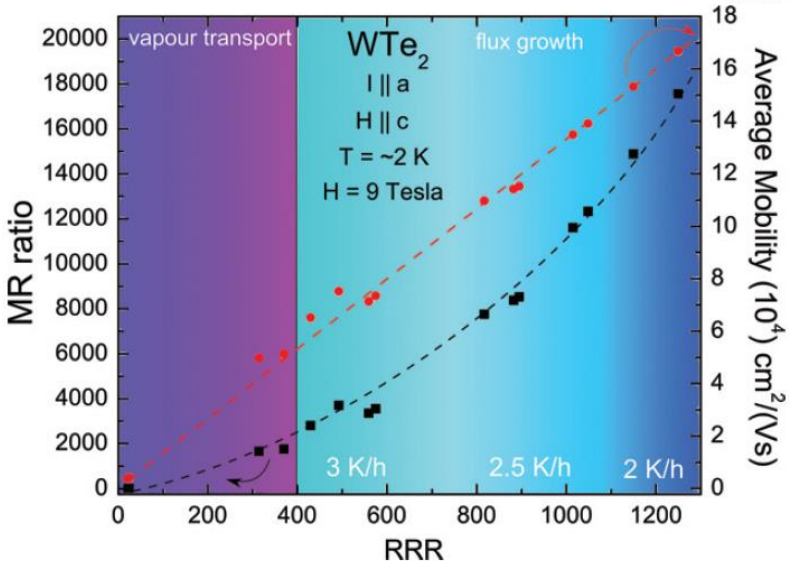

Figure 1-8. MR ratio and average carrier mobility vs. RRR. MR ratio follows the left axis (black squares) while μ_{avg} follows the right axis (red circles)[30].

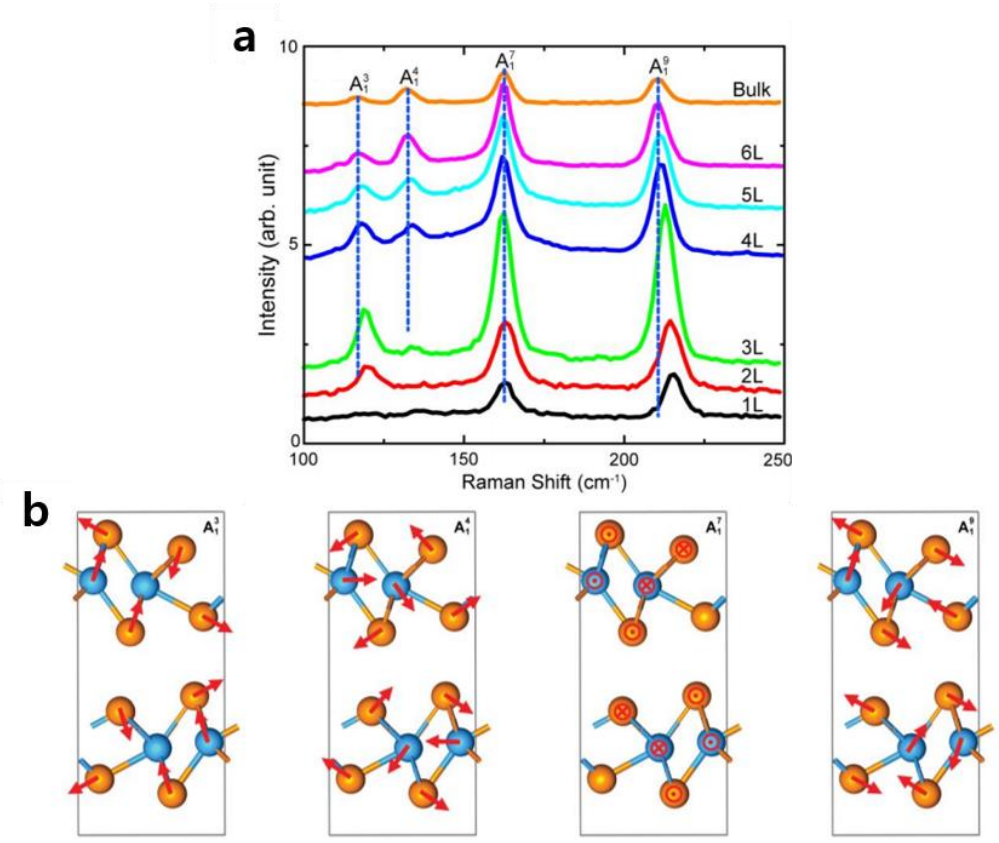

Figure 1-9. (a) The Raman spectra of and mono- to six-layer and bulk WTe_2. The blue dashed lines indicate the frequencies of the Raman modes in bulk WTe_2; (b) Atomic illustration for the lattice vibrations of the Raman modes in bulk WTe_2[31].

1.2.2 Conventional Synthesis Methods of WTe_2

Many researchers have tried several growth techniques for making the WTe_2 crystal either in bulk and nanoscale form, but synthesis of nanostructured-WTe_2 has not been reported yet, in contrast with any other TMDs.

Currently, single-crystalline WTe_2 in bulk form has been synthesized by chemical vapor transport methods or solid state reaction, and these methods produce only bulk crystal[17,28,32,39,40]. Previously, most of the studies on WTe_2 crystal have been demonstrated in mechanically or chemically exfoliated layers (flakes) from the bulk crystal. Accordingly, investigation of WTe_2 with controlled its thickness has been limited. Moreover, these methods are highly unsuitable for mass production because a high growth temperature (~1000°C) and growth time for several days (usually more than 24 hours) must be required, as shown in Table 1-3.

Synthesis of nanostructured-WTe_2 was very challenging due to the high vapor pressure (low sublimation temperature) of tellurium and low reaction activity of tungsten with tellurium. In chemical vapor deposition process, the probability of creating nucleation sites is extremely low because of the Te deficiency because desorption of tellurium vapor precursors occurs easily. For these reasons, making the Te-rich condition is critical to synthesize WTe_2 nanostructures. To obtain stoichiometric and nucleate tungsten ditelluride crystal, desorption of tellurium vapor precursor must be prevented and activate tungsten atoms to be reacted with tellurium precursor.

Table 1-3. Conventional growth methods of WTe_2 single crystal, only obtaining bulk crystal.

Growth method	Crystal Type	Growth temperature	Growth time	Transport agent	References
Chemical Vapor Transport	bulk	950°C	7 days	Br_2	[28]
	bulk	890°C	4 days	WCl_6	[32]
	bulk	750°C	7 days	Br_2	[17]
Solid state reaction	bulk	1100°C	96 hr	None	[39]
	bulk	1000°C	5hr	None	[40]

1.2.3 Unique Properties of WTe_2

1.2.3.1 Large & Unsaturated Magnetoresistance (MR) in WTe_2

The investigation of WTe_2 has been attracted significant attention since an unusual magnetoresistance (MR) in WTe_2 crystal was discovered in 2014. Mazhar N. Ali et.al[17] reported the observation of an extremely large positive magnetoresistance: 13 million percent at 0.53 kelvins in a magnetic field of 60 T (Teslas), as displayed in figure 1-10.

MR is defined as a change in material's electrical resistance (ρ) in response to an applied magnetic field H and is expressed as $\mathrm{MR} = [\rho(\mathrm{H}) - \rho(0)]/\rho(0)$. The large MR can be observed also in other semimetals such as bismuth and graphite because of the compensated hole-electron resonance; however, the unsaturated MR in WTe_2 up to 13,000,000% at 0.53 K in an applied magnetic field of ~60T is quite unique. This extraordinary MR behavior in WTe_2 is known to originate from a nearly perfect compensation of electron and hole concentrations (first known material for nearly perfect resonance) and this is explained by two band model for magneto-transport in semimetals. In two band theory, the MR is given by as follows:

$$MR = \frac{\Delta\rho}{\rho} = \frac{\rho_{xx}(B) - \rho_{xx}(0)}{\rho_{xx}(0)} = \mu_e \mu_h B^2 \ (if\ n = p)$$

, where μ_e and μ_h is the mobility of the electrons and holes, respectively, and B is the applied magnetic field (n=p, where n and p are the electron and hole concertation, respectively)[32].

In semimetals, large positive magnetoresistances are attributed to a balanced electron–hole 'resonance' condition; the positive MR is proportional to B in nearly perfectly compensated semimetal of WTe_2. In this regard, it is expected that WTe_2 has potential to be applied in magnetic field sensing device with extremely high sensitivity, especially at low temperatures, as displayed in figure 1-11.

1.2.3.2 Type-II Weyl fermion in bulk WTe_2

Interestingly, the existence of new type of Weyl point (type-II Weyl point) in WTe_2 was discovered[35]. Whereas Weyl semimetals hosting Weyl fermions were previously recognized to have Weyl point with a point like Fermi surface (referred as type-I)[36], the Weyl point appears at the contact of hole and electron pocket in type-II Weyl semimetal. The new type-II Weyl points exist at the boundaries between hole and electron pockets, as illustrated in figure 1-12. The existence of type-II Weyl fermion at the

boundary between hole and electron pockets in new phase of matter in WTe_2 crystal are expected to explore new physical properties and phenomena arising in the new topological semimetal phase (being different to those of standard Weyl semimetals with point-like Fermi surface) and as a potential platform for the realizing novel Weyl semimetal applications.

1.2.3.3 Quantum spin Hall effect in Nanostructured WTe_2

Layered WTe_2 are layered compounds that can be mechanically exfoliated, therefore very promising for achieving stable 2-dimensional QSH phase. A Monolayer 1T′-WTe_2 was predicted to be quantum spin hall (QSH) semi-metallic materials with QSH gaps[37]. Feipeng Zheng et.al revealed that computational and experimental results all point to one clearly promising possibility, that monolayer 1T′- WTe_2 is a QSH insulator with a positive band gap[38]. In figure 1-13, optical measurements (transient reflection experiment, optically probed transient carrier dynamics) are performed on ultrathin 1T′- WTe_2 layer, showing a systematic increase in the interband relaxation time as the number of layers decreases. Electro-transport characteristics of the sample also exhibits Schottky barrier in atomically thin samples, which is absent for thicker samples, as indicated in figure 1-14. These independent pieces of evidence clearly indicate that monolayer 1T′-WTe_2 is a truly 2D QSH insulator, but further researches should be conducted more.

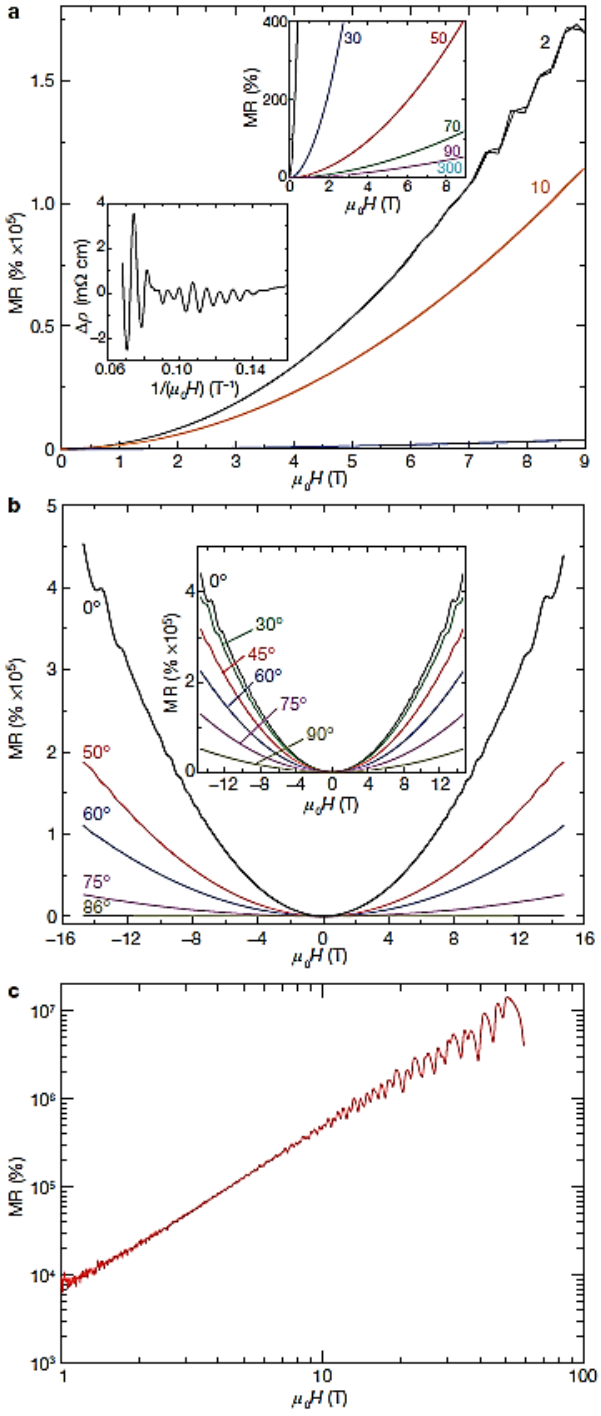

Figure 1-10. Field and angular dependence of the XMR in WTe_2 crystal. (a) Field dependence of the XMR in WTe_2 with the current along the a-axis (W–W chains) and the applied field parallel to the c-axis. (b) Angular dependence of the XMR in WTe_2 crystal at 4.5K. (c) XMR of WTe_2 up to 60 T at 0.53 K, with I parallel to a-axis and H parallel to c-axis[17].

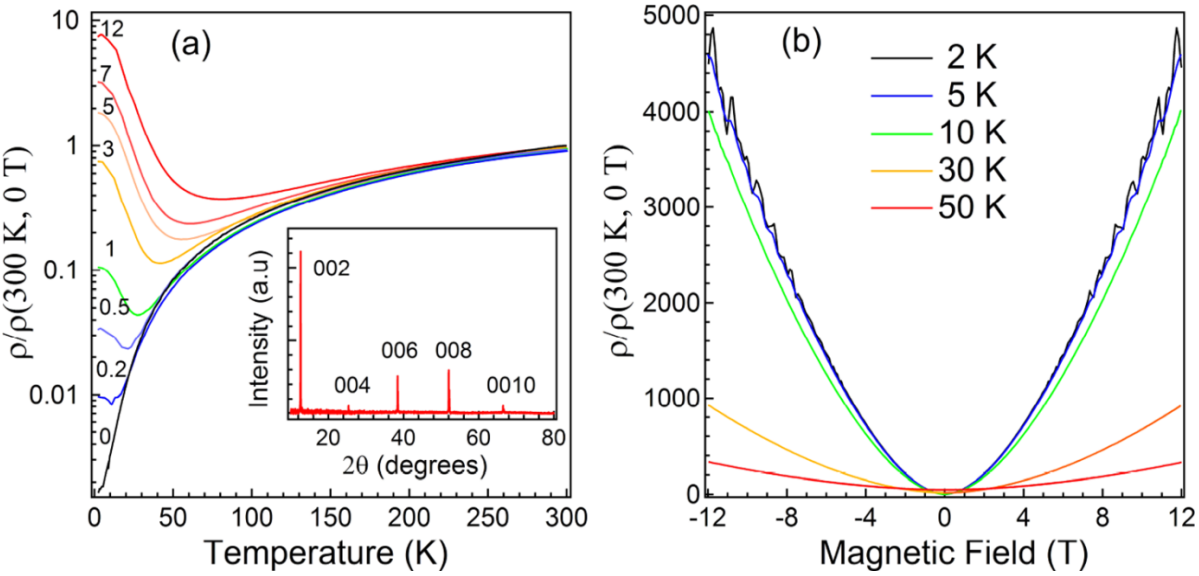

Figure 1-11. Temperature and field dependence of the MR in WTe_2, with the current along the W–W chains (a-axis) and the applied field parallel to the c-axis. (a) Normalized resistivity (at 300K and 0 T) as a function of temperature, with different magnitudes of the external magnetic field. (b) MR of WTe_2 at different temperatures[34].

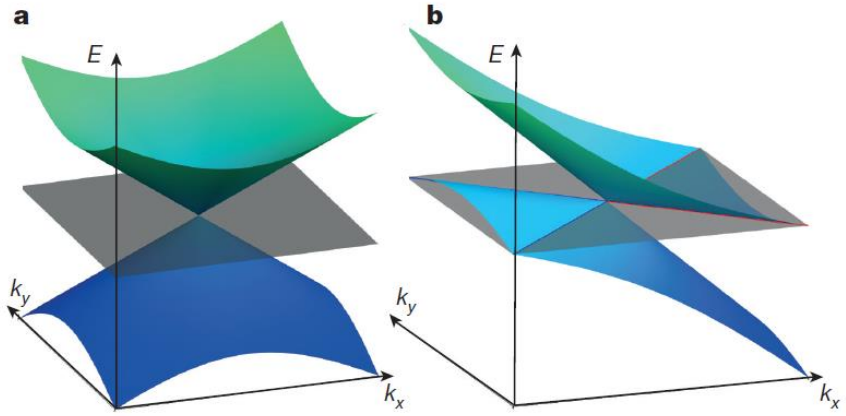

Figure 1-12. (a) Type-I Weyl point with a point-like Fermi surface, (b) A type-II Weyl point appears as the contact point between hole and electron pockets. The grey plane is the position of the Fermi levels[35].

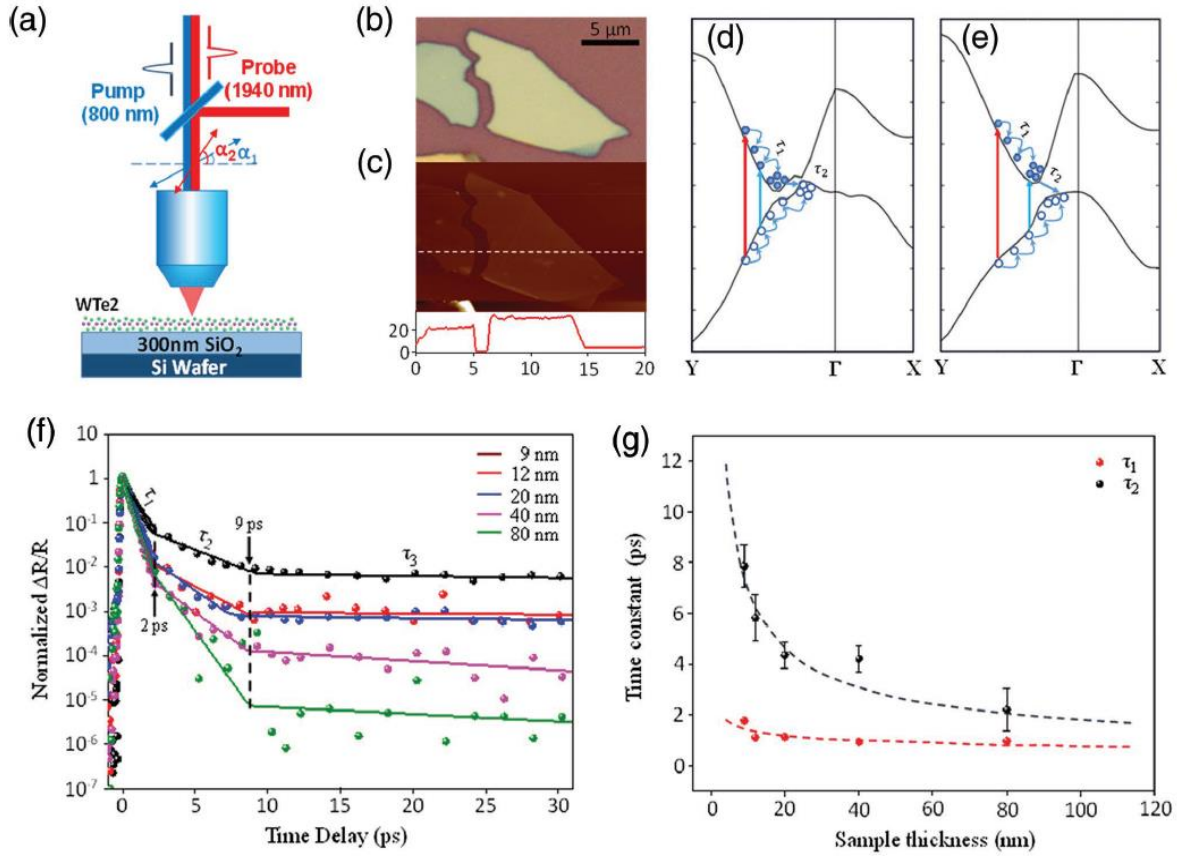

Figure 1-13. Experimental data of optical measurements of QSH nanomaterial WTe_2. (a) Schematic diagram of transient reflection experiment. (b) The OM Image and (c) AFM Image of a WTe_2 used with thickness of 20 nm. Schematic band diagram and carrier relaxation dynamics of (d) bulk and (e) monolayer 1T′-WTe_2 crystal and pump (blue) & probe (red) photon transition configuration. (f) The normalized transient reflection spectrum of 1T′-WTe_2 with different thicknesses. (g) τ_1, τ_2 as functions of the sample thickness[38].

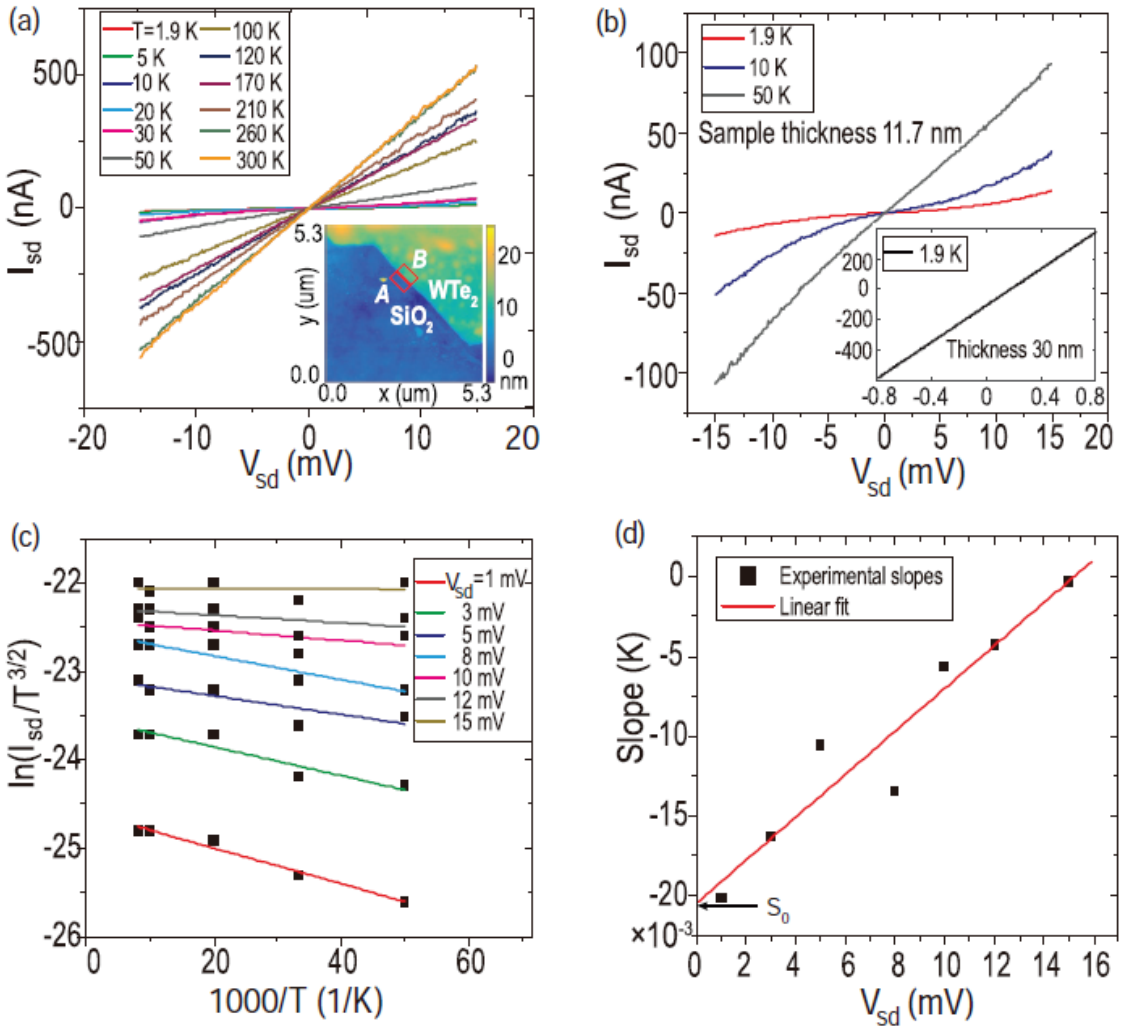

Figure 1-14. Experimental data of (a) I–V curves of an 11.7 nm thick 1T′-WTe_2 sample from 1.8 to 300 K and (b) three low temperatures (1.8, 10, 50 K). (c) Arrhenius plot of ln ($I_{sd}/T^{3/2}$) versus the inverse of temperature and linear fits. (d) Slopes of linear fits in (c), S_0 suggests the value of Schottky barrier of the 1T′-WTe_2 device[38].

1.3 Preceding Researches on Eutectic Metal Alloy Assisted Crystal Growth

Here, some previous researches for the crystal growth by means of eutectic metal alloys are introduced. In this growth mode, the reaction between gas precursors and pre-deposited metal catalyst would make liquid state eutectic alloys above its eutectic temperature. This as-reacted liquid eutectic alloy will have catalytic effect, assisting synthesis of desired nanostructures from the supersaturated liquid eutectic phase. This fundamental principle has been widely used in nanowires' fabrication via the vapor-liquid-solid (VLS) mechanism. Moreover, eutectic metal alloy assisted synthesis of WS_2 and WC nanostructure were investigated, showing the possibility of applying this growth mode to make nanostructured WTe_2. Therefore, review of the preceding researches on eutectic metal alloys assisted nano-crystal growth for low-dimensional nanostructure is very important.

1.3.1 Vapor-Liquid-Solid (VLS) Growth

Figure. 1-15 shows a schematic of the conventional VLS synthesis mechanism for 1D structured nanowire. Since the *vapor* precursor, *liquid* state alloy, and *solid* nanowires are involved in this mode, thus this growth mechanism is called as the VLS (vapor-liquid-solid) process. In this VLS growth mechanism, the pre-deposited metal catalyst forms droplets of a liquid state metal alloy by reacting with supplied vapor precursors (eutectic reaction) over the eutectic temperatures. At the elevated temperature, the vapor flux is absorbed into the catalytic liquid metal alloys to supersaturation level, holding the higher concentration of precursor elements originally from the gas source. Then, crystal growth can subsequently occurs at the vapor-liquid interface, precipitating out supersaturated solid 1D-nanowires. To be specific, the liquid state eutectic metal alloy can act as vapor flux reservoir and nucleation helper of nanowires. Nanowires can be grown only in the areas activated by the metal catalysts and the size and position of the nanowires are determined by that of the metal catalysts.

Previous researches demonstrate that metals which encounter the requirements for pre-deposited metal catalysts can be used in the VLS mechanism[41]. First, these metals must react with gas precursor and then form a liquid solution. Secondly, the equilibrium vapor pressure of the catalyst over the liquid alloy should be small, so the droplet does not vaporize during growth.

The most widely researched VLS process is a growth of Si nanowire assisted by Au particles which adsorb Si from the vapor state. Figure. 1-16 shows the phase diagram of Au-Si system. Here, the eutectic point is 364^{o}C, which means that this VLS process is conducted at elevated temperature over the eutectic temperature, resulting in the formation of supersaturated liquid alloy withheld pure solid elements that can be precipitated out. Au can form a solid-solution with Si (concentrations up to 100%) until reaching

a supersaturated state of Si in Au (the composition of liquid Au-Si alloy track the liquidus line). Consequently, Si atoms precipitate out of the supersaturated liquid state metal alloy droplet at the liquid-alloy/solid-Si interface, resulting that crystal growth can subsequently occur from the nucleated seeds.

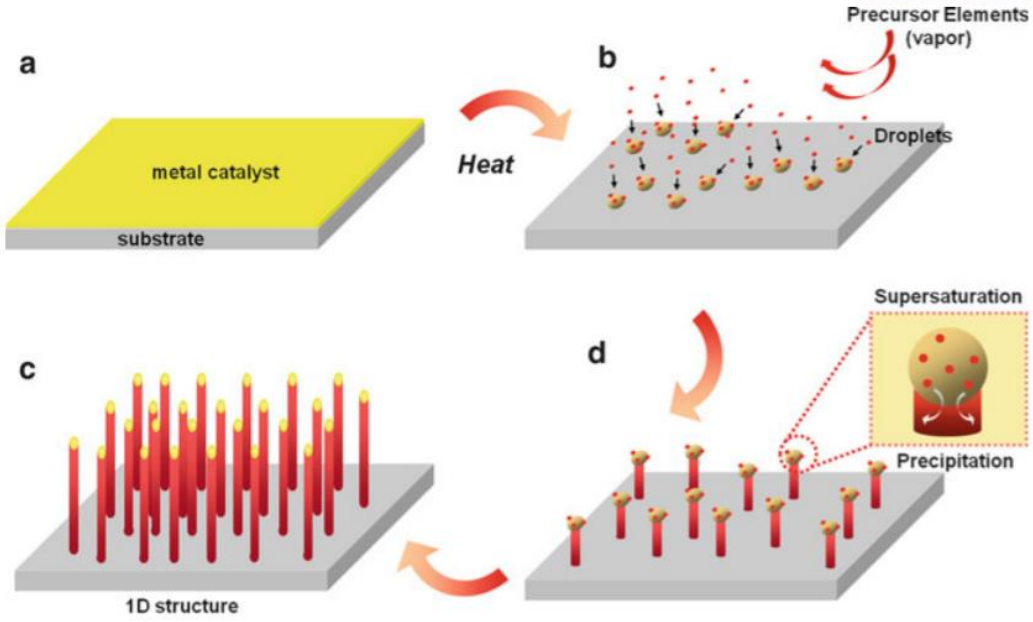

Figure 1-15. Growth of 1D nanostructures by VLS mechanism[41].

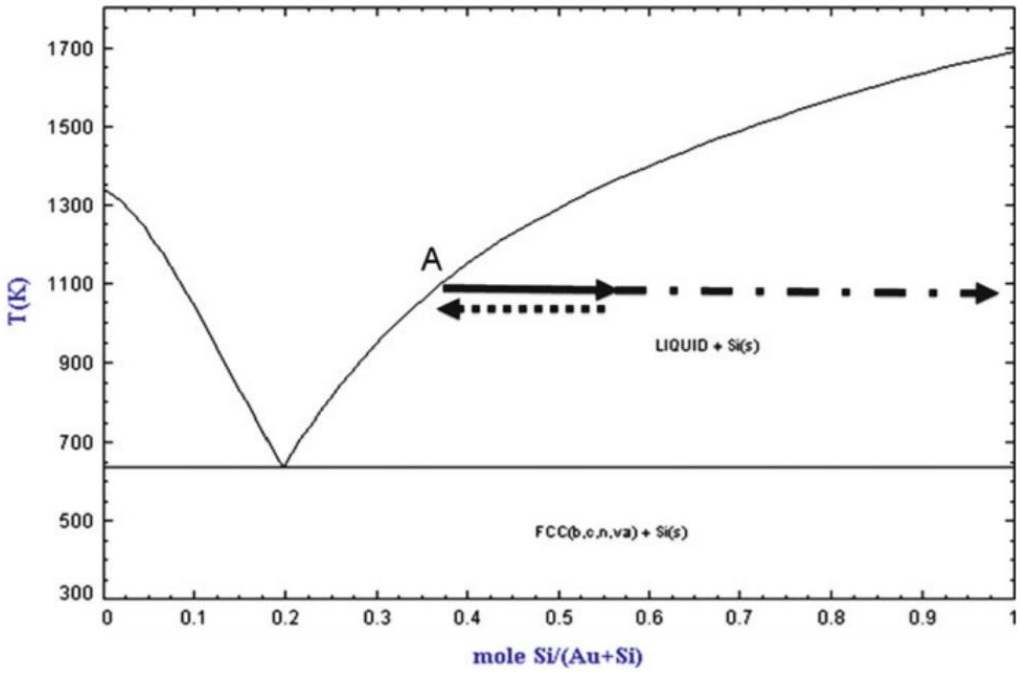

Figure 1-16. Phase diagram of Au–Si system which indicates the composition of liquid metal alloy catalyst in the course of growth of 1D nanostructures by VLS mechanism[41].

1.3.2 Rapid-Crystallization

The nickel sulfide (NiS_x) assisted crystal growth of WS_2 films has been reported[42,43]. The WS_2 films were prepared by the amorphous-solid-liquid-crystalline-solid (aSLcS) rapid-crystallization process from a Ni–S eutectic metal alloys. The mechanism was explained by the recrystallization induced by formation of liquid phase nickel sulfide droplets above the Ni-S eutectic temperature of 637˚C. The method of nickel sulfide promoter-assisted crystallization from the liquid phase could be powerful preparation technique for highly (001) textured WS_2 thin films with large crystallites (lateral dimensions of several micrometers), which are mainly oriented parallel to the substrate. This crystallization by the amorphous solid-liquid-crystalline solid rapid-crystallization process which is comparable with the vapor–liquid–solid (VLS) mechanism, displayed in figure 1-17.

First, amorphous WS_{3+x} was deposited onto Ni coated oxidized silicon substrate and then the substrate was heated. When the eutectic temperature of the Ni–S (T_{eu} = 637 °C) system is reached, the NiS_x crystallites become liquid state and dissolve tungsten or tungsten sulfide. When supersaturation is reached, the crystallization of the WS_2 starts at the bottom of the NiS_x droplets, leading to rapid lateral growth of WS_2 nanosheets. During the aSLcS process, a phase separation between WS_2 and NiS_x crystallites occurred, where the WS_2 crystallizes from the NiS_x:W melt. After cooling, the liquid NiS_x droplets crystallize and mainly float on top of the WS_2 nanosheets. This as-grown nanosheets can be clearly seen in the cross-sectional SEM image displayed in figure 1-18.

.

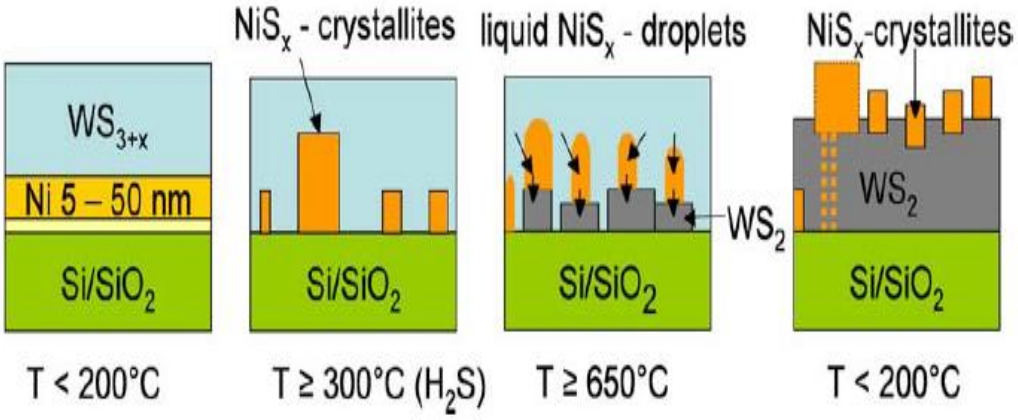

Figure 1-17. Schematic of the steps of the rapid crystallization of WS_2 by the amorphous solid-liquid-crystalline solid (aSLcS) process[42].

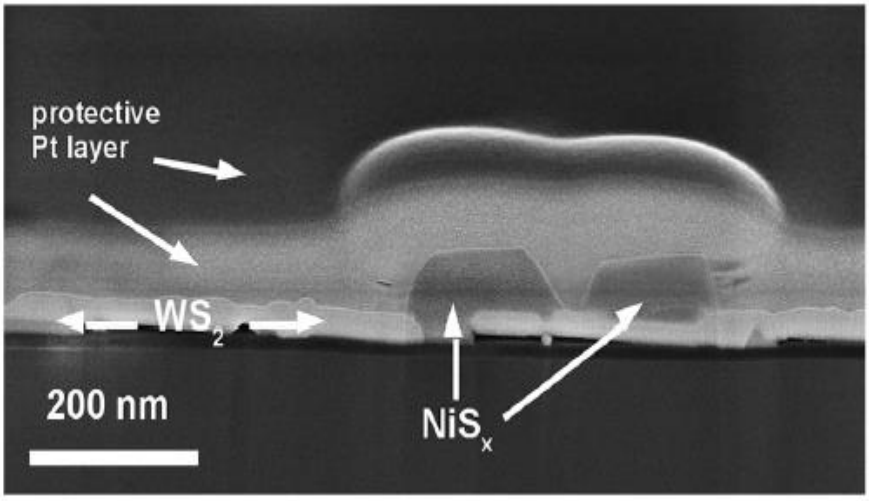

Figure 1-18. Cross-sectional SEM image of a rapidly crystallized WS_2 film. Preparation parameters: 300nm WS_{3+x}/20 nm Ni/SiO_2/Si substrate, annealed at 700˚C for 5 min[43].

1.3.3 Eutectic Solidification

A novel method to prepare low-dimensional WC nanostructure such as nanowire and nanowalls has been developed[44]. To realize the synthesis of WC nanostructure, the most serious obstacle which must be overcome is that W atoms must be provided during the growth of WC nanostructure. The key approach for supplementation of W atom is eutectic solidification in W-Al-C solution, which means a precipitation of W and C atoms in ternary W–Al–C. The active temperature of W atoms can be decreased in an W–Al environment. Transportation of C atoms through the atmosphere and W atoms enable the supplementation of W resources to be continuous through the melting liquid across the whole process. Large-scale WC nanowalls with a thickness of tens of nanometers with several micrometers in the other two dimensions were obtained through the bottom-up growth, as shown in figure 1-19. In addition, 1-D WC nanostructures can be obtained in suitable conditions.

In this work, WC nanostructures were grown on polycrystalline tungsten substrate at 1310˚C in CH_4, H_2 ambient. In detail, Al sheets were placed neared the tungsten foil. During the annealing step, Al atoms would be evaporated onto the W substrate continuously at temperature higher than 660˚C, leading to formation of eutectic metal alloys (W atoms melts in Al liquid). Continuous supplementation of Al and W atoms keeps the metal alloys in liquid state as a W-Al eutectic metal alloys. Over the temperature at 1000˚C, carbon source is introduced into the chamber from CH_4 cracking and would diffuse into the liquid, forming ternary alloys of W–Al–C. The growth of the WC nanostructures can be attributed to the eutectic precipitation in W–Al–C solution. Interestingly, there exists a solute convection area because W is supplied from bottom to top and C from top to bottom. The formation of WC nanostructure was induced by nucleation at the convection area and precipitation. The details of growth model are shown in figure 1-20.

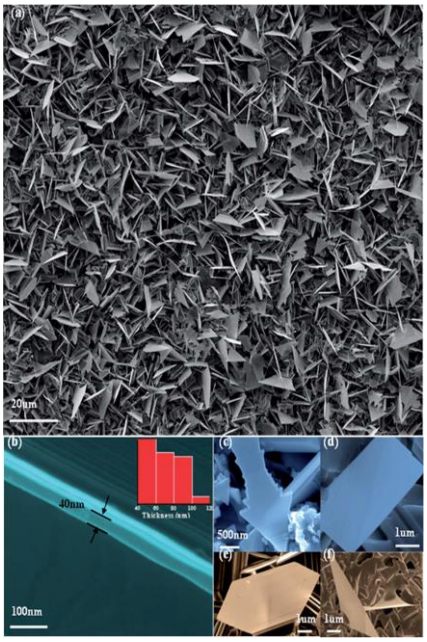

Figure 1-19. Scanning electron microscopy analysis of WC nanowalls structure. (a) Typical SEM image of as-synthesized WC nanowalls. (b) Thickness characterization of the nanowalls. (c–f) Various polygons can be found among the synthesized nanowalls but the main shape is triangle[44].

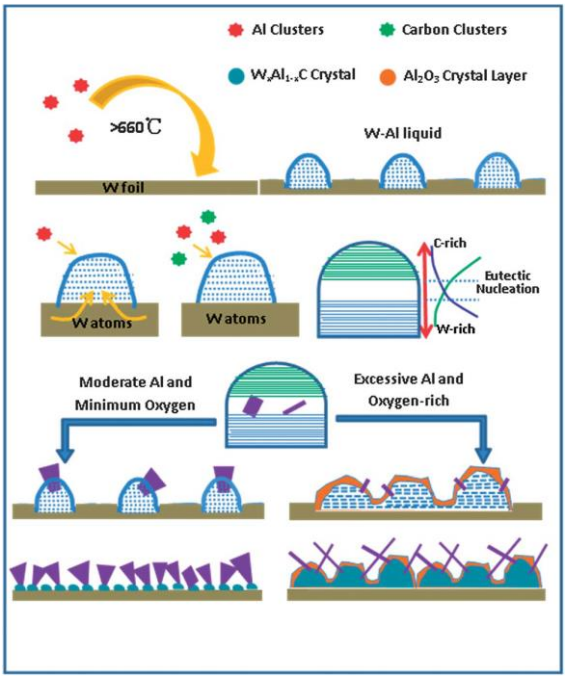

Figure 1-20. Growth model proposed for synthesis of low-dimensional WC nanostructures. The active temperature of W atoms decreased in an Al–W environment[44].

Chapter 2. Experimental Details

2.1 Deposition of Metal Films

In this study for synthesis of transition metal telluride nanostructures, we deposited 50nm-thick copper layer on a 300 nm SiO_2/Si substrate by using UHV e-beam evaporator (UEE-UHV series, ULTECH) to form eutectic metal alloys. To minimize environmental impurities and copper oxide layer on the copper film surface, the copper film was prepared in UHV main chamber, using high-purity copper solid source (99.99% Cu pellet) for deposition. Then, the tungsten layer (thickness was various depending on the experiments. e.g. 20, 100, 200, 300nm) was deposited by DC magnetron sputtering (SRN-120, SORONA) in optimized deposition condition (uniformity: less than ± 5 % within wafer). Figure. 2-1 displays the UHV e-beam evaporator and DC magnetron sputtering system used in this work.

In this work, we proposed the new type of structure of a W/Cu deposited metal layer for growth of WTe_2 nanostructures which is the inverse structure of essential structure (a Cu/W film) in previous research. In previous research, a Cu film was deposited on the pre-deposited W layer onto desired substrates (SiO_2/Si or Al_2O_3), followed by tellurization of the Cu/W/substrate at 500°C in Te atmosphere using Te powders with inert Ar gas, forming Te-rich copper telluride (Cu_xTe_y)/WTe_2/W/substrate and finally etching away Cu_xTe_y to obtain WTe_2 nanostructures on the W/substrate, as illustrated in figure 2-2.

The surface morphology of as-deposited poly-crystalline W(20nm)/Cu(50nm) was confirmed by SEM (S-4800, Hitach High-Technologies), as displayed in figure 2-3a. The size of W crystalline was confirmed by using Scherrer equation (crystalline size: ~20nm). Figure 2-3b exhibits XRD data of W(20nm)/Cu(50nm) films deposited on SiO_2/Si substrate. Moreover, feasibility of synthesis for $MoTe_2$ nanostructure as a member of the layered TMDs family was evaluated through our methods. The sample for synthesis of $MoTe_2$ nanostructure was prepared in the same way as above (Mo layer of 300nm was deposited and thickness of Cu layer was fixed).

2.2 Synthesis Methods

First of all, a W/Cu (or Mo/Cu) film deposited on SiO_2/Si was placed in a crucible containing tellurium powder (Product 264865, Aldrich). Secondly, the chamber in our furnace system (DMTF 12/150-HVAC, Daemyoung Enterprise) was evacuated to ~ 10^{-3} Torr and then filled with Ar gas to maintain atmospheric pressure and protect the system from oxygen. Figure 2-4 shows a schematic drawing of the chamber in our furnace system. The furnace was subsequently heated up to 500-600 °C and then tellurium powder

was evaporated to vapor and transported to the sample. Next, the W/Cu film is tellurized after absorption of tellurium vapor at the pre-deposited film. Here, the conversion of the pre-deposited copper films into liquid state Te-rich copper tellurides (Cu_xTe_y) droplets occurs at the atmosphere of tellurium vapors. The crystallization of nanostructures inside of Te-rich Cu_xTe_y droplets takes place at a temperature of 500 °C, above the Cu–Te eutectic temperature of 340 °C (see figure 2-5). This model describes the growth of a liquid-phase crystallization from Cu_xTe_y droplets as a role of the nucleation helper for the crystal growth of the WTe_2 and $MoTe_2$ nanostructure. Lastly, the chamber was cooled down to RT (room temperature) under atmospheric condition.

2.3 Preparation of Transition Metal Telluride Nanostructures on the Desired Substrate

First of all, in order to expose the as-synthesized transition metal telluride nanostructures in Cu_xTe_y droplets, the Cu_xTe_y droplets must be removed. For this to occur, the as-grown sample was dipped in 1M of APS (ammonium persulfates) aqueous solution for 1hr to etch the Cu_xTe_y droplet. After that, the sample was rinsed with deionized water to remove residual etchant. Through the wet etching process, we can simply get tellurides nanostructure without Cu compounds. However, the use of oxidant etchant and water induce inevitable chemical damage, leading to critical oxidation and degradation of as-synthesized products.

The as-obtained nanostructures can be easily transferred to different substrates and/or solutions by using conventional dispersion method. The nanostructures were dispersed in isopropanol (IPA) through a sonication process. Then, nanostructures were placed on the desired substrate by dispersion method and the substrate was dried at 80 °C for 10min using a hot plate. In this process, the disadvantage is that the as-synthesized nanostructures could be broken and damaged due to physical attacks during the sonication process.

To sum up, the intrinsic properties of as-synthesized nanostructures could be degraded by inevitable chemical and physical damage. In addition, fabrication of various applications has difficulties due to residue products. So-called “coffee ring effect” could be a critical problem as well, which is caused by capillary flow induced by the differential evaporation rates across the drop during the conventional dispersion methods.

To solve the problems, our approach is to mechanically peel off the Cu_xTe_y and metal layer (W and Mo layer) by using scotch tape, as shown in figure 2-6. To expose the as-synthesized nanostructures inside of the Cu_xTe_y droplets without use of chemical oxidant (APS etchant), we tried to peel off Cu_xTe_y droplets and W layer by using scotch tape. Figure 2-7a indicates the as-obtained WTe_2 nanobelts onto

desired substrate without additional chemical etching and transfer steps. This simple method of mechanical peeling off by using scotch tape can reduce the process to obtain nanostructures as well as prevent degradation of WTe_2.

2.4 Fabrication of Electronic Device

For the measurements on electrical properties of as-synthesized WTe_2 and $MoTe_2$, conventional nano-fabrication techniques (electron-beam lithography, metals evaporation and lift off) were employed to attach electrical contacts (consisting of Ti/Au bilayers, typically used 10/80 nm thick), as shown in figure 2-7b. Throughout the procedure of crystal identification and device fabrication, care was taken to minimize exposure of the material to air in order to minimize degradation. The electrical properties of WTe_2 samples with different thicknesses were investigated. The current was applied along the tungsten chains along the tungsten zigzag chains (a-axis) of WTe_2 nanostructure. Also, $MoTe_2$ was tested using two Ti/Au contacts made by a lift-off process at both edges of the synthesized $MoTe_2$ nanostructure.

(a)

(b)

Figure 2-1. (a) A UHV e-beam evaporator system (UEE-UHV series, ULTECH) used in this work for preparation of the metal (Cu) films. (b) A DC sputter system (SRN-120, SORONA) used in this work for deposition of W (and Mo) layer.

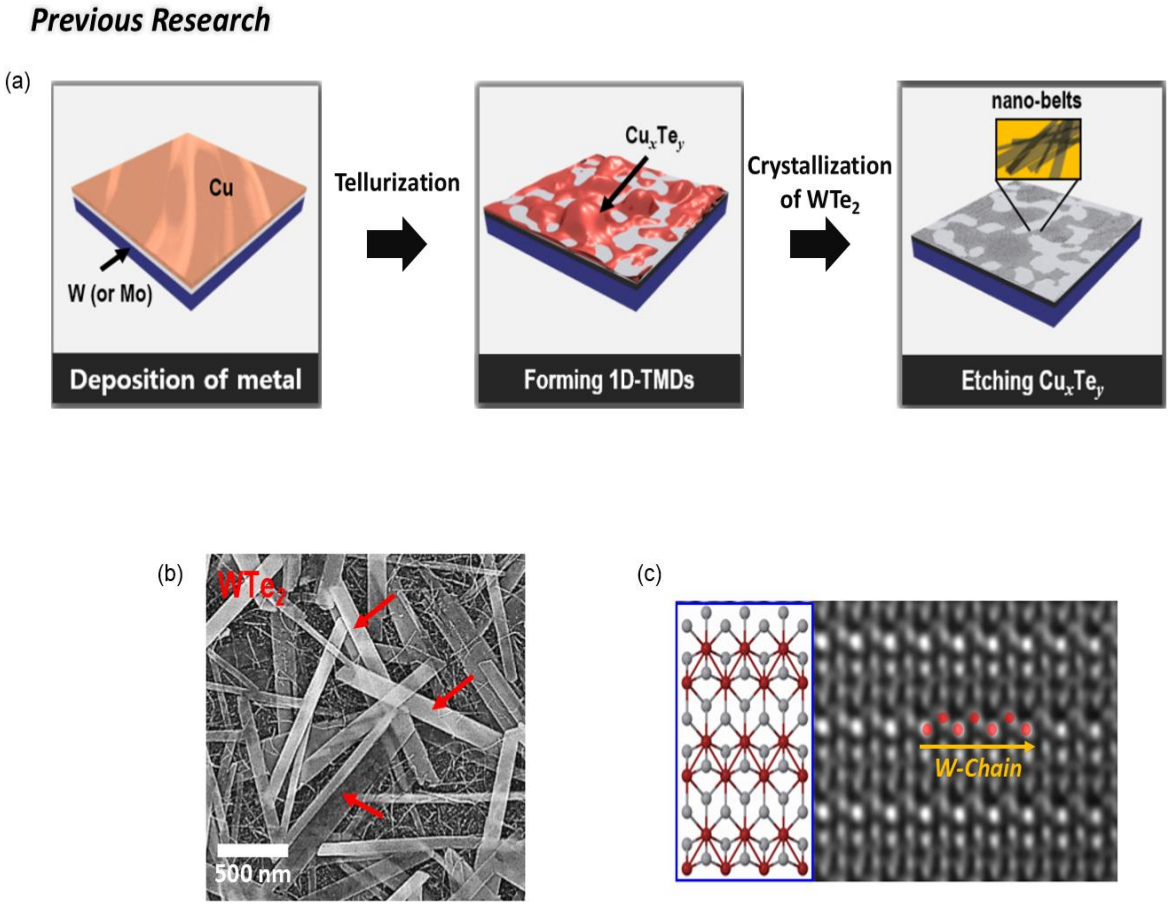

Figure 2-2. Introduction of previous research. (a) Schematic diagrams of the elementary steps for growing 1D-TMDs and obtaining WTe_2 nano-belts. In this process, a Cu film deposited on a W layer plays a key role as the Te vapor flux reservoir and promotor of improving crystallinity. Representative (b) SEM Image and (c) TEM image of the synthesized-WTe_2 nano-belts.

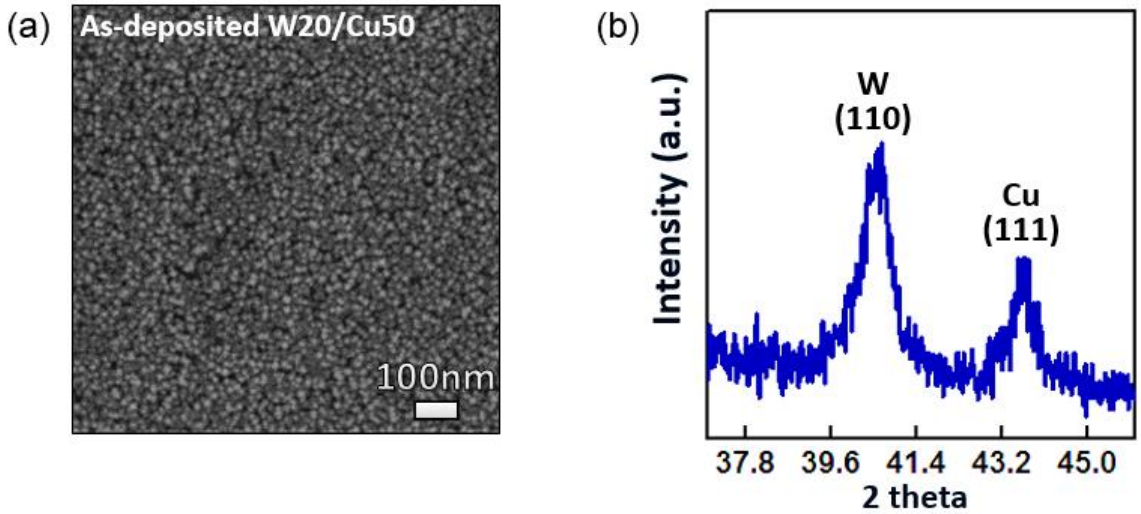

Figure 2-3. (a) Representative SEM Images of surface morphology of poly-crystalline W20/Cu50 films deposited on Sio_2/Si substrate. (b) XRD pattern for the W20/Cu50 films deposited on Sio_2/Si substrate. The size of W crystalline is within 20nm verified by using Scherrer equation.

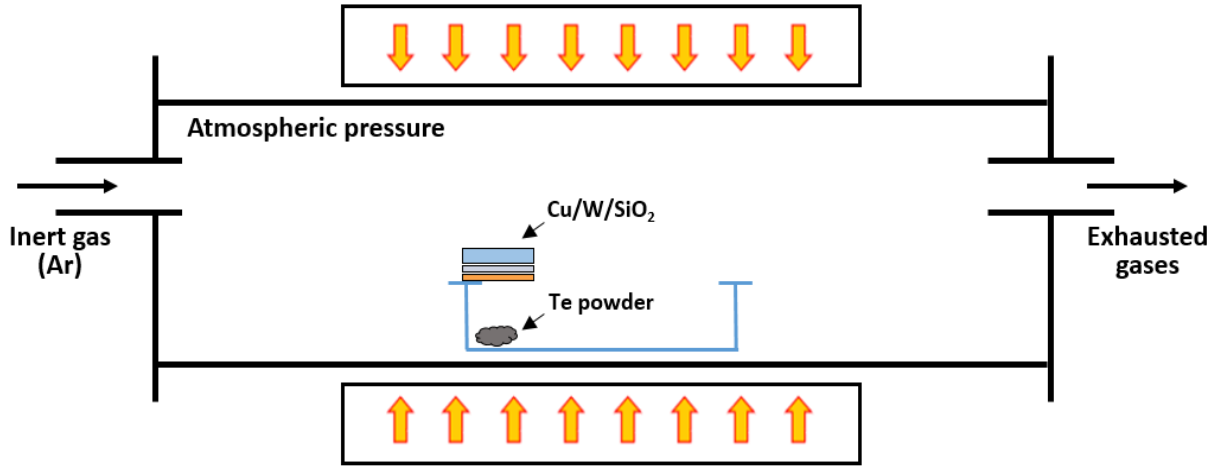

Figure 2-4. Schematic drawing of the chamber in our furnace system (DMTF 12/150-HVAC, Daemyoung Enterprise) for growth of WTe_2 nanostructures. The chamber was evacuated to ~ 10^{-3} Torr and then filled with Ar gas to maintain atmospheric pressure and protect the system from oxygen

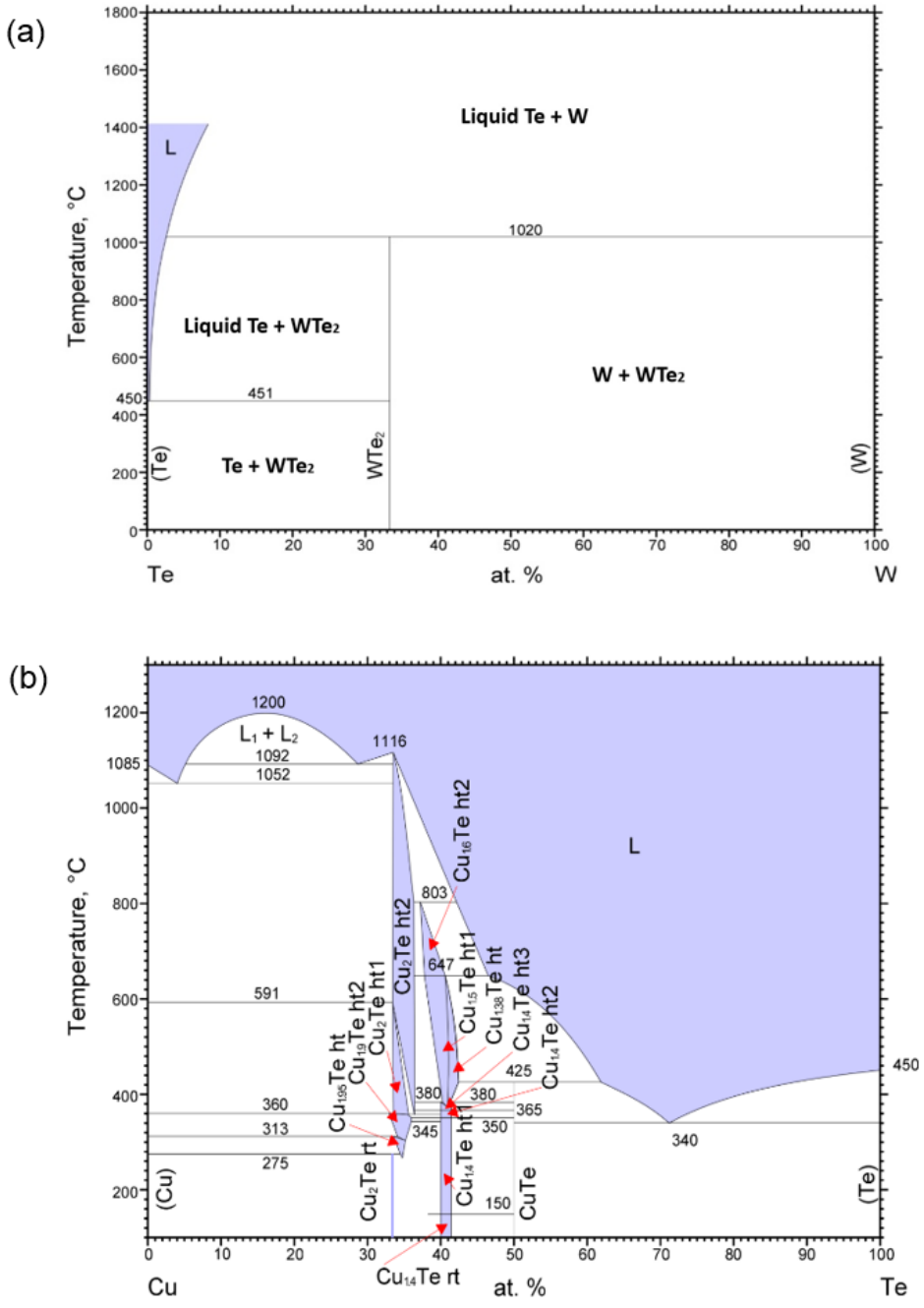

Figure 2-5. Phase diagrams of (a) the W-Te system (b) the Cu-Te system (From ASM Alloy Phase Diagram Database).

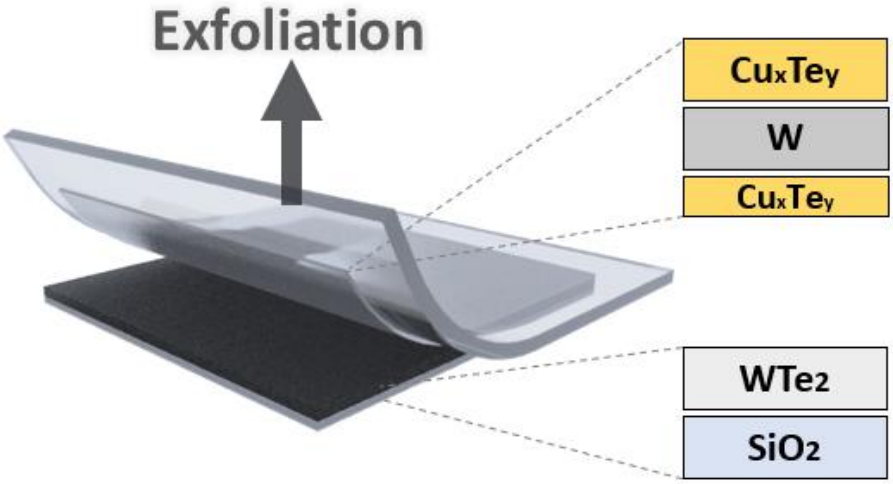

Figure 2-6. Schematic image of method of mechanical peeling off using scotch tape. The simple method of peeling off using scotch tape can reduce the whole process to form WTe_2 nanostructures on the desired substrate.

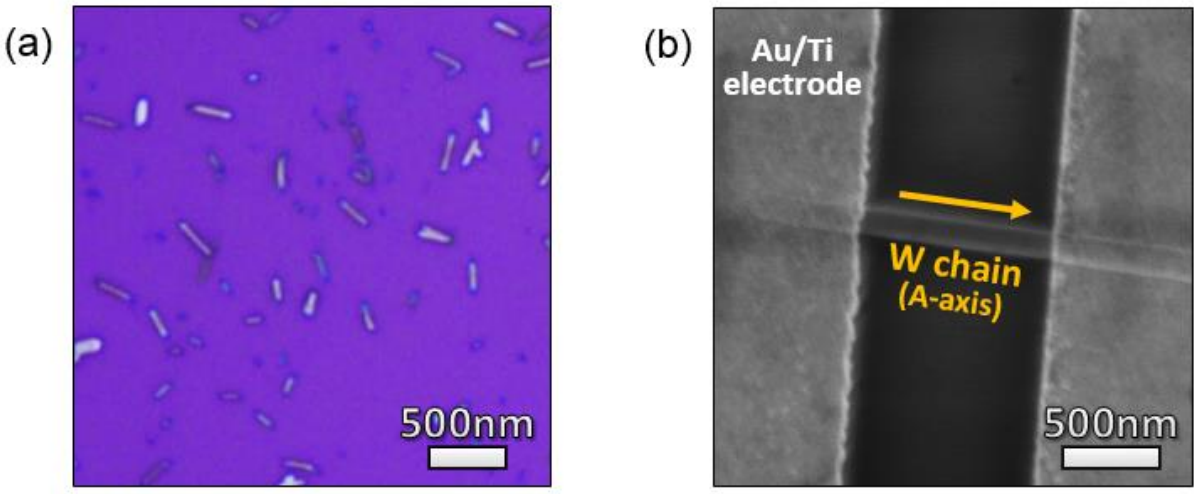

Figure 2-7. (a) Representative OM Image of as-synthesized WTe_2 nanostructures onto the desired substrate by peeling W and Cu_xTe_y droplets off using scotch tape. (b) SEM Image of fabricated WTe_2 nanostructures device, showing the channel (with current along the a-axis of W-W zigzag chains, lengths of 1μm) perpendicular to Au/Ti electrode.

Chapter 3. Results and Discussion

3.1 Role of Eutectic Metal Alloys for Synthesis of WTe_2

Previously, most of the studies on tungsten ditelluride (WTe_2) have been demonstrated in mechanically exfoliated layers from bulk crystal. Therefore, the development of direct synthesis of high quality few-layer WTe_2 is essential to study the emergent properties of nanostructured WTe_2 and for large-scale applications.

So far, a single- or few-layer WTe_2 has only been prepared by mechanical exfoliation from bulk crystals which are synthesized by chemical vapor transport method, usually conducted at high temperatures over 700˚C for several days. The products are poor-crystallinity crystals, and are limited to only large bulk-type crystals with millimeter scale. The high vapor pressure of tellurium and low chemical reaction activity of tungsten with tellurium make synthesis challenging. To obtain stoichiometric WTe_2 crystals, it needs to hinder desorption of tellurium vapor precursor and activate tungsten atoms to be reacted with tellurium atoms. To overcome these problems, we suggested a novel method for the growth of the WTe_2 nanostructure. Using our method, we can directly obtain the desired WTe_2 nanostructures with nano-scaled thickness and high quality. In comparison to conventional chemical vapor transport methods, our method requires a lower growth temperature & shorter time, which is good for mass production and novel applications.

To solve the challenge in tellurization of tungsten films and obtain stoichiometric WTe_2, our key approach is the eutectic metal alloy assisting mechanism. When above the copper-tellurium eutectic temperature, the diffused copper atoms react with tellurium vapor, resulting in the formation of Cu_xTe_y liquid state droplets holding tellurium vapor as a role of vapor flux reservoir. In addition, in liquid state Cu_xTe_y droplets, tungsten atoms from the interface between the W layer and droplets were activated to be reacted with Te. Consequently, WTe_2 crystals can be nucleated (and crystallized) in liquid-phase eutectic metal alloys. The crystal of WTe_2 grew as anisotropic nano-belts due to its intrinsic 1T'-pahse, compared to other 2H-TMDs. In short, we obtained the desired high quality single-crystalline WTe_2 nanostructures inside of the Cu_xTe_y droplet.

In this research, we proposed a method using new type of structure of deposited a W/Cu metal layer on SiO_2/Si substrate that is the inverse structure of the essential structure in our previous research (Cu/W/SiO_2/Si). We deposited the copper layer on the desired substrate (SiO_2) and then conducted the deposition of W layer. This work should be studied in terms of the different morphology of Cu_xTe_y

droplet depending on synthesis parameters as well as growth conditions.

Figure 3-1 indicates as-grown Cu_xTe_y droplet on W layer via SEM Images. The W and pre-deposited Cu layer with thickness of 100nm was used as a standard process condition. To identify the Cu_xTe_y droplet, the Raman and EDAX analysis of the droplet was carried out. The Raman spectra shows that all the measured Raman shifts indicate tellurium, at 140, 189, 224, 270 cm^{-1}. And, the Te-rich Cu_xTe_y droplet was confirmed by the EDAX analysis. We confirmed that, by introducing the pre-deposited copper layer, the Cu_xTe_y droplet was formed. Interestingly, the Cu_xTe_y droplet was observed on the surface of W layer, penetrated through the W layer, although the Cu layer was deposited under the W layer. This suggests that diffusion of copper atoms into W layer occurs through the grain boundary of the W layer. Then, diffused copper atoms would combine with the Te vapor precursor, resulting in formation of Cu_xTe_y droplets at the surface of the W layer. Another view of this phenomena is that the penetration of liquid state Cu_xTe_y through the W layer, following the formation of liquid state Cu_xTe_y over the eutectic temperature (~394°C) under the W layer, but the further study needs to be done for the mechanism confirmation. The morphology of as-grown Cu_xTe_y droplets are shown via SEM, displayed in figure 3-2. And Raman, EDAX spectra and its composition are shown in figure 3-2, corresponding the red circle in figure 3-2 (b).

The Cu_xTe_y was fully etched by dipping into Ammonium Persulfate (APS) etchant for 1hr. At the same site where the Cu_xTe_y droplet was located, we observed as-synthesized WTe_2 nanostructures on the W layer. This was confirmed by Raman analysis, and corresponds to the red circles in the figure 3-3, indicated at 163, 211 cm^{-1} of Raman shift. In addition, to check the composition and stoichiometry of the as-synthesized nanostructure which was transferred onto Al_2O_3 substrate to prevent main peak from overlapping with other signals, EDX analysis was carried out. This corresponds to the red point in the inset image. The indicated main elements of the synthesized nanostructures are tungsten and tellurium. The EDX analysis result indicates that the as-synthesized WTe_2 is highly stoichiometric with a W : Te ratio of 1:2. The use of Te-rich eutectic metal alloys eliminates the Te deficiency in the resulting products and the contamination by impurities encountered with vapor deposition process. As a result, the as-synthesized WTe_2 nanostructures are highly pure, stoichiometric, and structurally uniform.

To sum up, the growth mechanism of WTe_2 was explained by the assistance of liquid Cu_xTe_y droplets, after oversaturation with dissolved tungsten, induced a WTe_2 crystal growth.The crystallization takes place at a temperature of ~500 °C, slightly above the Cu–Te eutectic temperature of 340°C. A liquid-state eutectic metal alloy from the promoter metal (Cu) and Tellurium is formed, which dissolves tungsten up to its solubility limit. When the solubility limit is reached, the excess WTe_2 rapidly

crystallizes out of the Cu_xTe_y droplet, leading to the formation of these highly (002)-textured WTe_2 nanostructures. Particularly, the as-synthesized WTe_2 nanostructures can be easily transferred to different substrates and/or solutions for further applications. Figure. 3-3 show that the as-synthesized WTe_2 nanostructure can successfully be transferred to desired substrate using conventional dispersion method. Our optimum process condition for obtaining WTe_2 nanostructures with a thickness in few-nanometers is a tungsten layer with a thickness of 20nm and a copper layer with a thickness of 50 nm, grown at 500°C for 10min with supplement of Tellurium from Te powder of 0.1g. The thickness distribution was measured by AFM profile. The average thickness of obtained WTe_2 nanostructures was measured to be 54±15 nm, shown in figure 3-3. Figure. 3-4 clearly show the XRD pattern of highly (002)-oriented single crystalline tungsten ditelluride texture. After transfer of WTe_2 nanobelts from W surface to desired substrate (SiO_2) using conventional dispersion methods, XRD measurement was performed, displayed in figure 3-4.

.

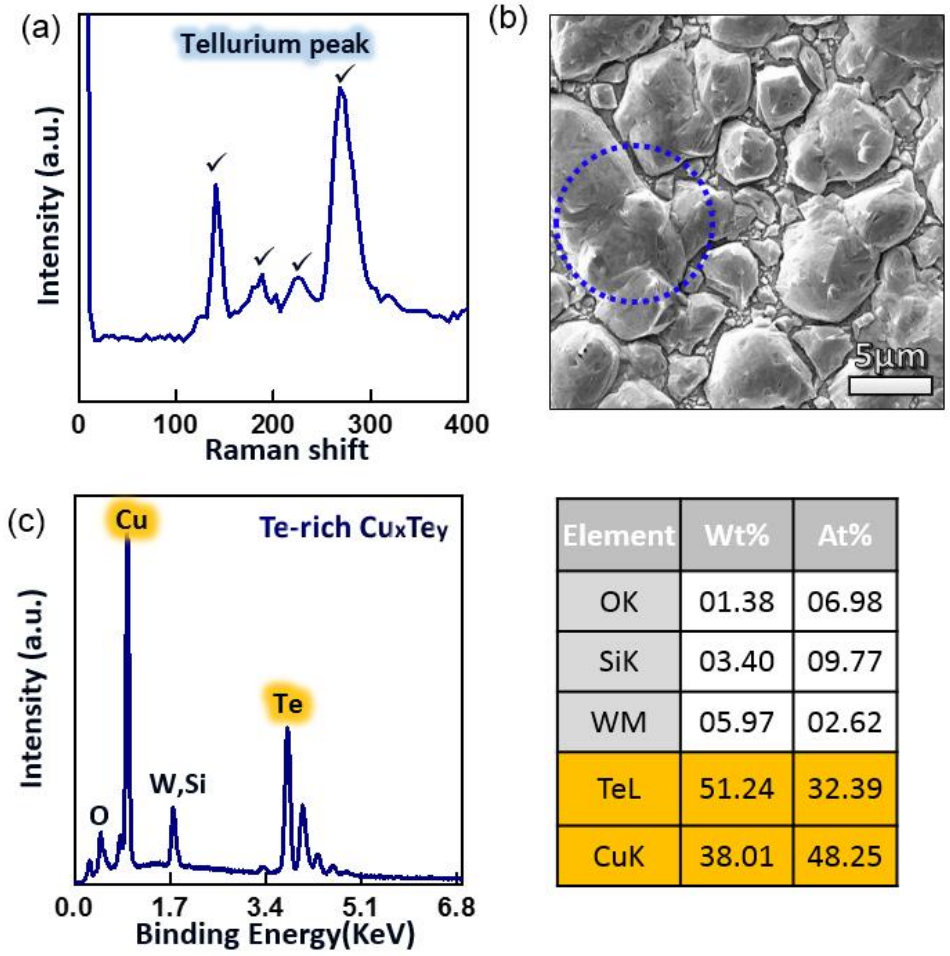

Element	Wt%	At%
OK	01.38	06.98
SiK	03.40	09.77
WM	05.97	02.62
TeL	51.24	32.39
CuK	38.01	48.25

Figure 3-1. (a) Raman spectra, corresponding to the colored blue spot in (b) image, identifying tellurium-rich Cu_xTe_y eutectic metal alloys. (b) SEM Image of tellurium-rich eutectic metal Cu_xTe_y alloys on W layer. (c) EDAX spectra, corresponding to the colored blue spot in (b) image.

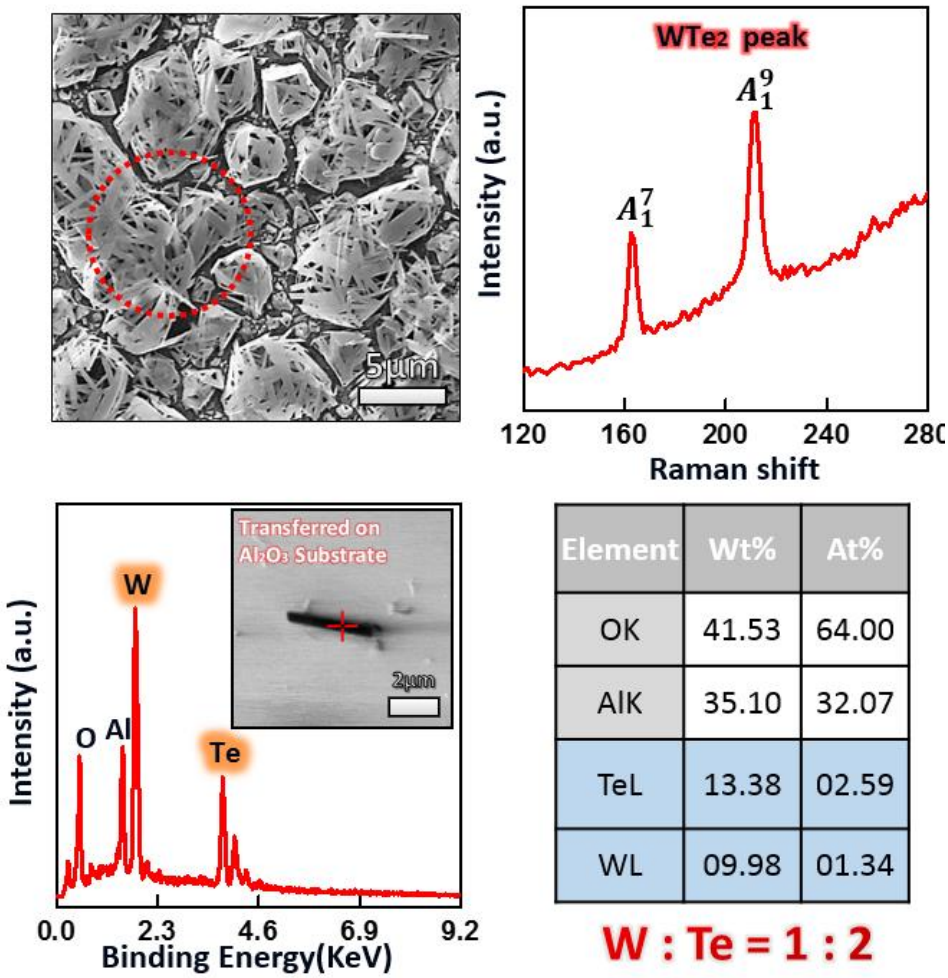

Figure 3-2. (a) Raman spectra, corresponding to the colored red spot in (b) image, identifying as synthesized-WTe_2. (b) SEM Image of as-synthesized WTe_2 nanostructures on W layer. (c) EDAX spectra, corresponding to the colored red spot in (b) image.

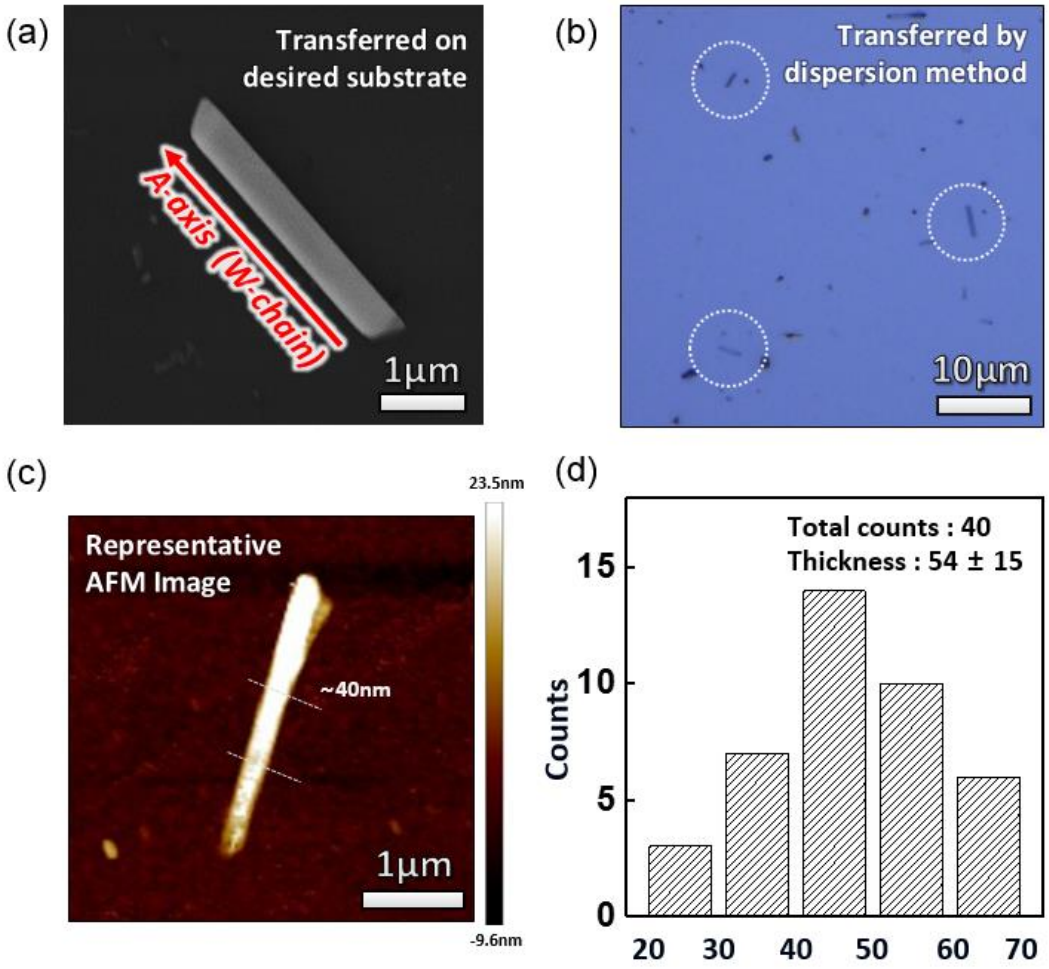

Figure 3-3. (a-c) OM, SEM and AFM images of transferred WTe_2 nanobelts on desired substrate by conventional dispersion method. (d) Diameter distribution of WTe_2 nanobelts obtained at W20/Cu50 500℃ for 10min.

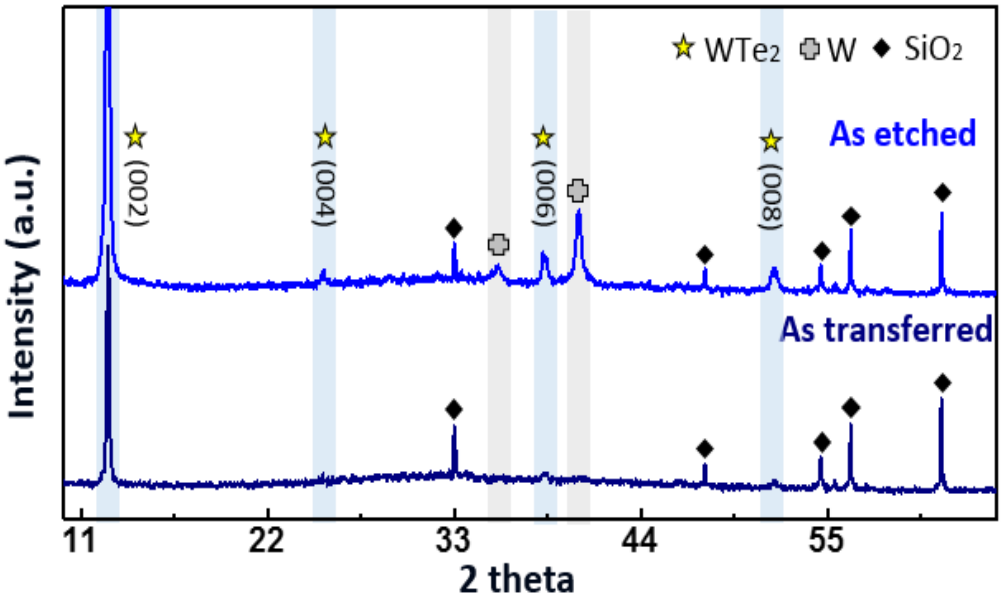

Figure 3-4. XRD data of as Cu_xTe_y etched and transferred WTe_2 nanobelts on SiO_2/Si substrate by conventional dispersion method.

3.2 Structural Morphology of Eutectic Metal Alloys on Synthesis Parameters

The role of eutectic metal and its behavior on synthesis parameters is a major factor in the synthesis of WTe_2 in our synthesis method, so studies on changes of Cu_xTe_y metal alloys on synthesis parameters were necessary. We studied the synthesis of WTe_2 by controlling the growth conditions and observing changes of Cu_xTe_y metal alloys.

3.2.1 Study on Behavior and Role of Cu_xTe_y depending on Growth Time

We examined effects of growth time first. The thickness of the sample under our optimum condition for obtaining few-nm thickness WTe_2 nanostructure (tungsten of 20nm, copper of 50nm on SiO_2/Si substrate) and growth at the temperature of 500°C with 0.1g of Te powder was fixed and only the synthesis time was adjusted. When the growth time was relatively short (2, 6 min), the Cu atoms from the copper layer below W layer did not react sufficiently with Te. As was such, Cu_xTe_y metal alloys could not form sufficiently, consequently affecting WTe_2 growth. Figure. 3-5 shows the intensities of XRD peak for Cu and Cu_xTe_y metal alloys depending on synthesis times of 2min, 6min, and 10min respectively. From the XRD analysis, the weak XRD peak of (002)-oriented Cu_xTe_y metal alloys were found at the growth time of 2 min and 6 min. The XRD peak of (002)-oriented Cu_xTe_y metal alloys is clearly shown in the case of growth time of 10min, where both Cu and Te sufficiently reacted. Correspondingly, XRD peak of the well-crystalized (002)-oriented WTe_2 is clearly identified. Figure 3-6 is the comparison of XRD intensity on as deposited, annealed w/o Te and as-grown Cu_xTe_y:W at 500°C for 10min. Compared to as deposited and annealed without Te source, our optimum condition with sufficient growth time of 10min exhibits clear XRD peaks of Cu_xTe_y metal alloys and WTe_2 nanostructure. From these results, we recognize that formation of Cu_xTe_y metal alloys from the reaction of Cu and Te has significant effects on growth of WTe_2. In figure 3-7, the Raman spectrum of as-grown Cu_xTe_y and WTe_2 shows several peaks approximately at 92, 121, 141 (tellurium peaks) and 80, 119, 134, 164, 212 (WTe_2 peaks) cm^{-1}, respectively.

Even as Cu_xTe_y metal alloys are formed, nucleation and crystallization of WTe_2 nanostructures must take place inside of eutectic metal alloys. In the case of insufficient growth time to nucleate WTe_2 nanostructure, only W nanowire can be observed. In figure 3-8, the SEM Image shows the as-obtained W nanowire at the same site where the Cu_xTe_y droplet was located. The activated W atoms induced by eutectic metal alloys did not react with Te atoms, resulting in formation of W nanowires along the [110] direction. This phenomenon is also observed in the Te deficiency region, where grown for 10min. In short, WTe_2 nanostructure can be synthesized at convection region with W atoms and Te atoms, followed by oversaturation and eventually crystallization followed by precipitation.

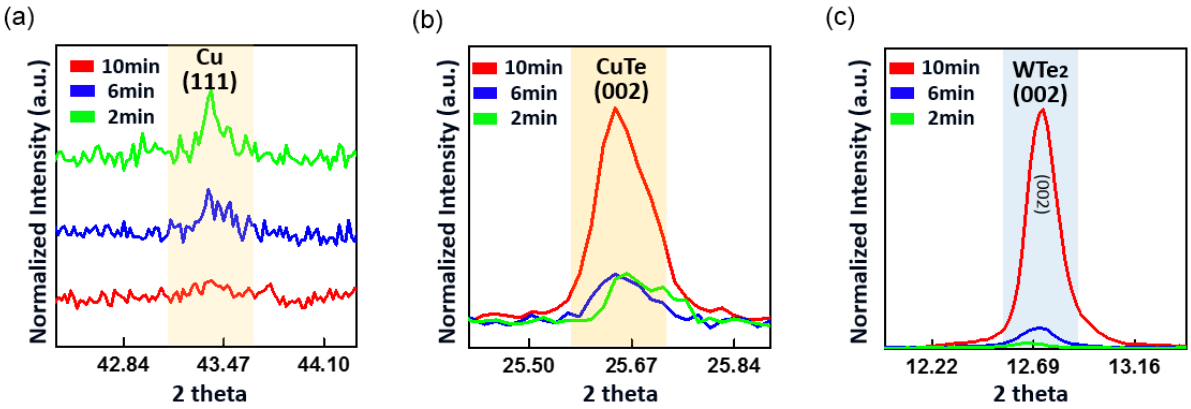

Figure 3-5. (a-c) Comparison of XRD intensity of as-grown Cu_xTe_y:W depending on growth time.

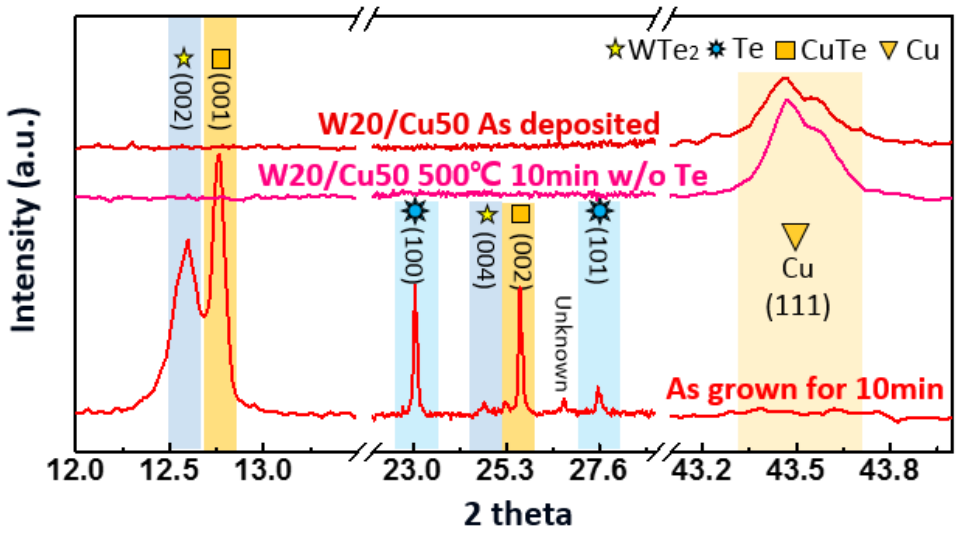

Figure 3-6. Comparison of XRD intensity of as deposited, annealed w/o Te and as-grown Cu_xTe_y:W at 500°C for 10min.

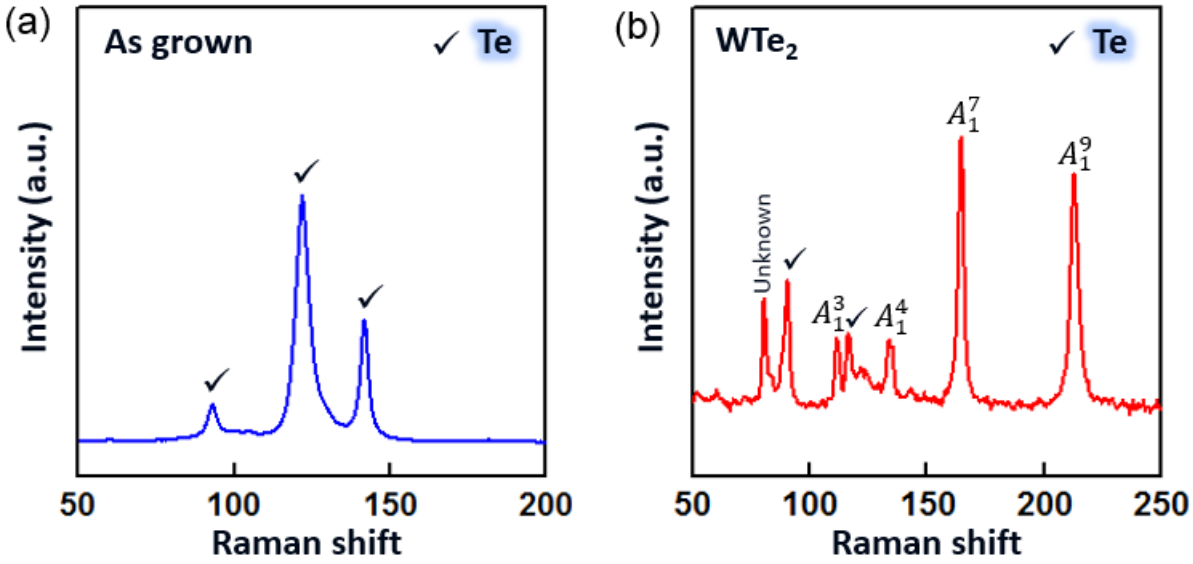

Figure 3-7. (a-b) Raman spectra of as-grown Cu_xTe_y droplet and as-synthesized WTe_2 nanostructures of a W(20 nm)/Cu(50 nm) sample at 500°C for 10min.

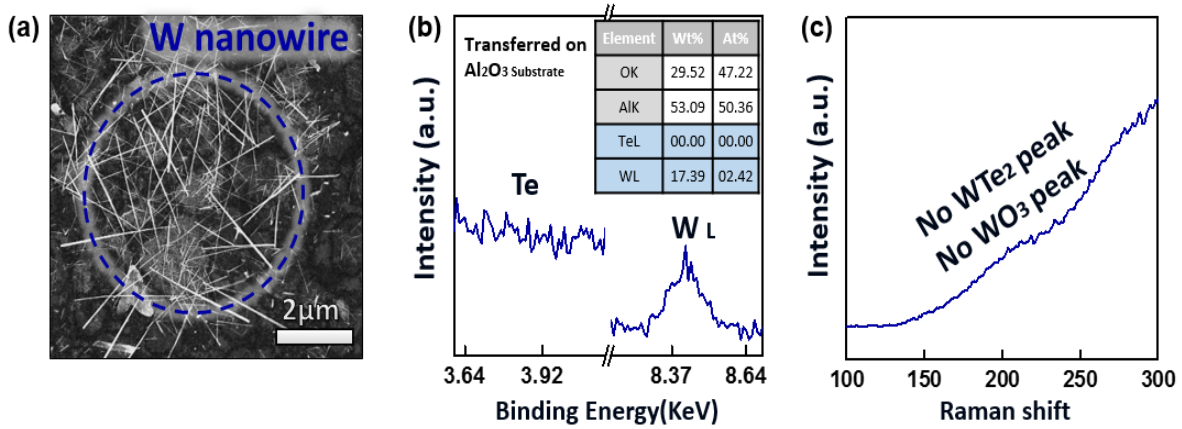

Figure 3-8. (a) SEM Image of as-synthesized W nanowires on W layer. (b-c) EDAX and Raman spectra, corresponding to the colored blue spot in (a) image.

3.2.2 Study on Behavior and Role of Cu_xTe_y depending on Growth Temperature

Next, we investigated the effect of growth temperature on formation of Cu_xTe_y droplets and synthesis of WTe_2 nanostructure. The thickness of the sample under the optimum condition for obtaining few-nm thickness WTe_2 nanostructure (tungsten of 20nm, copper of 50nm on SiO_2/Si substrate) and growth time for 10min with 0.1g of Te powder was fixed and only the synthesis temperature was adjusted. The dependency of Cu_xTe_y droplet and nanobelts structural morphology on synthesis parameters is shown in SEM images, displayed in figure 3-9. The average size of Cu_xTe_y droplet obtained from growth at 600 °C is about four times larger than Cu_xTe_y droplet grown at a temperature of 500 °C. Correspondingly, as the reaction temperature is increased, thick and long nanobelts can be obtained. The higher the temperature, the reaction of tungsten and tellurium are activated more inside of the larger Cu_xTe_y droplet, resulting in a thicker and improved crystallinity of WTe_2, as shown in figure 3-10. Figure. 3-11 indicates changes in length of nanobelts for the a-axis and b-axis and thickness of nanobelts as growth temperature is increased. From these results, we became aware that the reaction temperature of Cu and Te has significant effects on formation of Cu_xTe_y metal alloys and growth of WTe_2 nanobelts. The growth temperature affects not only the diffusion of the copper atoms from the pre-deposited copper layer into the upper layer but also activation of W atoms to be reacted with Te atoms from the W layer despite the low reactivity of W due to the high active temperature of W.

In our growth modes, the Cu_xTe_y dissolves W atoms from the W surface and forms WTe_2 nanostructures in side of Cu_xTe_y droplets. Interestingly, at a growth temperature of 600°C, an enormous amount of W nanowire grown in the (110) direction was found compared to growth temperature of 500°C. The SEM Images, as shown in figure 3-12, indicate that W nanowire have a diameter ranging from 50nm to 500nm, showing perfect straightness and grassy appearance.

Lee. Yun-Hi, et.al have reported fabrication of tungsten nanowire without use of any heterogeneous catalyst[45]. They examined X-ray diffraction (XRD) patterns that show remarkable changes of the crystallographic structure after W-nanowire formation. The XRD data for grown nanowires suggested that the interplanar distances were increased and the relative peak intensities of W (110) were increased. By HRTEM, they confirmed that the wavelength of the modulation in the HRTEM image was about 0.22 nanometers, which is the wavelength that corresponds to the inter-planar distance of (110) lattice planes of bcc W, as shown in figure 3-13.

Our results showed formation of W nanowires grown in (110) directions, and could be confirmed by XRD, indicated in figure 3-14. This figure shows that the intensity of W (100) after the growth of 600 °C

was highly increased (relatively higher than the intensity before growth). This is because the activated W atoms induced by eutectic metal alloy did not react with Te atoms, resulting in formation of W nanowires along the [110] direction. The W nanowire was dominantly observed when the temperature was increased and the amount of Te was decreased. As shown in figure 3-15, we confirmed that the size and density of the W nanowires increased significantly when the Te amount was reduced. Based on our mechanism, W atoms are dissolved in liquid state Cu_xTe_y droplets above the eutectic temperature of the Cu–Te system. These results strongly suggest that when the dissolved W atoms cannot react with Te due to deficiency of Te source, the activated W atoms grew as a nanowire shape in the (110) direction, followed by supersaturation and the crystallization from the liquid-phase. From these results, we can understand that the reaction of activated W atoms and Te precursor has a significant effects on supersaturation of WTe_2 in liquid state Cu_xTe_y droplet for growth of single-crystalline WTe_2 nanobelts.

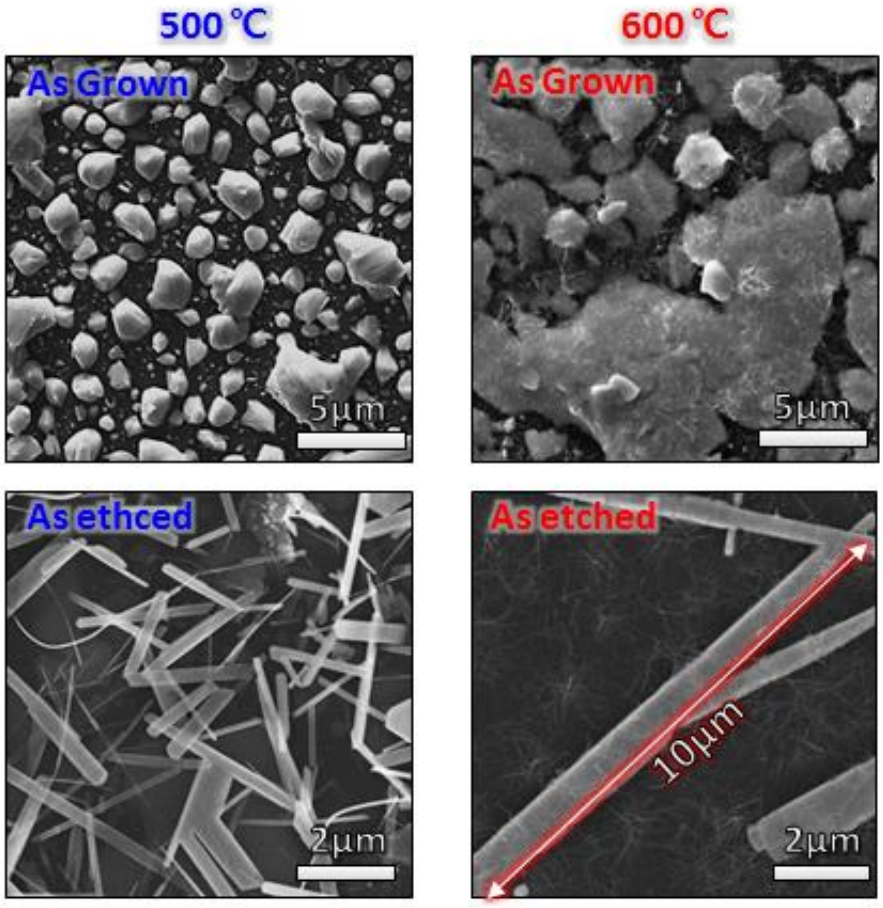

Figure 3-9. Representative SEM images of Cu_xTe_y droplet and WTe_2 nanobelts obtained at 500°C and 600°C for 10min, respectively.

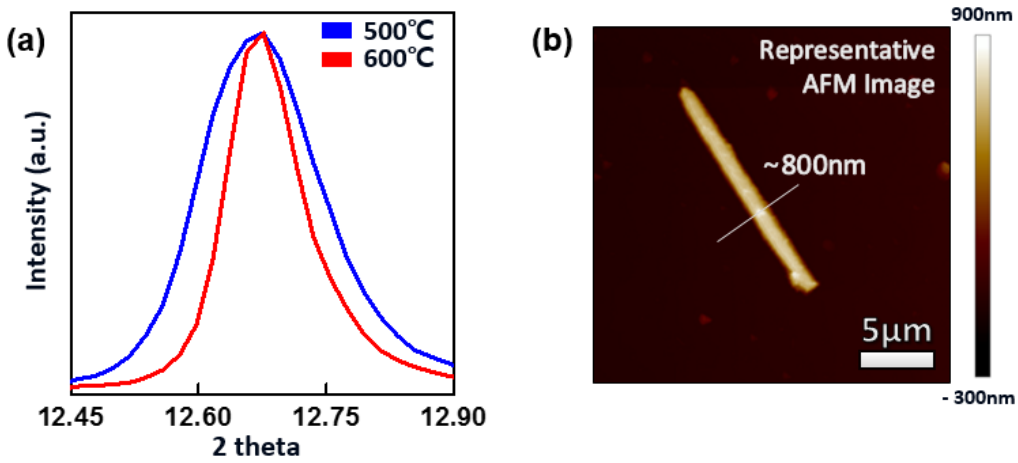

Figure 3-10. (a) XRD data of WTe_2 nanobelts obtained at 500°C and 600°C for 10min, respectively. (b) Representative AFM Image of WTe_2 nanobelts obtained at 600°C for 10min, showing highly thick nanobelts.

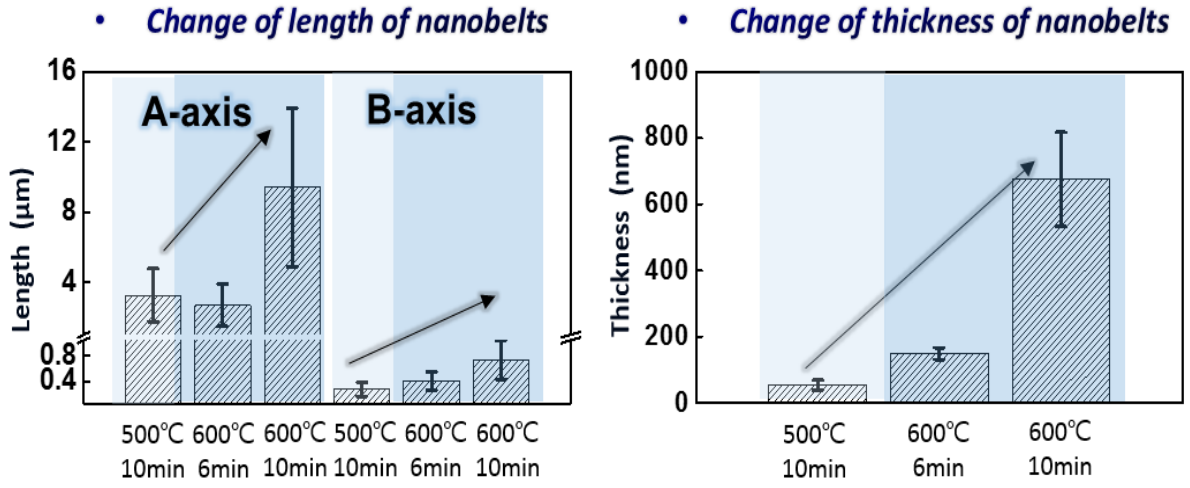

Figure 3-11. Changes of length and thickness of as-synthesized WTe_2 nanobelts as growth temperature and time increase.

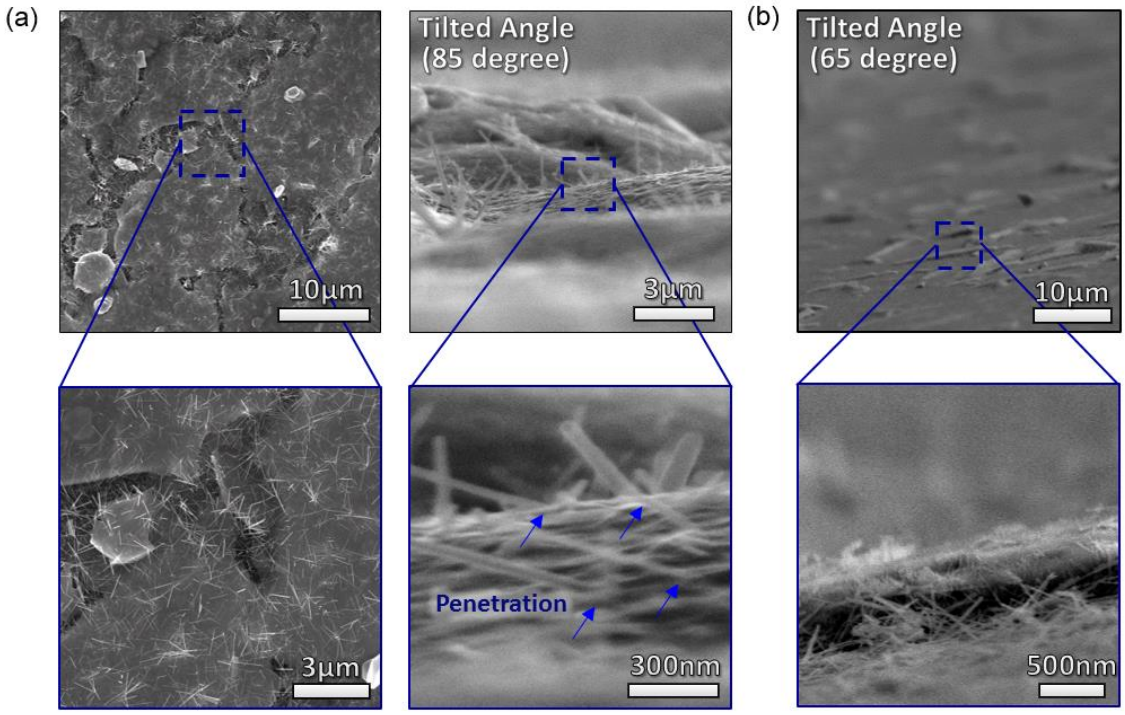

Figure 3-12. (a) Representative SEM images of Cu_xTe_y droplet & W nanowires. It is shown that the W nanowires penetrated the Cu_xTe_y droplet. (b) Cross sectional SEM Images of WTe_2 nanobelts & W nanowires.

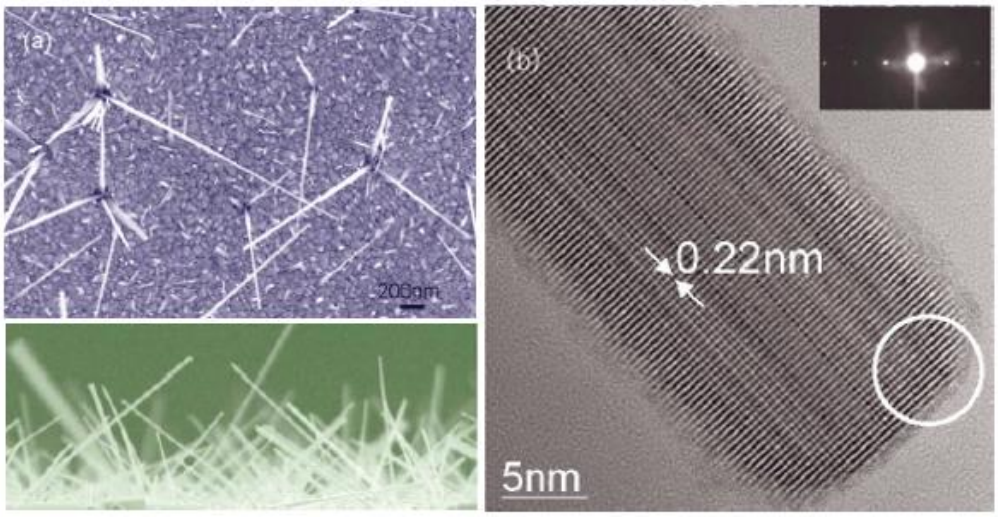

Figure 3-13. (a) SEM images of tungsten (W) nanowires at initial growth (b) The modulation phase HRTEM images of a chosen W nanowires. The inset figure is selected area electron diffraction pattern showing the growth of a well-crystallized bcc-phase W nanowire[45].

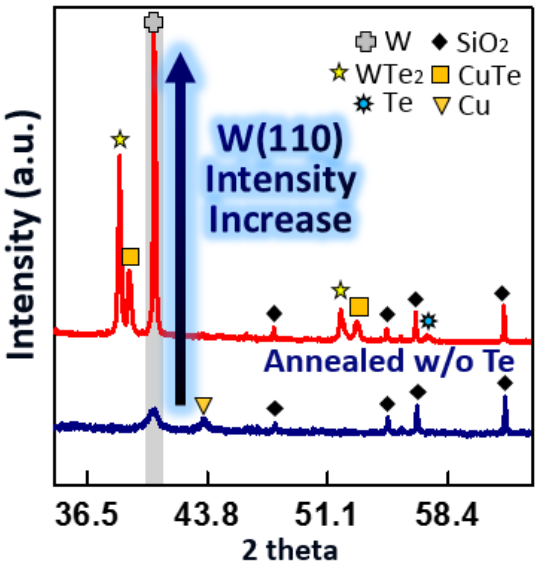

Figure 3-14. XRD data of as grown Cu_xTe_y droplet and as-annealed w/o Te at 600°C for 10min on SiO_2 substrate.

.

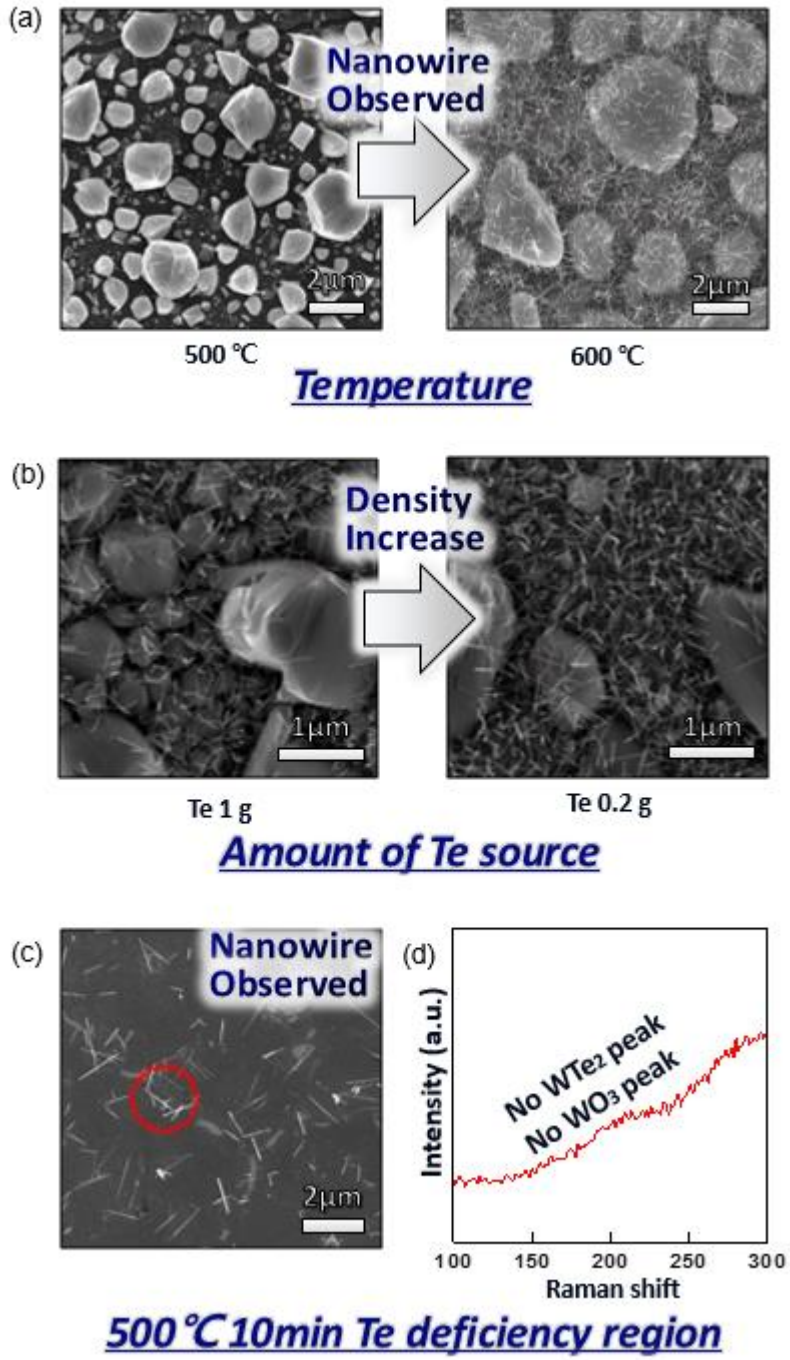

Figure 3-15. (a) Changes in the surface morphologies depending on the growth temperature. (b) Changes in the surface morphologies depending on the amount of Te source. (c) Representative SEM Images of W nanowire obtained from Te deficiency region at 500°C for 10min. (d) Raman spectra, corresponding to the colored red spot in (c) image, identifying the W nanowire.

3.2.3 Study on Behavior and Role of CuxTey depending on thickness of W layer

We have investigated the changes in the formation of Cu_xTe_y when the tungsten thickness is relatively increased. For this study, the thickness of the W layer was changed from 20 nm (optimum condition forobtaining few-nm thickness WTe_2 nanostructure) to a thickness of 100 nm. Other processes and growth conditions (copper of 50nm on Sio_2/Si substrate, growth for 10min at 500°C) were fixed and only the thickness of the W layer was changed. In this work, interestingly, as-grown Cu_xTe_y droplets couldn't be observed on W layer. This can be seen in the OM Images shown in figure 3-16a of as-grown Cu_xTe_y droplets after dipping APS etchant. However, we could not recognize any changes of the surface morphology. It is clearly shown that Cu_xTe_y droplets were formed under the W layer. We detached the W layer using a method of sonication to verify the synthesized WTe_2 underneath the W layer. At the same site where the Cu_xTe_y droplet was located, the synthesized WTe_2 was found on SiO_2/Si substrate, as shown in figure 3-16b,c. From these results, we confirm that Cu_xTe_y droplets do not penetrate the W layer as the thickness of W layer becomes relatively thick. In addition, it can be seen that WTe_2 does not grow only at the interface between W layer and Cu_xTe_y droplet. The cross sectional SEM Images (see figure 3-17) clearly exhibit the formation of WTe_2 nanostructures on the SiO_2, not on the W layer, compared to the case where the W layer is relatively thin (thickness = 20nm). Also, we investigated a change of structural morphology of synthesized WTe_2 nanobelts, as shown in figure 3-18. As we increased the thickness of W layer from 20nm to 100nm, the size of the synthesized WTe_2 increased slightly. The formation of WTe_2 nanobelts below W layer was confirmed, even at higher temperature of 600 °C, where diffusion of Cu atoms is increased, under a fixed growth and process condition. From previous experiments for studying effects of growth temperature, we found that the reaction temperature of Cu and Te has a significant effect on formation of Cu_xTe_y metal alloys. The growth temperature affects not only the diffusion of the copper atoms from the pre-deposited copper layer into the upper layer but also diffusion of Te vapor into copper layer. Compared to the case of 500°C, the larger size as-grown Cu_xTe_y metal alloys underneath W layer were exposed as they were etched by dipping APS etchant for 1hr. WTe_2 nanobelts covered with W layer and Te products can be observed in figure 3-19 and 3-20. In contrast to structural morphology of case of relatively thick W layer (t = 100nm), in the case of relatively thin W layers (t = 20nm), the Cu_xTe_y metal alloys were formed on W layer. This was clearly identified by the changes in surface morphology of Cu_xTe_y droplets depending on etching time. The Cu_xTe_y droplets on W layer were etched gradually as etching time increased, shown in figure 3-21. This shows that WTe_2 nanobelts are underneath Cu_xTe_y droplets. From these results, it was confirmed that the formation of Cu_xTe_y metal alloys and WTe_2 nanobelts are strongly dependent on the relative thickness of W layer. And we realized that the Cu_xTe_y dissolves W atoms from the W surface and helps WTe_2 to be nucleated, not just only on the W surface, but on the Sio_2/Si substrate.

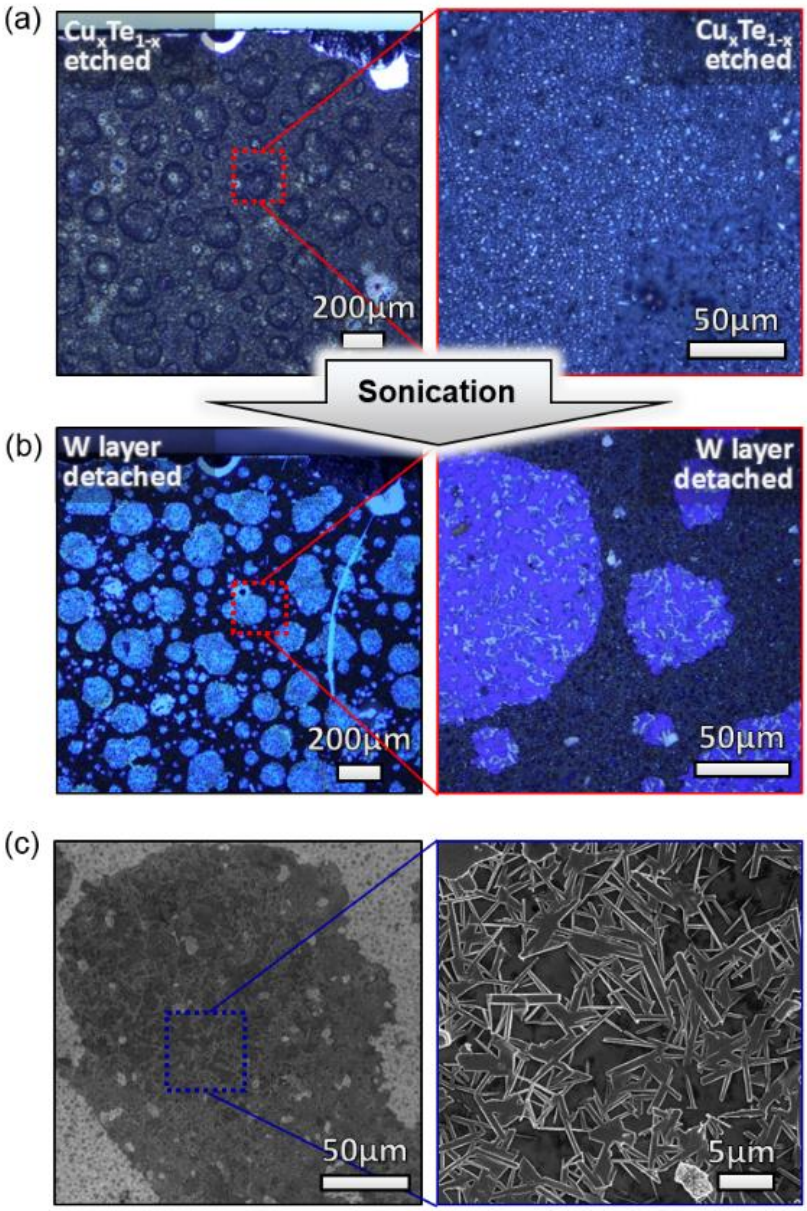

Figure 3-16. (a) OM Images of Cu_xTe_y droplets grown at W100/Cu50 at 500°C for 10min. It is shown that Cu_xTe_y droplets were formed under W layer. (b) OM Images of WTe_2 nanobelts at the same site after sonication for 1hr to detach W layer. (c) Representative SEM Images of WTe_2 nanobelts on SiO_2 substrate obtained at W100/Cu50 500°C for 10min.

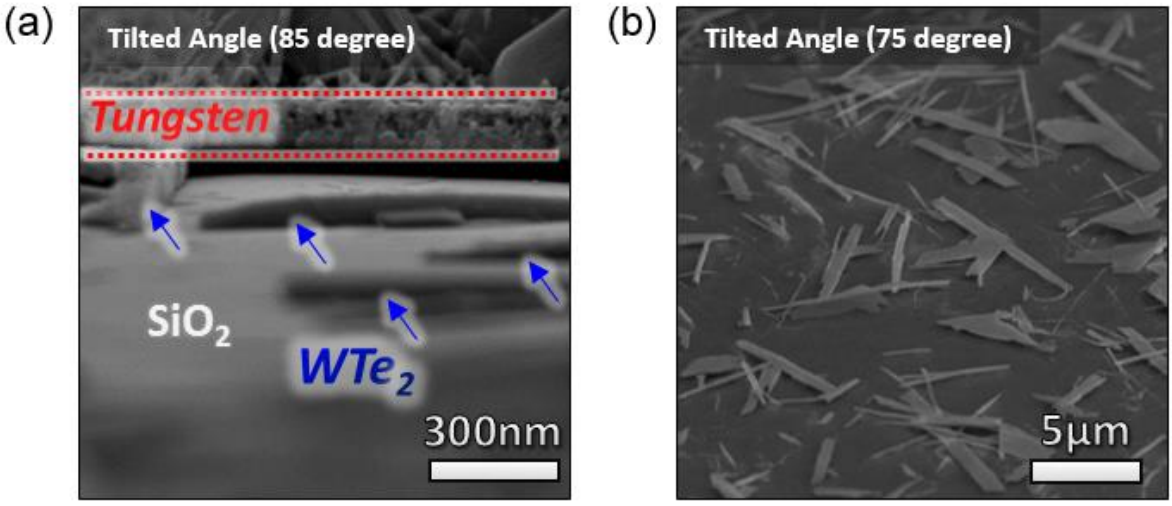

Figure 3-17. Cross sectional SEM Images of (a) WTe_2 grown on SiO_2 substrate (b) on W layer, respectively, depending on process condition of thickness of W layer.

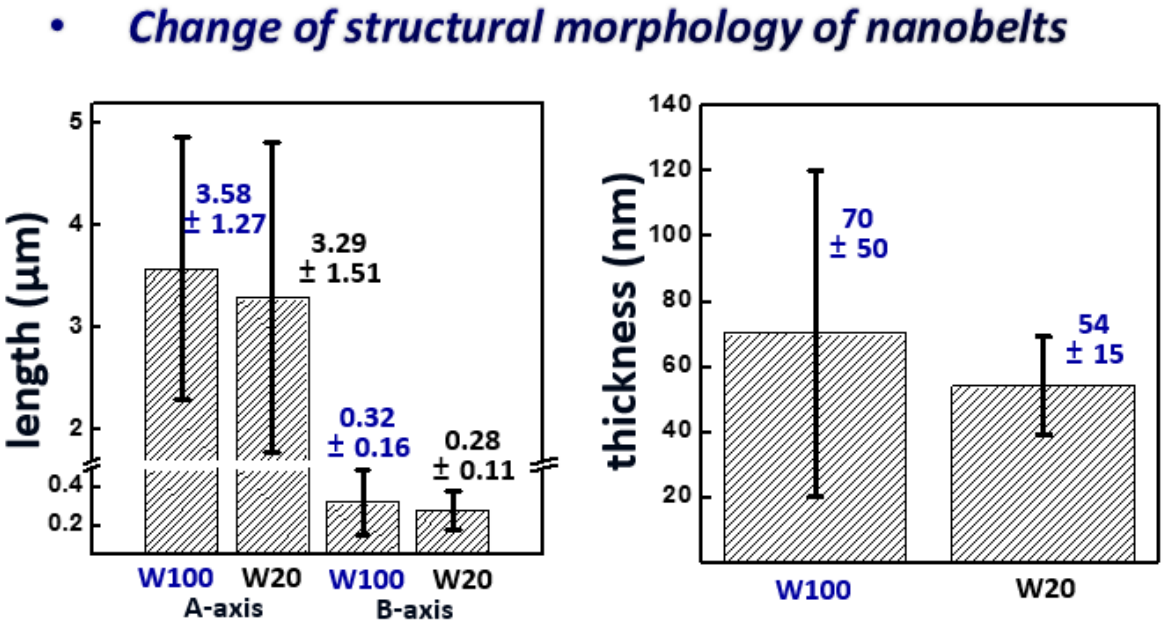

Figure 3-18. Change of structural morphology of as-synthesized WTe_2 nanobelts depending on process condition of thickness of W layer.

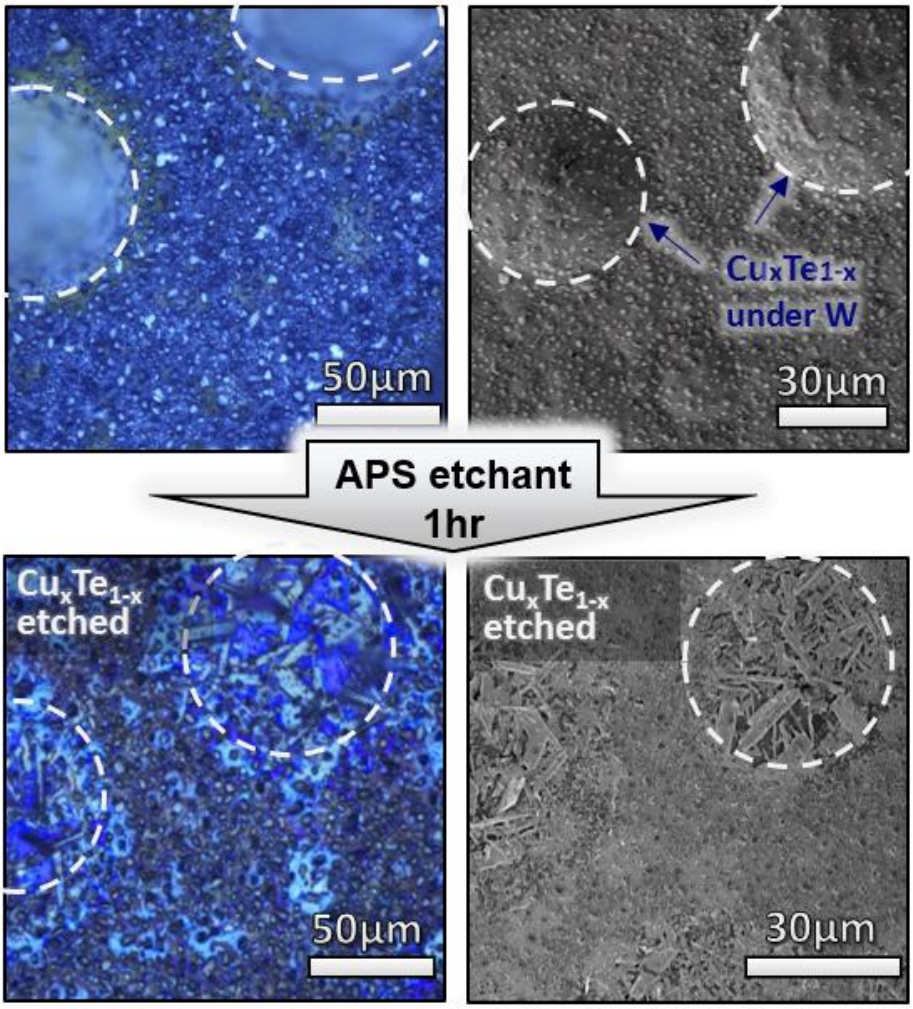

Figure 3-19. SEM Image and OM Images of Cu_xTe_y droplets grown at W100/Cu50 at 600°C for 10min. It is shown that Cu_xTe_y droplets were formed under W layer. After Cu_xTe_y etching, WTe_2 nanobelts can be observed under W layer.

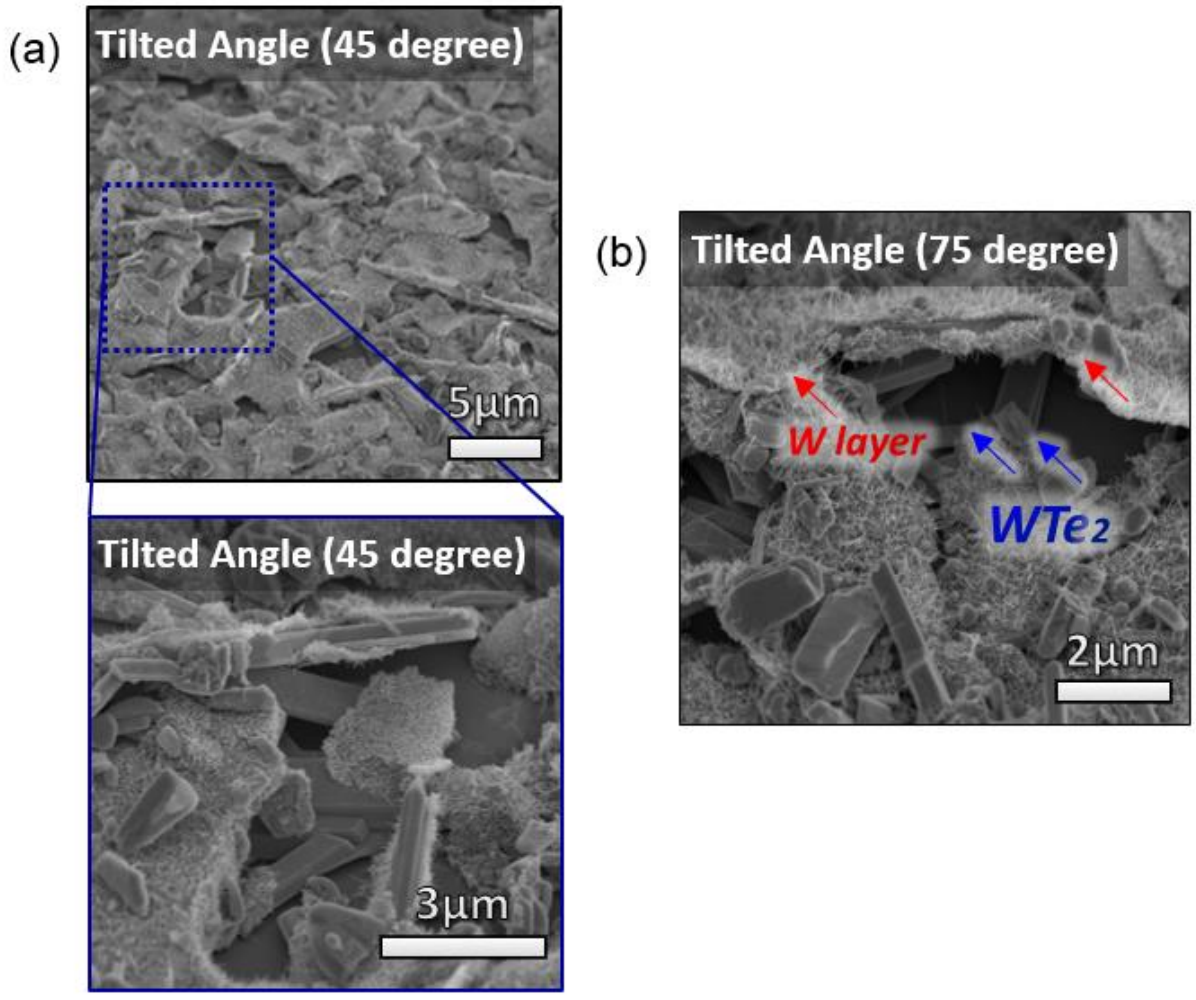

Figure. 3-20 (a-b) Cross sectional SEM images of Cu_xTe_y droplets grown at W100/Cu50 600°C for 10min. It is shown that WTe_2 nanobelts are covered with W layer and Tellurium product.

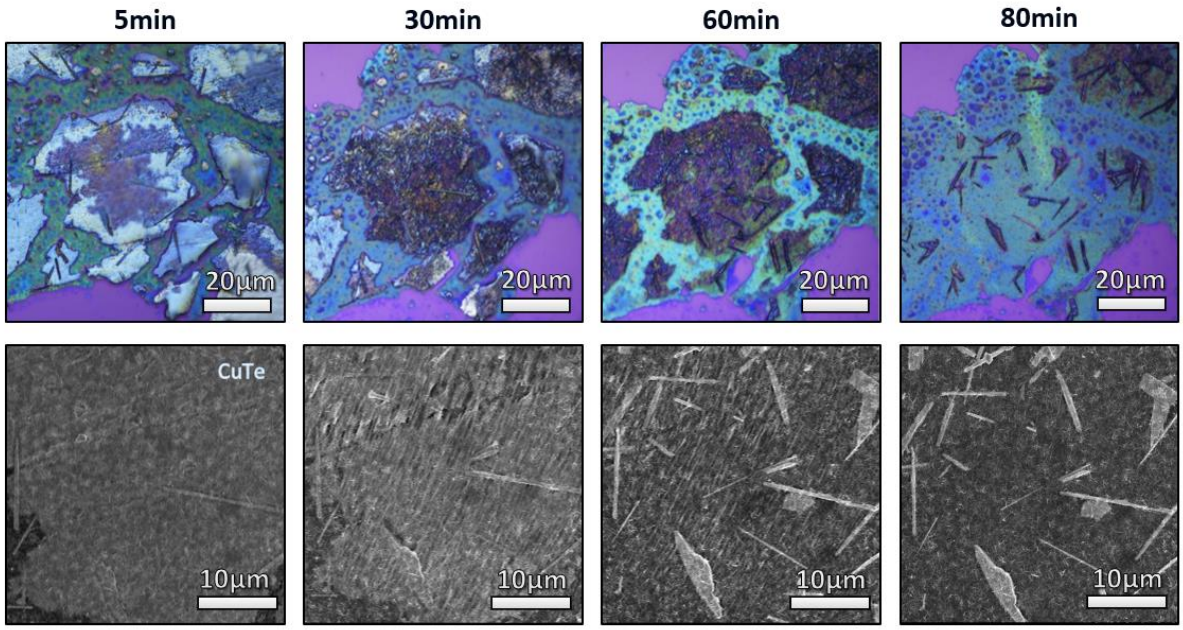

Figure 3-21. The changes in surface morphology of Cu_xTe_y droplets depending on etching time. The Cu_xTe_y droplets on SiO_2 substrate were etched gradually as etching time increased. It is found that WTe_2 nanobelts are underneath Cu_xTe_y droplets.

3.3 Transfer-Free Formation of Transition Metal Telluride Nanostructures on the Desired Substrate and Investigation of Electrical Properties

Recently, transfer-free growth of TMDs without the need for after-growth transfer process has been attracted for a fundamental research and practical applications[46]. To minimize degradation of TMDs' intrinsic properties and difficulty in fabrication of devices due to residues in process of complex transfer procedure, the development of direct formation of TMDs without necessity of an additional transfer step has been required.

In previous research, we confirmed that Cu_xTe_y metal alloys was formed on the desired substrate as the thickness of W layers became relatively thick. As shown in figure 3-22, the Cu_xTe_y was formed directly on SiO_2 /Si substrate. To expose the nanobelts inside of Cu_xTe_y droplets, we tried to mechanical peel Cu_xTe_y droplets off by using the method of peeling off using scotch tape. We confirmed that WTe_2 nanobelts were formed under the W layer and Cu_xTe_y droplet, by observing the back surface of the peeled scotch tape. As shown in figure 3-23, OM and SEM Images exhibit high density of WTe_2 nanobelts on the back surface of scotch tape. To confirm the WTe_2 nanobelts, Raman analysis was carried out, displayed in figure 3-24a.

We were able to observe as-synthesized WTe_2 nanobelts at the surface of SiO_2/Si substrate without using after-growth transfer processes. The Cu_xTe_y droplet and W layer were clearly peeled off by tape peeling off method, confirmed by EDAX and XRD analysis, indicated in figure 3-25b,c. Also, the as-obtained WTe_2 nanobelts directly on the desired substrate was confirmed by Raman spectroscopy, as shown in figure 3-24b. In short, we succeed to form WTe_2 nanobelts directly on the desired substrate without possibilities in degradation by inevitable chemical and physical damage in wet etching and transfer process.

Moreover, the feasibility of synthesis of $MoTe_2$ nanostructure as a member of the layered TMDs family was evaluated through our approaches. The formation of 2H-$MoTe_2$ and 1T'- $MoTe_2$ nanostructure on SiO_2 substrate was achieved by peeling the Cu_xTe_y droplets and Mo layer off, confirmed by Raman and Edax analysis of $MoTe_2$ nanostructure on SiO_2/Si substrate, indicated in figure 3-26.

The transfer-free formation of transition metal telluride nanostructure on desired substrate enables to investigate its electrical properties by fabricating test device directly on SiO_2/Si substrate without the needs for a further transfer process. Interestingly, we confirmed that the as-synthesized WTe_2 nanostructure by our method exhibits the similar resistivity as the exfoliated few-layer WTe_2 from the bulk crystal. The resistivity of few-layer WTe_2 nanostructure is in the range of ~ 10^{-4} to 10^{-3} Ω·cm, as shown in figure 3-7. To sum up, our approach of mechanical removal of Cu_xTe_y droplet by method of peeling off using scotch tape can reduce the whole process to obtain WTe_2 nanostructures as well as prevent degradation of WTe_2.

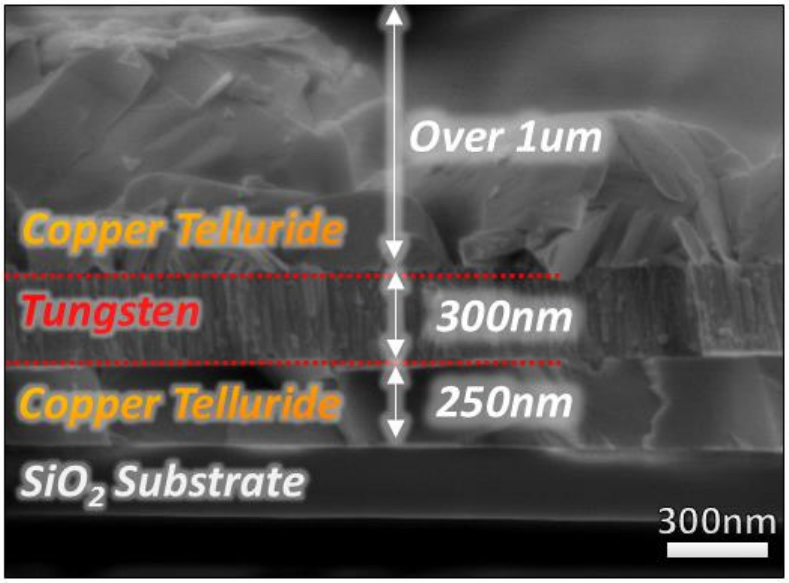

Figure 3-22. Cross sectional Image of as-grown Cu_xTe_y/W on SiO_2/Si substrate.

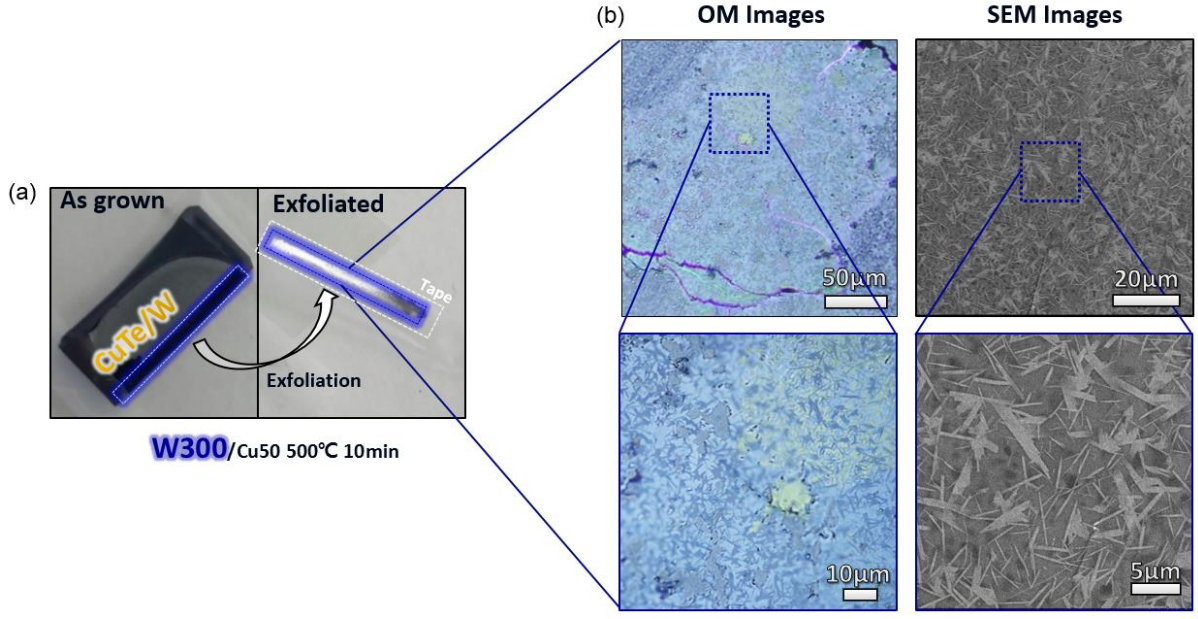

Figure 3-23. (a) Photograph of peeling off process by using scotch tape. (b) SEM and OM Images of WTe_2 nanobelts on the back side of exfoliated tape. It clearly suggests that synthesized WTe_2 nanobelts can be formed under Cu_xTe_y droplet/W layer.

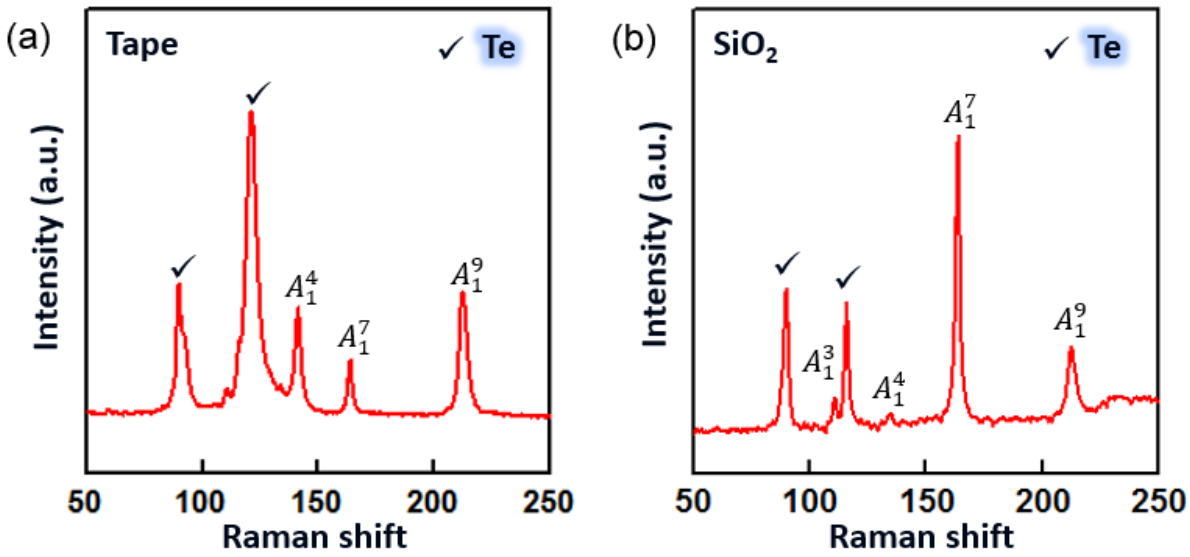

Figure 3-24. Raman spectra of WTe_2 nanobelts (a) on scotch tape and (b) on SiO_2/Si substrate, respectively.

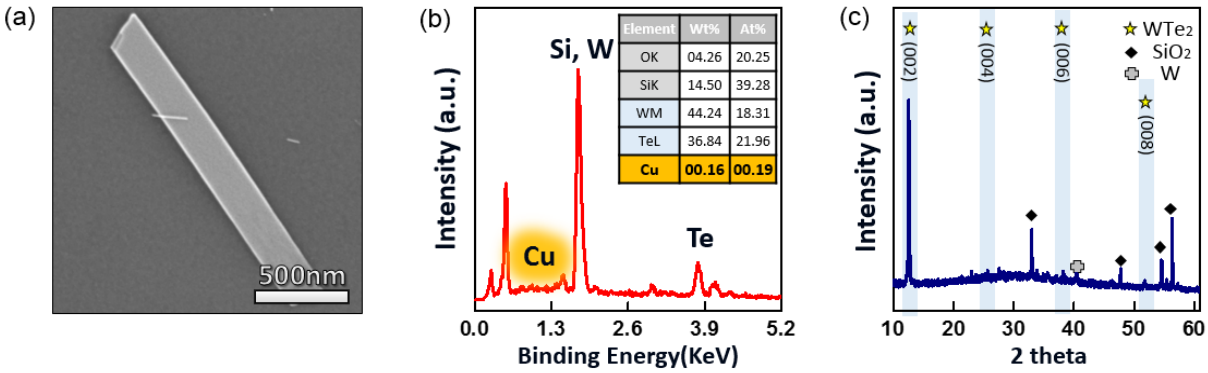

Figure 3-25. (a) Mechanical removal of Cu_xTe_y droplet by method of peeling off using scotch tape (b-c) Edax analysis and XRD data of WTe_2 nanobelts on SiO_2/Si substrate by peeling W and Cu_xTe_y droplets off, identifying that Cu_xTe_y droplets and W layer are clearly peeled off by method of peeling off using scotch tape

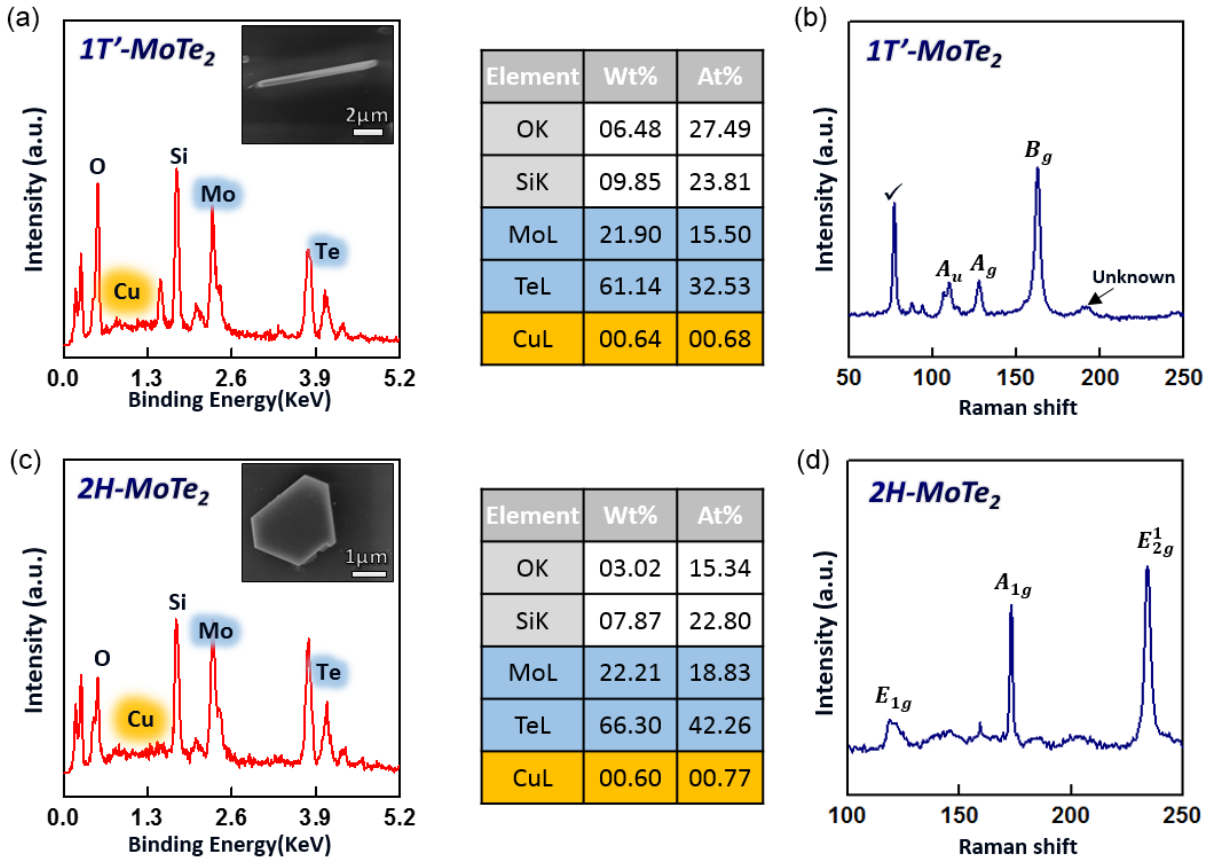

Element	Wt%	At%
OK	06.48	27.49
SiK	09.85	23.81
MoL	21.90	15.50
TeL	61.14	32.53
CuL	00.64	00.68

Element	Wt%	At%
OK	03.02	15.34
SiK	07.87	22.80
MoL	22.21	18.83
TeL	66.30	42.26
CuL	00.60	00.77

Figure 3-26. (a-d) Mechanical removal of Cu_xTe_y droplets and Mo layer by method of peeling off using scotch tape. The formation of 2H-$MoTe_2$ and 1T'-$MoTe_2$ nanostructure on SiO_2/Si substrate can be achieved by peeling Cu_xTe_y droplets and Mo layer off, confirmed in Raman and Edax spectra of $MoTe_2$ nanostructure on SiO_2/Si substrate

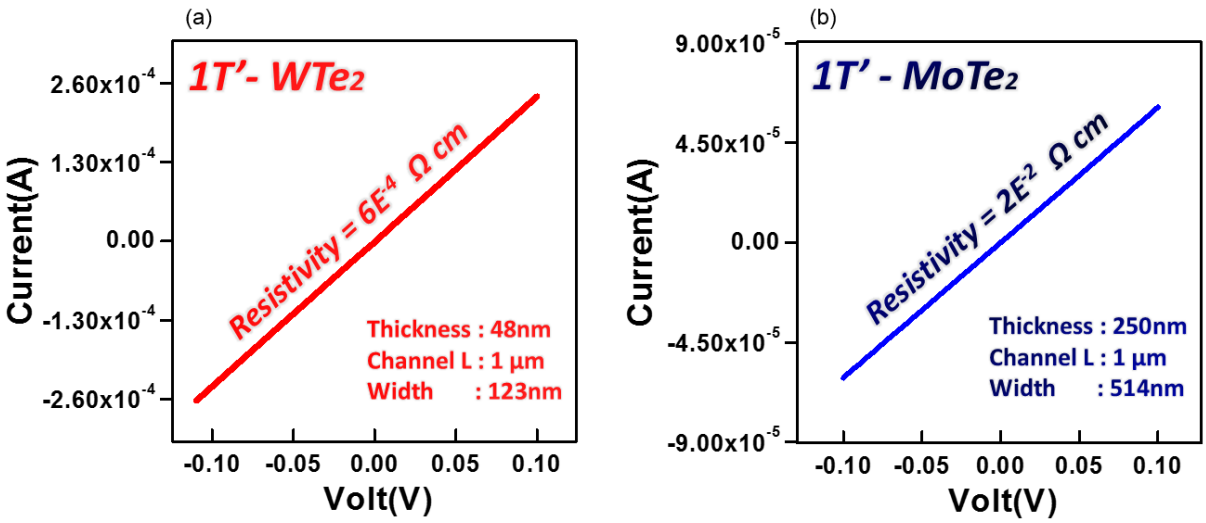

Figure 3-27. (a-b) Current vs voltage characteristics for fabricated 1T'- WTe_2 and $MoTe_2$ device, respectively. We successfully can obtain both 1T'- WTe_2 and $MoTe_2$ nanostructure directly on SiO_2/Si substrate with no needs for a further transfer process.

Chapter 4. Conclusion

Summary

In this research, the role of eutectic metal and its behavior on synthesis parameters in the synthesis of WTe_2 by using the pre-deposited films of W/Cu on SiO_2/Si substrate was studied.

First of all, the tungsten ditelluride (WTe_2) nanostructure were successfully synthesized by using eutectic metal alloys. The growth mechanism of WTe_2 was explained by the assistance of liquid Te-rich Cu_xTe_y droplets, after oversaturation with dissolved tungsten, induced a WTe_2 crystal growth. The crystallization takes place inside of Cu_xTe_y droplet at a temperature of ~500°C, above the Cu–Te eutectic temperature of 340°C. We described the crystallization of WTe_2 from solution-phase Cu_xTe_y droplets, resulting in 1-D preferential crystal growth of the single-crystalline WTe_2 nanobelts which has a stable distorted octahedral phase (1T'-WTe_2). The use of Te-rich eutectic metal alloys eliminates the Te deficiency in the resulting products and the contamination by impurities encountered with vapor deposition process. As a result, the as-synthesized WTe_2 nanostructures inside of Cu_xTe_y droplet by simple solution-phase reaction are highly pure, stoichiometric, and structurally uniform.

A different behavior of the Cu_xTe_y droplets were observed, which is strongly dependent on synthesis parameters such as growth temperature, time and process conditions of a metal film before WTe_2 growth. The structural characteristics and the formation of the products can be varied by controlling the synthesis parameters.

Particularly, we succeed to control the eutectic alloy to produce WTe_2 nanobelts where on the top of desired substrate directly. Our simple method of peeling off using scotch tape can reduce the whole process to form WTe_2 nanostructures on the desired substrate as well as prevent degradation of intrinsic properties of WTe_2, without using chemical wet etching and after-growth transfer processes. It enables to investigate its electrical properties by fabricating test device directly on SiO_2/Si substrate with no needs for a further transfer process. Moreover, the feasibility of synthesis of $MoTe_2$ nanostructure as a member of the layered TMDs family was evaluated through our approaches.

In conclusion, we develop reliable growth method of WTe_2 nanostructure using eutectic metal alloys and simple transfer-free growth method without the needs for a further transfer process. Our results provide not only a basis for optimizing WTe_2 nanostructure growth using eutectic metal alloys, but also can be adopted to research the novel properties of WTe_2 nanostructure without any degradation of the characteristics.

References

1. Butler, S. Z., *et al.* "Progress, challenges, and opportunities in two-dimensional materials beyond graphene." *ACS Nano* 7.4 (2013): 2898-2926.
2. Chhowalla, M., *et al.* "Two-dimensional semiconductors for transistors." *Nature Reviews Materials* 1 (2016): 16052.
3. Podzorov, V., *et al.* "High-mobility field-effect transistors based on transition metal dichalcogenides." *Applied Physics Letters* 84.17 (2004): 3301-3303
4. Liu, L., *et al.* "Performance limits of monolayer transition metal dichalcogenide transistors." *IEEE Transactions on Electron Devices* 58.9 (2011): 3042-3047
5. Fang, H., *et al.* "High-performance single layered WSe_2 p-FETs with chemically doped contacts." *Nano Letters* 12.7 (2012): 3788-3792.
6. Wang, Q. H., *et al.* "Electronics and optoelectronics of two-dimensional transition metal dichalcogenides." *Nature Nanotechnology* 7.11 (2012): 699-712.
7. Deng, Y., *et al.* "Black phosphorus–monolayer MoS_2 van der waals heterojunction p–n diode." *ACS Nano* 8.8 (2014): 8292-8299.
8. Furchi, M. M., *et al.* "Photovoltaic effect in an electrically tunable van der Waals heterojunction." *Nano Letters* 14.8 (2014): 4785-4791.
9. Fang, H., *et al.* "Strong interlayer coupling in van der Waals heterostructures built from single-layer chalcogenides." *Proceedings of the National Academy of Sciences* 111.17 (2014): 6198-6202.
10. Akinwande, D., *et al.* "Two-dimensional flexible nanoelectronics." *Nature Communications* 5 (2014).
11. Fiori, G., *et al.* "Electronics based on two-dimensional materials." *Nature Nanotechnology* 9.10 (2014): 768-779.
12. Chhowalla, M., *et al.* "The chemistry of two-dimensional layered transition metal dichalcogenide nanosheets." *Nature Chemistry* 5.4 (2013): 263-275.
13. Mak, K. F., *et al.* "Atomically thin MoS_2: a new direct-gap semiconductor." *Physical Review Letters* 105.13 (2010): 136805
14. Britnell, L., *et al.* "Strong light-matter interactions in heterostructures of atomically thin films." *Science* 340.6138 (2013): 1311-1314.

15. Cheiwchanchamnangij, T., *et al.* "Quasiparticle band structure calculation of monolayer, bilayer, and bulk MoS_2." *Physical Review B* 85.20 (2012): 205302.

16. Song, S., *et al.* "Room temperature semiconductor–metal transition of $MoTe_2$ thin films engineered by strain." *Nano Letters* 16.1 (2015): 188-193.

17. Ali, M. N., *et al.* "Large, non-saturating magnetoresistance in WTe_2." *Nature* 514.7521 (2014): 205-208.

18. Huang, H. H., *et al.* "Controlling phase transition for single-layer MTe_2 (M= Mo and W): modulation of the potential barrier under strain." *Physical Chemistry Chemical Physics* 18.5 (2016): 4086-4094.

19. Park, J. C., *et al.* "Phase-Engineered Synthesis of Centimeter-Scale 1T′-and 2H-Molybdenum Ditelluride Thin Films." *ACS Nano* 9.6 (2015): 6548-6554.

20. Shi, Y., *et al.* "Recent advances in controlled synthesis of two-dimensional transition metal dichalcogenides via vapour deposition techniques." *Chemical Society Reviews* 44.9 (2015): 2744-2756.

21. Novoselov, K. S., *et al.* "Two-dimensional crystals-based heterostructures: materials with tailored properties." *Physica Scripta* 2012.T146 (2012): 014006.

22. Gupta, A. *et al.* "Recent development in 2D materials beyond graphene." *Progress in Materials Science* 73 (2015): 44-126.

23. Li, J., *et al*. "Scalable Fabrication of 2D Semiconducting crystals for future electronics." *Electronics* 4.4 (2015): 1033-1061.

24. Ji, Q., *et al.* "Chemical vapour deposition of group-VIB metal dichalcogenide monolayers: engineered substrates from amorphous to single crystalline." *Chemical Society Reviews* 44.9 (2015): 2587-2602

25. Lv, H. Y., *et al.* "Perfect charge compensation in WTe_2 for the extraordinary magnetoresistance: From bulk to monolayer." *EPL (Europhysics Letters)* 110.3 (2015): 37004

26. Keum, D. H., *et al.* "Bandgap opening in few-layered monoclinic $MoTe_2$." *Nature Physics* 11.6 (2015): 482-486

27. Duerloo, K. A. N., *et al.* "Structural phase transitions in two-dimensional Mo- and W- di chalcogenide monolayers." *Nature Communications* 5 (2014).

28. Lee, C. H., *et al.* "Tungsten ditelluride: a layered semimetal." *Scientific Reports* 5 (2015).

29. Lu, N., *et al.* "Atomic and electronic structures of WTe_2 probed by high resolution electron microscopy and ab initio calculations." *The Journal of Physical Chemistry C* 120.15 (2016): 8364-8369.

30. Ali, M. N., *et al.* "Correlation of crystal quality and extreme magnetoresistance of WTe_2." *EPL (Europhysics Letters)* 110.6 (2015): 67002.

31. Kim, Y., *et al.* "Anomalous Raman scattering and lattice dynamics in mono-and few-layer WTe_2." *Nanoscale* 8.4 (2016): 2309-2316.

32. Wang, L, *et al.* "Tuning magnetotransport in a compensated semimetal at the atomic scale." *Nature Communications* 6 (2015).

33. Dai, Y. M., *et al.* "Ultrafast carrier dynamics in the large-magnetoresistance material WTe_2." *Physical Review B* 92.16 (2015): 161104.

34. Kong, W. D., *et al.* "Raman scattering investigation of large positive magnetoresistance material WTe_2." *Applied Physics Letters* 106.8 (2015): 081906.

35. Soluyanov, A. A., *et al.* "Type-II Weyl semimetals." *Nature* 527.7579 (2015): 495-498

36. Burkov, A. A., *et al.* "Weyl semimetal in a topological insulator multilayer." *Physical Review Letters* 107.12 (2011): 127205.

37. Qian, X., *et al.* "Quantum spin Hall effect in two-dimensional transition metal dichalcogenides." *Science* 346.6215 (2014): 1344-1347.

38. Zheng, F., *et al.* "On the Quantum Spin Hall Gap of Monolayer 1T′-WTe_2." *Advanced Materials* (2016).

39. Zhao, Y., *et al.* "Anisotropic magnetotransport and exotic longitudinal linear magnetoresistance in WTe_2 crystals." *Physical Review B* 92.4 (2015): 041104.

40. Kang, D., *et al.* "Superconductivity emerging from a suppressed large magnetoresistance state in tungsten ditelluride." *Nature Communications 6* (2015).

41. Choi, H. J., *et al.* "Vapor–liquid–solid growth of semiconductor nanowires." *Semiconductor Nanostructures for Optoelectronic Devices.* Springer Berlin Heidelberg, 2012. 1-36

42. Ellmer, K. *et al.* "Preparation routes based on magnetron sputtering for tungsten disulfide (WS_2) films for thin-film solar cells." *Physica Status Solidi (b)* 245.9 (2008): 1745-1760.

43. Brunken, S., *et al.* "Analysis of the early stages of the rapid, nickel-assisted crystallization of WS_2 films." *Journal of Applied Physics* 120.16 (2016): 165307.

44. Sun, Y., *et al.* "Eutectic solidification applied to nanofabrication: a strategy to prepare large-scale tungsten carbide nanowalls." *Journal of Materials Chemistry* 22.32 (2012): 16566-16571.

45. Lee, Y. H., *et al.* "Tungsten nanowires and their field electron emission properties." *Applied Physics Letters* 81.4 (2002): 745-747.

46. Huang, C. C., *et al.* "Transfer-free growth of atomically thin transition metal disulfides using a solution precursor by a laser irradiation process and their application in low-power photodetectors." *Nano Letters* 16.4 (2016): 2463-2470.

ULSAN NATIONAL INSTITUTE OF SCIENCE AND TECHNOLOGY

Master's Thesis

Synthesis of Single-Crystalline Tungsten Ditelluride (WTe_2) Nanostructures Using Eutectic Metal Alloys

Jong Hwa Lee

Department of Materials Science and Engineering

Graduate School of UNIST

2017

ULSAN NATIONAL INSTITUTE OF SCIENCE AND TECHNOLOGY

Synthesis of Single-Crystalline Tungsten Ditelluride (WTe_2) Nanostructures Using Eutectic Metal Alloys

Jong Hwa Lee

Department of Materials Science and Engineering

Graduate School of UNIST

ULSAN NATIONAL INSTITUTE OF SCIENCE AND TECHNOLOGY

Synthesis of Single-Crystalline Tungsten Ditelluride (WTe_2) Nanostructures Using Eutectic Metal Alloys

A thesis/dissertation
submitted to the Graduate School of UNIST
in partial fulfillment of the
requirements for the degree of
Master of Science

Jong Hwa Lee

01. 19. 2017.

Approved by

Advisor
Soon-Yong Kwon

ULSAN NATIONAL INSTITUTE OF SCIENCE AND TECHNOLOGY

Synthesis of Single-Crystalline Tungsten Ditelluride (WTe_2) Nanostructures Using Eutectic Metal Alloys

Jong Hwa Lee

This certifies that the dissertation of Jong Hwa Lee is approved.

01. 19. 2017

Adviser: Soon-Yong Kwon

Zonghoon Lee : Thesis Committee Member #1

Sung Youb Kim : Thesis Committee Member #2

Abstract

Beyond graphene, group-VI transition metal dichalcogenides (TMDs) which is compound of transition metal and chalcogen have recently attracted much attention and mechanically exfoliated flakes of two-dimensional TMDs hold great promise due to their rich variety of properties. As a member of the TMDs family, tungsten ditelluride (WTe_2), which has a stable distorted octahedral phase (1T') among several polymorphs, are appealing because of their unique properties such as an unusual magnetoresistance and quantum spin Hall effect. In an effort to synthesize WTe_2 nanostructures, researchers have tried to develop many growth techniques. Nonetheless, there remains considerable difficulty in obtaining high-quality WTe_2 nanostructures due to a high equilibrium vapor pressure of tellurium at growth temperatures and a weak binding energy of W-Te than other chalcogens.

Here, we suggest a novel facile method to realize the synthesis of single-crystalline WTe_2 nanostructures using eutectic metal alloys. In our work, we studied on the role of eutectic metal alloys and its behavior on synthesis parameters and more details will be presented. In addition, the as-synthesized WTe_2 nanostructures can be easily transferred to different substrates and/or solutions as well as successfully formed on desired substrate without the needs for a further transfer process. The transfer-free formation of WTe_2 nanostructures can be adopted to research the novel properties of WTe_2 nanostructure without any degradation of the intrinsic characteristics. Moreover, feasibility of synthesis for $MoTe_2$ nanostructure as a member of the layered TMDs family was evaluated through our methods. We expect that the emergence of new type of transition metal telluride nanostructures will create exciting prospects for further technical devices and applications in nano-electronics, catalysts and other fields.

Keywords : Transition Metal Dichalcogenides (TMDs), Tungsten ditelluride (WTe_2), Eutectic metal alloys, Nanostructures, Molibdenum ditellruide ($MoTe_2$)

Contents

List of Figures

List of tables

Chapter 1. Overviews

1.1 Transition Metal Dichalcogenides (TMDs)

1.1.1 Introduction of TMDs

Beyond 2D Graphene, scientific interest has been extended to low-dimensional materials because of the wealth of unusual and unique properties that occur when scaled down from bulk to nanoscale dimensions[1]. Recent progress suggests that such truly atomically-thin low-dimensional materials could be one pathway for future electronic devices. The advantages of low-dimensional (2D) materials compared with 3D materials for FETs are demonstrated by the differences that occur in the charge transport between the bulk and the single layer[2]. In 2D materials, charge carriers are confined in atomically thin channels because of the vdW materials' low density of dangling bonds and minimal surface roughness, resulting in excellent gate electrostatics (see figure 1-1). These features make them promising candidates for the revolutionary applications, such as truly atomically-thin field-effect transistors (FET)[3-6], stacked vdW layered hetero-junctions[7-9], and flexible and transparent electronic devices[10-11].

Layered group-VI transition metal dichalcogenides (TMDs) which is compound of transition metal and chalcogen have a chemical formula of MX_2, where M is the transition metal (i.e. Mo or W in group VI metal) and X stands for chalcogen atoms. (i.e. S, Se or Te). Since layered TMDs have a layered stacked structure with weak van der Waals (vdW) force along out-of-plane and strong covalent bonding along in-plane, it could be mechanically and chemically exfoliated into single and/or few layers. Each layer typically has a thickness of 7~9 Å, which consists of a hexagonally packed layer of metal atoms sandwiched between chalcogen atoms.

The layered TMDs exhibit a variety of polymorphs, which are 1T, 2H where the letters stand for trigonal, hexagonal and the digit indicates the number of X–M–X units in the unit cell respectively, as displayed in figure 1-2 (single-layer TMDs exhibit two polymorphs: trigonal prismatic and octahedral phases.)[12].

For most TMDs, the crystal coordination and combination of metal and chalcogen atoms have effects on the material's electrical properties. The bandgap decreases as the atomic number (atomic mass) of the chalcogen atom increases (from S to Se to Te). For example, the bandgap of 2H-MoS_2, 2H-$MoSe_2$ and 2H-$MoTe_2$ decreases gradually from 1.3 to 1.0 eV. The tungsten (or molybdenum) sulfides and selenides shows the semiconducting behavior, but the tellurides are known as semimetal. The group-VI TMDs' electrical properties are summarized in table 1-1.

Among the group-VI TMDs, Mo (or W) sulfides and selenides are semiconductors and possess bandgaps in the range of 1-2 eV with the unit cell of trigonal prismatic (2H-phase, in figure 1-2b). Since the material has discrete band gap level, high carrier mobility and the absence of dangling bonds, they have a possibility for the novel applications of electronics. Since semiconducting TMDs have sizable bandgap, they are a promising optical materials having the energy spectrum ranged from visible to near infrared wavelength. The observation of indirect-to-direct bandgap transition at the monolayer regime[13], strong light-matter interactions[14], and large exciton binding energies[15] can be used for the potential platform for investigation of unusual physical properties as well as the application of the photonic devices in the next-generation.

On the other hand, semi-metallic group-VI metal tellurides display the semi-metallic properties when it has a distorted 1T-phase (1T' or Td, also called distorted orthorhombic, see figure 1-2c)[16-17]. In addition, the tellurides have low energy barriers for the phase transition, so phase transition can be controlled by growth temperature, pressure, or strain[18-19].

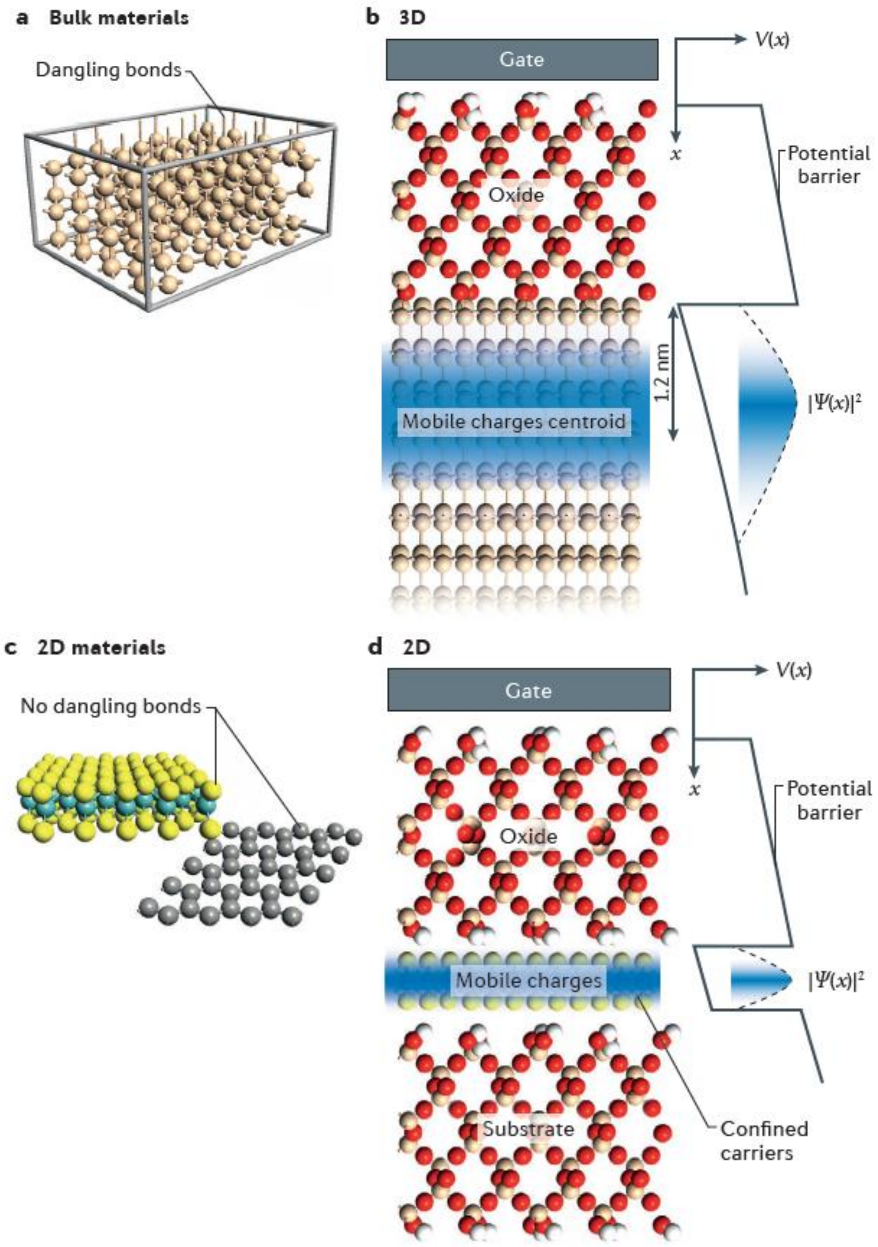

Figure 1-1. Advantage of 2D materials compared with 3D materials. (a) 3D (bulk) semiconductors reduce the performance of field-effect transistors (FETs) due to its dangling bonds that form traps for carriers. (b) Mobile charge distribution in 3D semiconductors and gate electrostatics. (c) 2D materials exhibit pristine surfaces. (d) In atomically thin materials, charge carriers are confined, resulting in a narrower mobile charge distribution. The confinement of charge carriers allows the mobile electrons to be easily controlled by the gate voltage[2].

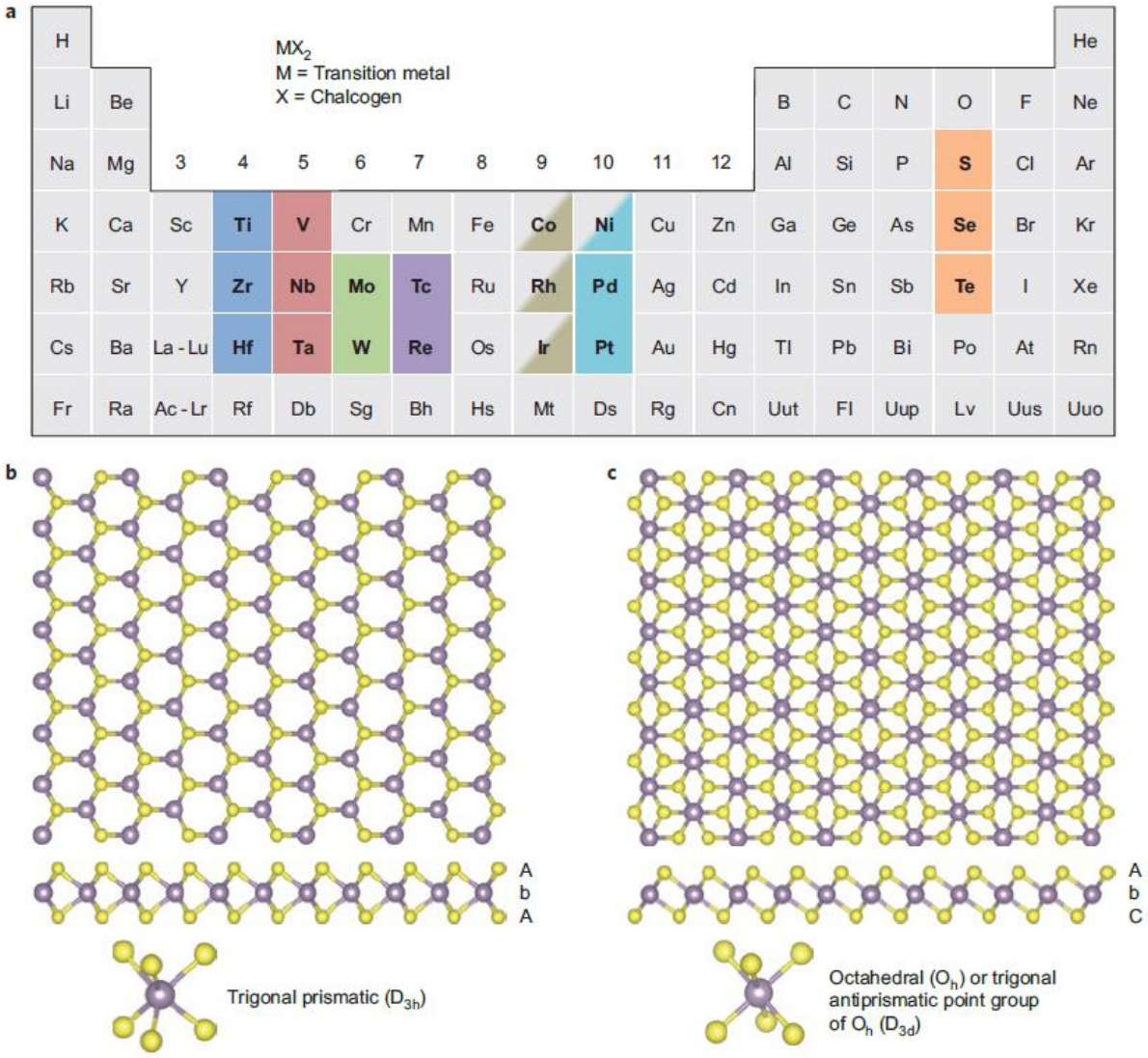

Figure 1-2. Structure of single-layered TMDs. (a) In the periodic table, the transition metals (M) and three chalcogen (X) elements that predominantly crystallize in those layered structure are highlighted. (b,c) c-axis and section view of monolayer TMDs with (b) trigonal prismatic and (c) octahedral coordinations (Atom colour code: purple- metal, yellow- chalcogen)[12].

Table 1-1. Comparison of the group-VI layered TMDs.

	Semiconducting TMDs					Semimetal TMDs	
Materials	**MoS_2**	**$MoSe_2$**	**$MoTe_2$**	**WS_2**	**WSe_2**	**$MoTe_2$**	**WTe_2**
Phase	2H (trigonal prismatic)					1T' (octahedral)	
Band gap	1.80	1.38	1.07	2.1	1.75	-0.20	-0.21
Mobility [$cm^2V^{-1}S^{-1}$]	0.01-200	0.01-23	5-12	12	7.3	10^3-10^4	
Spectral range	Visible, UV		NIR, Visible, UV	Visible, UV		THz, FIR, MIR, NIR, visible, UV	

1.1.2 Synthesis of TMDs

Low-dimensional TMDs have attracted significant attention due to their exotic properties associated with their defined dimensionalities. Due to unique electronic properties and high specific surface areas of low-dimensional TMDs, it has been seen as a promising and ideal candidates in various fields including optoelectronics, catalysis, flexible and wearable electronic devices. To achieve the practical applications mentioned above, developing controllable and scalable synthesis method of atomically thin or few-layer TMDs with layer controllability and large-area uniformity must be an essential requirement.

So far, lots of different ways have been developed[20-23], as presented in table 1-2. Until now, both *top-down* exfoliation and *bottom-up* synthesis methods are developed for preparation of atomically thin or few-layer TMDs.

Top-down exfoliation methods, such as mechanical exfoliation and chemical exfoliations, are method to separate single- or few- layers TMDs from their corresponding bulk TMDs. The individual layers of the 3D bulk material can be successfully separated from each other. This common top-down method have been studied widely, but there are some problems in obtaining reproducibility for large-area thin layers and difficulty to scale up.

Bottom-up methods may present alternative approaches. The chemical vapor deposition technique (CVD) has shown great promise to gain high-quality TMDs layers with a scalable size, controllable thickness. But they still need to be developed further to attain high-quality and large-area TMDs on the desired substrates. The large area and uniform synthesis of low-dimensional TMDs has remained a challenge for a long time. Table 1-2 also shows the conventionally used bottom-up synthesis methods and advantages/disadvantages of them. The synthesis methods include solid-precursor based vapor phase deposition, vapor phase chalcogenization, vapor-precursor based chemical vapor deposition. These scalable synthesis techniques enable to produce highly-crystalline large-area 2D TMDs crystals for wafer-scale and have tremendous potential for manufacturing in future nano-electronics.

Currently, most promising scalable synthesis technique is vapor phase deposition. In general, vapor phase deposition methods relies on physical transport (usually with inert carrier gases) and chemical reaction of vaporized precursors to deposit TMDs onto the desired substrate.

In terms of the initial precursor state, vapor phase deposition technique can be classified into solid- and gas-precursor based vapor phase technique. Firstly, there are two classes of solid-precursor based vapor phase deposition technique: (1) chemical vapor deposition (CVD) based on the reaction of solid-metal and chalcogen precursors, where both solid- metal precursors and chalcogen powders are heated into the vapor phase, and then transported to form TMDs layers; (2) chalcogenization of pre-deposited film based precursor, where the metal (or metal oxide) thin films are firstly deposited onto the substrates, then chalcogen powders are heated to be vapors and transported to the substrates to produce TMDs

films by conversion of the pre-deposited metal(metal oxide) film into TMDs films at the atmosphere of chalcogen vapors[24], as shown in figure 1-3a.

In addition, recent studies have also employed gas-precursors to improve the controllability during vapor phase growth. The reaction of gaseous metal and chalcogen feedstocks is illustrated in figure 1-3a. Here, the H_2 gas can be used for promoting the reduction of precursors. The desired substrates including SiO_2, quartz, mica and sapphire can be used (figure 1-3b) due to their high thermal stability and chemical inertness. The hexagonal crystal structure of quartz, mica and sapphire also helps to arrange the absorbed TMDs molecules.

Table 1-2. Table showing the different growth methods for layered TMDs.[1, 12, 19-24]

Technique		Schematics showing each technique	TMDs available to date	Achievements	Challenges
Top-down	Mechanical exfoliation	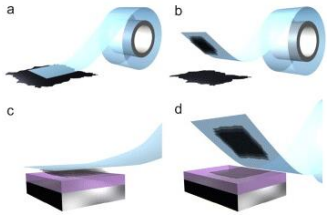	**Single phase TMDs** (MoX_2, WX_2, etc.)	High crystallinity	Thickness control, Yield, Not scalable
	Liquid exfoliation	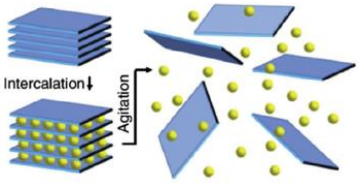		High productivity	Small crystallites, Thickness control, Yield
Bottom-up	Solid-precursor vapor phase deposition	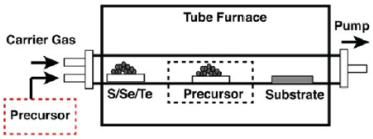	**Single phase TMDs** (MoS_2,$MoSe_2$,WS_2,WSe_2) **TMDs alloy** ($Mo_xW_{1-x}S_2$) **Doped TMDs** (Mn-, Co-doped MoS_2) **Hetero-structures** (MoS_2-WS_2,WS_2-BN MoS_2-graphene etc.)	High scalability, Hetero-structure availability	Defects, Stoichiometry control, Crystal quality
	Vapor phase chalcogen-ization	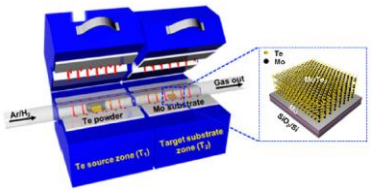	**Single phase TMDs** (MoS_2, $MoTe_2$,WSe_2 etc.) **Hetero-structures** (MoS_2-WSe_2-graphene)		Defects, Stoichiometry control, Crystal quality
	Gas-precursor vapor phase deposition	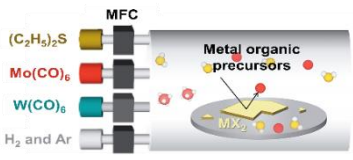	**Single phase TMDs** ($MoSe_2$,WSe_2)		Defects, Crystal quality

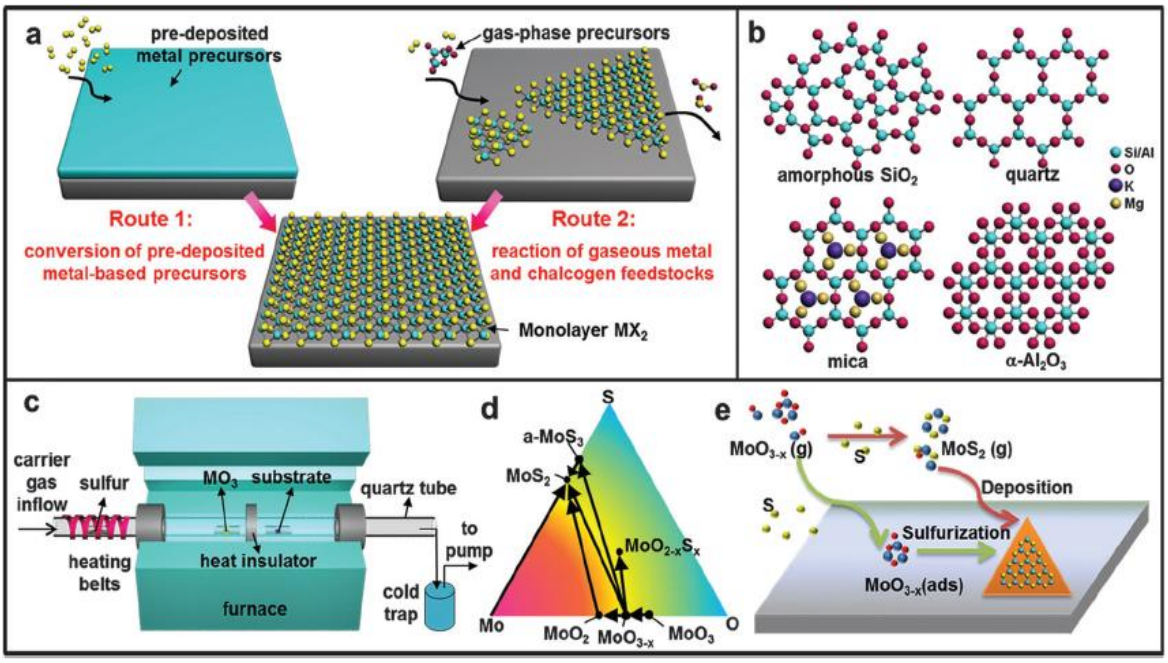

Figure 1-3. Introduction to the CVD synthesis of MX_2 thin layers. (a) Two routes for synthesis of MX_2. (b) Commonly used the insulating desired substrates for MX_2 growth. (c) Typical setup of a LP-CVD system. (d) Mo–S–O ternary phase diagram, in which the labelled arrows indicate reaction pathways for the CVD growth of MoS_2 from MoO_3 precursors. (e) Possible growth processes of MoS_2 by the reaction of S and MoO_{3-x}[24].

1.2 Tungsten ditelluride (WTe_2)

1.2.1 Introduction of WTe_2

Layered group-VI TMDs have been investigated widely because of its noticeable unique characteristics when thinned down from bulk to nanoscale. However, the semi-metallic TMDs such as tungsten ditelluride (WTe_2) and molybdenum ditelluride ($MoTe_2$) have not been examined relatively compared to the semiconducting TMDs. As shown in figure 1-4, the semi-metallic WTe_2 crystal exhibit a distortion of the octahedral 1T structure[25]. The tungsten atoms in the Td crystal structure are octahedrally coordinated by tellurium with alternating long and short distances between tungsten atoms due to strong intermetallic bonding. Even though $MoTe_2$ can have either 1T'- or 2H - phases and show the reversible structural phase transition by external stimulation such as strain and temperature[26-27], WTe_2 only crystallizes in distorted octahedral phase (1T' or Td) in nature among several polymorphs, regardless of growth condition and external strain.

It is found that WTe_2 has its stable energy in a distorted 1T (Td) structure and semi-metallic electronic characteristics[17, 28-29]. Figure. 1-5 shows the calculated band structure of 2H- and 1T'- WTe_2. While the 2H-phase WTe_2 has an indirect 0.702 eV bandgap, 1T'-WTe_2 has small overlap of electron and hole pockets at the Fermi energy along the Γ direction (corresponding to the a-axis, along the tungsten chains in crystal), indicating its semi-metallic properties. Figure. 1-6 shows the representative x-ray diffraction (XRD) patterns of WTe_2 experimentally grown by chemical vapor transport method, with the theoretical XRD patterns of 1T'- and 2H- phase WTe_2.

The semi-metallic properties of WTe_2 can be confirmed directly by using temperature-dependent resistance measurements. In general, the resistivity of a metal decreases linearly as the temperature decrease. Regarding the resistivity of metal at zero kelvin, there are only scattered electrons caused by crystal defects such as grain boundaries, impurities, etc. In semiconductor, the resistivity decreases at the elevated temperature induced by excitation of carriers. Therefore, characterization of temperature-dependent resistivity allows us to recognize whether the materials is a semiconductor or metal. Figure. 1-7 exhibits the typical temperature-dependent resistivity of layered WTe_2 crystal with different thickness, showing a well-metallic behavior of WTe_2 on temperature dependence. Moreover, extraction of residual-resistivity ratio (RRR=ρ_{300K}/ρ_{oK}) is a good indicator of crystal quality, the relationship between the electrical mobility and RRR is indicated[30], in figure 1-8.

The vibrational behavior of WTe_2 can be explored by using the incident photon energy via Raman spectroscopy[31]. Raman spectroscopy measurements is an useful technique as the fingerprint recognition

for confirming the existence of the material and assuming its thickness of WTe_2, already commonly used in the research of graphene and other 2D materials. Figure 1-9 (a) shows the representative Raman spectra of WTe_2, as a function of its thickness. The Raman spectrum of WTe_2 shows four main peaks approximately at 118, 134, 164, and 212cm^{-1}, and they are noted as the A_1^3, A_1^4, A_1^7 and A_1^9, respectively. The simulated lattice vibration of the Raman modes in bulk WTe_2 is illustrated in figure 1-9b, as well.

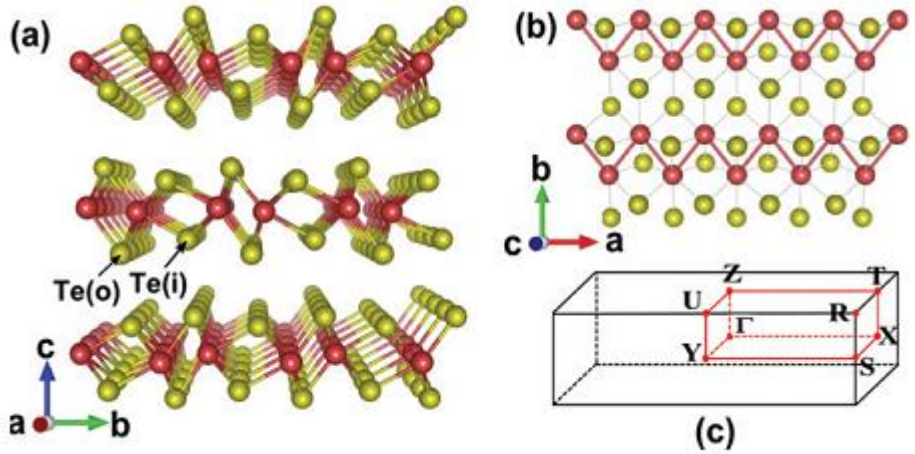

Figure 1-4. Crystal structure of WTe_2 viewed along (a) the a-axis (parallel to the zigzag W-W chains) and (b) the c-axis (perpendicular to the stacked layers); (c) the corresponding Brillouin zone. The red and yellow balls represent W and Te atoms, respectively[25].

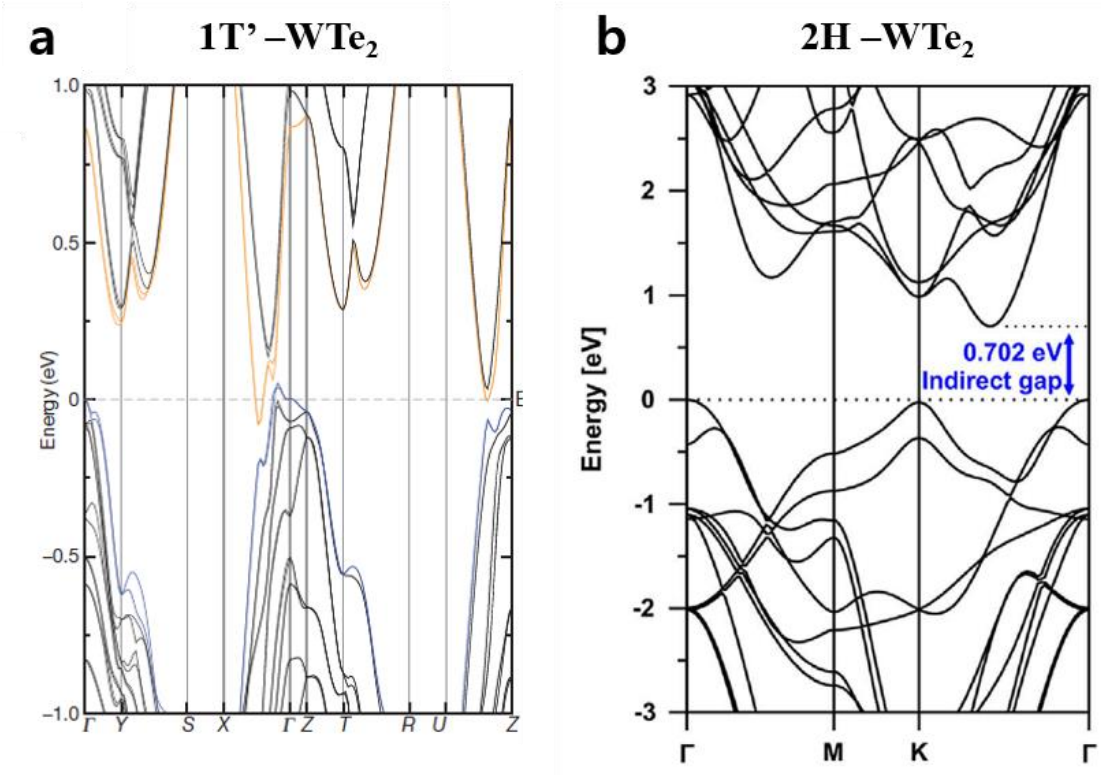

Figure 1-5. The electronic band structures indicate that bulk WTe_2 (a) in the 1T' phase has a 0.21 eV band overlap and (b) in the 2H structure has an indirect 0.702 eV bandgap[17, 28].

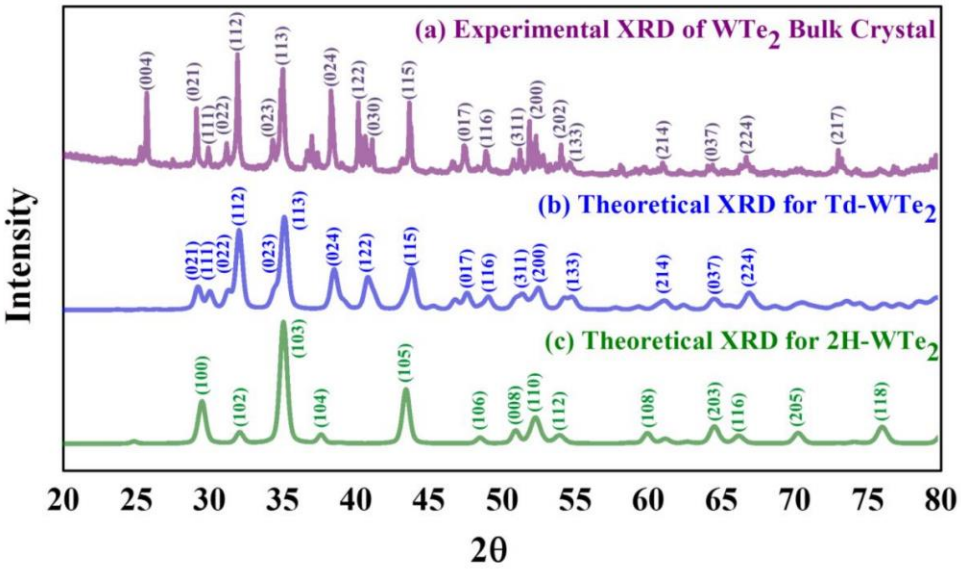

Figure 1-6. The representative X-ray Diffraction Patterns (XRD) for (a) experimental WTe_2 bulk crystal; (b) theoretical 1T' (or Td) WTe_2; (c) theoretical 2H-WTe_2[28].

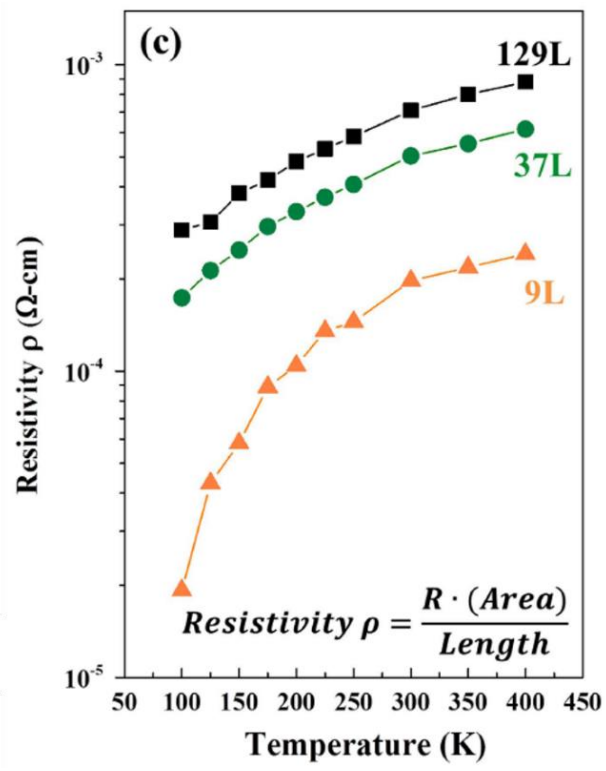

Figure 1-7. The temperature-dependent resistivity depending on the WTe_2 layer thickness, showing the WTe_2 is metallic in nature (resistivity proportional to temperature) rather than the semiconducting behavior[28].

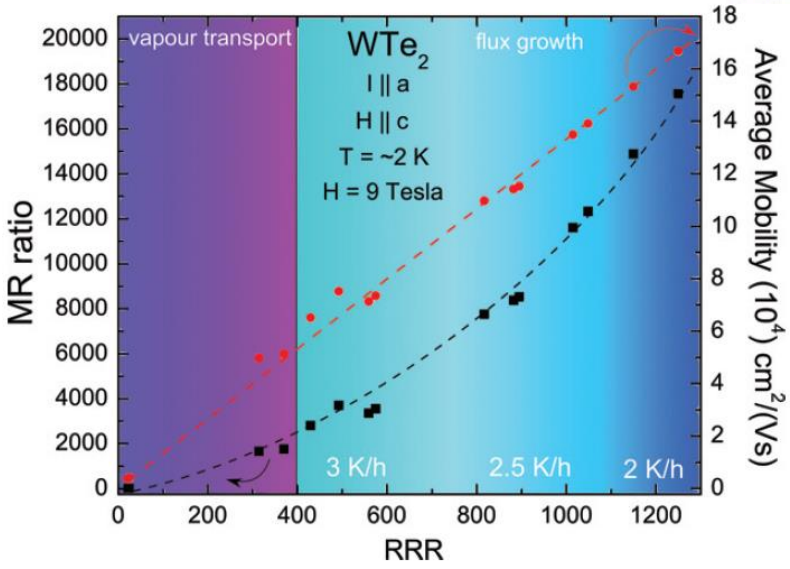

Figure 1-8. MR ratio and average carrier mobility vs. RRR. MR ratio follows the left axis (black squares) while μ_{avg} follows the right axis (red circles)[30].

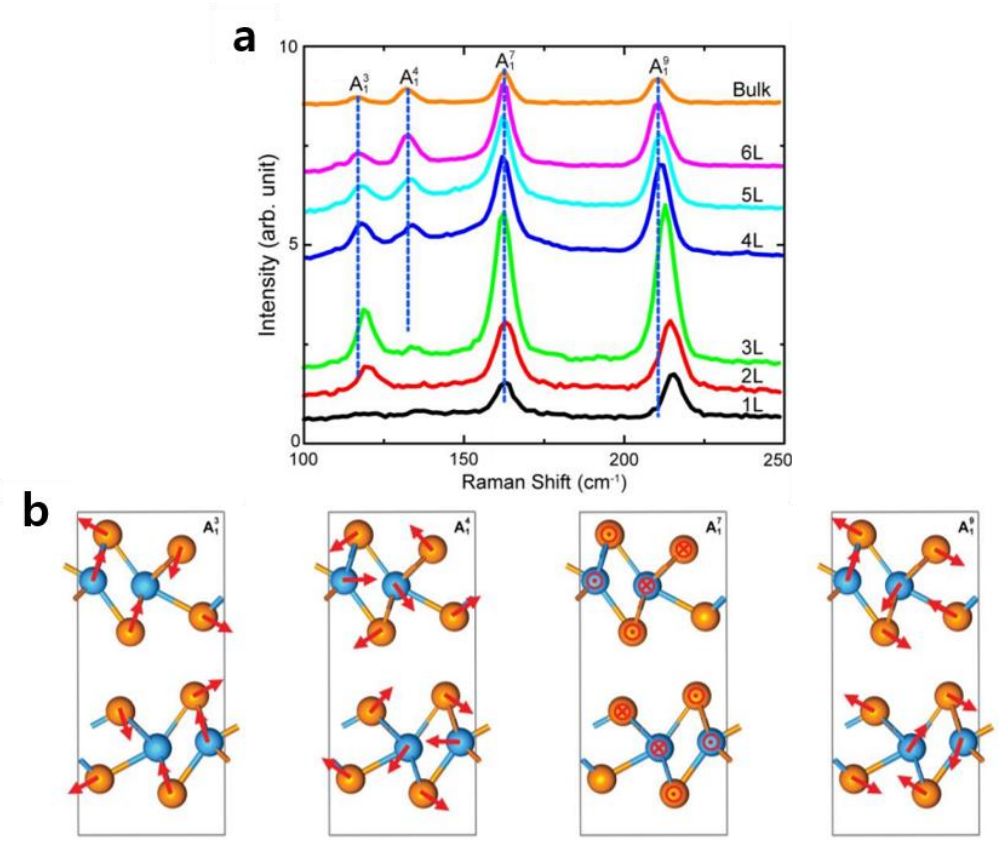

Figure 1-9. (a) The Raman spectra of and mono- to six-layer and bulk WTe_2. The blue dashed lines indicate the frequencies of the Raman modes in bulk WTe_2; (b) Atomic illustration for the lattice vibrations of the Raman modes in bulk WTe_2[31].

1.2.2 Conventional Synthesis Methods of WTe_2

Many researchers have tried several growth techniques for making the WTe_2 crystal either in bulk and nanoscale form, but synthesis of nanostructured-WTe_2 has not been reported yet, in contrast with any other TMDs.

Currently, single-crystalline WTe_2 in bulk form has been synthesized by chemical vapor transport methods or solid state reaction, and these methods produce only bulk crystal[17,28,32,39,40]. Previously, most of the studies on WTe_2 crystal have been demonstrated in mechanically or chemically exfoliated layers (flakes) from the bulk crystal. Accordingly, investigation of WTe_2 with controlled its thickness has been limited. Moreover, these methods are highly unsuitable for mass production because a high growth temperature (~1000°C) and growth time for several days (usually more than 24 hours) must be required, as shown in Table 1-3.

Synthesis of nanostructured-WTe_2 was very challenging due to the high vapor pressure (low sublimation temperature) of tellurium and low reaction activity of tungsten with tellurium. In chemical vapor deposition process, the probability of creating nucleation sites is extremely low because of the Te deficiency because desorption of tellurium vapor precursors occurs easily. For these reasons, making the Te-rich condition is critical to synthesize WTe_2 nanostructures. To obtain stoichiometric and nucleate tungsten ditelluride crystal, desorption of tellurium vapor precursor must be prevented and activate tungsten atoms to be reacted with tellurium precursor.

Table 1-3. Conventional growth methods of WTe_2 single crystal, only obtaining bulk crystal.

Growth method	Crystal Type	Growth temperature	Growth time	Transport agent	References
Chemical Vapor Transport	bulk	950°C	7 days	Br_2	[28]
	bulk	890°C	4 days	WCl_6	[32]
	bulk	750°C	7 days	Br_2	[17]
Solid state reaction	bulk	1100°C	96 hr	None	[39]
	bulk	1000°C	5hr	None	[40]

1.2.3 Unique Properties of WTe_2

1.2.3.1 Large & Unsaturated Magnetoresistance (MR) in WTe_2

The investigation of WTe_2 has been attracted significant attention since an unusual magnetoresistance (MR) in WTe_2 crystal was discovered in 2014. Mazhar N. Ali et.al[17] reported the observation of an extremely large positive magnetoresistance: 13 million percent at 0.53 kelvins in a magnetic field of 60 T (Teslas), as displayed in figure 1-10.

MR is defined as a change in material's electrical resistance (ρ) in response to an applied magnetic field H and is expressed as $\mathrm{MR} = [\rho(\mathrm{H}) - \rho(0)]/\rho(0)$. The large MR can be observed also in other semimetals such as bismuth and graphite because of the compensated hole-electron resonance; however, the unsaturated MR in WTe_2 up to 13,000,000% at 0.53 K in an applied magnetic field of ~60T is quite unique. This extraordinary MR behavior in WTe_2 is known to originate from a nearly perfect compensation of electron and hole concentrations (first known material for nearly perfect resonance) and this is explained by two band model for magneto-transport in semimetals. In two band theory, the MR is given by as follows:

$$MR = \frac{\Delta\rho}{\rho} = \frac{\rho_{xx}(B) - \rho_{xx}(0)}{\rho_{xx}(0)} = \mu_e \mu_h B^2 \ (if\ n = p)$$

, where μ_e and μ_h is the mobility of the electrons and holes, respectively, and B is the applied magnetic field (n=p, where n and p are the electron and hole concertation, respectively)[32].

In semimetals, large positive magnetoresistances are attributed to a balanced electron–hole 'resonance' condition; the positive MR is proportional to B in nearly perfectly compensated semimetal of WTe_2. In this regard, it is expected that WTe_2 has potential to be applied in magnetic field sensing device with extremely high sensitivity, especially at low temperatures, as displayed in figure 1-11.

1.2.3.2 Type-II Weyl fermion in bulk WTe_2

Interestingly, the existence of new type of Weyl point (type-II Weyl point) in WTe_2 was discovered[35]. Whereas Weyl semimetals hosting Weyl fermions were previously recognized to have Weyl point with a point like Fermi surface (referred as type-I)[36], the Weyl point appears at the contact of hole and electron pocket in type-II Weyl semimetal. The new type-II Weyl points exist at the boundaries between hole and electron pockets, as illustrated in figure 1-12. The existence of type-II Weyl fermion at the

boundary between hole and electron pockets in new phase of matter in WTe_2 crystal are expected to explore new physical properties and phenomena arising in the new topological semimetal phase (being different to those of standard Weyl semimetals with point-like Fermi surface) and as a potential platform for the realizing novel Weyl semimetal applications.

1.2.3.3 Quantum spin Hall effect in Nanostructured WTe_2

Layered WTe_2 are layered compounds that can be mechanically exfoliated, therefore very promising for achieving stable 2-dimensional QSH phase. A Monolayer 1T′-WTe_2 was predicted to be quantum spin hall (QSH) semi-metallic materials with QSH gaps[37]. Feipeng Zheng et.al revealed that computational and experimental results all point to one clearly promising possibility, that monolayer 1T′- WTe_2 is a QSH insulator with a positive band gap[38]. In figure 1-13, optical measurements (transient reflection experiment, optically probed transient carrier dynamics) are performed on ultrathin 1T′- WTe_2 layer, showing a systematic increase in the interband relaxation time as the number of layers decreases. Electro-transport characteristics of the sample also exhibits Schottky barrier in atomically thin samples, which is absent for thicker samples, as indicated in figure 1-14. These independent pieces of evidence clearly indicate that monolayer 1T′-WTe_2 is a truly 2D QSH insulator, but further researches should be conducted more.

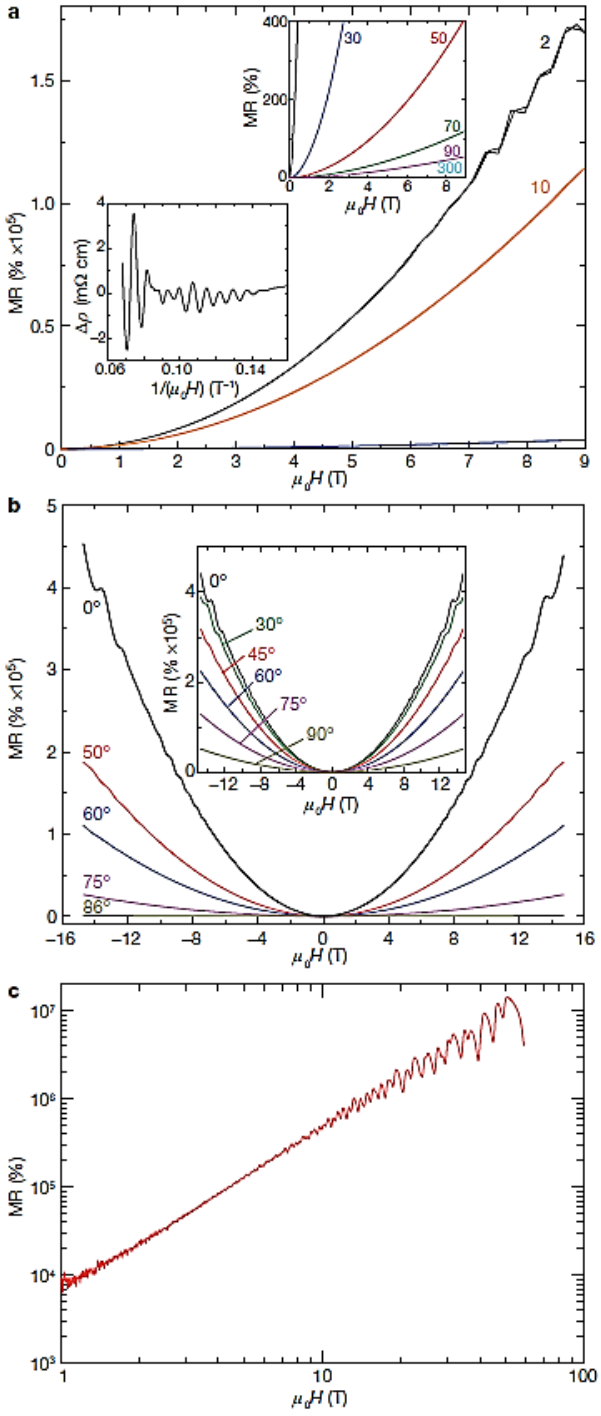

Figure 1-10. Field and angular dependence of the XMR in WTe_2 crystal. (a) Field dependence of the XMR in WTe_2 with the current along the a-axis (W–W chains) and the applied field parallel to the c-axis. (b) Angular dependence of the XMR in WTe_2 crystal at 4.5K. (c) XMR of WTe_2 up to 60 T at 0.53 K, with I parallel to a-axis and H parallel to c-axis[17].

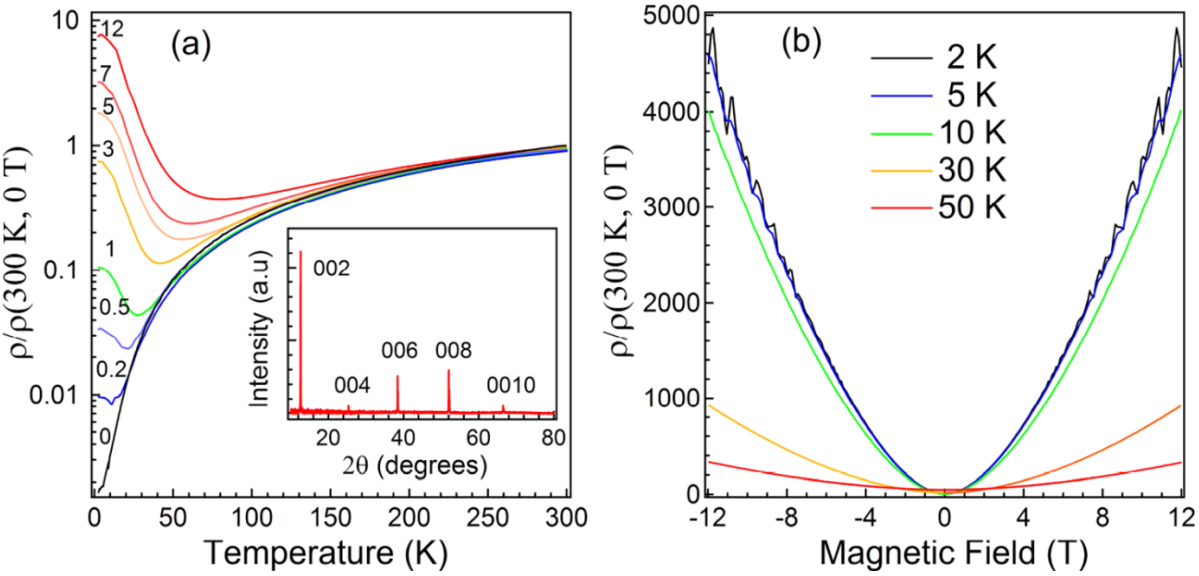

Figure 1-11. Temperature and field dependence of the MR in WTe_2, with the current along the W–W chains (a-axis) and the applied field parallel to the c-axis. (a) Normalized resistivity (at 300K and 0 T) as a function of temperature, with different magnitudes of the external magnetic field. (b) MR of WTe_2 at different temperatures[34].

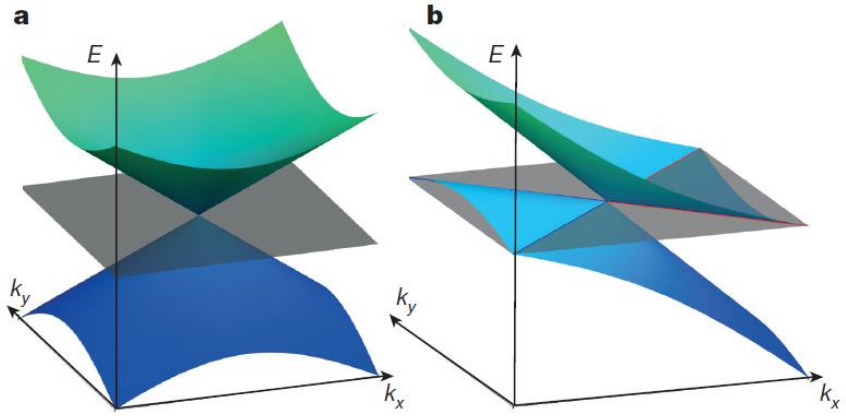

Figure 1-12. (a) Type-I Weyl point with a point-like Fermi surface, (b) A type-II Weyl point appears as the contact point between hole and electron pockets. The grey plane is the position of the Fermi levels[35].

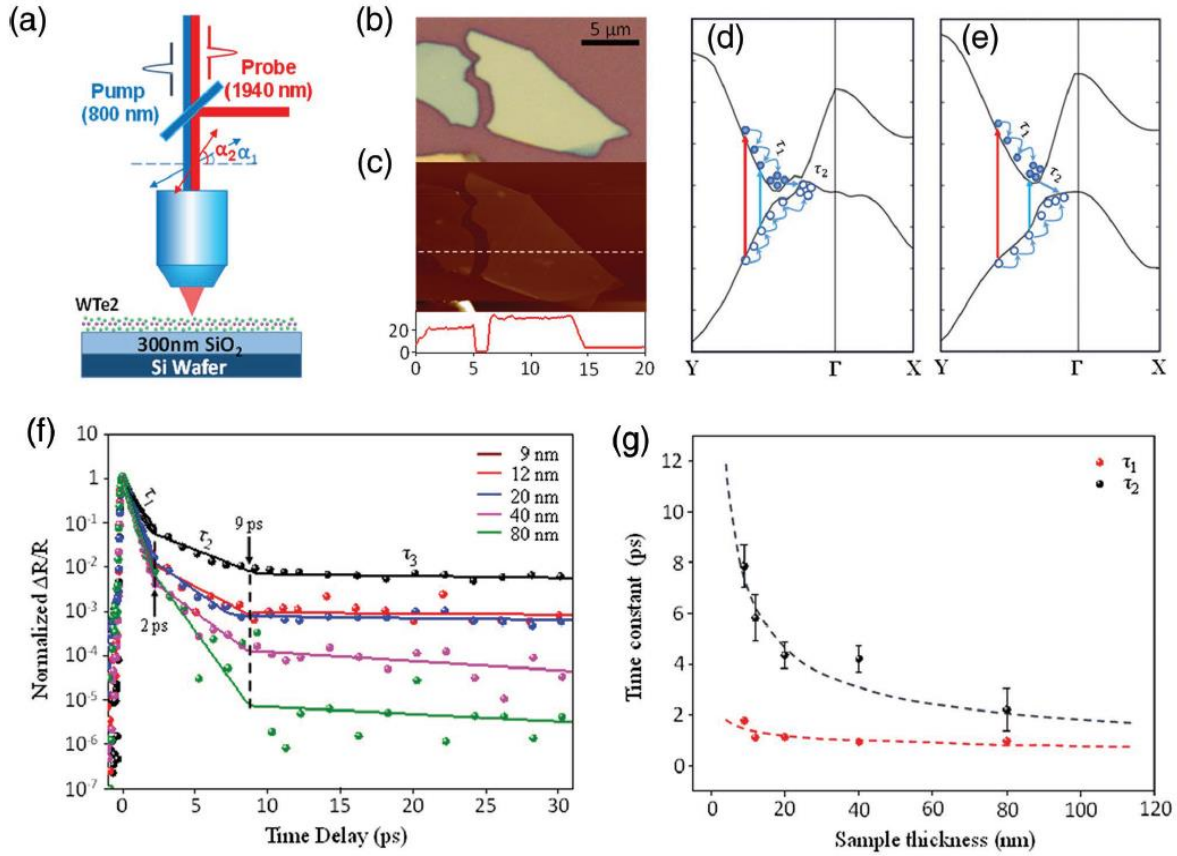

Figure 1-13. Experimental data of optical measurements of QSH nanomaterial WTe_2. (a) Schematic diagram of transient reflection experiment. (b) The OM Image and (c) AFM Image of a WTe_2 used with thickness of 20 nm. Schematic band diagram and carrier relaxation dynamics of (d) bulk and (e) monolayer 1T′-WTe_2 crystal and pump (blue) & probe (red) photon transition configuration. (f) The normalized transient reflection spectrum of 1T′-WTe_2 with different thicknesses. (g) τ_1, τ_2 as functions of the sample thickness[38].

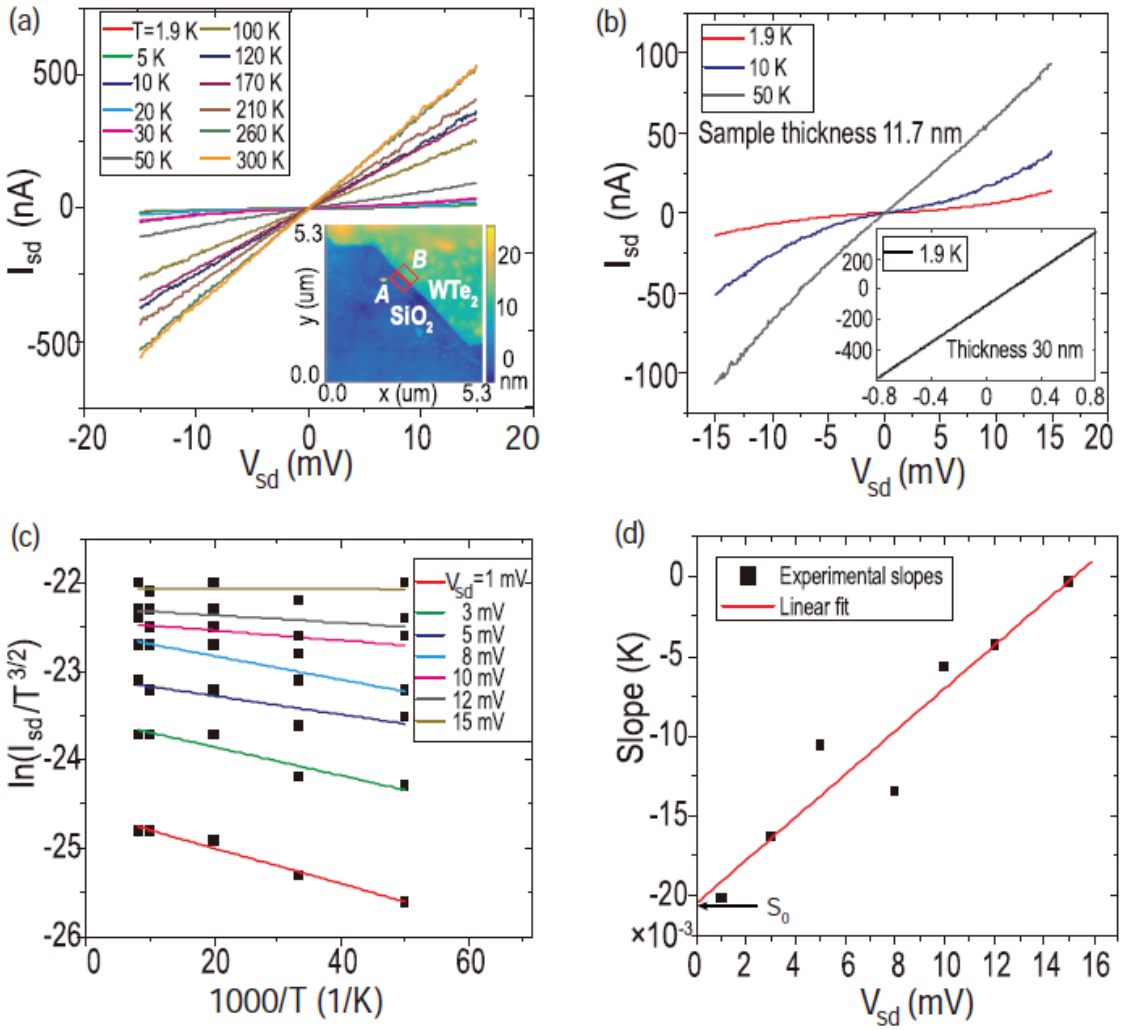

Figure 1-14. Experimental data of (a) I–V curves of an 11.7 nm thick 1T′-WTe_2 sample from 1.8 to 300 K and (b) three low temperatures (1.8, 10, 50 K). (c) Arrhenius plot of ln ($I_{sd}/T^{3/2}$) versus the inverse of temperature and linear fits. (d) Slopes of linear fits in (c), S_0 suggests the value of Schottky barrier of the 1T′-WTe_2 device[38].

1.3 Preceding Researches on Eutectic Metal Alloy Assisted Crystal Growth

Here, some previous researches for the crystal growth by means of eutectic metal alloys are introduced. In this growth mode, the reaction between gas precursors and pre-deposited metal catalyst would make liquid state eutectic alloys above its eutectic temperature. This as-reacted liquid eutectic alloy will have catalytic effect, assisting synthesis of desired nanostructures from the supersaturated liquid eutectic phase. This fundamental principle has been widely used in nanowires' fabrication via the vapor-liquid-solid (VLS) mechanism. Moreover, eutectic metal alloy assisted synthesis of WS_2 and WC nanostructure were investigated, showing the possibility of applying this growth mode to make nanostructured WTe_2. Therefore, review of the preceding researches on eutectic metal alloys assisted nano-crystal growth for low-dimensional nanostructure is very important.

1.3.1 Vapor-Liquid-Solid (VLS) Growth

Figure. 1-15 shows a schematic of the conventional VLS synthesis mechanism for 1D structured nanowire. Since the *vapor* precursor, *liquid* state alloy, and *solid* nanowires are involved in this mode, thus this growth mechanism is called as the VLS (vapor-liquid-solid) process. In this VLS growth mechanism, the pre-deposited metal catalyst forms droplets of a liquid state metal alloy by reacting with supplied vapor precursors (eutectic reaction) over the eutectic temperatures. At the elevated temperature, the vapor flux is absorbed into the catalytic liquid metal alloys to supersaturation level, holding the higher concentration of precursor elements originally from the gas source. Then, crystal growth can subsequently occurs at the vapor-liquid interface, precipitating out supersaturated solid 1D-nanowires. To be specific, the liquid state eutectic metal alloy can act as vapor flux reservoir and nucleation helper of nanowires. Nanowires can be grown only in the areas activated by the metal catalysts and the size and position of the nanowires are determined by that of the metal catalysts.

Previous researches demonstrate that metals which encounter the requirements for pre-deposited metal catalysts can be used in the VLS mechanism[41]. First, these metals must react with gas precursor and then form a liquid solution. Secondly, the equilibrium vapor pressure of the catalyst over the liquid alloy should be small, so the droplet does not vaporize during growth.

The most widely researched VLS process is a growth of Si nanowire assisted by Au particles which adsorb Si from the vapor state. Figure. 1-16 shows the phase diagram of Au-Si system. Here, the eutectic point is 364^{o}C, which means that this VLS process is conducted at elevated temperature over the eutectic temperature, resulting in the formation of supersaturated liquid alloy withheld pure solid elements that can be precipitated out. Au can form a solid-solution with Si (concentrations up to 100%) until reaching

a supersaturated state of Si in Au (the composition of liquid Au-Si alloy track the liquidus line). Consequently, Si atoms precipitate out of the supersaturated liquid state metal alloy droplet at the liquid-alloy/solid-Si interface, resulting that crystal growth can subsequently occur from the nucleated seeds.

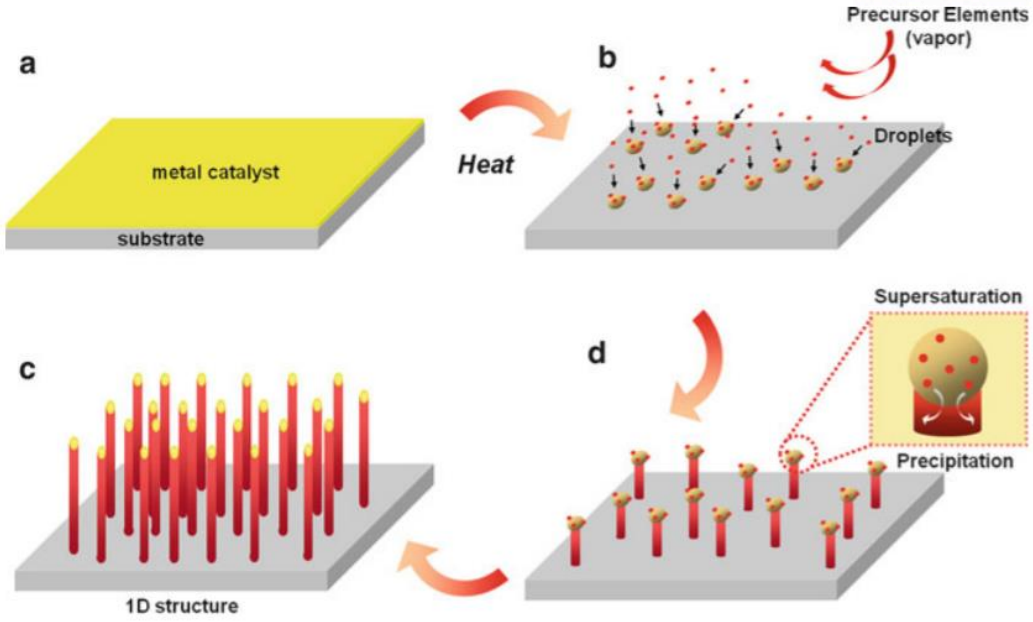

Figure 1-15. Growth of 1D nanostructures by VLS mechanism[41].

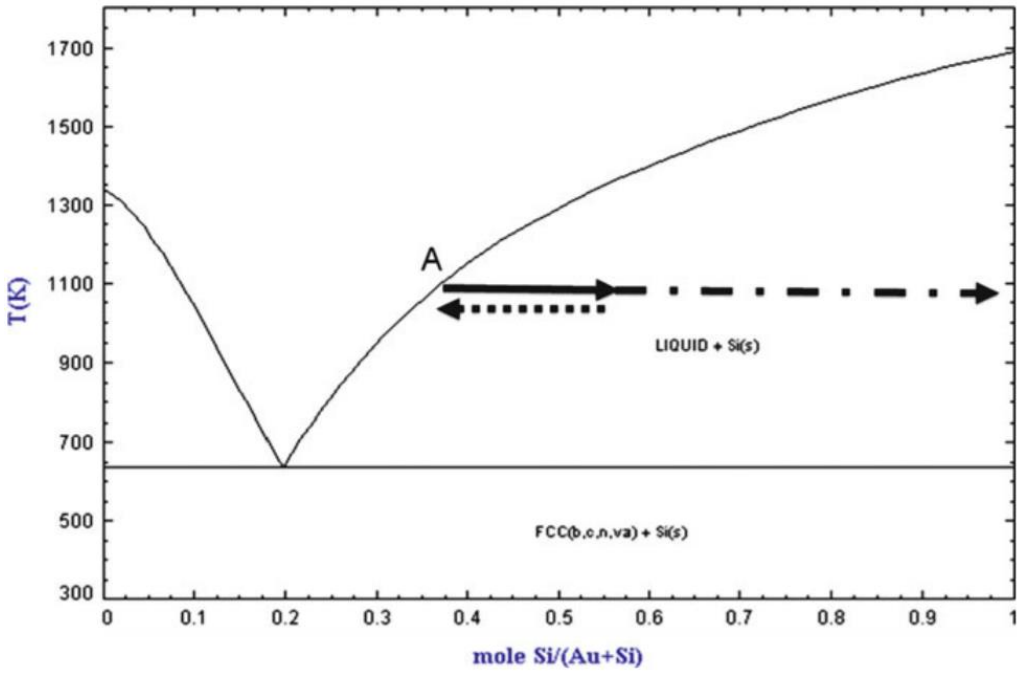

Figure 1-16. Phase diagram of Au–Si system which indicates the composition of liquid metal alloy catalyst in the course of growth of 1D nanostructures by VLS mechanism[41].

1.3.2 Rapid-Crystallization

The nickel sulfide (NiS_x) assisted crystal growth of WS_2 films has been reported[42,43]. The WS_2 films were prepared by the amorphous-solid-liquid-crystalline-solid (aSLcS) rapid-crystallization process from a Ni–S eutectic metal alloys. The mechanism was explained by the recrystallization induced by formation of liquid phase nickel sulfide droplets above the Ni-S eutectic temperature of 637˚C. The method of nickel sulfide promoter-assisted crystallization from the liquid phase could be powerful preparation technique for highly (001) textured WS_2 thin films with large crystallites (lateral dimensions of several micrometers), which are mainly oriented parallel to the substrate. This crystallization by the amorphous solid-liquid-crystalline solid rapid-crystallization process which is comparable with the vapor–liquid–solid (VLS) mechanism, displayed in figure 1-17.

First, amorphous WS_{3+x} was deposited onto Ni coated oxidized silicon substrate and then the substrate was heated. When the eutectic temperature of the Ni–S (T_{eu} = 637 °C) system is reached, the NiS_x crystallites become liquid state and dissolve tungsten or tungsten sulfide. When supersaturation is reached, the crystallization of the WS_2 starts at the bottom of the NiS_x droplets, leading to rapid lateral growth of WS_2 nanosheets. During the aSLcS process, a phase separation between WS_2 and NiS_x crystallites occurred, where the WS_2 crystallizes from the NiS_x:W melt. After cooling, the liquid NiS_x droplets crystallize and mainly float on top of the WS_2 nanosheets. This as-grown nanosheets can be clearly seen in the cross-sectional SEM image displayed in figure 1-18.

.

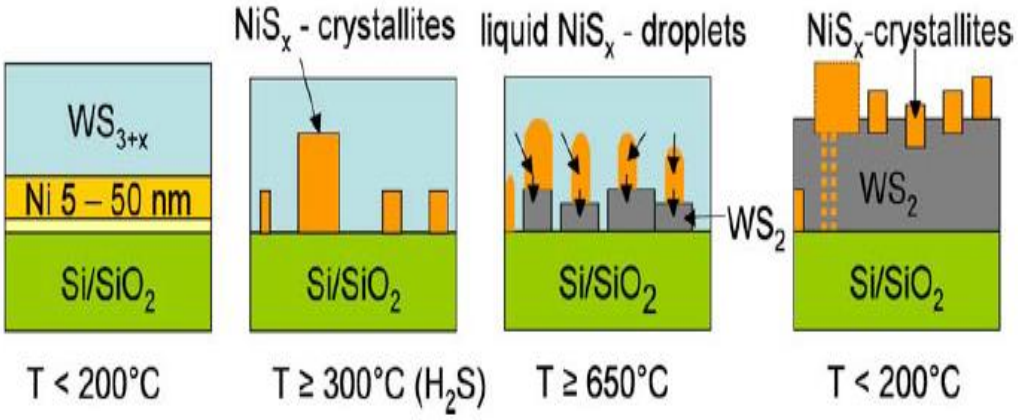

Figure 1-17. Schematic of the steps of the rapid crystallization of WS_2 by the amorphous solid-liquid-crystalline solid (aSLcS) process[42].

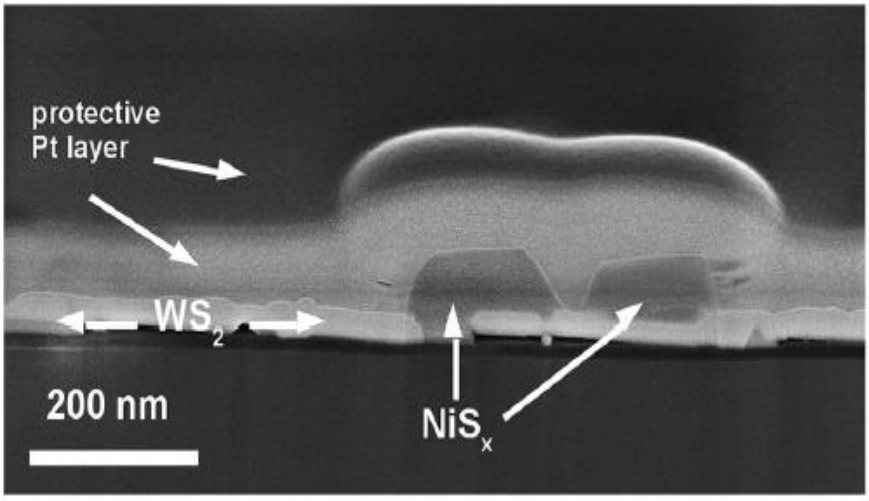

Figure 1-18. Cross-sectional SEM image of a rapidly crystallized WS_2 film. Preparation parameters: 300nm WS_{3+x}/20 nm Ni/SiO_2/Si substrate, annealed at 700˚C for 5 min[43].

1.3.3 Eutectic Solidification

A novel method to prepare low-dimensional WC nanostructure such as nanowire and nanowalls has been developed[44]. To realize the synthesis of WC nanostructure, the most serious obstacle which must be overcome is that W atoms must be provided during the growth of WC nanostructure. The key approach for supplementation of W atom is eutectic solidification in W-Al-C solution, which means a precipitation of W and C atoms in ternary W–Al–C. The active temperature of W atoms can be decreased in an W–Al environment. Transportation of C atoms through the atmosphere and W atoms enable the supplementation of W resources to be continuous through the melting liquid across the whole process. Large-scale WC nanowalls with a thickness of tens of nanometers with several micrometers in the other two dimensions were obtained through the bottom-up growth, as shown in figure 1-19. In addition, 1-D WC nanostructures can be obtained in suitable conditions.

In this work, WC nanostructures were grown on polycrystalline tungsten substrate at 1310˚C in CH_4, H_2 ambient. In detail, Al sheets were placed neared the tungsten foil. During the annealing step, Al atoms would be evaporated onto the W substrate continuously at temperature higher than 660˚C, leading to formation of eutectic metal alloys (W atoms melts in Al liquid). Continuous supplementation of Al and W atoms keeps the metal alloys in liquid state as a W-Al eutectic metal alloys. Over the temperature at 1000˚C, carbon source is introduced into the chamber from CH_4 cracking and would diffuse into the liquid, forming ternary alloys of W–Al–C. The growth of the WC nanostructures can be attributed to the eutectic precipitation in W–Al–C solution. Interestingly, there exists a solute convection area because W is supplied from bottom to top and C from top to bottom. The formation of WC nanostructure was induced by nucleation at the convection area and precipitation. The details of growth model are shown in figure 1-20.

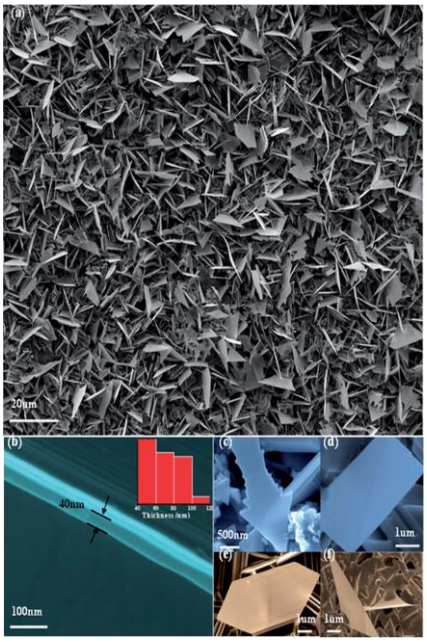

Figure 1-19. Scanning electron microscopy analysis of WC nanowalls structure. (a) Typical SEM image of as-synthesized WC nanowalls. (b) Thickness characterization of the nanowalls. (c–f) Various polygons can be found among the synthesized nanowalls but the main shape is triangle[44].

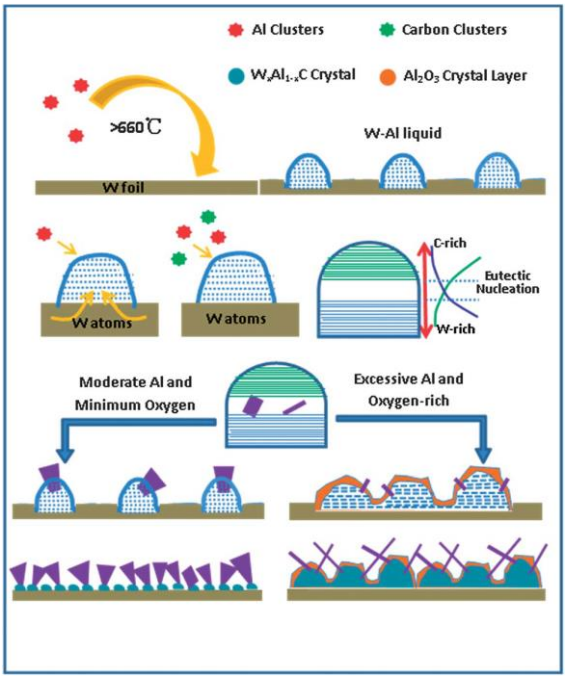

Figure 1-20. Growth model proposed for synthesis of low-dimensional WC nanostructures. The active temperature of W atoms decreased in an Al–W environment[44].

Chapter 2. Experimental Details

2.1 Deposition of Metal Films

In this study for synthesis of transition metal telluride nanostructures, we deposited 50nm-thick copper layer on a 300 nm SiO_2/Si substrate by using UHV e-beam evaporator (UEE-UHV series, ULTECH) to form eutectic metal alloys. To minimize environmental impurities and copper oxide layer on the copper film surface, the copper film was prepared in UHV main chamber, using high-purity copper solid source (99.99% Cu pellet) for deposition. Then, the tungsten layer (thickness was various depending on the experiments. e.g. 20, 100, 200, 300nm) was deposited by DC magnetron sputtering (SRN-120, SORONA) in optimized deposition condition (uniformity: less than ± 5 % within wafer). Figure. 2-1 displays the UHV e-beam evaporator and DC magnetron sputtering system used in this work.

In this work, we proposed the new type of structure of a W/Cu deposited metal layer for growth of WTe_2 nanostructures which is the inverse structure of essential structure (a Cu/W film) in previous research. In previous research, a Cu film was deposited on the pre-deposited W layer onto desired substrates (SiO_2/Si or Al_2O_3), followed by tellurization of the Cu/W/substrate at 500°C in Te atmosphere using Te powders with inert Ar gas, forming Te-rich copper telluride (Cu_xTe_y)/WTe_2/W/substrate and finally etching away Cu_xTe_y to obtain WTe_2 nanostructures on the W/substrate, as illustrated in figure 2-2.

The surface morphology of as-deposited poly-crystalline W(20nm)/Cu(50nm) was confirmed by SEM (S-4800, Hitach High-Technologies), as displayed in figure 2-3a. The size of W crystalline was confirmed by using Scherrer equation (crystalline size: ~20nm). Figure 2-3b exhibits XRD data of W(20nm)/Cu(50nm) films deposited on SiO_2/Si substrate. Moreover, feasibility of synthesis for $MoTe_2$ nanostructure as a member of the layered TMDs family was evaluated through our methods. The sample for synthesis of $MoTe_2$ nanostructure was prepared in the same way as above (Mo layer of 300nm was deposited and thickness of Cu layer was fixed).

2.2 Synthesis Methods

First of all, a W/Cu (or Mo/Cu) film deposited on SiO_2/Si was placed in a crucible containing tellurium powder (Product 264865, Aldrich). Secondly, the chamber in our furnace system (DMTF 12/150-HVAC, Daemyoung Enterprise) was evacuated to ~ 10^{-3} Torr and then filled with Ar gas to maintain atmospheric pressure and protect the system from oxygen. Figure 2-4 shows a schematic drawing of the chamber in our furnace system. The furnace was subsequently heated up to 500-600 °C and then tellurium powder

was evaporated to vapor and transported to the sample. Next, the W/Cu film is tellurized after absorption of tellurium vapor at the pre-deposited film. Here, the conversion of the pre-deposited copper films into liquid state Te-rich copper tellurides (Cu_xTe_y) droplets occurs at the atmosphere of tellurium vapors. The crystallization of nanostructures inside of Te-rich Cu_xTe_y droplets takes place at a temperature of 500 °C, above the Cu–Te eutectic temperature of 340 °C (see figure 2-5). This model describes the growth of a liquid-phase crystallization from Cu_xTe_y droplets as a role of the nucleation helper for the crystal growth of the WTe_2 and $MoTe_2$ nanostructure. Lastly, the chamber was cooled down to RT (room temperature) under atmospheric condition.

2.3 Preparation of Transition Metal Telluride Nanostructures on the Desired Substrate

First of all, in order to expose the as-synthesized transition metal telluride nanostructures in Cu_xTe_y droplets, the Cu_xTe_y droplets must be removed. For this to occur, the as-grown sample was dipped in 1M of APS (ammonium persulfates) aqueous solution for 1hr to etch the Cu_xTe_y droplet. After that, the sample was rinsed with deionized water to remove residual etchant. Through the wet etching process, we can simply get tellurides nanostructure without Cu compounds. However, the use of oxidant etchant and water induce inevitable chemical damage, leading to critical oxidation and degradation of as-synthesized products.

The as-obtained nanostructures can be easily transferred to different substrates and/or solutions by using conventional dispersion method. The nanostructures were dispersed in isopropanol (IPA) through a sonication process. Then, nanostructures were placed on the desired substrate by dispersion method and the substrate was dried at 80 °C for 10min using a hot plate. In this process, the disadvantage is that the as-synthesized nanostructures could be broken and damaged due to physical attacks during the sonication process.

To sum up, the intrinsic properties of as-synthesized nanostructures could be degraded by inevitable chemical and physical damage. In addition, fabrication of various applications has difficulties due to residue products. So-called “coffee ring effect” could be a critical problem as well, which is caused by capillary flow induced by the differential evaporation rates across the drop during the conventional dispersion methods.

To solve the problems, our approach is to mechanically peel off the Cu_xTe_y and metal layer (W and Mo layer) by using scotch tape, as shown in figure 2-6. To expose the as-synthesized nanostructures inside of the Cu_xTe_y droplets without use of chemical oxidant (APS etchant), we tried to peel off Cu_xTe_y droplets and W layer by using scotch tape. Figure 2-7a indicates the as-obtained WTe_2 nanobelts onto

desired substrate without additional chemical etching and transfer steps. This simple method of mechanical peeling off by using scotch tape can reduce the process to obtain nanostructures as well as prevent degradation of WTe_2.

2.4 Fabrication of Electronic Device

For the measurements on electrical properties of as-synthesized WTe_2 and $MoTe_2$, conventional nano-fabrication techniques (electron-beam lithography, metals evaporation and lift off) were employed to attach electrical contacts (consisting of Ti/Au bilayers, typically used 10/80 nm thick), as shown in figure 2-7b. Throughout the procedure of crystal identification and device fabrication, care was taken to minimize exposure of the material to air in order to minimize degradation. The electrical properties of WTe_2 samples with different thicknesses were investigated. The current was applied along the tungsten chains along the tungsten zigzag chains (a-axis) of WTe_2 nanostructure. Also, $MoTe_2$ was tested using two Ti/Au contacts made by a lift-off process at both edges of the synthesized $MoTe_2$ nanostructure.

(a)

(b)

Figure 2-1. (a) A UHV e-beam evaporator system (UEE-UHV series, ULTECH) used in this work for preparation of the metal (Cu) films. (b) A DC sputter system (SRN-120, SORONA) used in this work for deposition of W (and Mo) layer.

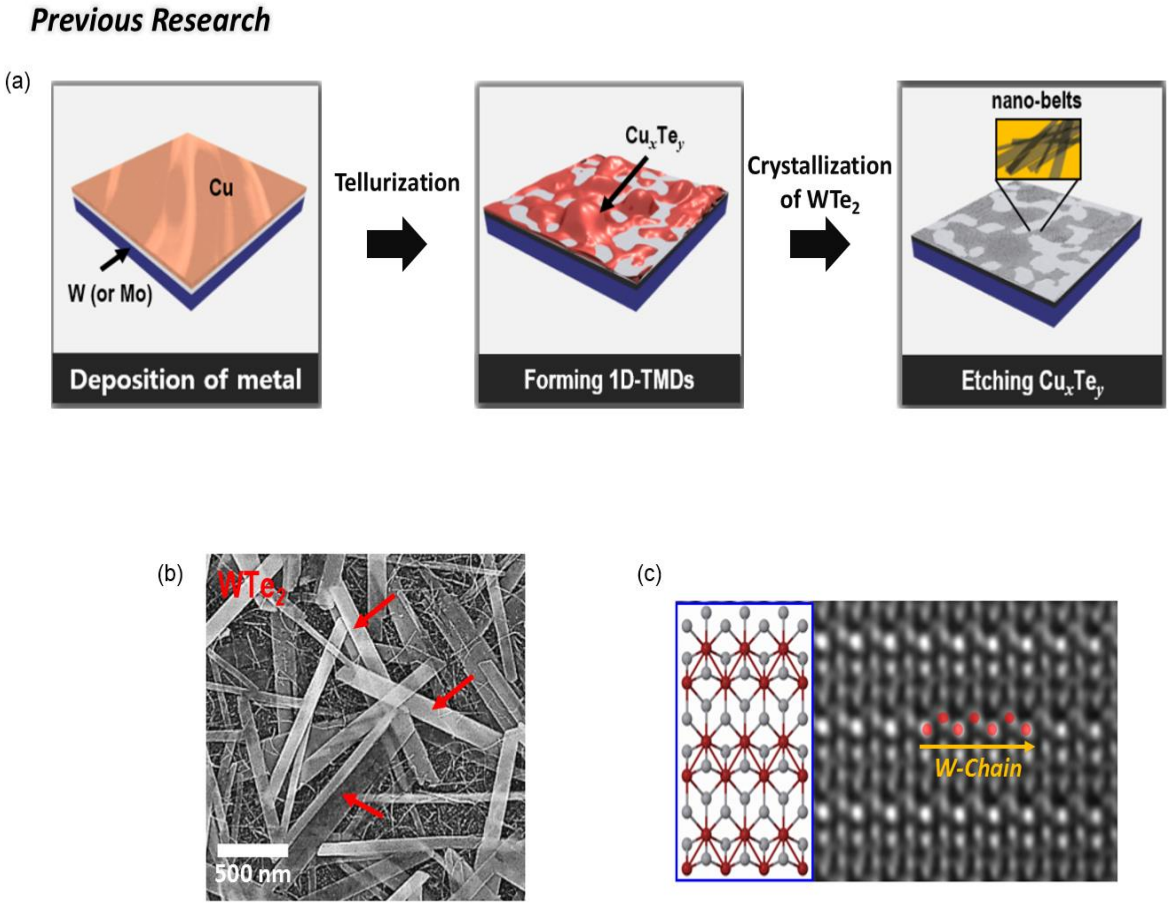

Figure 2-2. Introduction of previous research. (a) Schematic diagrams of the elementary steps for growing 1D-TMDs and obtaining WTe_2 nano-belts. In this process, a Cu film deposited on a W layer plays a key role as the Te vapor flux reservoir and promotor of improving crystallinity. Representative (b) SEM Image and (c) TEM image of the synthesized-WTe_2 nano-belts.

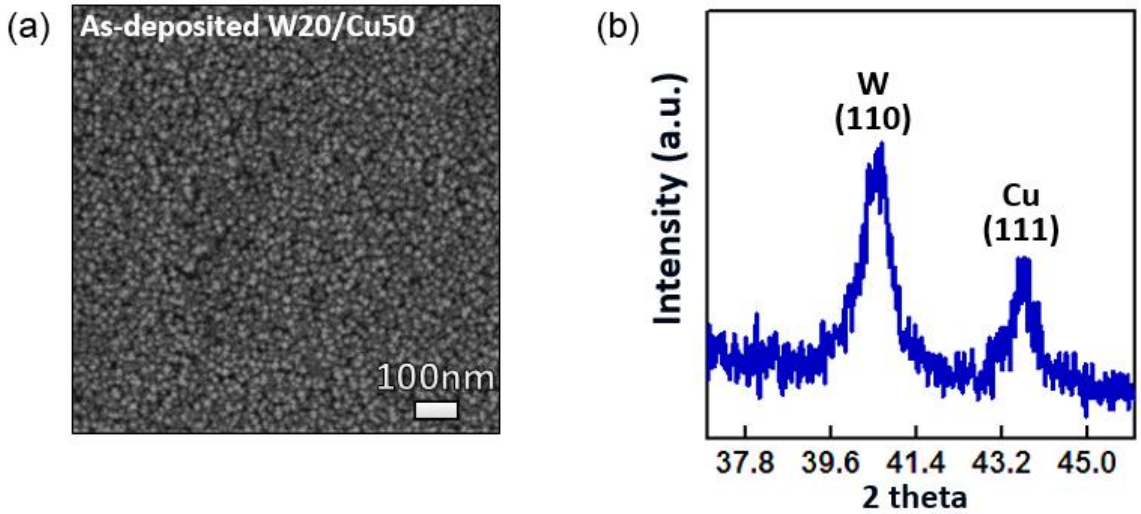

Figure 2-3. (a) Representative SEM Images of surface morphology of poly-crystalline W20/Cu50 films deposited on Sio_2/Si substrate. (b) XRD pattern for the W20/Cu50 films deposited on Sio_2/Si substrate. The size of W crystalline is within 20nm verified by using Scherrer equation.

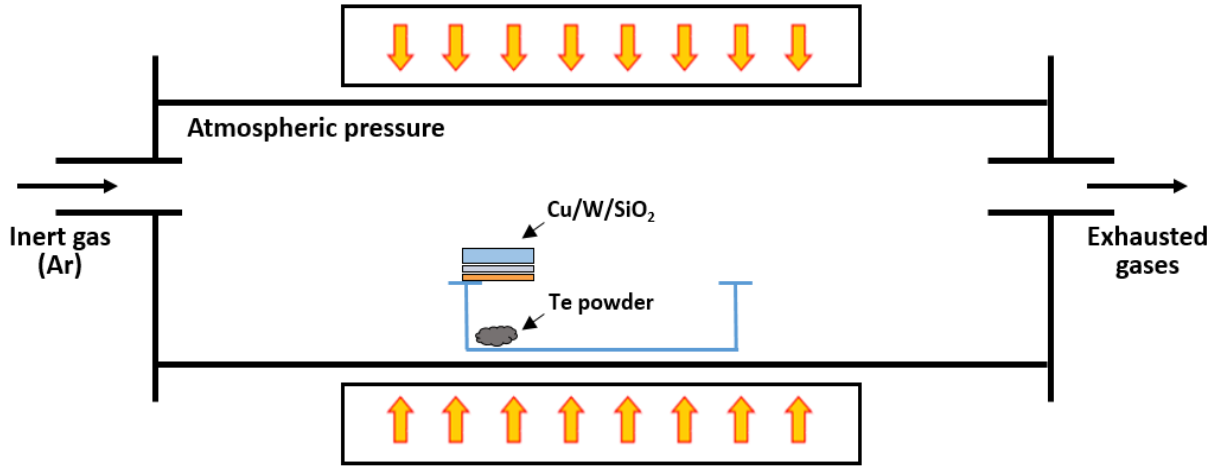

Figure 2-4. Schematic drawing of the chamber in our furnace system (DMTF 12/150-HVAC, Daemyoung Enterprise) for growth of WTe_2 nanostructures. The chamber was evacuated to ~ 10^{-3} Torr and then filled with Ar gas to maintain atmospheric pressure and protect the system from oxygen

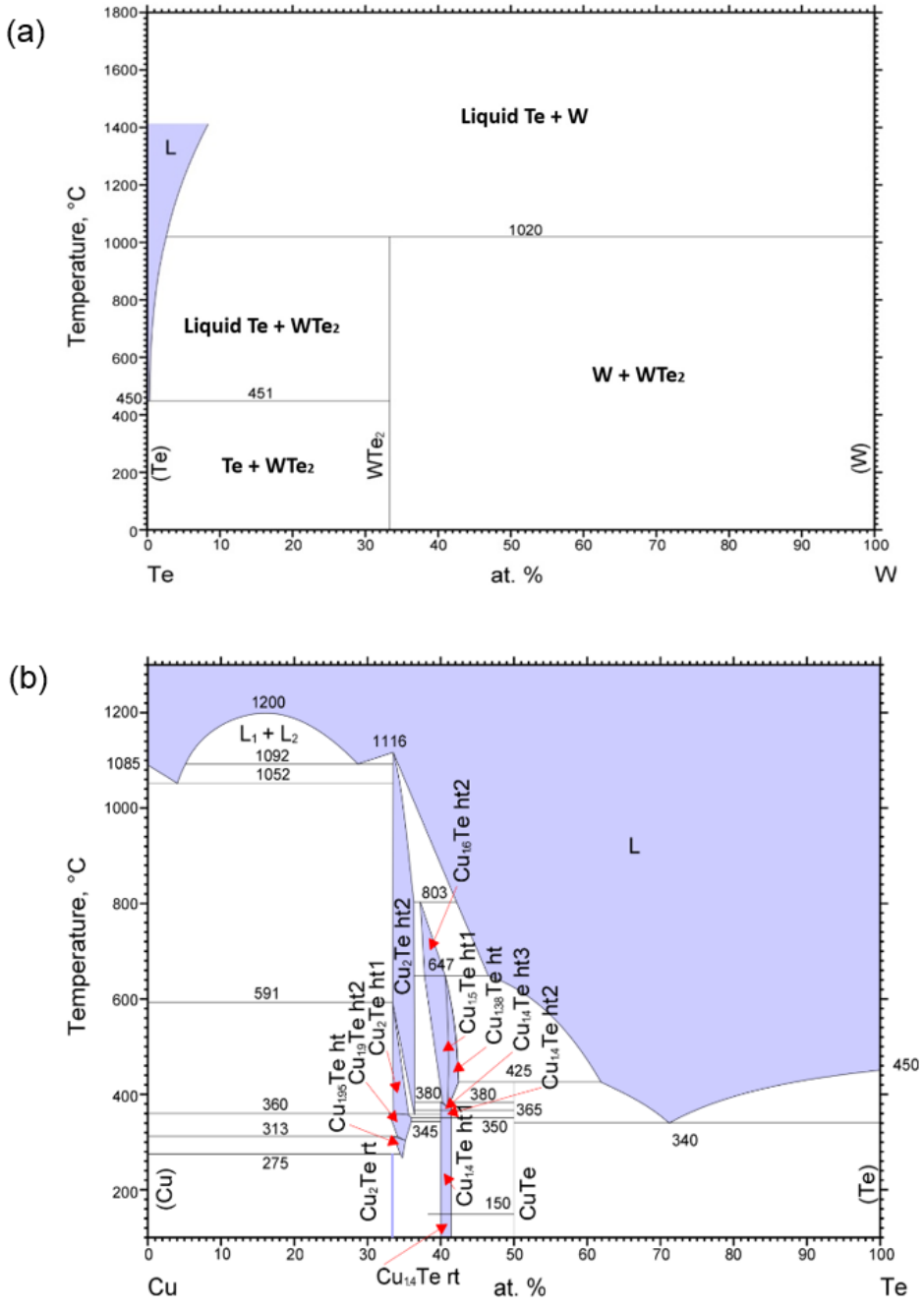

Figure 2-5. Phase diagrams of (a) the W-Te system (b) the Cu-Te system (From ASM Alloy Phase Diagram Database).

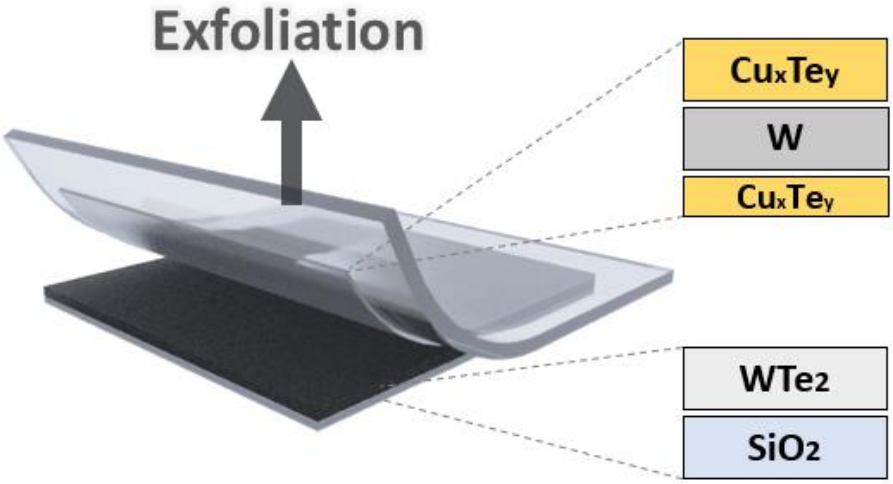

Figure 2-6. Schematic image of method of mechanical peeling off using scotch tape. The simple method of peeling off using scotch tape can reduce the whole process to form WTe_2 nanostructures on the desired substrate.

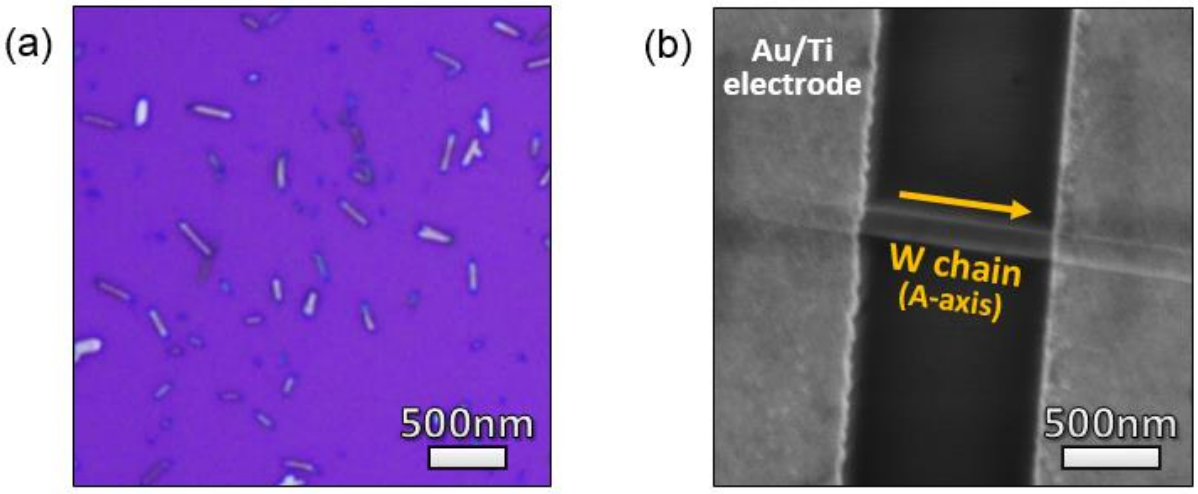

Figure 2-7. (a) Representative OM Image of as-synthesized WTe_2 nanostructures onto the desired substrate by peeling W and Cu_xTe_y droplets off using scotch tape. (b) SEM Image of fabricated WTe_2 nanostructures device, showing the channel (with current along the a-axis of W-W zigzag chains, lengths of 1μm) perpendicular to Au/Ti electrode.

Chapter 3. Results and Discussion

3.1 Role of Eutectic Metal Alloys for Synthesis of WTe_2

Previously, most of the studies on tungsten ditelluride (WTe_2) have been demonstrated in mechanically exfoliated layers from bulk crystal. Therefore, the development of direct synthesis of high quality few-layer WTe_2 is essential to study the emergent properties of nanostructured WTe_2 and for large-scale applications.

So far, a single- or few-layer WTe_2 has only been prepared by mechanical exfoliation from bulk crystals which are synthesized by chemical vapor transport method, usually conducted at high temperatures over 700˚C for several days. The products are poor-crystallinity crystals, and are limited to only large bulk-type crystals with millimeter scale. The high vapor pressure of tellurium and low chemical reaction activity of tungsten with tellurium make synthesis challenging. To obtain stoichiometric WTe_2 crystals, it needs to hinder desorption of tellurium vapor precursor and activate tungsten atoms to be reacted with tellurium atoms. To overcome these problems, we suggested a novel method for the growth of the WTe_2 nanostructure. Using our method, we can directly obtain the desired WTe_2 nanostructures with nano-scaled thickness and high quality. In comparison to conventional chemical vapor transport methods, our method requires a lower growth temperature & shorter time, which is good for mass production and novel applications.

To solve the challenge in tellurization of tungsten films and obtain stoichiometric WTe_2, our key approach is the eutectic metal alloy assisting mechanism. When above the copper-tellurium eutectic temperature, the diffused copper atoms react with tellurium vapor, resulting in the formation of Cu_xTe_y liquid state droplets holding tellurium vapor as a role of vapor flux reservoir. In addition, in liquid state Cu_xTe_y droplets, tungsten atoms from the interface between the W layer and droplets were activated to be reacted with Te. Consequently, WTe_2 crystals can be nucleated (and crystallized) in liquid-phase eutectic metal alloys. The crystal of WTe_2 grew as anisotropic nano-belts due to its intrinsic 1T'-pahse, compared to other 2H-TMDs. In short, we obtained the desired high quality single-crystalline WTe_2 nanostructures inside of the Cu_xTe_y droplet.

In this research, we proposed a method using new type of structure of deposited a W/Cu metal layer on SiO_2/Si substrate that is the inverse structure of the essential structure in our previous research (Cu/W/SiO_2/Si). We deposited the copper layer on the desired substrate (SiO_2) and then conducted the deposition of W layer. This work should be studied in terms of the different morphology of Cu_xTe_y

droplet depending on synthesis parameters as well as growth conditions.

Figure 3-1 indicates as-grown Cu_xTe_y droplet on W layer via SEM Images. The W and pre-deposited Cu layer with thickness of 100nm was used as a standard process condition. To identify the Cu_xTe_y droplet, the Raman and EDAX analysis of the droplet was carried out. The Raman spectra shows that all the measured Raman shifts indicate tellurium, at 140, 189, 224, 270 cm^{-1}. And, the Te-rich Cu_xTe_y droplet was confirmed by the EDAX analysis. We confirmed that, by introducing the pre-deposited copper layer, the Cu_xTe_y droplet was formed. Interestingly, the Cu_xTe_y droplet was observed on the surface of W layer, penetrated through the W layer, although the Cu layer was deposited under the W layer. This suggests that diffusion of copper atoms into W layer occurs through the grain boundary of the W layer. Then, diffused copper atoms would combine with the Te vapor precursor, resulting in formation of Cu_xTe_y droplets at the surface of the W layer. Another view of this phenomena is that the penetration of liquid state Cu_xTe_y through the W layer, following the formation of liquid state Cu_xTe_y over the eutectic temperature (~394°C) under the W layer, but the further study needs to be done for the mechanism confirmation. The morphology of as-grown Cu_xTe_y droplets are shown via SEM, displayed in figure 3-2. And Raman, EDAX spectra and its composition are shown in figure 3-2, corresponding the red circle in figure 3-2 (b).

The Cu_xTe_y was fully etched by dipping into Ammonium Persulfate (APS) etchant for 1hr. At the same site where the Cu_xTe_y droplet was located, we observed as-synthesized WTe_2 nanostructures on the W layer. This was confirmed by Raman analysis, and corresponds to the red circles in the figure 3-3, indicated at 163, 211 cm^{-1} of Raman shift. In addition, to check the composition and stoichiometry of the as-synthesized nanostructure which was transferred onto Al_2O_3 substrate to prevent main peak from overlapping with other signals, EDX analysis was carried out. This corresponds to the red point in the inset image. The indicated main elements of the synthesized nanostructures are tungsten and tellurium. The EDX analysis result indicates that the as-synthesized WTe_2 is highly stoichiometric with a W : Te ratio of 1:2. The use of Te-rich eutectic metal alloys eliminates the Te deficiency in the resulting products and the contamination by impurities encountered with vapor deposition process. As a result, the as-synthesized WTe_2 nanostructures are highly pure, stoichiometric, and structurally uniform.

To sum up, the growth mechanism of WTe_2 was explained by the assistance of liquid Cu_xTe_y droplets, after oversaturation with dissolved tungsten, induced a WTe_2 crystal growth.The crystallization takes place at a temperature of ~500 °C, slightly above the Cu–Te eutectic temperature of 340°C. A liquid-state eutectic metal alloy from the promoter metal (Cu) and Tellurium is formed, which dissolves tungsten up to its solubility limit. When the solubility limit is reached, the excess WTe_2 rapidly

crystallizes out of the Cu_xTe_y droplet, leading to the formation of these highly (002)-textured WTe_2 nanostructures. Particularly, the as-synthesized WTe_2 nanostructures can be easily transferred to different substrates and/or solutions for further applications. Figure. 3-3 show that the as-synthesized WTe_2 nanostructure can successfully be transferred to desired substrate using conventional dispersion method. Our optimum process condition for obtaining WTe_2 nanostructures with a thickness in few-nanometers is a tungsten layer with a thickness of 20nm and a copper layer with a thickness of 50 nm, grown at 500°C for 10min with supplement of Tellurium from Te powder of 0.1g. The thickness distribution was measured by AFM profile. The average thickness of obtained WTe_2 nanostructures was measured to be 54±15 nm, shown in figure 3-3. Figure. 3-4 clearly show the XRD pattern of highly (002)-oriented single crystalline tungsten ditelluride texture. After transfer of WTe_2 nanobelts from W surface to desired substrate (SiO_2) using conventional dispersion methods, XRD measurement was performed, displayed in figure 3-4.

.

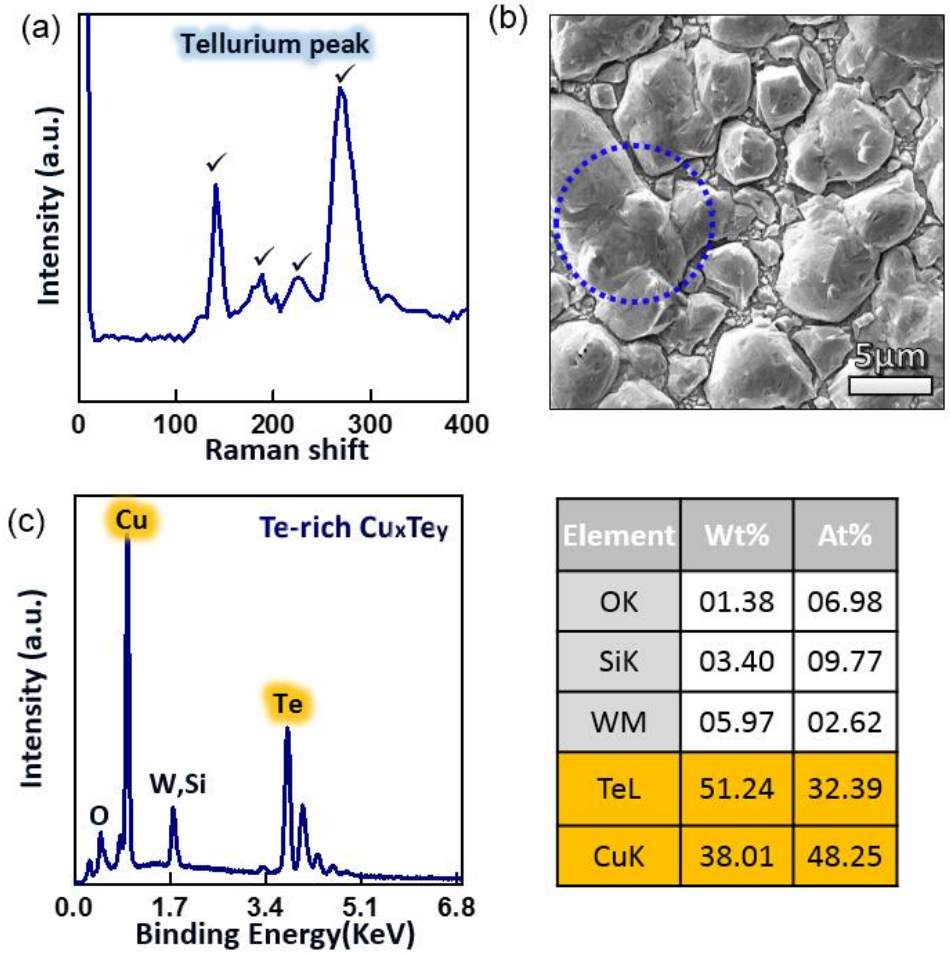

Element	Wt%	At%
OK	01.38	06.98
SiK	03.40	09.77
WM	05.97	02.62
TeL	51.24	32.39
CuK	38.01	48.25

Figure 3-1. (a) Raman spectra, corresponding to the colored blue spot in (b) image, identifying tellurium-rich Cu_xTe_y eutectic metal alloys. (b) SEM Image of tellurium-rich eutectic metal Cu_xTe_y alloys on W layer. (c) EDAX spectra, corresponding to the colored blue spot in (b) image.

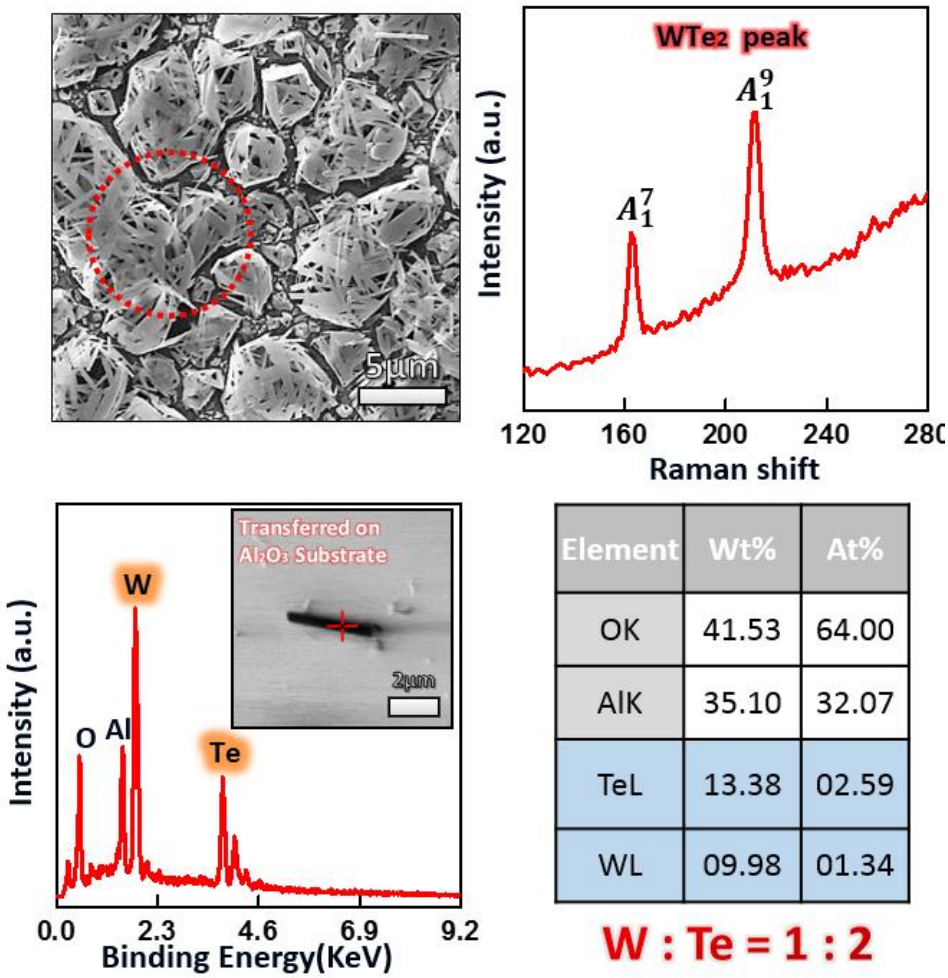

Figure 3-2. (a) Raman spectra, corresponding to the colored red spot in (b) image, identifying as synthesized-WTe_2. (b) SEM Image of as-synthesized WTe_2 nanostructures on W layer. (c) EDAX spectra, corresponding to the colored red spot in (b) image.

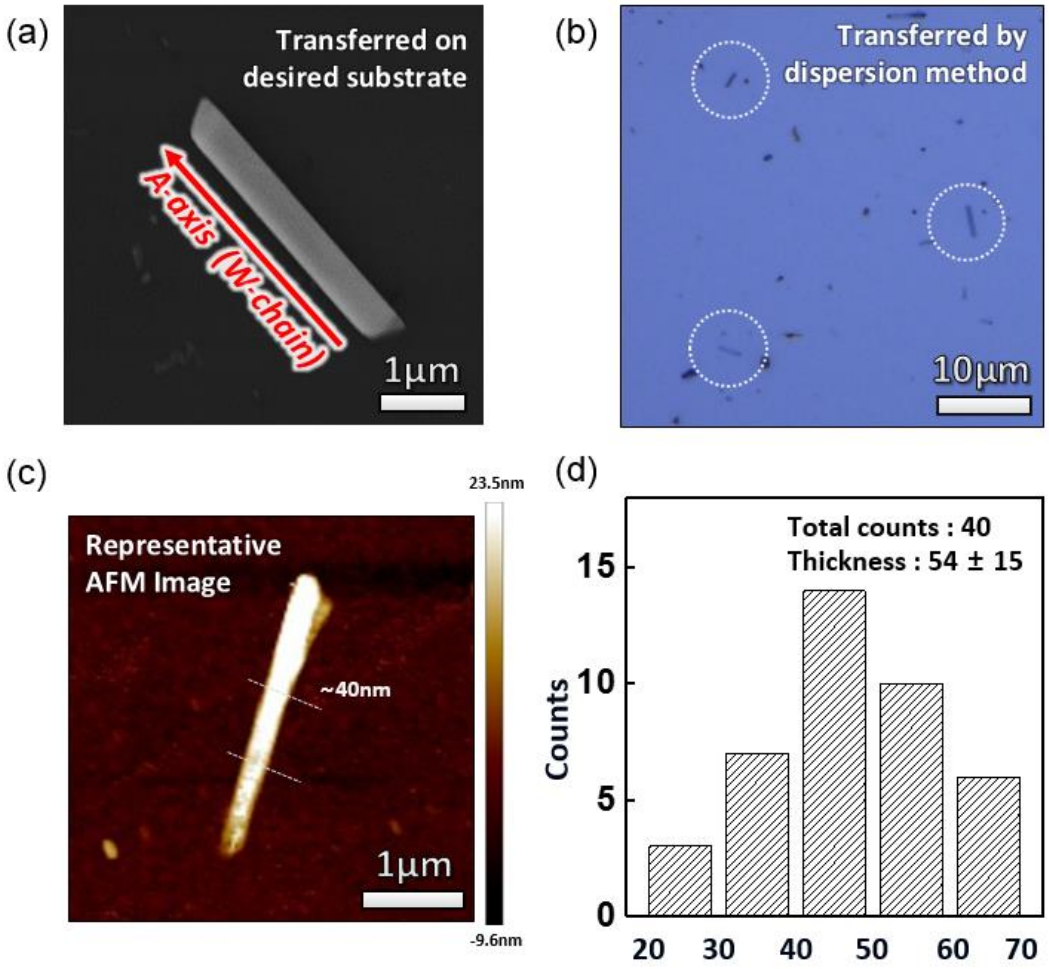

Figure 3-3. (a-c) OM, SEM and AFM images of transferred WTe_2 nanobelts on desired substrate by conventional dispersion method. (d) Diameter distribution of WTe_2 nanobelts obtained at W20/Cu50 500℃ for 10min.

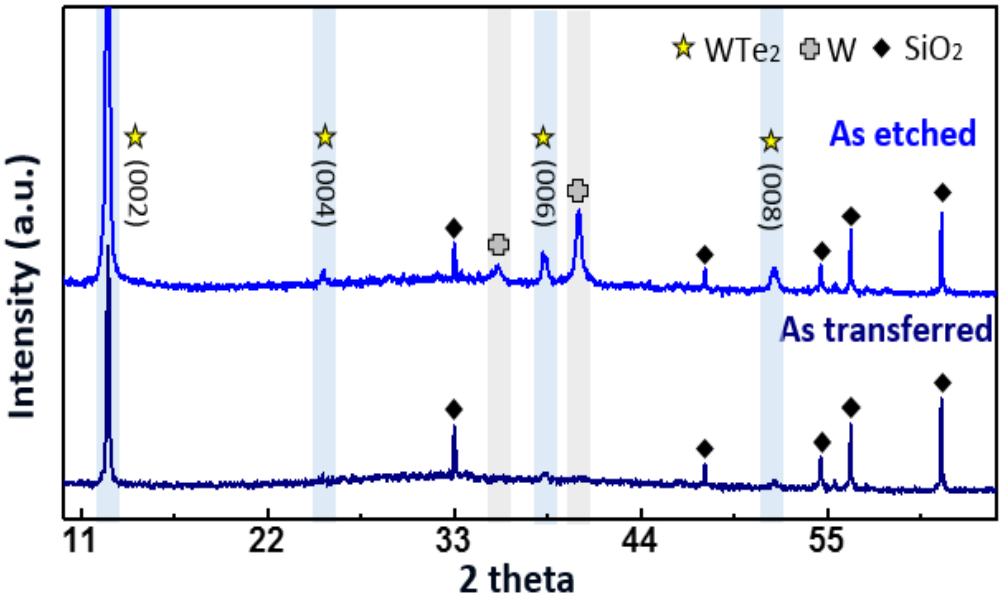

Figure 3-4. XRD data of as Cu_xTe_y etched and transferred WTe_2 nanobelts on SiO_2/Si substrate by conventional dispersion method.

3.2 Structural Morphology of Eutectic Metal Alloys on Synthesis Parameters

The role of eutectic metal and its behavior on synthesis parameters is a major factor in the synthesis of WTe_2 in our synthesis method, so studies on changes of Cu_xTe_y metal alloys on synthesis parameters were necessary. We studied the synthesis of WTe_2 by controlling the growth conditions and observing changes of Cu_xTe_y metal alloys.

3.2.1 Study on Behavior and Role of Cu_xTe_y depending on Growth Time

We examined effects of growth time first. The thickness of the sample under our optimum condition for obtaining few-nm thickness WTe_2 nanostructure (tungsten of 20nm, copper of 50nm on SiO_2/Si substrate) and growth at the temperature of 500°C with 0.1g of Te powder was fixed and only the synthesis time was adjusted. When the growth time was relatively short (2, 6 min), the Cu atoms from the copper layer below W layer did not react sufficiently with Te. As was such, Cu_xTe_y metal alloys could not form sufficiently, consequently affecting WTe_2 growth. Figure. 3-5 shows the intensities of XRD peak for Cu and Cu_xTe_y metal alloys depending on synthesis times of 2min, 6min, and 10min respectively. From the XRD analysis, the weak XRD peak of (002)-oriented Cu_xTe_y metal alloys were found at the growth time of 2 min and 6 min. The XRD peak of (002)-oriented Cu_xTe_y metal alloys is clearly shown in the case of growth time of 10min, where both Cu and Te sufficiently reacted. Correspondingly, XRD peak of the well-crystalized (002)-oriented WTe_2 is clearly identified. Figure 3-6 is the comparison of XRD intensity on as deposited, annealed w/o Te and as-grown Cu_xTe_y:W at 500°C for 10min. Compared to as deposited and annealed without Te source, our optimum condition with sufficient growth time of 10min exhibits clear XRD peaks of Cu_xTe_y metal alloys and WTe_2 nanostructure. From these results, we recognize that formation of Cu_xTe_y metal alloys from the reaction of Cu and Te has significant effects on growth of WTe_2. In figure 3-7, the Raman spectrum of as-grown Cu_xTe_y and WTe_2 shows several peaks approximately at 92, 121, 141 (tellurium peaks) and 80, 119, 134, 164, 212 (WTe_2 peaks) cm^{-1}, respectively.

Even as Cu_xTe_y metal alloys are formed, nucleation and crystallization of WTe_2 nanostructures must take place inside of eutectic metal alloys. In the case of insufficient growth time to nucleate WTe_2 nanostructure, only W nanowire can be observed. In figure 3-8, the SEM Image shows the as-obtained W nanowire at the same site where the Cu_xTe_y droplet was located. The activated W atoms induced by eutectic metal alloys did not react with Te atoms, resulting in formation of W nanowires along the [110] direction. This phenomenon is also observed in the Te deficiency region, where grown for 10min. In short, WTe_2 nanostructure can be synthesized at convection region with W atoms and Te atoms, followed by oversaturation and eventually crystallization followed by precipitation.

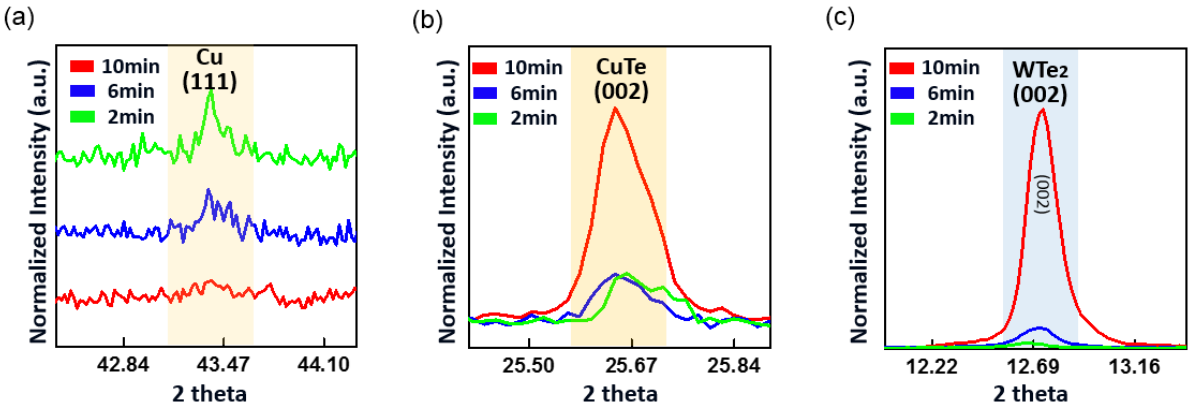

Figure 3-5. (a-c) Comparison of XRD intensity of as-grown Cu_xTe_y:W depending on growth time.

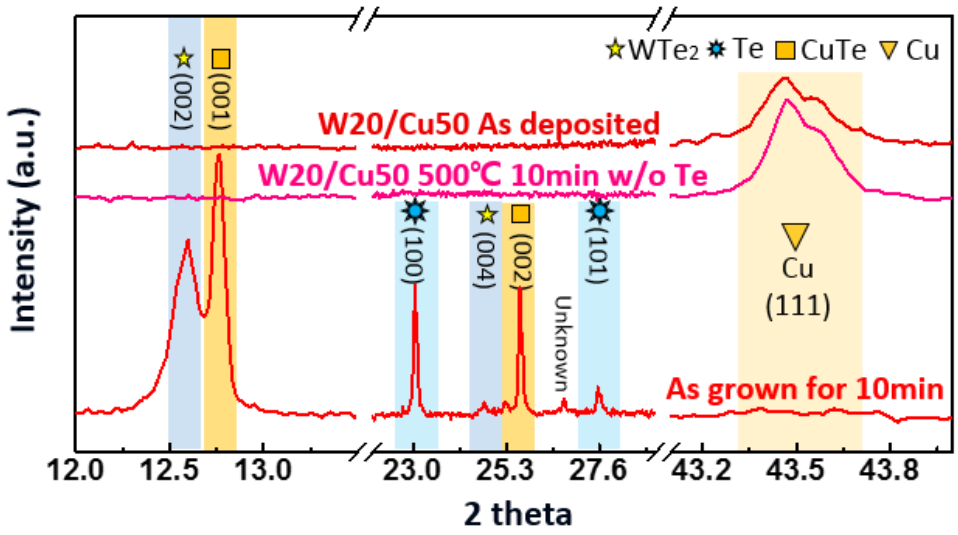

Figure 3-6. Comparison of XRD intensity of as deposited, annealed w/o Te and as-grown Cu_xTe_y:W at 500°C for 10min.

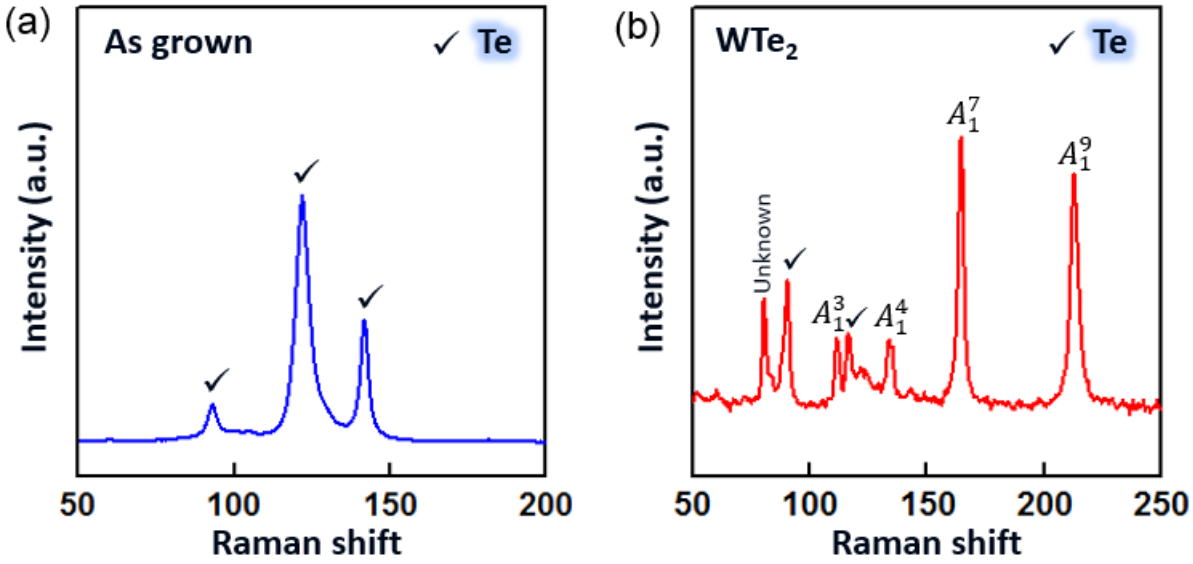

Figure 3-7. (a-b) Raman spectra of as-grown Cu_xTe_y droplet and as-synthesized WTe_2 nanostructures of a W(20 nm)/Cu(50 nm) sample at 500°C for 10min.

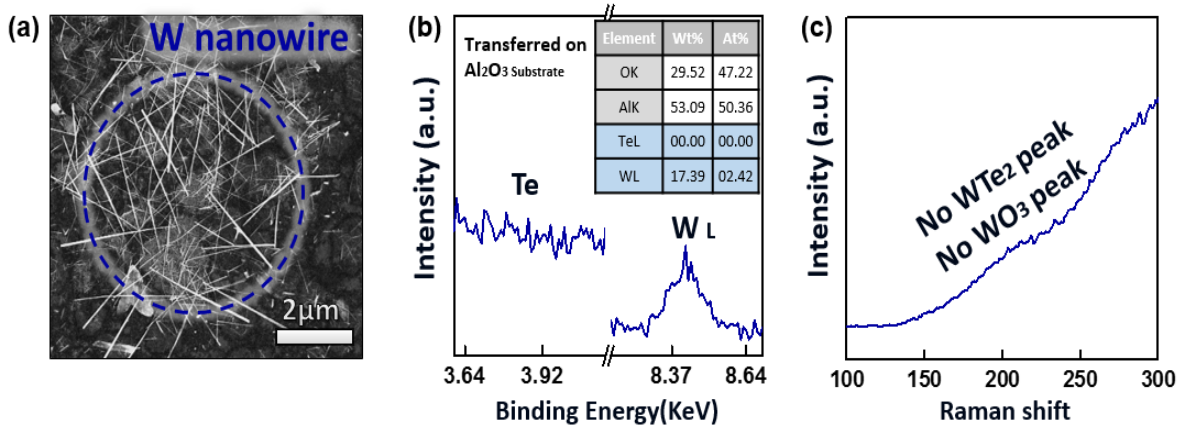

Figure 3-8. (a) SEM Image of as-synthesized W nanowires on W layer. (b-c) EDAX and Raman spectra, corresponding to the colored blue spot in (a) image.

3.2.2 Study on Behavior and Role of Cu_xTe_y depending on Growth Temperature

Next, we investigated the effect of growth temperature on formation of Cu_xTe_y droplets and synthesis of WTe_2 nanostructure. The thickness of the sample under the optimum condition for obtaining few-nm thickness WTe_2 nanostructure (tungsten of 20nm, copper of 50nm on SiO_2/Si substrate) and growth time for 10min with 0.1g of Te powder was fixed and only the synthesis temperature was adjusted. The dependency of Cu_xTe_y droplet and nanobelts structural morphology on synthesis parameters is shown in SEM images, displayed in figure 3-9. The average size of Cu_xTe_y droplet obtained from growth at 600 °C is about four times larger than Cu_xTe_y droplet grown at a temperature of 500 °C. Correspondingly, as the reaction temperature is increased, thick and long nanobelts can be obtained. The higher the temperature, the reaction of tungsten and tellurium are activated more inside of the larger Cu_xTe_y droplet, resulting in a thicker and improved crystallinity of WTe_2, as shown in figure 3-10. Figure. 3-11 indicates changes in length of nanobelts for the a-axis and b-axis and thickness of nanobelts as growth temperature is increased. From these results, we became aware that the reaction temperature of Cu and Te has significant effects on formation of Cu_xTe_y metal alloys and growth of WTe_2 nanobelts. The growth temperature affects not only the diffusion of the copper atoms from the pre-deposited copper layer into the upper layer but also activation of W atoms to be reacted with Te atoms from the W layer despite the low reactivity of W due to the high active temperature of W.

In our growth modes, the Cu_xTe_y dissolves W atoms from the W surface and forms WTe_2 nanostructures in side of Cu_xTe_y droplets. Interestingly, at a growth temperature of 600°C, an enormous amount of W nanowire grown in the (110) direction was found compared to growth temperature of 500°C. The SEM Images, as shown in figure 3-12, indicate that W nanowire have a diameter ranging from 50nm to 500nm, showing perfect straightness and grassy appearance.

Lee. Yun-Hi, et.al have reported fabrication of tungsten nanowire without use of any heterogeneous catalyst[45]. They examined X-ray diffraction (XRD) patterns that show remarkable changes of the crystallographic structure after W-nanowire formation. The XRD data for grown nanowires suggested that the interplanar distances were increased and the relative peak intensities of W (110) were increased. By HRTEM, they confirmed that the wavelength of the modulation in the HRTEM image was about 0.22 nanometers, which is the wavelength that corresponds to the inter-planar distance of (110) lattice planes of bcc W, as shown in figure 3-13.

Our results showed formation of W nanowires grown in (110) directions, and could be confirmed by XRD, indicated in figure 3-14. This figure shows that the intensity of W (100) after the growth of 600 °C

was highly increased (relatively higher than the intensity before growth). This is because the activated W atoms induced by eutectic metal alloy did not react with Te atoms, resulting in formation of W nanowires along the [110] direction. The W nanowire was dominantly observed when the temperature was increased and the amount of Te was decreased. As shown in figure 3-15, we confirmed that the size and density of the W nanowires increased significantly when the Te amount was reduced. Based on our mechanism, W atoms are dissolved in liquid state Cu_xTe_y droplets above the eutectic temperature of the Cu–Te system. These results strongly suggest that when the dissolved W atoms cannot react with Te due to deficiency of Te source, the activated W atoms grew as a nanowire shape in the (110) direction, followed by supersaturation and the crystallization from the liquid-phase. From these results, we can understand that the reaction of activated W atoms and Te precursor has a significant effects on supersaturation of WTe_2 in liquid state Cu_xTe_y droplet for growth of single-crystalline WTe_2 nanobelts.

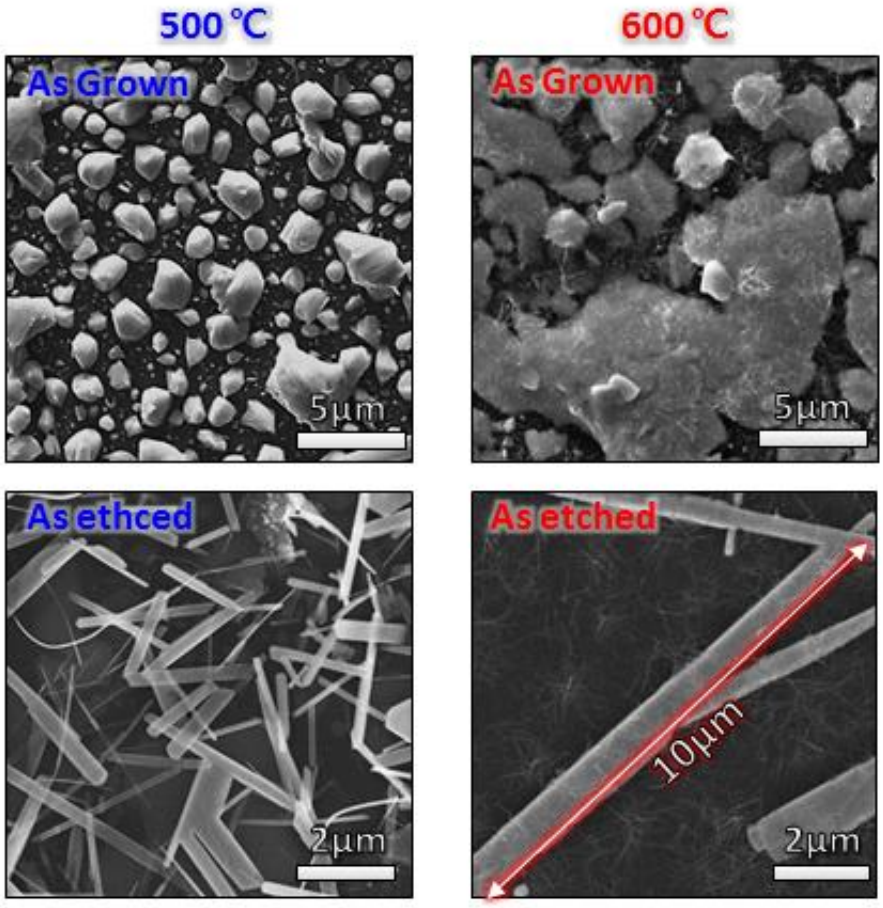

Figure 3-9. Representative SEM images of Cu_xTe_y droplet and WTe_2 nanobelts obtained at 500°C and 600°C for 10min, respectively.

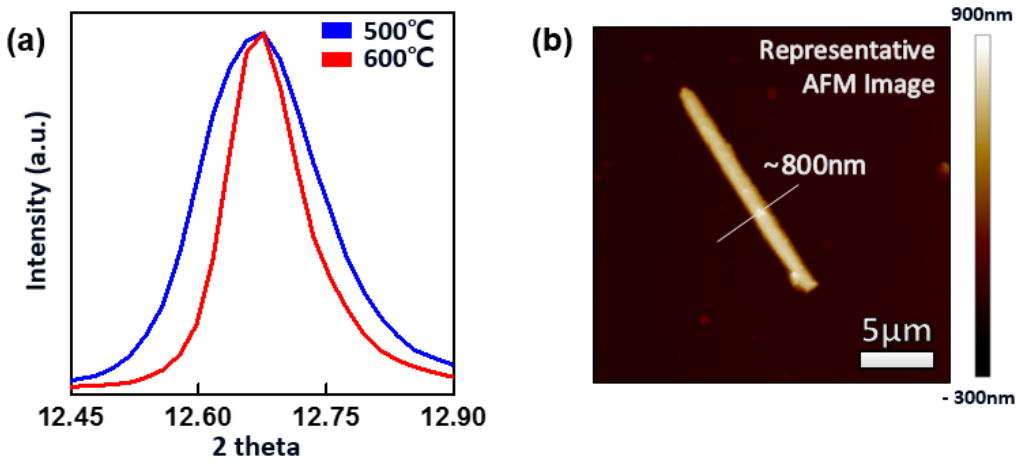

Figure 3-10. (a) XRD data of WTe_2 nanobelts obtained at 500°C and 600°C for 10min, respectively. (b) Representative AFM Image of WTe_2 nanobelts obtained at 600°C for 10min, showing highly thick nanobelts.

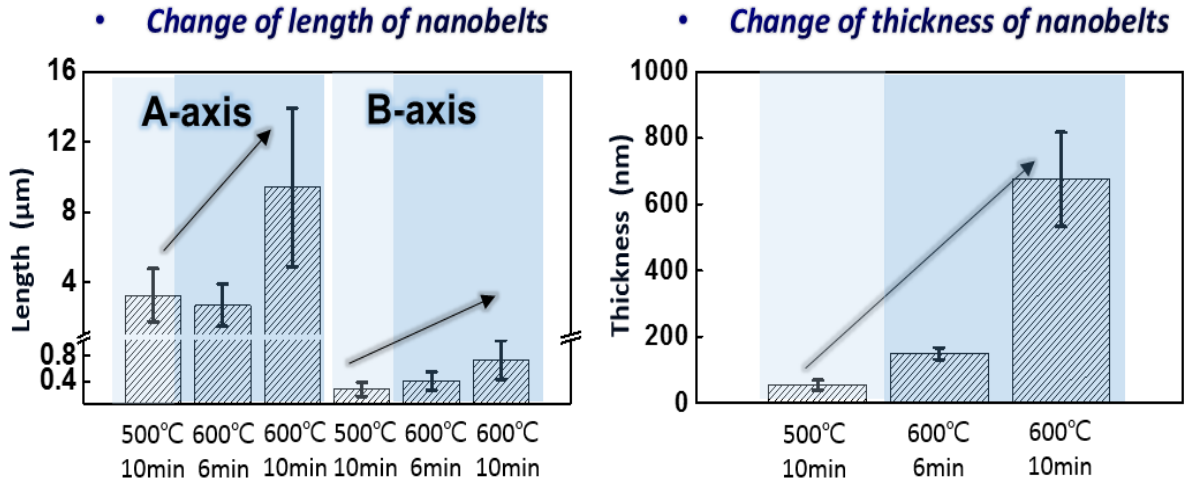

Figure 3-11. Changes of length and thickness of as-synthesized WTe_2 nanobelts as growth temperature and time increase.

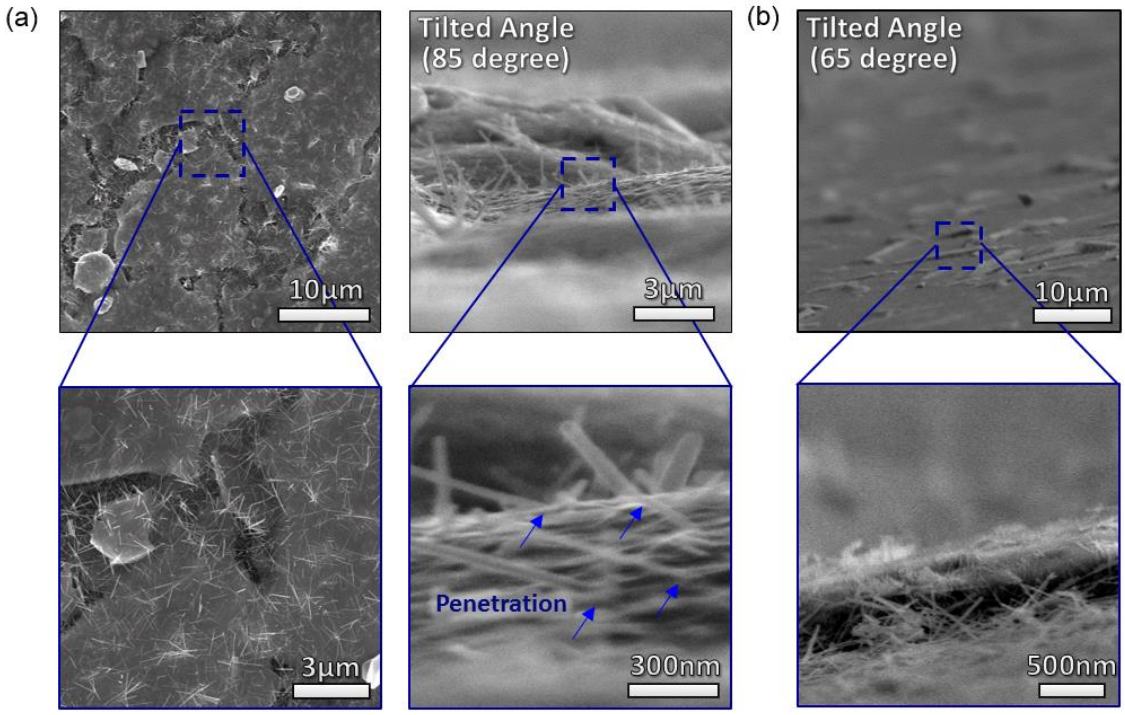

Figure 3-12. (a) Representative SEM images of Cu_xTe_y droplet & W nanowires. It is shown that the W nanowires penetrated the Cu_xTe_y droplet. (b) Cross sectional SEM Images of WTe_2 nanobelts & W nanowires.

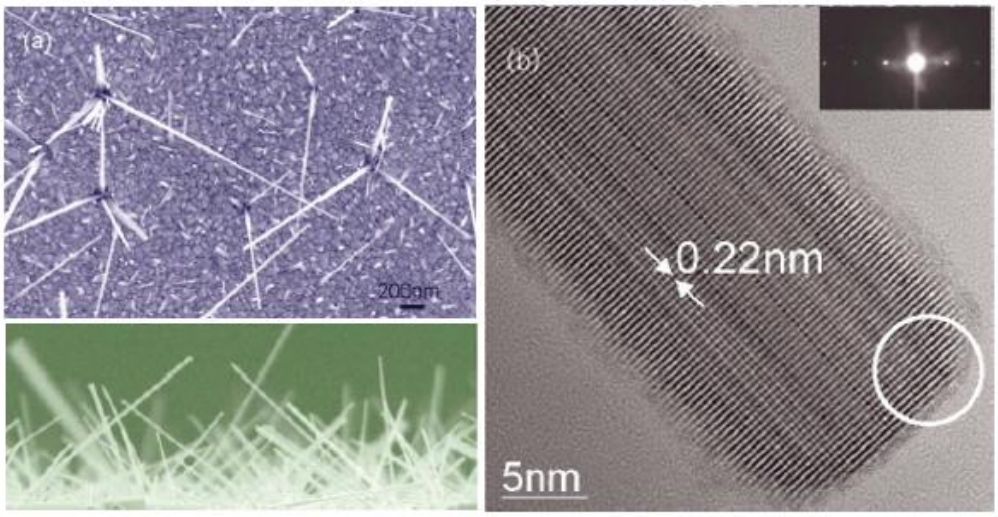

Figure 3-13. (a) SEM images of tungsten (W) nanowires at initial growth (b) The modulation phase HRTEM images of a chosen W nanowires. The inset figure is selected area electron diffraction pattern showing the growth of a well-crystallized bcc-phase W nanowire[45].

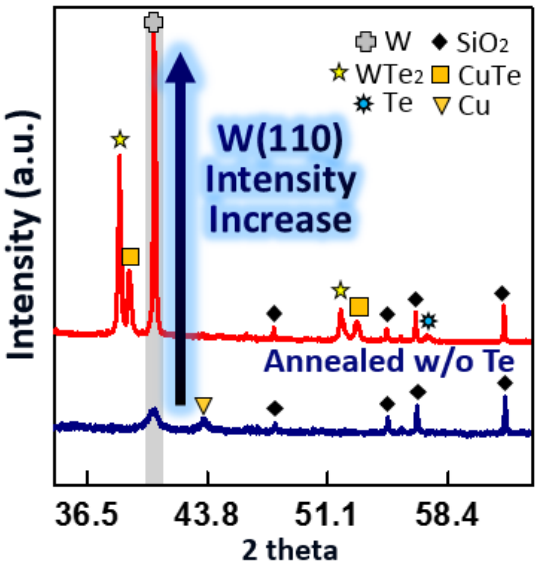

Figure 3-14. XRD data of as grown Cu_xTe_y droplet and as-annealed w/o Te at 600°C for 10min on SiO_2 substrate.

.

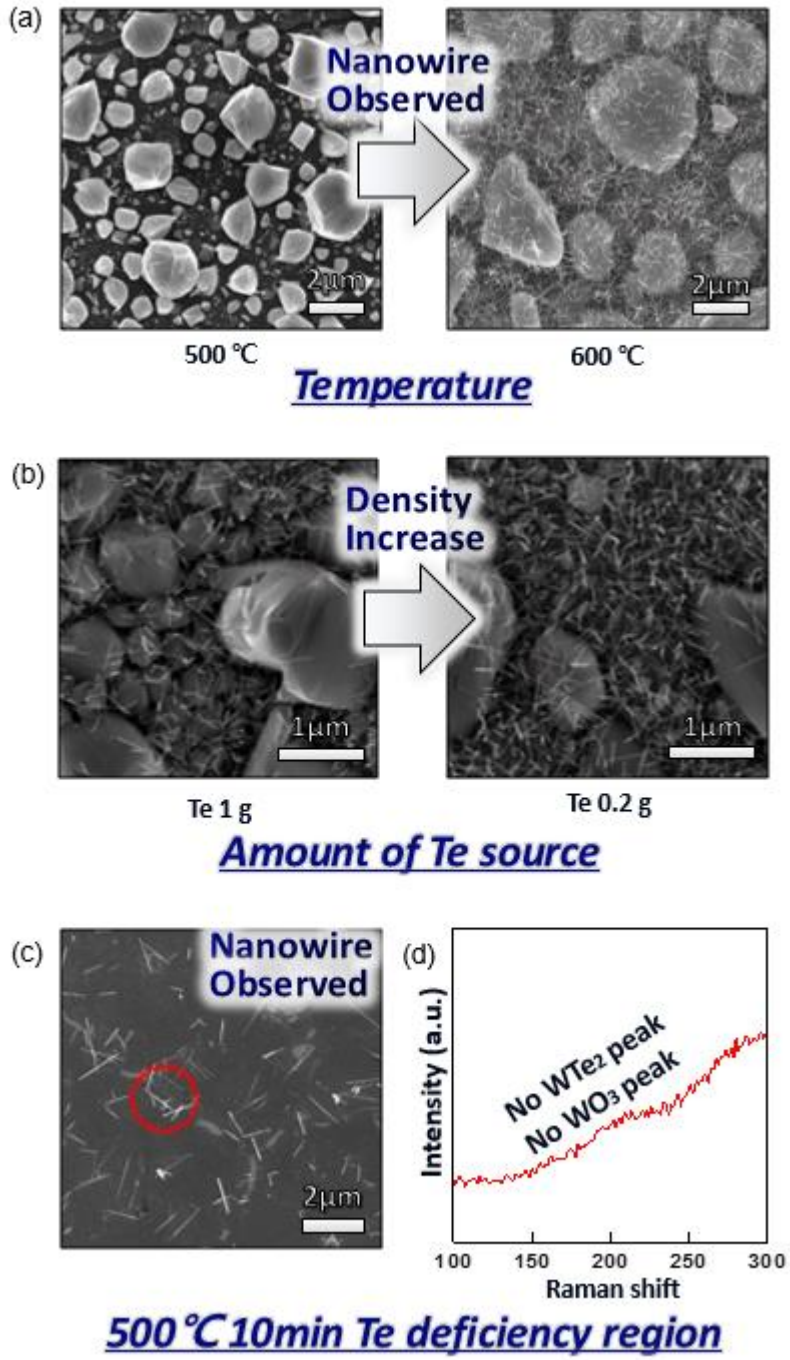

Figure 3-15. (a) Changes in the surface morphologies depending on the growth temperature. (b) Changes in the surface morphologies depending on the amount of Te source. (c) Representative SEM Images of W nanowire obtained from Te deficiency region at 500°C for 10min. (d) Raman spectra, corresponding to the colored red spot in (c) image, identifying the W nanowire.

3.2.3 Study on Behavior and Role of CuxTey depending on thickness of W layer

We have investigated the changes in the formation of Cu_xTe_y when the tungsten thickness is relatively increased. For this study, the thickness of the W layer was changed from 20 nm (optimum condition forobtaining few-nm thickness WTe_2 nanostructure) to a thickness of 100 nm. Other processes and growth conditions (copper of 50nm on Sio_2/Si substrate, growth for 10min at 500°C) were fixed and only the thickness of the W layer was changed. In this work, interestingly, as-grown Cu_xTe_y droplets couldn't be observed on W layer. This can be seen in the OM Images shown in figure 3-16a of as-grown Cu_xTe_y droplets after dipping APS etchant. However, we could not recognize any changes of the surface morphology. It is clearly shown that Cu_xTe_y droplets were formed under the W layer. We detached the W layer using a method of sonication to verify the synthesized WTe_2 underneath the W layer. At the same site where the Cu_xTe_y droplet was located, the synthesized WTe_2 was found on SiO_2/Si substrate, as shown in figure 3-16b,c. From these results, we confirm that Cu_xTe_y droplets do not penetrate the W layer as the thickness of W layer becomes relatively thick. In addition, it can be seen that WTe_2 does not grow only at the interface between W layer and Cu_xTe_y droplet. The cross sectional SEM Images (see figure 3-17) clearly exhibit the formation of WTe_2 nanostructures on the SiO_2, not on the W layer, compared to the case where the W layer is relatively thin (thickness = 20nm). Also, we investigated a change of structural morphology of synthesized WTe_2 nanobelts, as shown in figure 3-18. As we increased the thickness of W layer from 20nm to 100nm, the size of the synthesized WTe_2 increased slightly. The formation of WTe_2 nanobelts below W layer was confirmed, even at higher temperature of 600 °C, where diffusion of Cu atoms is increased, under a fixed growth and process condition. From previous experiments for studying effects of growth temperature, we found that the reaction temperature of Cu and Te has a significant effect on formation of Cu_xTe_y metal alloys. The growth temperature affects not only the diffusion of the copper atoms from the pre-deposited copper layer into the upper layer but also diffusion of Te vapor into copper layer. Compared to the case of 500°C, the larger size as-grown Cu_xTe_y metal alloys underneath W layer were exposed as they were etched by dipping APS etchant for 1hr. WTe_2 nanobelts covered with W layer and Te products can be observed in figure 3-19 and 3-20. In contrast to structural morphology of case of relatively thick W layer (t = 100nm), in the case of relatively thin W layers (t = 20nm), the Cu_xTe_y metal alloys were formed on W layer. This was clearly identified by the changes in surface morphology of Cu_xTe_y droplets depending on etching time. The Cu_xTe_y droplets on W layer were etched gradually as etching time increased, shown in figure 3-21. This shows that WTe_2 nanobelts are underneath Cu_xTe_y droplets. From these results, it was confirmed that the formation of Cu_xTe_y metal alloys and WTe_2 nanobelts are strongly dependent on the relative thickness of W layer. And we realized that the Cu_xTe_y dissolves W atoms from the W surface and helps WTe_2 to be nucleated, not just only on the W surface, but on the Sio_2/Si substrate.

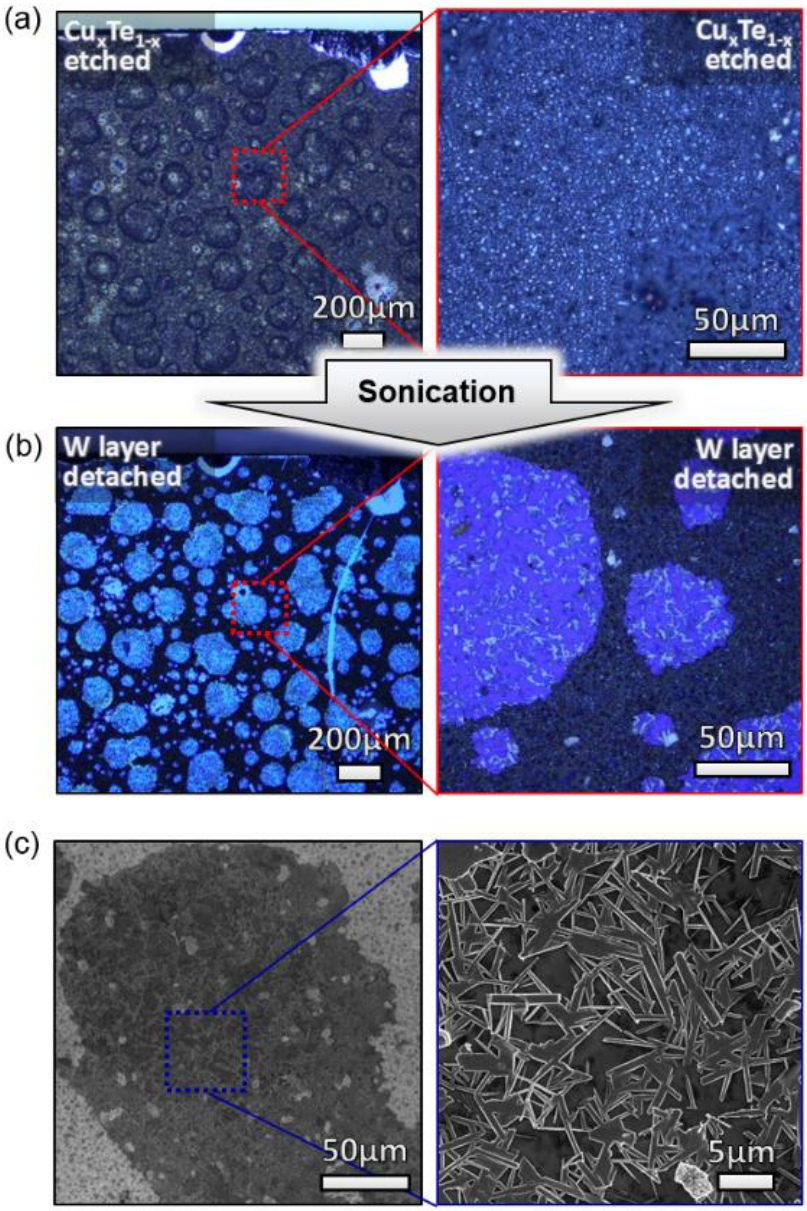

Figure 3-16. (a) OM Images of Cu_xTe_y droplets grown at W100/Cu50 at 500°C for 10min. It is shown that Cu_xTe_y droplets were formed under W layer. (b) OM Images of WTe_2 nanobelts at the same site after sonication for 1hr to detach W layer. (c) Representative SEM Images of WTe_2 nanobelts on SiO_2 substrate obtained at W100/Cu50 500°C for 10min.

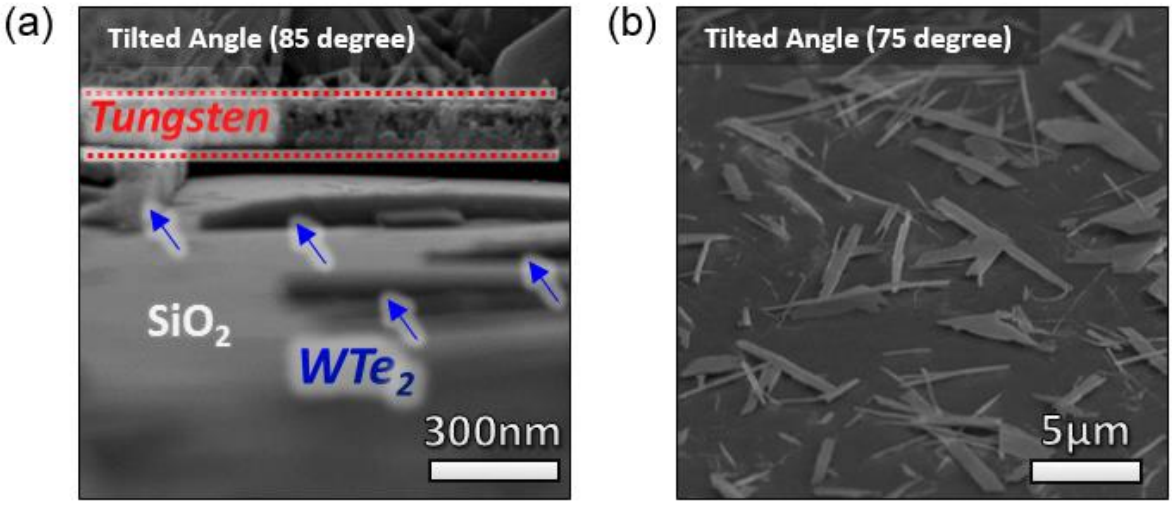

Figure 3-17. Cross sectional SEM Images of (a) WTe_2 grown on SiO_2 substrate (b) on W layer, respectively, depending on process condition of thickness of W layer.

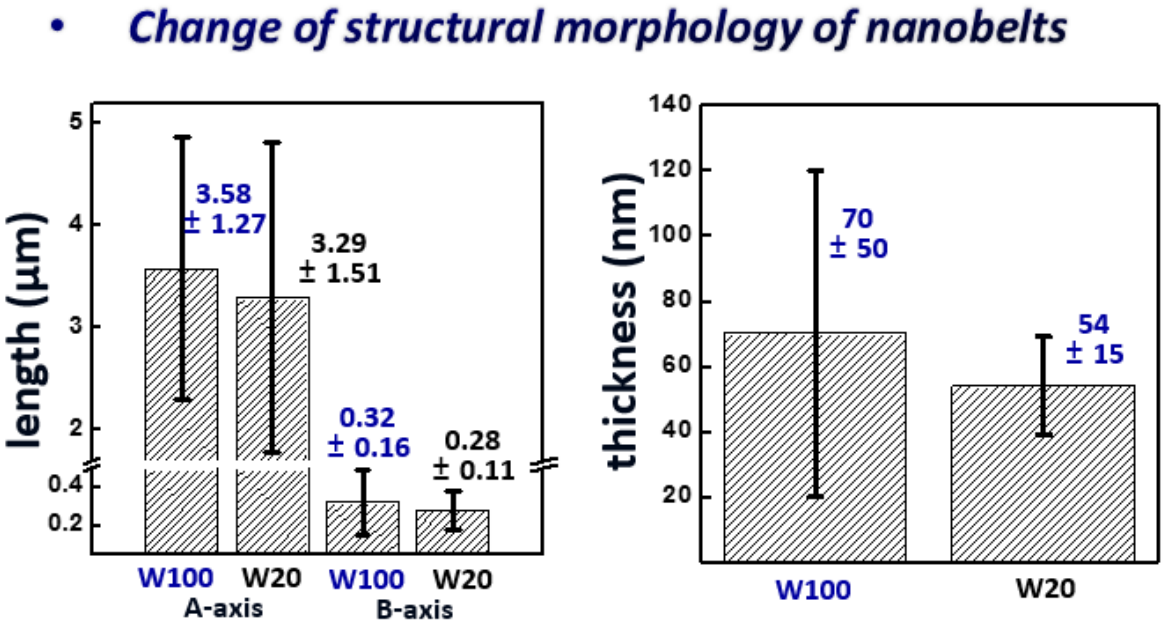

Figure 3-18. Change of structural morphology of as-synthesized WTe_2 nanobelts depending on process condition of thickness of W layer.

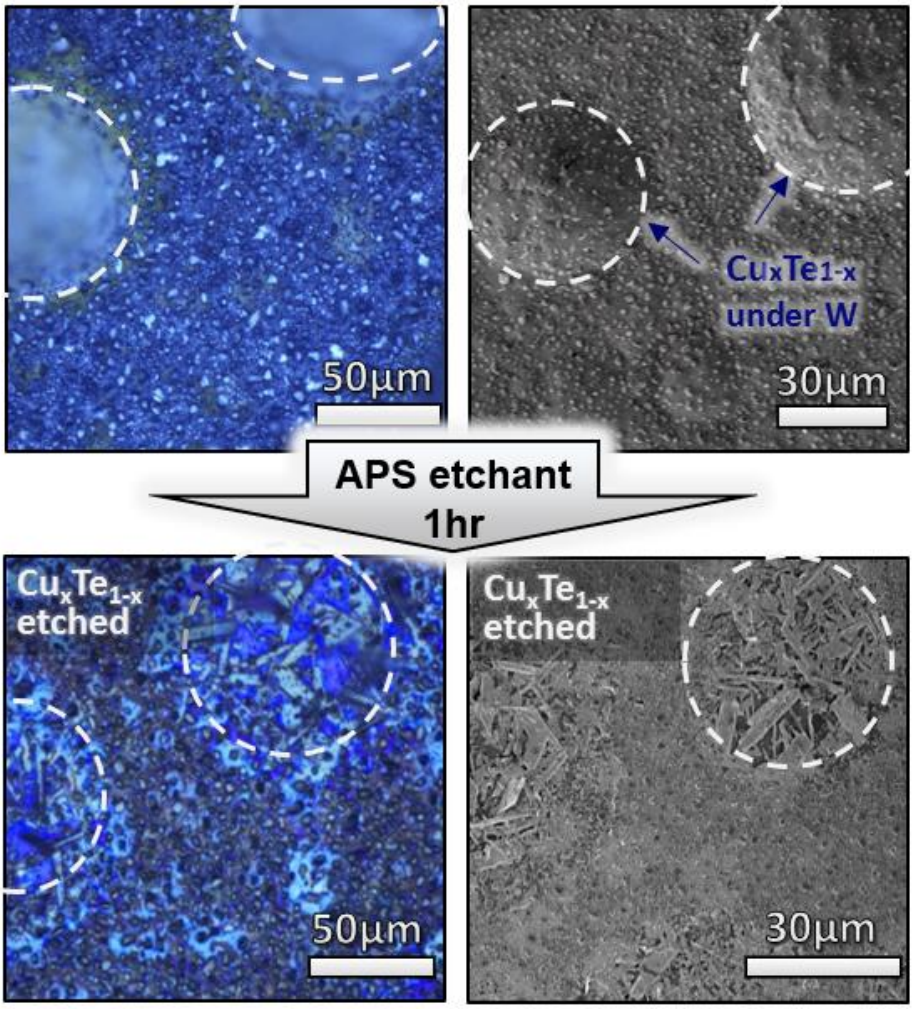

Figure 3-19. SEM Image and OM Images of Cu_xTe_y droplets grown at W100/Cu50 at 600°C for 10min. It is shown that Cu_xTe_y droplets were formed under W layer. After Cu_xTe_y etching, WTe_2 nanobelts can be observed under W layer.

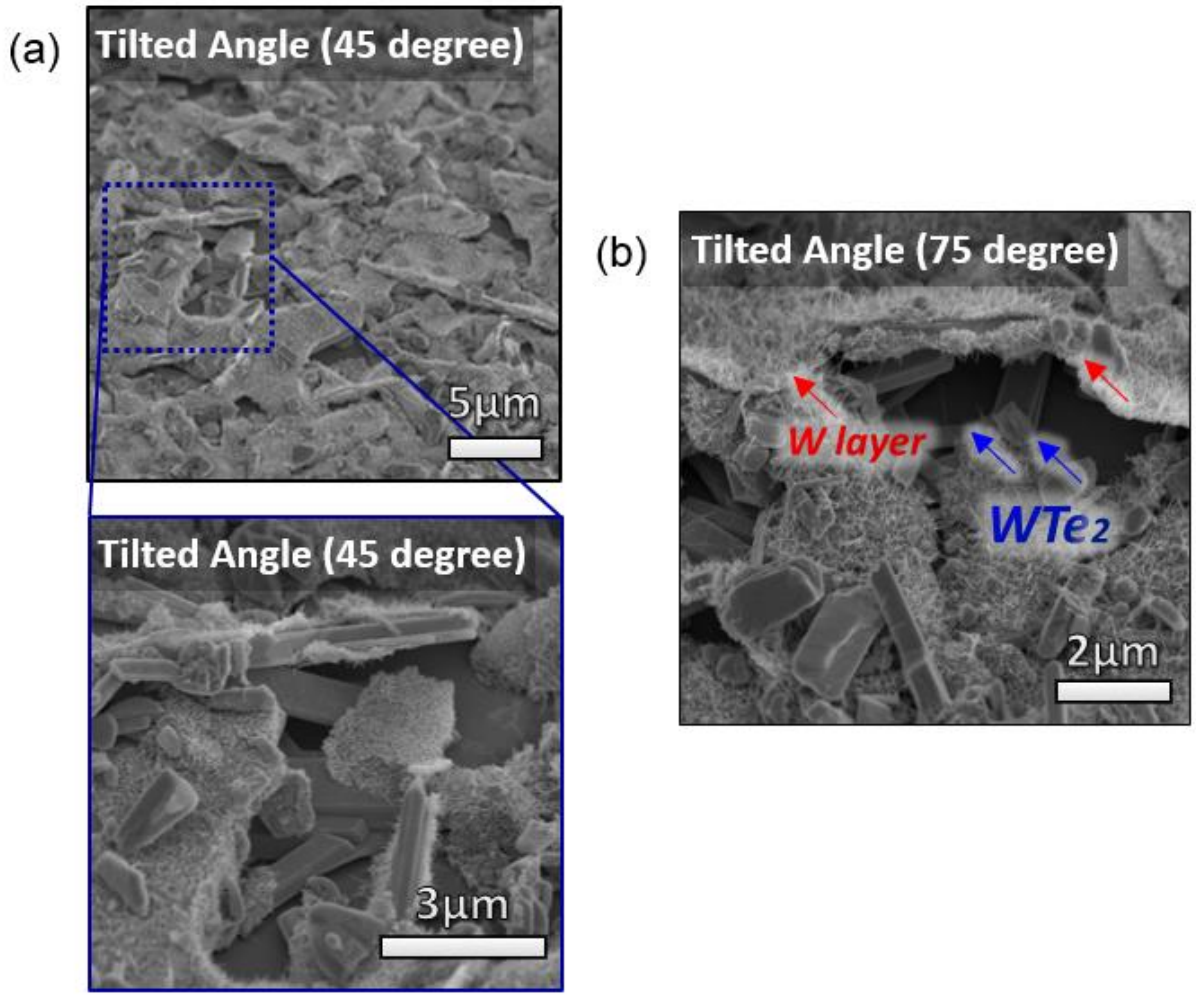

Figure. 3-20 (a-b) Cross sectional SEM images of Cu_xTe_y droplets grown at W100/Cu50 600°C for 10min. It is shown that WTe_2 nanobelts are covered with W layer and Tellurium product.

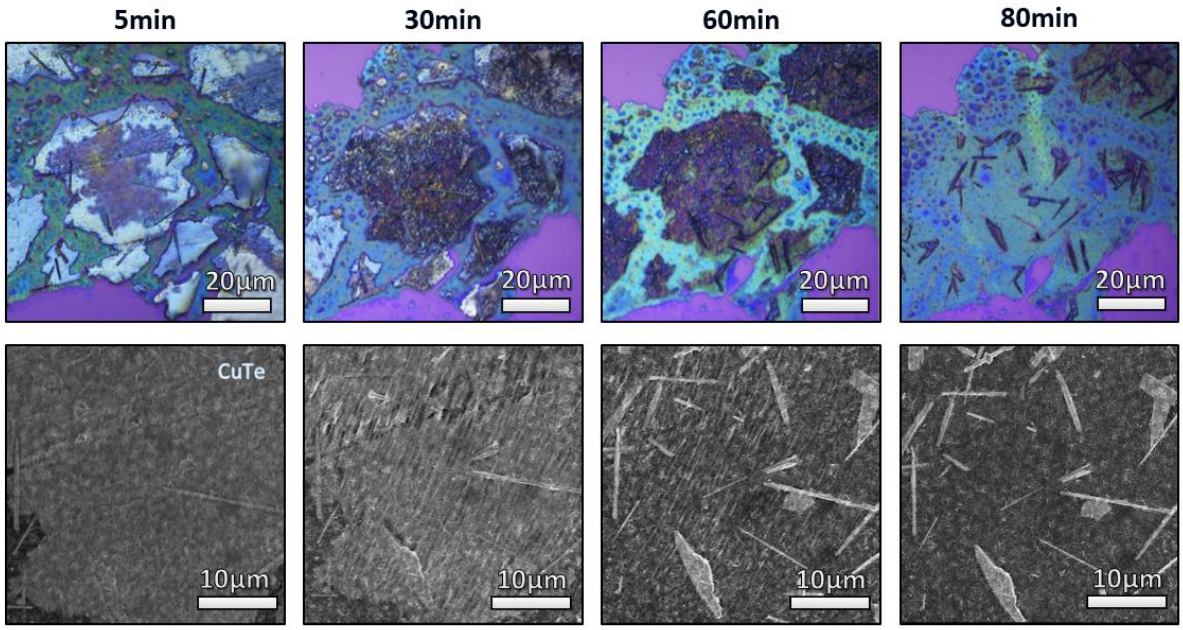

Figure 3-21. The changes in surface morphology of Cu_xTe_y droplets depending on etching time. The Cu_xTe_y droplets on SiO_2 substrate were etched gradually as etching time increased. It is found that WTe_2 nanobelts are underneath Cu_xTe_y droplets.

3.3 Transfer-Free Formation of Transition Metal Telluride Nanostructures on the Desired Substrate and Investigation of Electrical Properties

Recently, transfer-free growth of TMDs without the need for after-growth transfer process has been attracted for a fundamental research and practical applications[46]. To minimize degradation of TMDs' intrinsic properties and difficulty in fabrication of devices due to residues in process of complex transfer procedure, the development of direct formation of TMDs without necessity of an additional transfer step has been required.

In previous research, we confirmed that Cu_xTe_y metal alloys was formed on the desired substrate as the thickness of W layers became relatively thick. As shown in figure 3-22, the Cu_xTe_y was formed directly on SiO_2 /Si substrate. To expose the nanobelts inside of Cu_xTe_y droplets, we tried to mechanical peel Cu_xTe_y droplets off by using the method of peeling off using scotch tape. We confirmed that WTe_2 nanobelts were formed under the W layer and Cu_xTe_y droplet, by observing the back surface of the peeled scotch tape. As shown in figure 3-23, OM and SEM Images exhibit high density of WTe_2 nanobelts on the back surface of scotch tape. To confirm the WTe_2 nanobelts, Raman analysis was carried out, displayed in figure 3-24a.

We were able to observe as-synthesized WTe_2 nanobelts at the surface of SiO_2/Si substrate without using after-growth transfer processes. The Cu_xTe_y droplet and W layer were clearly peeled off by tape peeling off method, confirmed by EDAX and XRD analysis, indicated in figure 3-25b,c. Also, the as-obtained WTe_2 nanobelts directly on the desired substrate was confirmed by Raman spectroscopy, as shown in figure 3-24b. In short, we succeed to form WTe_2 nanobelts directly on the desired substrate without possibilities in degradation by inevitable chemical and physical damage in wet etching and transfer process.

Moreover, the feasibility of synthesis of $MoTe_2$ nanostructure as a member of the layered TMDs family was evaluated through our approaches. The formation of 2H-$MoTe_2$ and 1T'- $MoTe_2$ nanostructure on SiO_2 substrate was achieved by peeling the Cu_xTe_y droplets and Mo layer off, confirmed by Raman and Edax analysis of $MoTe_2$ nanostructure on SiO_2/Si substrate, indicated in figure 3-26.

The transfer-free formation of transition metal telluride nanostructure on desired substrate enables to investigate its electrical properties by fabricating test device directly on SiO_2/Si substrate without the needs for a further transfer process. Interestingly, we confirmed that the as-synthesized WTe_2 nanostructure by our method exhibits the similar resistivity as the exfoliated few-layer WTe_2 from the bulk crystal. The resistivity of few-layer WTe_2 nanostructure is in the range of ~ 10^{-4} to 10^{-3} Ω·cm, as shown in figure 3-7. To sum up, our approach of mechanical removal of Cu_xTe_y droplet by method of peeling off using scotch tape can reduce the whole process to obtain WTe_2 nanostructures as well as prevent degradation of WTe_2.

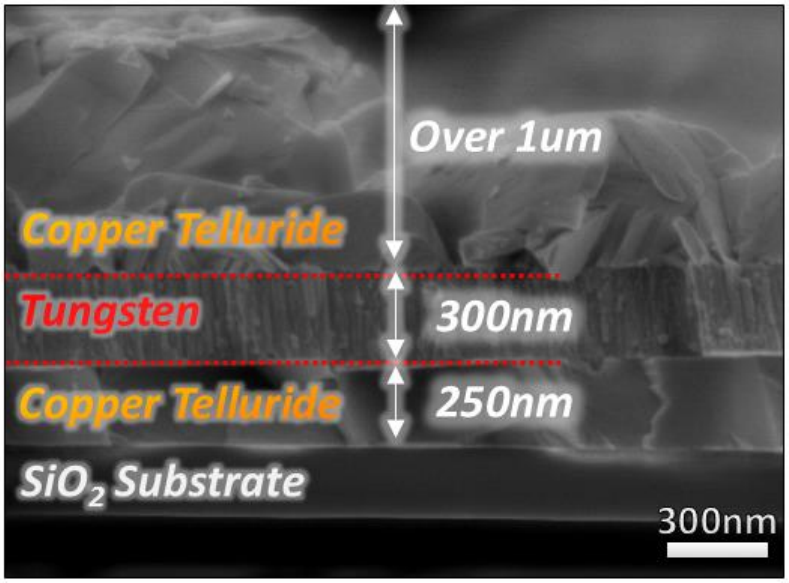

Figure 3-22. Cross sectional Image of as-grown Cu_xTe_y/W on SiO_2/Si substrate.

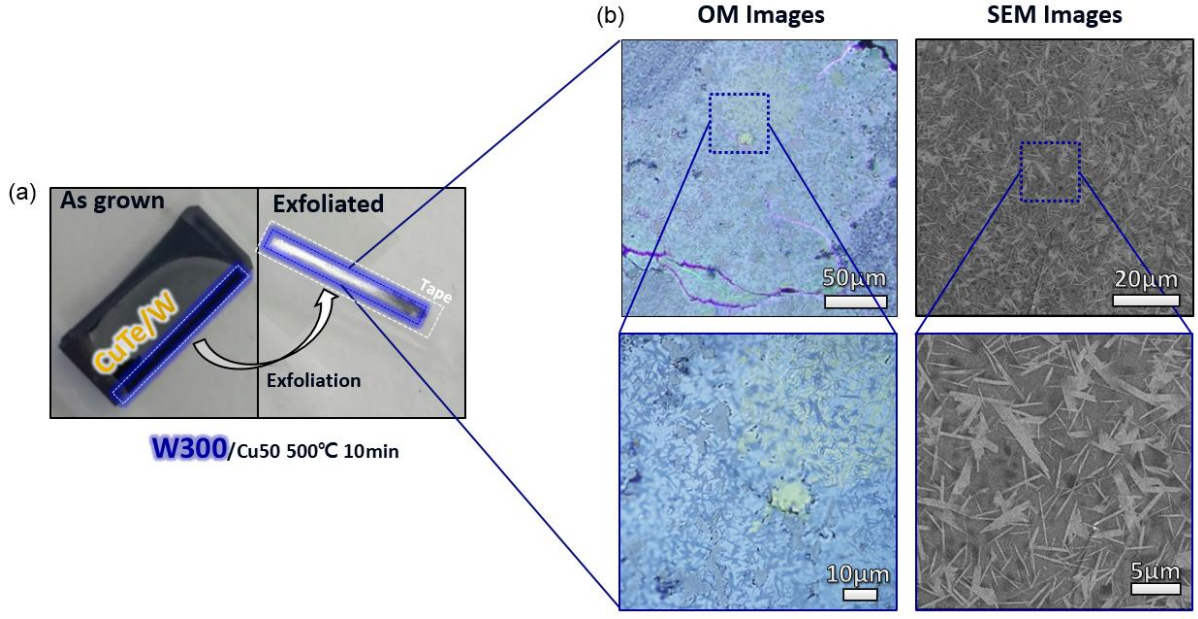

Figure 3-23. (a) Photograph of peeling off process by using scotch tape. (b) SEM and OM Images of WTe_2 nanobelts on the back side of exfoliated tape. It clearly suggests that synthesized WTe_2 nanobelts can be formed under Cu_xTe_y droplet/W layer.

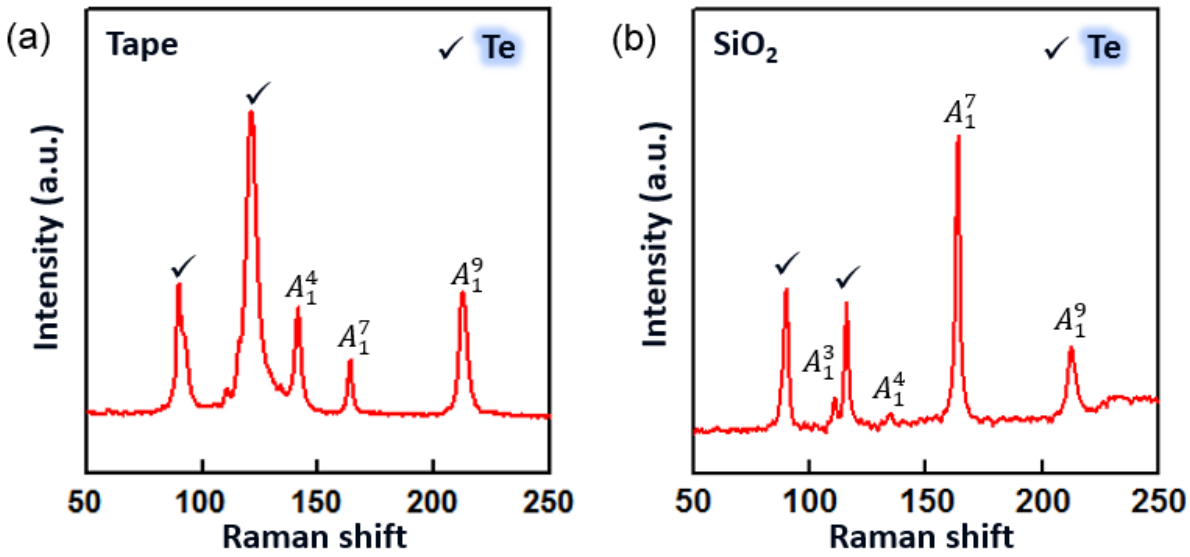

Figure 3-24. Raman spectra of WTe_2 nanobelts (a) on scotch tape and (b) on SiO_2/Si substrate, respectively.

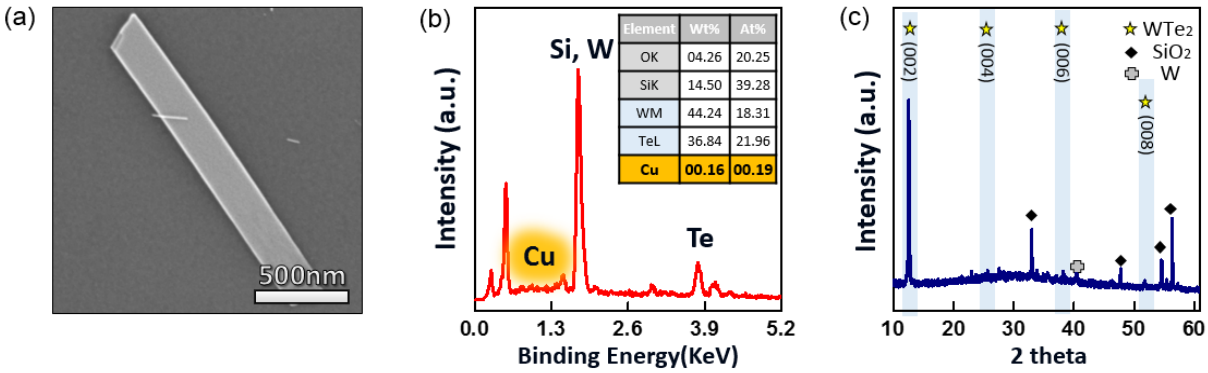

Figure 3-25. (a) Mechanical removal of Cu_xTe_y droplet by method of peeling off using scotch tape (b-c) Edax analysis and XRD data of WTe_2 nanobelts on SiO_2/Si substrate by peeling W and Cu_xTe_y droplets off, identifying that Cu_xTe_y droplets and W layer are clearly peeled off by method of peeling off using scotch tape

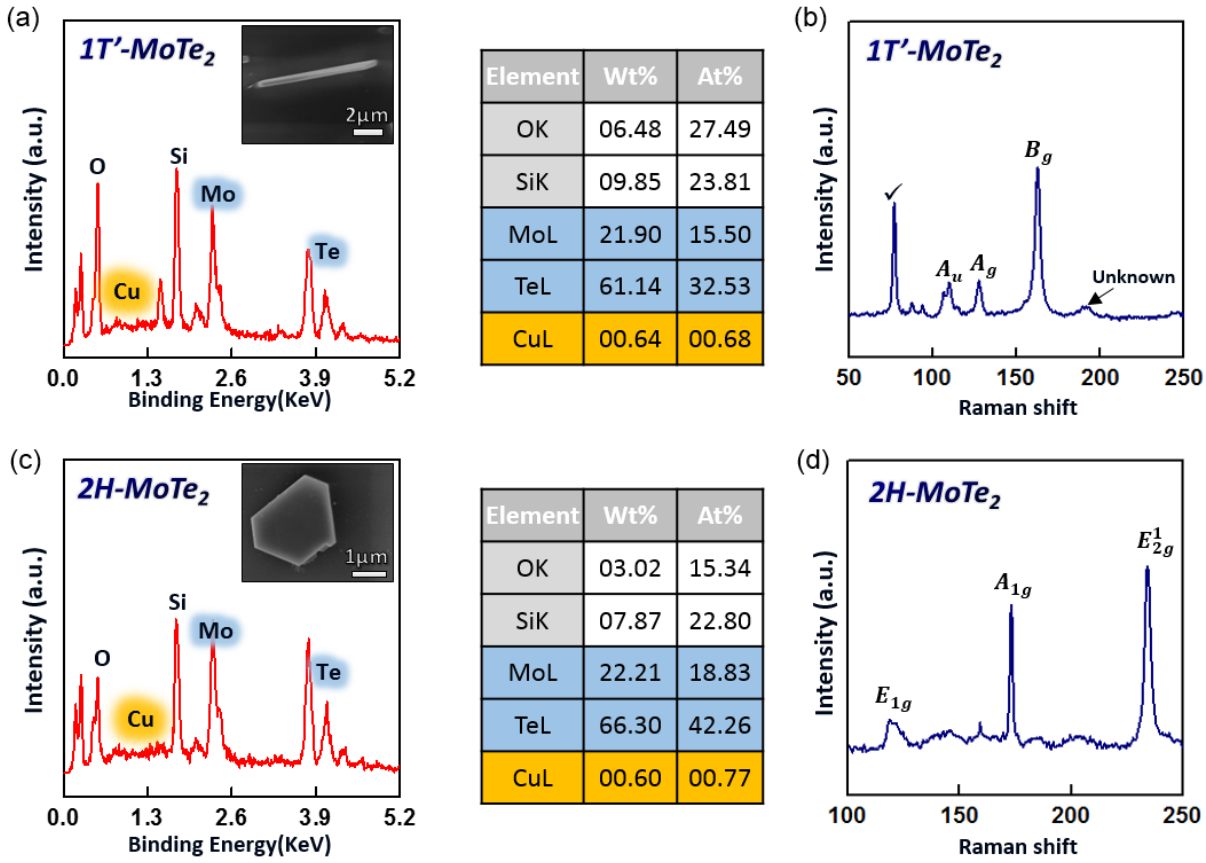

Element	Wt%	At%
OK	06.48	27.49
SiK	09.85	23.81
MoL	21.90	15.50
TeL	61.14	32.53
CuL	00.64	00.68

Element	Wt%	At%
OK	03.02	15.34
SiK	07.87	22.80
MoL	22.21	18.83
TeL	66.30	42.26
CuL	00.60	00.77

Figure 3-26. (a-d) Mechanical removal of Cu_xTe_y droplets and Mo layer by method of peeling off using scotch tape. The formation of 2H-$MoTe_2$ and 1T'-$MoTe_2$ nanostructure on SiO_2/Si substrate can be achieved by peeling Cu_xTe_y droplets and Mo layer off, confirmed in Raman and Edax spectra of $MoTe_2$ nanostructure on SiO_2/Si substrate

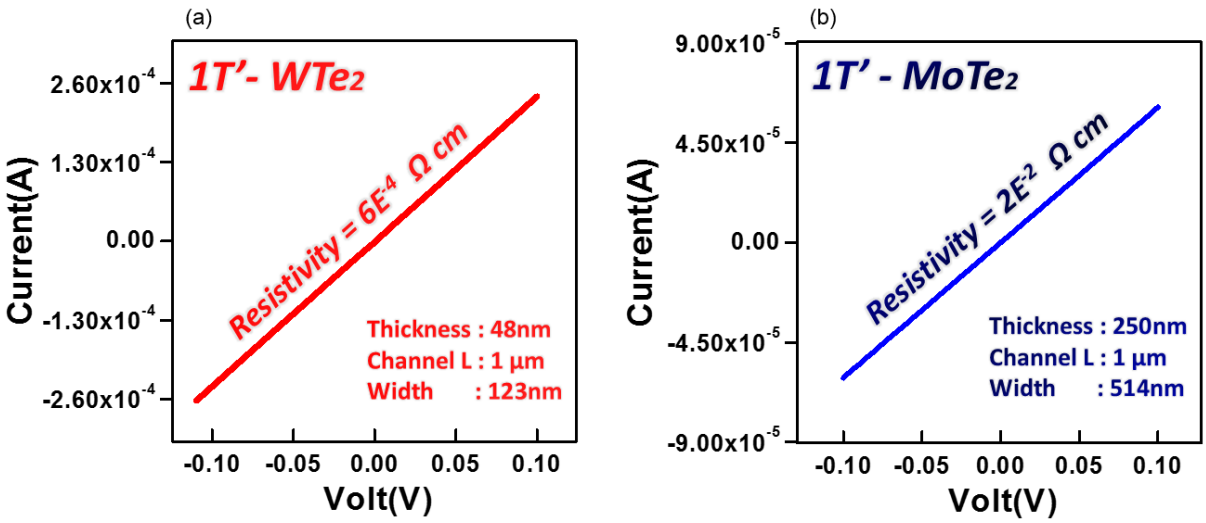

Figure 3-27. (a-b) Current vs voltage characteristics for fabricated 1T'- WTe_2 and $MoTe_2$ device, respectively. We successfully can obtain both 1T'- WTe_2 and $MoTe_2$ nanostructure directly on SiO_2/Si substrate with no needs for a further transfer process.

Chapter 4. Conclusion

Summary

In this research, the role of eutectic metal and its behavior on synthesis parameters in the synthesis of WTe_2 by using the pre-deposited films of W/Cu on SiO_2/Si substrate was studied.

First of all, the tungsten ditelluride (WTe_2) nanostructure were successfully synthesized by using eutectic metal alloys. The growth mechanism of WTe_2 was explained by the assistance of liquid Te-rich Cu_xTe_y droplets, after oversaturation with dissolved tungsten, induced a WTe_2 crystal growth. The crystallization takes place inside of Cu_xTe_y droplet at a temperature of ~500°C, above the Cu–Te eutectic temperature of 340°C. We described the crystallization of WTe_2 from solution-phase Cu_xTe_y droplets, resulting in 1-D preferential crystal growth of the single-crystalline WTe_2 nanobelts which has a stable distorted octahedral phase (1T'-WTe_2). The use of Te-rich eutectic metal alloys eliminates the Te deficiency in the resulting products and the contamination by impurities encountered with vapor deposition process. As a result, the as-synthesized WTe_2 nanostructures inside of Cu_xTe_y droplet by simple solution-phase reaction are highly pure, stoichiometric, and structurally uniform.

A different behavior of the Cu_xTe_y droplets were observed, which is strongly dependent on synthesis parameters such as growth temperature, time and process conditions of a metal film before WTe_2 growth. The structural characteristics and the formation of the products can be varied by controlling the synthesis parameters.

Particularly, we succeed to control the eutectic alloy to produce WTe_2 nanobelts where on the top of desired substrate directly. Our simple method of peeling off using scotch tape can reduce the whole process to form WTe_2 nanostructures on the desired substrate as well as prevent degradation of intrinsic properties of WTe_2, without using chemical wet etching and after-growth transfer processes. It enables to investigate its electrical properties by fabricating test device directly on SiO_2/Si substrate with no needs for a further transfer process. Moreover, the feasibility of synthesis of $MoTe_2$ nanostructure as a member of the layered TMDs family was evaluated through our approaches.

In conclusion, we develop reliable growth method of WTe_2 nanostructure using eutectic metal alloys and simple transfer-free growth method without the needs for a further transfer process. Our results provide not only a basis for optimizing WTe_2 nanostructure growth using eutectic metal alloys, but also can be adopted to research the novel properties of WTe_2 nanostructure without any degradation of the characteristics.

References

1. Butler, S. Z., *et al.* "Progress, challenges, and opportunities in two-dimensional materials beyond graphene." *ACS Nano* 7.4 (2013): 2898-2926.
2. Chhowalla, M., *et al.* "Two-dimensional semiconductors for transistors." *Nature Reviews Materials* 1 (2016): 16052.
3. Podzorov, V., *et al.* "High-mobility field-effect transistors based on transition metal dichalcogenides." *Applied Physics Letters* 84.17 (2004): 3301-3303
4. Liu, L., *et al.* "Performance limits of monolayer transition metal dichalcogenide transistors." *IEEE Transactions on Electron Devices* 58.9 (2011): 3042-3047
5. Fang, H., *et al.* "High-performance single layered WSe_2 p-FETs with chemically doped contacts." *Nano Letters* 12.7 (2012): 3788-3792.
6. Wang, Q. H., *et al.* "Electronics and optoelectronics of two-dimensional transition metal dichalcogenides." *Nature Nanotechnology* 7.11 (2012): 699-712.
7. Deng, Y., *et al.* "Black phosphorus–monolayer MoS_2 van der waals heterojunction p–n diode." *ACS Nano* 8.8 (2014): 8292-8299.
8. Furchi, M. M., *et al.* "Photovoltaic effect in an electrically tunable van der Waals heterojunction." *Nano Letters* 14.8 (2014): 4785-4791.
9. Fang, H., *et al.* "Strong interlayer coupling in van der Waals heterostructures built from single-layer chalcogenides." *Proceedings of the National Academy of Sciences* 111.17 (2014): 6198-6202.
10. Akinwande, D., *et al.* "Two-dimensional flexible nanoelectronics." *Nature Communications* 5 (2014).
11. Fiori, G., *et al.* "Electronics based on two-dimensional materials." *Nature Nanotechnology* 9.10 (2014): 768-779.
12. Chhowalla, M., *et al.* "The chemistry of two-dimensional layered transition metal dichalcogenide nanosheets." *Nature Chemistry* 5.4 (2013): 263-275.
13. Mak, K. F., *et al.* "Atomically thin MoS_2: a new direct-gap semiconductor." *Physical Review Letters* 105.13 (2010): 136805
14. Britnell, L., *et al.* "Strong light-matter interactions in heterostructures of atomically thin films." *Science* 340.6138 (2013): 1311-1314.

15. Cheiwchanchamnangij, T., *et al.* "Quasiparticle band structure calculation of monolayer, bilayer, and bulk MoS_2." *Physical Review B* 85.20 (2012): 205302.

16. Song, S., *et al.* "Room temperature semiconductor–metal transition of $MoTe_2$ thin films engineered by strain." *Nano Letters* 16.1 (2015): 188-193.

17. Ali, M. N., *et al.* "Large, non-saturating magnetoresistance in WTe_2." *Nature* 514.7521 (2014): 205-208.

18. Huang, H. H., *et al.* "Controlling phase transition for single-layer MTe_2 (M= Mo and W): modulation of the potential barrier under strain." *Physical Chemistry Chemical Physics* 18.5 (2016): 4086-4094.

19. Park, J. C., *et al.* "Phase-Engineered Synthesis of Centimeter-Scale 1T′-and 2H-Molybdenum Ditelluride Thin Films." *ACS Nano* 9.6 (2015): 6548-6554.

20. Shi, Y., *et al.* "Recent advances in controlled synthesis of two-dimensional transition metal dichalcogenides via vapour deposition techniques." *Chemical Society Reviews* 44.9 (2015): 2744-2756.

21. Novoselov, K. S., *et al.* "Two-dimensional crystals-based heterostructures: materials with tailored properties." *Physica Scripta* 2012.T146 (2012): 014006.

22. Gupta, A. *et al.* "Recent development in 2D materials beyond graphene." *Progress in Materials Science* 73 (2015): 44-126.

23. Li, J., *et al*. "Scalable Fabrication of 2D Semiconducting crystals for future electronics." *Electronics* 4.4 (2015): 1033-1061.

24. Ji, Q., *et al.* "Chemical vapour deposition of group-VIB metal dichalcogenide monolayers: engineered substrates from amorphous to single crystalline." *Chemical Society Reviews* 44.9 (2015): 2587-2602

25. Lv, H. Y., *et al.* "Perfect charge compensation in WTe_2 for the extraordinary magnetoresistance: From bulk to monolayer." *EPL (Europhysics Letters)* 110.3 (2015): 37004

26. Keum, D. H., *et al.* "Bandgap opening in few-layered monoclinic $MoTe_2$." *Nature Physics* 11.6 (2015): 482-486

27. Duerloo, K. A. N., *et al.* "Structural phase transitions in two-dimensional Mo- and W- di chalcogenide monolayers." *Nature Communications* 5 (2014).

28. Lee, C. H., *et al.* "Tungsten ditelluride: a layered semimetal." *Scientific Reports* 5 (2015).

29. Lu, N., *et al.* "Atomic and electronic structures of WTe_2 probed by high resolution electron microscopy and ab initio calculations." *The Journal of Physical Chemistry C* 120.15 (2016): 8364-8369.

30. Ali, M. N., *et al.* "Correlation of crystal quality and extreme magnetoresistance of WTe_2." *EPL (Europhysics Letters)* 110.6 (2015): 67002.

31. Kim, Y., *et al.* "Anomalous Raman scattering and lattice dynamics in mono-and few-layer WTe_2." *Nanoscale* 8.4 (2016): 2309-2316.

32. Wang, L, *et al.* "Tuning magnetotransport in a compensated semimetal at the atomic scale." *Nature Communications* 6 (2015).

33. Dai, Y. M., *et al.* "Ultrafast carrier dynamics in the large-magnetoresistance material WTe_2." *Physical Review B* 92.16 (2015): 161104.

34. Kong, W. D., *et al.* "Raman scattering investigation of large positive magnetoresistance material WTe_2." *Applied Physics Letters* 106.8 (2015): 081906.

35. Soluyanov, A. A., *et al.* "Type-II Weyl semimetals." *Nature* 527.7579 (2015): 495-498

36. Burkov, A. A., *et al.* "Weyl semimetal in a topological insulator multilayer." *Physical Review Letters* 107.12 (2011): 127205.

37. Qian, X., *et al.* "Quantum spin Hall effect in two-dimensional transition metal dichalcogenides." *Science* 346.6215 (2014): 1344-1347.

38. Zheng, F., *et al.* "On the Quantum Spin Hall Gap of Monolayer 1T′-WTe_2." *Advanced Materials* (2016).

39. Zhao, Y., *et al.* "Anisotropic magnetotransport and exotic longitudinal linear magnetoresistance in WTe_2 crystals." *Physical Review B* 92.4 (2015): 041104.

40. Kang, D., *et al.* "Superconductivity emerging from a suppressed large magnetoresistance state in tungsten ditelluride." *Nature Communications 6* (2015).

41. Choi, H. J., *et al.* "Vapor–liquid–solid growth of semiconductor nanowires." *Semiconductor Nanostructures for Optoelectronic Devices.* Springer Berlin Heidelberg, 2012. 1-36

42. Ellmer, K. *et al.* "Preparation routes based on magnetron sputtering for tungsten disulfide (WS_2) films for thin-film solar cells." *Physica Status Solidi (b)* 245.9 (2008): 1745-1760.

43. Brunken, S., *et al.* "Analysis of the early stages of the rapid, nickel-assisted crystallization of WS_2 films." *Journal of Applied Physics* 120.16 (2016): 165307.

44. Sun, Y., *et al.* "Eutectic solidification applied to nanofabrication: a strategy to prepare large-scale tungsten carbide nanowalls." *Journal of Materials Chemistry* 22.32 (2012): 16566-16571.

45. Lee, Y. H., *et al.* "Tungsten nanowires and their field electron emission properties." *Applied Physics Letters* 81.4 (2002): 745-747.

46. Huang, C. C., *et al.* "Transfer-free growth of atomically thin transition metal disulfides using a solution precursor by a laser irradiation process and their application in low-power photodetectors." *Nano Letters* 16.4 (2016): 2463-2470.

Master's Thesis

Synthesis of Single-Crystalline Tungsten Ditelluride (WTe_2) Nanostructures Using Eutectic Metal Alloys

Jong Hwa Lee

Department of Materials Science and Engineering

Graduate School of UNIST

2017

Synthesis of Single-Crystalline Tungsten Ditelluride (WTe_2) Nanostructures Using Eutectic Metal Alloys

Jong Hwa Lee

Department of Materials Science and Engineering

Graduate School of UNIST

Synthesis of Single-Crystalline Tungsten Ditelluride (WTe_2) Nanostructures Using Eutectic Metal Alloys

A thesis/dissertation
submitted to the Graduate School of UNIST
in partial fulfillment of the
requirements for the degree of
Master of Science

Jong Hwa Lee

01. 19. 2017.
Approved by

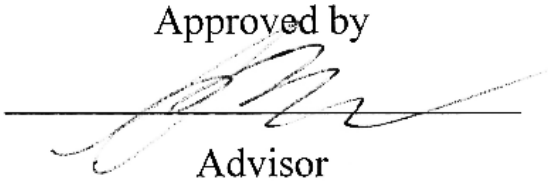

Advisor
Soon-Yong Kwon

Synthesis of Single-Crystalline Tungsten Ditelluride (WTe_2) Nanostructures Using Eutectic Metal Alloys

Jong Hwa Lee

This certifies that the dissertation of Jong Hwa Lee is approved.

01. 19. 2017

Adviser: Soon-Yong Kwon

Zonghoon Lee : Thesis Committee Member #1

Sung Youb Kim : Thesis Committee Member #2

Abstract

Beyond graphene, group-VI transition metal dichalcogenides (TMDs) which is compound of transition metal and chalcogen have recently attracted much attention and mechanically exfoliated flakes of two-dimensional TMDs hold great promise due to their rich variety of properties. As a member of the TMDs family, tungsten ditelluride (WTe_2), which has a stable distorted octahedral phase (1T') among several polymorphs, are appealing because of their unique properties such as an unusual magnetoresistance and quantum spin Hall effect. In an effort to synthesize WTe_2 nanostructures, researchers have tried to develop many growth techniques. Nonetheless, there remains considerable difficulty in obtaining high-quality WTe_2 nanostructures due to a high equilibrium vapor pressure of tellurium at growth temperatures and a weak binding energy of W-Te than other chalcogens.

Here, we suggest a novel facile method to realize the synthesis of single-crystalline WTe_2 nanostructures using eutectic metal alloys. In our work, we studied on the role of eutectic metal alloys and its behavior on synthesis parameters and more details will be presented. In addition, the as-synthesized WTe_2 nanostructures can be easily transferred to different substrates and/or solutions as well as successfully formed on desired substrate without the needs for a further transfer process. The transfer-free formation of WTe_2 nanostructures can be adopted to research the novel properties of WTe_2 nanostructure without any degradation of the intrinsic characteristics. Moreover, feasibility of synthesis for $MoTe_2$ nanostructure as a member of the layered TMDs family was evaluated through our methods. We expect that the emergence of new type of transition metal telluride nanostructures will create exciting prospects for further technical devices and applications in nano-electronics, catalysts and other fields.

Keywords : Transition Metal Dichalcogenides (TMDs), Tungsten ditelluride (WTe_2), Eutectic metal alloys, Nanostructures, Molibdenum ditellruide ($MoTe_2$)

Contents

List of Figures

List of tables

Chapter 1. Overviews

1.1 Transition Metal Dichalcogenides (TMDs)

1.1.1 Introduction of TMDs

Beyond 2D Graphene, scientific interest has been extended to low-dimensional materials because of the wealth of unusual and unique properties that occur when scaled down from bulk to nanoscale dimensions[1]. Recent progress suggests that such truly atomically-thin low-dimensional materials could be one pathway for future electronic devices. The advantages of low-dimensional (2D) materials compared with 3D materials for FETs are demonstrated by the differences that occur in the charge transport between the bulk and the single layer[2]. In 2D materials, charge carriers are confined in atomically thin channels because of the vdW materials' low density of dangling bonds and minimal surface roughness, resulting in excellent gate electrostatics (see figure 1-1). These features make them promising candidates for the revolutionary applications, such as truly atomically-thin field-effect transistors (FET)[3-6], stacked vdW layered hetero-junctions[7-9], and flexible and transparent electronic devices[10-11].

Layered group-VI transition metal dichalcogenides (TMDs) which is compound of transition metal and chalcogen have a chemical formula of MX_2, where M is the transition metal (i.e. Mo or W in group VI metal) and X stands for chalcogen atoms. (i.e. S, Se or Te). Since layered TMDs have a layered stacked structure with weak van der Waals (vdW) force along out-of-plane and strong covalent bonding along in-plane, it could be mechanically and chemically exfoliated into single and/or few layers. Each layer typically has a thickness of 7~9 Å, which consists of a hexagonally packed layer of metal atoms sandwiched between chalcogen atoms.

The layered TMDs exhibit a variety of polymorphs, which are 1T, 2H where the letters stand for trigonal, hexagonal and the digit indicates the number of X–M–X units in the unit cell respectively, as displayed in figure 1-2 (single-layer TMDs exhibit two polymorphs: trigonal prismatic and octahedral phases.)[12].

For most TMDs, the crystal coordination and combination of metal and chalcogen atoms have effects on the material's electrical properties. The bandgap decreases as the atomic number (atomic mass) of the chalcogen atom increases (from S to Se to Te). For example, the bandgap of 2H-MoS_2, 2H-$MoSe_2$ and 2H-$MoTe_2$ decreases gradually from 1.3 to 1.0 eV. The tungsten (or molybdenum) sulfides and selenides shows the semiconducting behavior, but the tellurides are known as semimetal. The group-VI TMDs' electrical properties are summarized in table 1-1.

Among the group-VI TMDs, Mo (or W) sulfides and selenides are semiconductors and possess bandgaps in the range of 1-2 eV with the unit cell of trigonal prismatic (2H-phase, in figure 1-2b). Since the material has discrete band gap level, high carrier mobility and the absence of dangling bonds, they have a possibility for the novel applications of electronics. Since semiconducting TMDs have sizable bandgap, they are a promising optical materials having the energy spectrum ranged from visible to near infrared wavelength. The observation of indirect-to-direct bandgap transition at the monolayer regime[13], strong light-matter interactions[14], and large exciton binding energies[15] can be used for the potential platform for investigation of unusual physical properties as well as the application of the photonic devices in the next-generation.

On the other hand, semi-metallic group-VI metal tellurides display the semi-metallic properties when it has a distorted 1T-phase (1T' or Td, also called distorted orthorhombic, see figure 1-2c)[16-17]. In addition, the tellurides have low energy barriers for the phase transition, so phase transition can be controlled by growth temperature, pressure, or strain[18-19].

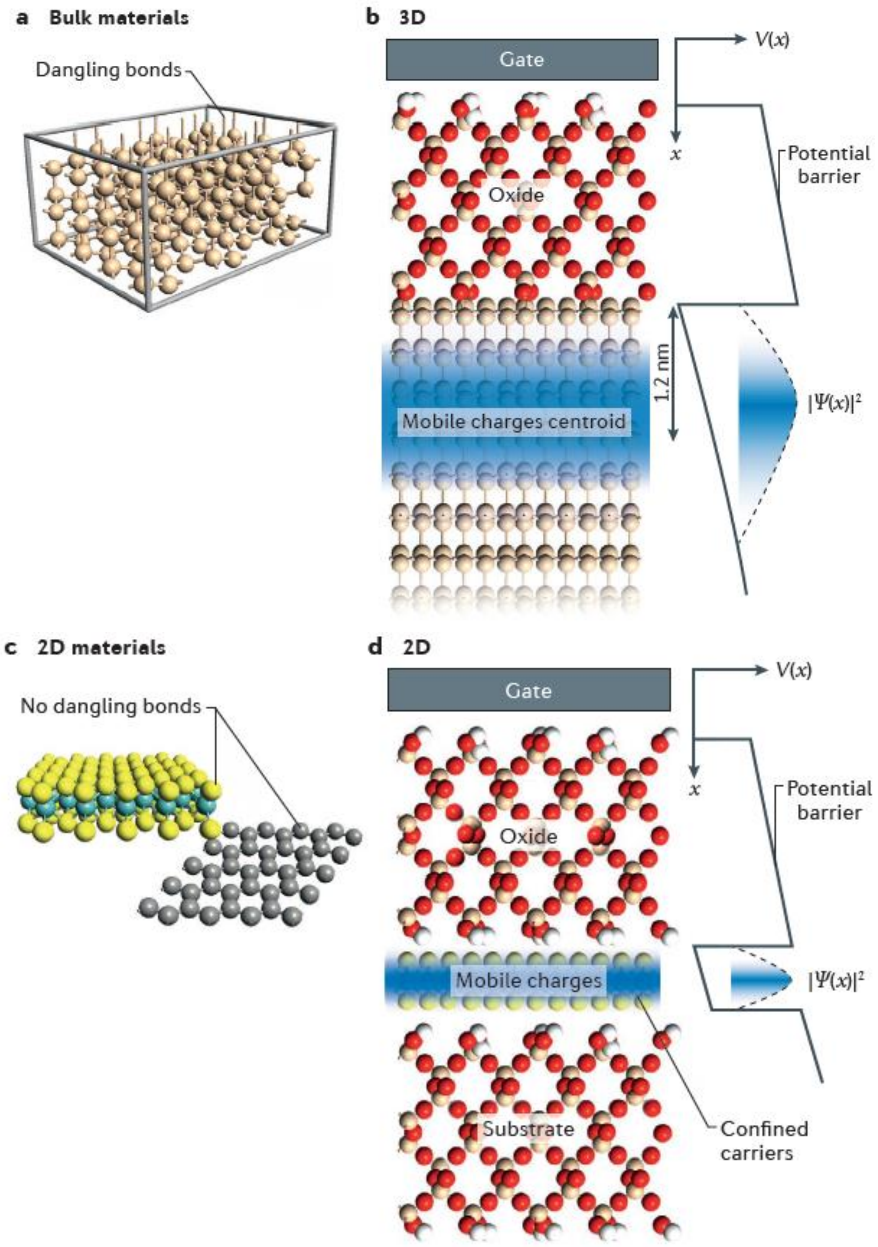

Figure 1-1. Advantage of 2D materials compared with 3D materials. (a) 3D (bulk) semiconductors reduce the performance of field-effect transistors (FETs) due to its dangling bonds that form traps for carriers. (b) Mobile charge distribution in 3D semiconductors and gate electrostatics. (c) 2D materials exhibit pristine surfaces. (d) In atomically thin materials, charge carriers are confined, resulting in a narrower mobile charge distribution. The confinement of charge carriers allows the mobile electrons to be easily controlled by the gate voltage[2].

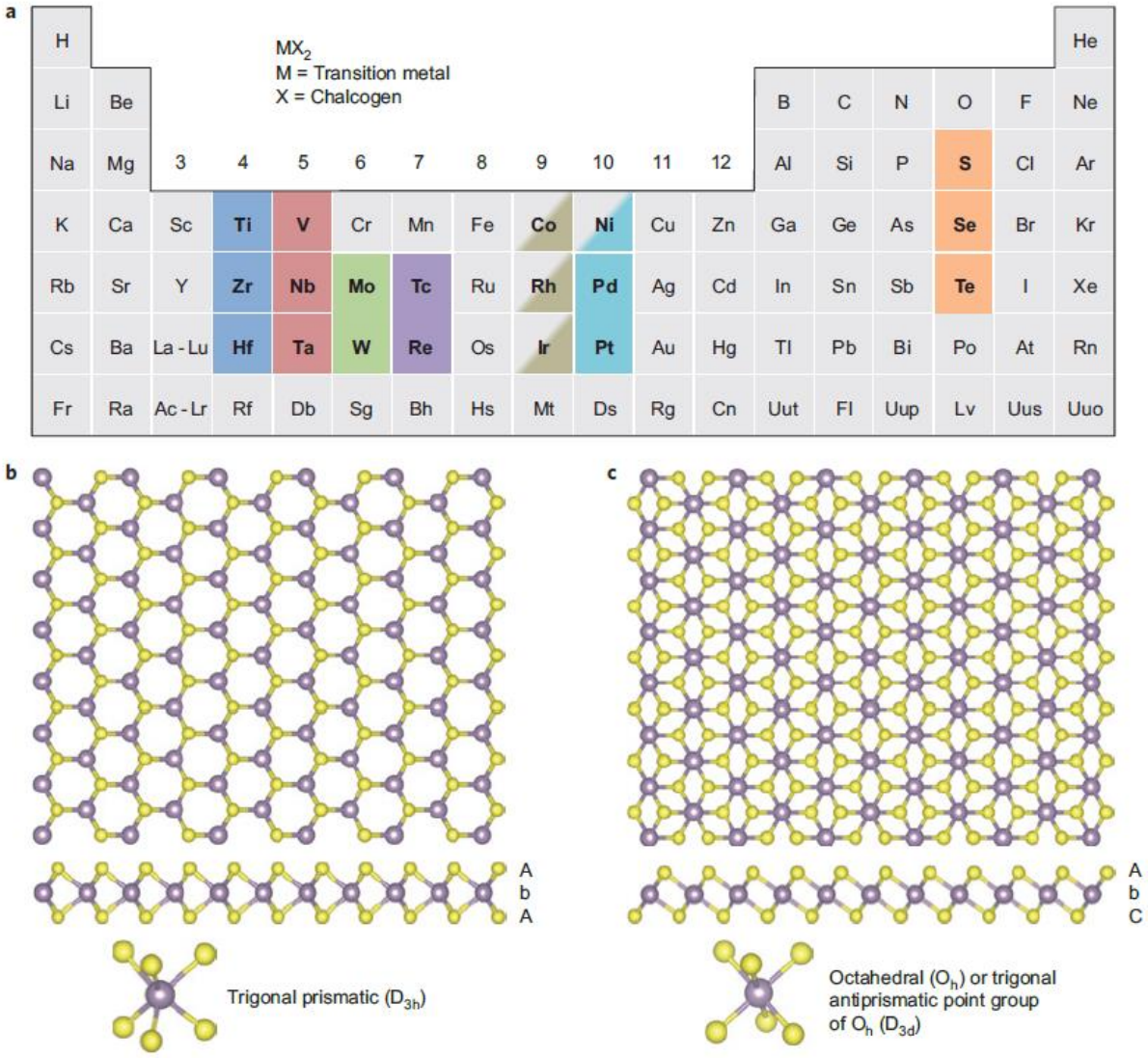

Figure 1-2. Structure of single-layered TMDs. (a) In the periodic table, the transition metals (M) and three chalcogen (X) elements that predominantly crystallize in those layered structure are highlighted. (b,c) c-axis and section view of monolayer TMDs with (b) trigonal prismatic and (c) octahedral coordinations (Atom colour code: purple- metal, yellow- chalcogen)[12].

Table 1-1. Comparison of the group-VI layered TMDs.

	Semiconducting TMDs					Semimetal TMDs	
Materials	**MoS_2**	**$MoSe_2$**	**$MoTe_2$**	**WS_2**	**WSe_2**	**$MoTe_2$**	**WTe_2**
Phase	2H (trigonal prismatic)					1T' (octahedral)	
Band gap	1.80	1.38	1.07	2.1	1.75	-0.20	-0.21
Mobility [$cm^2V^{-1}S^{-1}$]	0.01-200	0.01-23	5-12	12	7.3	10^3-10^4	
Spectral range	Visible, UV		NIR, Visible, UV	Visible, UV		THz, FIR, MIR, NIR, visible, UV	

1.1.2 Synthesis of TMDs

Low-dimensional TMDs have attracted significant attention due to their exotic properties associated with their defined dimensionalities. Due to unique electronic properties and high specific surface areas of low-dimensional TMDs, it has been seen as a promising and ideal candidates in various fields including optoelectronics, catalysis, flexible and wearable electronic devices. To achieve the practical applications mentioned above, developing controllable and scalable synthesis method of atomically thin or few-layer TMDs with layer controllability and large-area uniformity must be an essential requirement.

So far, lots of different ways have been developed[20-23], as presented in table 1-2. Until now, both *top-down* exfoliation and *bottom-up* synthesis methods are developed for preparation of atomically thin or few-layer TMDs.

Top-down exfoliation methods, such as mechanical exfoliation and chemical exfoliations, are method to separate single- or few- layers TMDs from their corresponding bulk TMDs. The individual layers of the 3D bulk material can be successfully separated from each other. This common top-down method have been studied widely, but there are some problems in obtaining reproducibility for large-area thin layers and difficulty to scale up.

Bottom-up methods may present alternative approaches. The chemical vapor deposition technique (CVD) has shown great promise to gain high-quality TMDs layers with a scalable size, controllable thickness. But they still need to be developed further to attain high-quality and large-area TMDs on the desired substrates. The large area and uniform synthesis of low-dimensional TMDs has remained a challenge for a long time. Table 1-2 also shows the conventionally used bottom-up synthesis methods and advantages/disadvantages of them. The synthesis methods include solid-precursor based vapor phase deposition, vapor phase chalcogenization, vapor-precursor based chemical vapor deposition. These scalable synthesis techniques enable to produce highly-crystalline large-area 2D TMDs crystals for wafer-scale and have tremendous potential for manufacturing in future nano-electronics.

Currently, most promising scalable synthesis technique is vapor phase deposition. In general, vapor phase deposition methods relies on physical transport (usually with inert carrier gases) and chemical reaction of vaporized precursors to deposit TMDs onto the desired substrate.

In terms of the initial precursor state, vapor phase deposition technique can be classified into solid- and gas-precursor based vapor phase technique. Firstly, there are two classes of solid-precursor based vapor phase deposition technique: (1) chemical vapor deposition (CVD) based on the reaction of solid-metal and chalcogen precursors, where both solid- metal precursors and chalcogen powders are heated into the vapor phase, and then transported to form TMDs layers; (2) chalcogenization of pre-deposited film based precursor, where the metal (or metal oxide) thin films are firstly deposited onto the substrates, then chalcogen powders are heated to be vapors and transported to the substrates to produce TMDs

films by conversion of the pre-deposited metal(metal oxide) film into TMDs films at the atmosphere of chalcogen vapors[24], as shown in figure 1-3a.

In addition, recent studies have also employed gas-precursors to improve the controllability during vapor phase growth. The reaction of gaseous metal and chalcogen feedstocks is illustrated in figure 1-3a. Here, the H_2 gas can be used for promoting the reduction of precursors. The desired substrates including SiO_2, quartz, mica and sapphire can be used (figure 1-3b) due to their high thermal stability and chemical inertness. The hexagonal crystal structure of quartz, mica and sapphire also helps to arrange the absorbed TMDs molecules.

Table 1-2. Table showing the different growth methods for layered TMDs.[1, 12, 19-24]

Technique		Schematics showing each technique	TMDs available to date	Achievements	Challenges
Top-down	Mechanical exfoliation	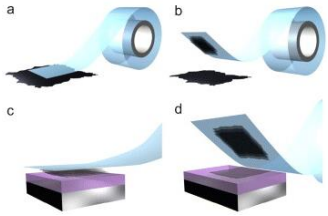	**Single phase TMDs** (MoX_2, WX_2, etc.)	High crystallinity	Thickness control, Yield, Not scalable
	Liquid exfoliation	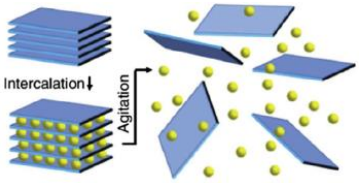		High productivity	Small crystallites, Thickness control, Yield
Bottom-up	Solid-precursor vapor phase deposition	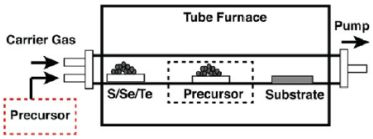	**Single phase TMDs** (MoS_2,$MoSe_2$,WS_2,WSe_2) **TMDs alloy** ($Mo_xW_{1-x}S_2$) **Doped TMDs** (Mn-, Co-doped MoS_2) **Hetero-structures** (MoS_2-WS_2,WS_2-BN MoS_2-graphene etc.)	High scalability, Hetero-structure availability	Defects, Stoichiometry control, Crystal quality
	Vapor phase chalcogen-ization	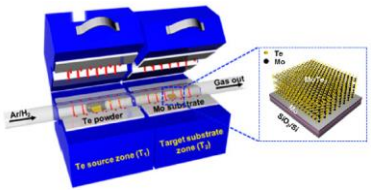	**Single phase TMDs** (MoS_2, $MoTe_2$,WSe_2 etc.) **Hetero-structures** (MoS_2-WSe_2-graphene)		Defects, Stoichiometry control, Crystal quality
	Gas-precursor vapor phase deposition	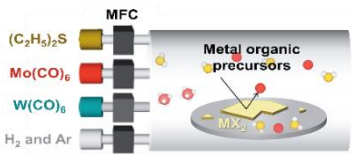	**Single phase TMDs** ($MoSe_2$,WSe_2)		Defects, Crystal quality

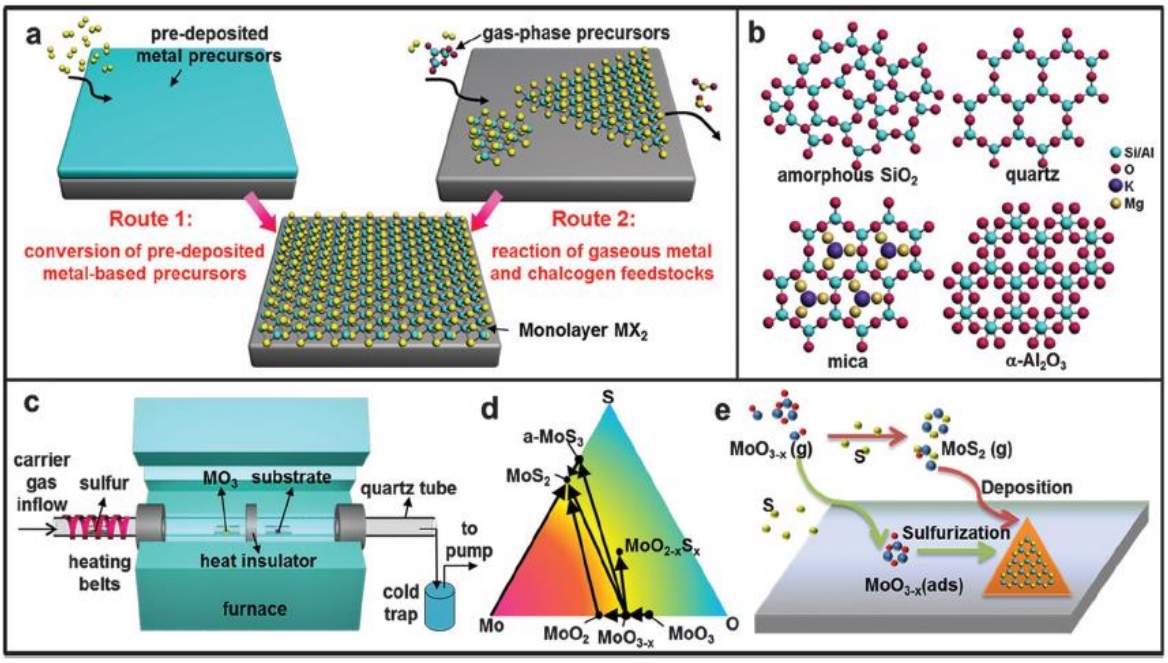

Figure 1-3. Introduction to the CVD synthesis of MX_2 thin layers. (a) Two routes for synthesis of MX_2. (b) Commonly used the insulating desired substrates for MX_2 growth. (c) Typical setup of a LP-CVD system. (d) Mo–S–O ternary phase diagram, in which the labelled arrows indicate reaction pathways for the CVD growth of MoS_2 from MoO_3 precursors. (e) Possible growth processes of MoS_2 by the reaction of S and MoO_{3-x}[24].

1.2 Tungsten ditelluride (WTe_2)

1.2.1 Introduction of WTe_2

Layered group-VI TMDs have been investigated widely because of its noticeable unique characteristics when thinned down from bulk to nanoscale. However, the semi-metallic TMDs such as tungsten ditelluride (WTe_2) and molybdenum ditelluride ($MoTe_2$) have not been examined relatively compared to the semiconducting TMDs. As shown in figure 1-4, the semi-metallic WTe_2 crystal exhibit a distortion of the octahedral 1T structure[25]. The tungsten atoms in the Td crystal structure are octahedrally coordinated by tellurium with alternating long and short distances between tungsten atoms due to strong intermetallic bonding. Even though $MoTe_2$ can have either 1T'- or 2H - phases and show the reversible structural phase transition by external stimulation such as strain and temperature[26-27], WTe_2 only crystallizes in distorted octahedral phase (1T' or Td) in nature among several polymorphs, regardless of growth condition and external strain.

It is found that WTe_2 has its stable energy in a distorted 1T (Td) structure and semi-metallic electronic characteristics[17, 28-29]. Figure. 1-5 shows the calculated band structure of 2H- and 1T'- WTe_2. While the 2H-phase WTe_2 has an indirect 0.702 eV bandgap, 1T'-WTe_2 has small overlap of electron and hole pockets at the Fermi energy along the Γ direction (corresponding to the a-axis, along the tungsten chains in crystal), indicating its semi-metallic properties. Figure. 1-6 shows the representative x-ray diffraction (XRD) patterns of WTe_2 experimentally grown by chemical vapor transport method, with the theoretical XRD patterns of 1T'- and 2H- phase WTe_2.

The semi-metallic properties of WTe_2 can be confirmed directly by using temperature-dependent resistance measurements. In general, the resistivity of a metal decreases linearly as the temperature decrease. Regarding the resistivity of metal at zero kelvin, there are only scattered electrons caused by crystal defects such as grain boundaries, impurities, etc. In semiconductor, the resistivity decreases at the elevated temperature induced by excitation of carriers. Therefore, characterization of temperature-dependent resistivity allows us to recognize whether the materials is a semiconductor or metal. Figure. 1-7 exhibits the typical temperature-dependent resistivity of layered WTe_2 crystal with different thickness, showing a well-metallic behavior of WTe_2 on temperature dependence. Moreover, extraction of residual-resistivity ratio (RRR=ρ_{300K}/ρ_{oK}) is a good indicator of crystal quality, the relationship between the electrical mobility and RRR is indicated[30], in figure 1-8.

The vibrational behavior of WTe_2 can be explored by using the incident photon energy via Raman spectroscopy[31]. Raman spectroscopy measurements is an useful technique as the fingerprint recognition

for confirming the existence of the material and assuming its thickness of WTe_2, already commonly used in the research of graphene and other 2D materials. Figure 1-9 (a) shows the representative Raman spectra of WTe_2, as a function of its thickness. The Raman spectrum of WTe_2 shows four main peaks approximately at 118, 134, 164, and 212cm^{-1}, and they are noted as the A_1^3, A_1^4, A_1^7 and A_1^9, respectively. The simulated lattice vibration of the Raman modes in bulk WTe_2 is illustrated in figure 1-9b, as well.

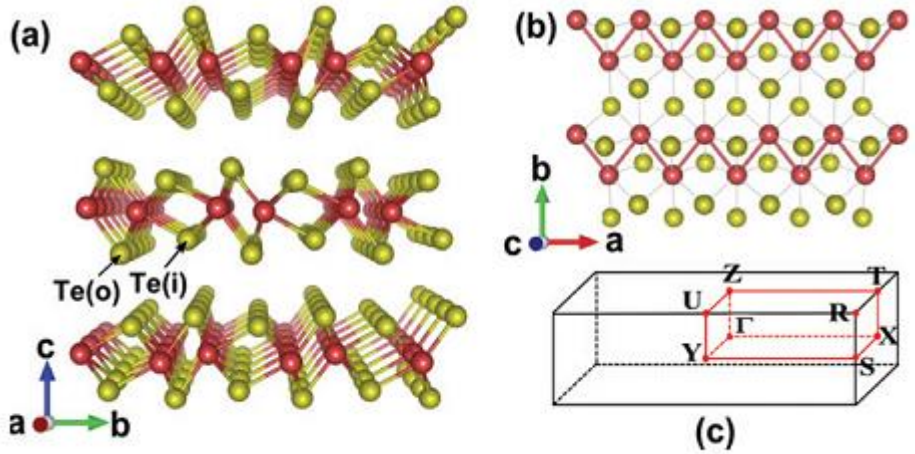

Figure 1-4. Crystal structure of WTe_2 viewed along (a) the a-axis (parallel to the zigzag W-W chains) and (b) the c-axis (perpendicular to the stacked layers); (c) the corresponding Brillouin zone. The red and yellow balls represent W and Te atoms, respectively[25].

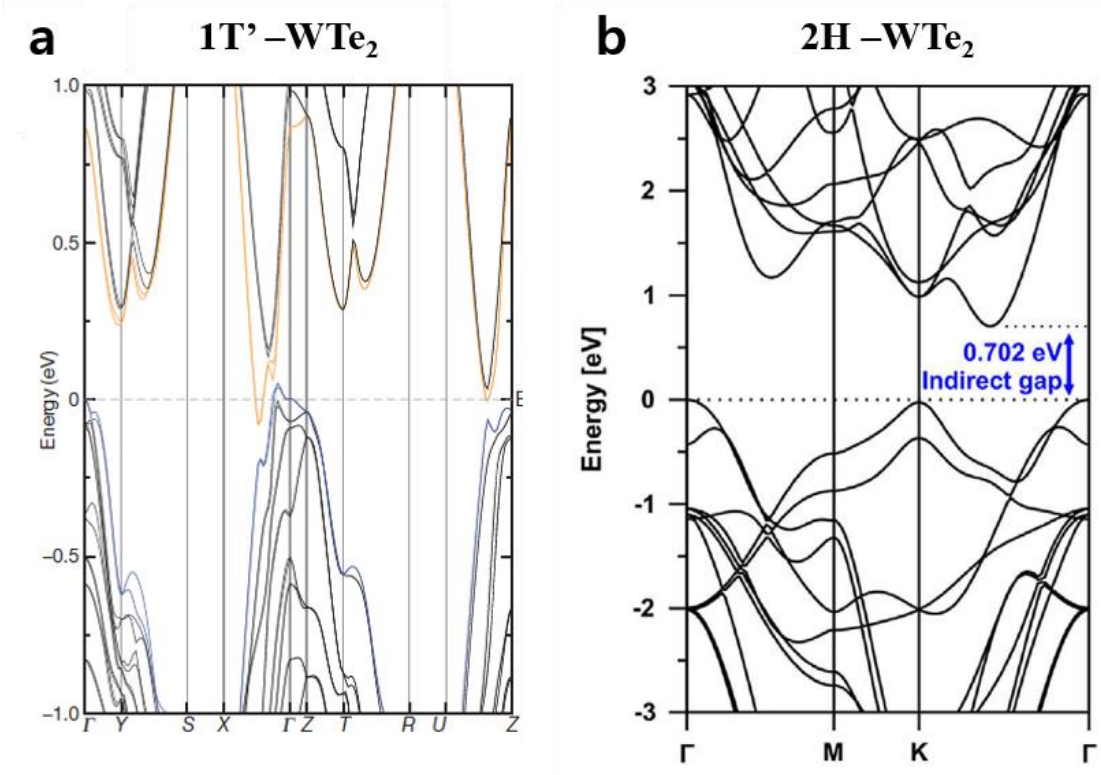

Figure 1-5. The electronic band structures indicate that bulk WTe_2 (a) in the 1T' phase has a 0.21 eV band overlap and (b) in the 2H structure has an indirect 0.702 eV bandgap[17, 28].

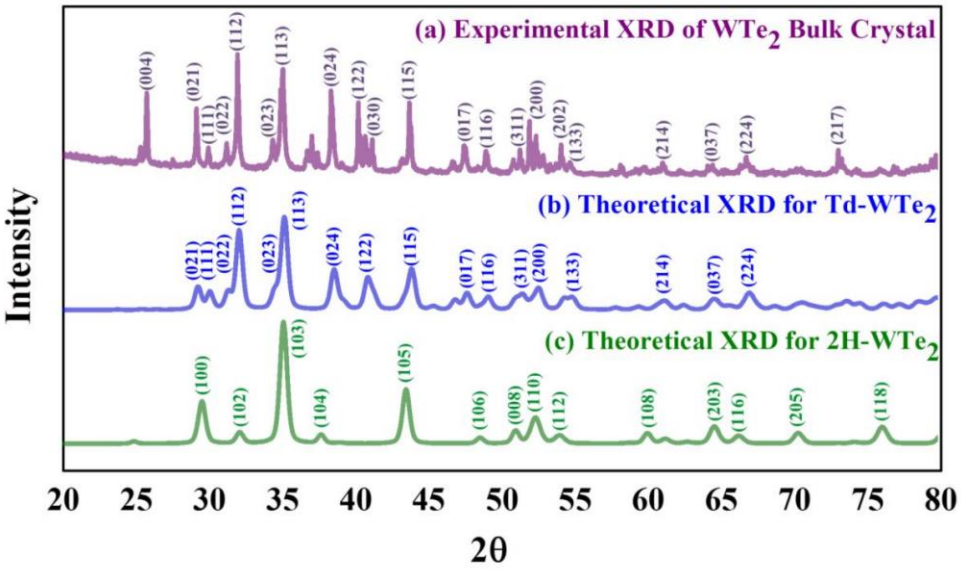

Figure 1-6. The representative X-ray Diffraction Patterns (XRD) for (a) experimental WTe_2 bulk crystal; (b) theoretical 1T' (or Td) WTe_2; (c) theoretical 2H-WTe_2[28].

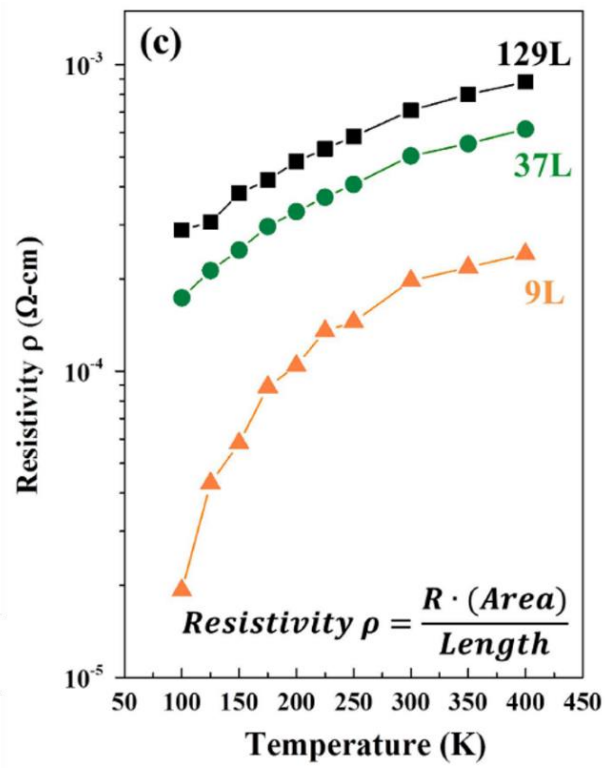

Figure 1-7. The temperature-dependent resistivity depending on the WTe_2 layer thickness, showing the WTe_2 is metallic in nature (resistivity proportional to temperature) rather than the semiconducting behavior[28].

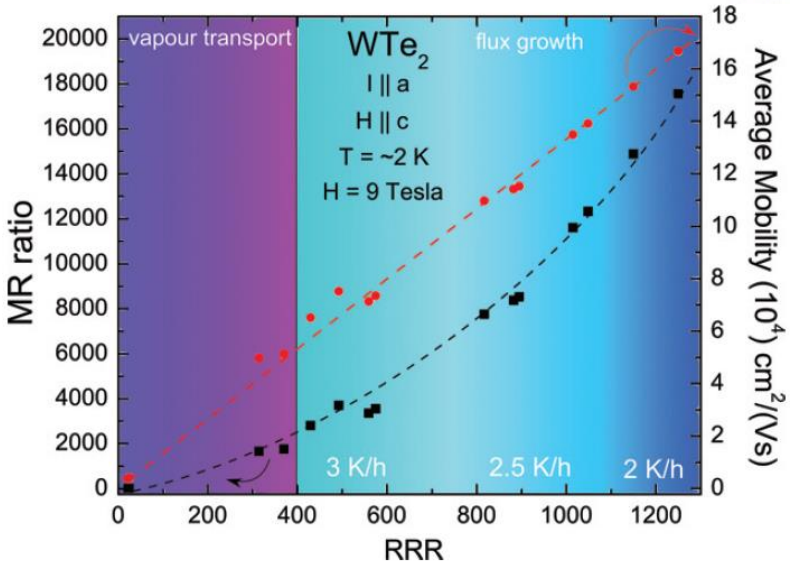

Figure 1-8. MR ratio and average carrier mobility vs. RRR. MR ratio follows the left axis (black squares) while μ_{avg} follows the right axis (red circles)[30].

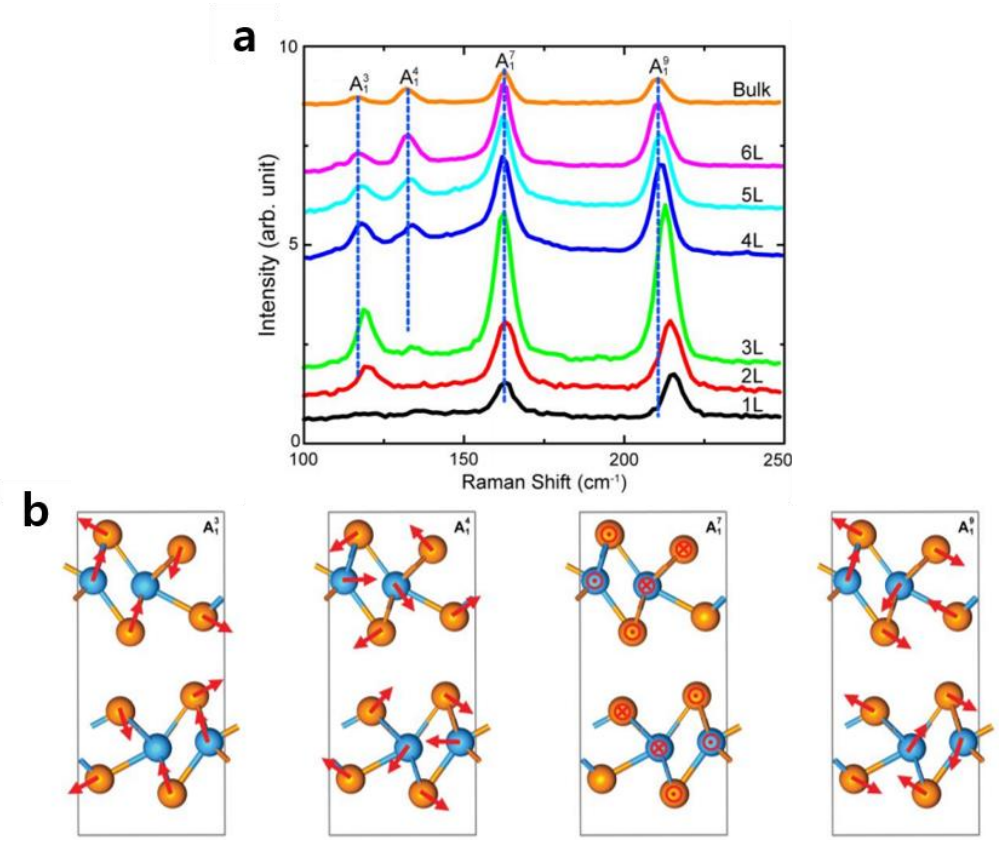

Figure 1-9. (a) The Raman spectra of and mono- to six-layer and bulk WTe_2. The blue dashed lines indicate the frequencies of the Raman modes in bulk WTe_2; (b) Atomic illustration for the lattice vibrations of the Raman modes in bulk WTe_2[31].

1.2.2 Conventional Synthesis Methods of WTe_2

Many researchers have tried several growth techniques for making the WTe_2 crystal either in bulk and nanoscale form, but synthesis of nanostructured-WTe_2 has not been reported yet, in contrast with any other TMDs.

Currently, single-crystalline WTe_2 in bulk form has been synthesized by chemical vapor transport methods or solid state reaction, and these methods produce only bulk crystal[17,28,32,39,40]. Previously, most of the studies on WTe_2 crystal have been demonstrated in mechanically or chemically exfoliated layers (flakes) from the bulk crystal. Accordingly, investigation of WTe_2 with controlled its thickness has been limited. Moreover, these methods are highly unsuitable for mass production because a high growth temperature (~1000°C) and growth time for several days (usually more than 24 hours) must be required, as shown in Table 1-3.

Synthesis of nanostructured-WTe_2 was very challenging due to the high vapor pressure (low sublimation temperature) of tellurium and low reaction activity of tungsten with tellurium. In chemical vapor deposition process, the probability of creating nucleation sites is extremely low because of the Te deficiency because desorption of tellurium vapor precursors occurs easily. For these reasons, making the Te-rich condition is critical to synthesize WTe_2 nanostructures. To obtain stoichiometric and nucleate tungsten ditelluride crystal, desorption of tellurium vapor precursor must be prevented and activate tungsten atoms to be reacted with tellurium precursor.

Table 1-3. Conventional growth methods of WTe_2 single crystal, only obtaining bulk crystal.

Growth method	Crystal Type	Growth temperature	Growth time	Transport agent	References
Chemical Vapor Transport	bulk	950°C	7 days	Br_2	[28]
	bulk	890°C	4 days	WCl_6	[32]
	bulk	750°C	7 days	Br_2	[17]
Solid state reaction	bulk	1100°C	96 hr	None	[39]
	bulk	1000°C	5hr	None	[40]

1.2.3 Unique Properties of WTe_2

1.2.3.1 Large & Unsaturated Magnetoresistance (MR) in WTe_2

The investigation of WTe_2 has been attracted significant attention since an unusual magnetoresistance (MR) in WTe_2 crystal was discovered in 2014. Mazhar N. Ali et.al[17] reported the observation of an extremely large positive magnetoresistance: 13 million percent at 0.53 kelvins in a magnetic field of 60 T (Teslas), as displayed in figure 1-10.

MR is defined as a change in material's electrical resistance (ρ) in response to an applied magnetic field H and is expressed as $\mathrm{MR} = [\rho(\mathrm{H}) - \rho(0)]/\rho(0)$. The large MR can be observed also in other semimetals such as bismuth and graphite because of the compensated hole-electron resonance; however, the unsaturated MR in WTe_2 up to 13,000,000% at 0.53 K in an applied magnetic field of ~60T is quite unique. This extraordinary MR behavior in WTe_2 is known to originate from a nearly perfect compensation of electron and hole concentrations (first known material for nearly perfect resonance) and this is explained by two band model for magneto-transport in semimetals. In two band theory, the MR is given by as follows:

$$MR = \frac{\Delta\rho}{\rho} = \frac{\rho_{xx}(B) - \rho_{xx}(0)}{\rho_{xx}(0)} = \mu_e \mu_h B^2 \ (if\ n = p)$$

, where μ_e and μ_h is the mobility of the electrons and holes, respectively, and B is the applied magnetic field (n=p, where n and p are the electron and hole concertation, respectively)[32].

In semimetals, large positive magnetoresistances are attributed to a balanced electron–hole 'resonance' condition; the positive MR is proportional to B in nearly perfectly compensated semimetal of WTe_2. In this regard, it is expected that WTe_2 has potential to be applied in magnetic field sensing device with extremely high sensitivity, especially at low temperatures, as displayed in figure 1-11.

1.2.3.2 Type-II Weyl fermion in bulk WTe_2

Interestingly, the existence of new type of Weyl point (type-II Weyl point) in WTe_2 was discovered[35]. Whereas Weyl semimetals hosting Weyl fermions were previously recognized to have Weyl point with a point like Fermi surface (referred as type-I)[36], the Weyl point appears at the contact of hole and electron pocket in type-II Weyl semimetal. The new type-II Weyl points exist at the boundaries between hole and electron pockets, as illustrated in figure 1-12. The existence of type-II Weyl fermion at the

boundary between hole and electron pockets in new phase of matter in WTe_2 crystal are expected to explore new physical properties and phenomena arising in the new topological semimetal phase (being different to those of standard Weyl semimetals with point-like Fermi surface) and as a potential platform for the realizing novel Weyl semimetal applications.

1.2.3.3 Quantum spin Hall effect in Nanostructured WTe_2

Layered WTe_2 are layered compounds that can be mechanically exfoliated, therefore very promising for achieving stable 2-dimensional QSH phase. A Monolayer 1T′-WTe_2 was predicted to be quantum spin hall (QSH) semi-metallic materials with QSH gaps[37]. Feipeng Zheng et.al revealed that computational and experimental results all point to one clearly promising possibility, that monolayer 1T′- WTe_2 is a QSH insulator with a positive band gap[38]. In figure 1-13, optical measurements (transient reflection experiment, optically probed transient carrier dynamics) are performed on ultrathin 1T′- WTe_2 layer, showing a systematic increase in the interband relaxation time as the number of layers decreases. Electro-transport characteristics of the sample also exhibits Schottky barrier in atomically thin samples, which is absent for thicker samples, as indicated in figure 1-14. These independent pieces of evidence clearly indicate that monolayer 1T′-WTe_2 is a truly 2D QSH insulator, but further researches should be conducted more.

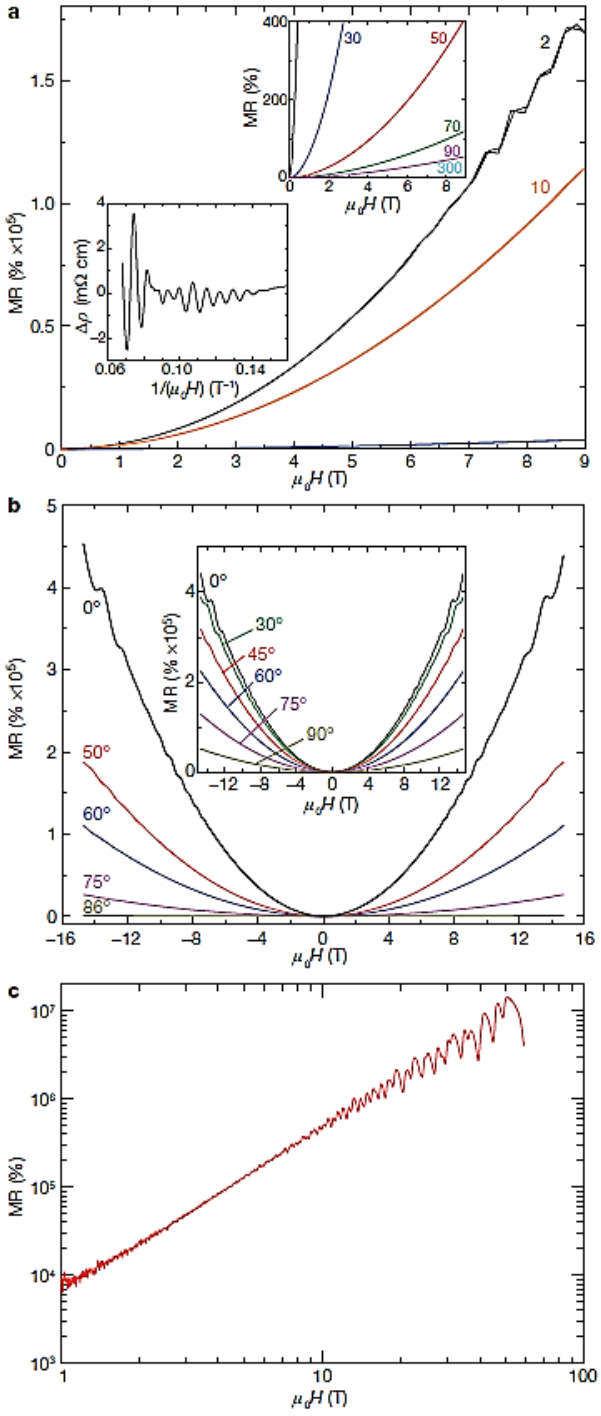

Figure 1-10. Field and angular dependence of the XMR in WTe_2 crystal. (a) Field dependence of the XMR in WTe_2 with the current along the a-axis (W–W chains) and the applied field parallel to the c-axis. (b) Angular dependence of the XMR in WTe_2 crystal at 4.5K. (c) XMR of WTe_2 up to 60 T at 0.53 K, with I parallel to a-axis and H parallel to c-axis[17].

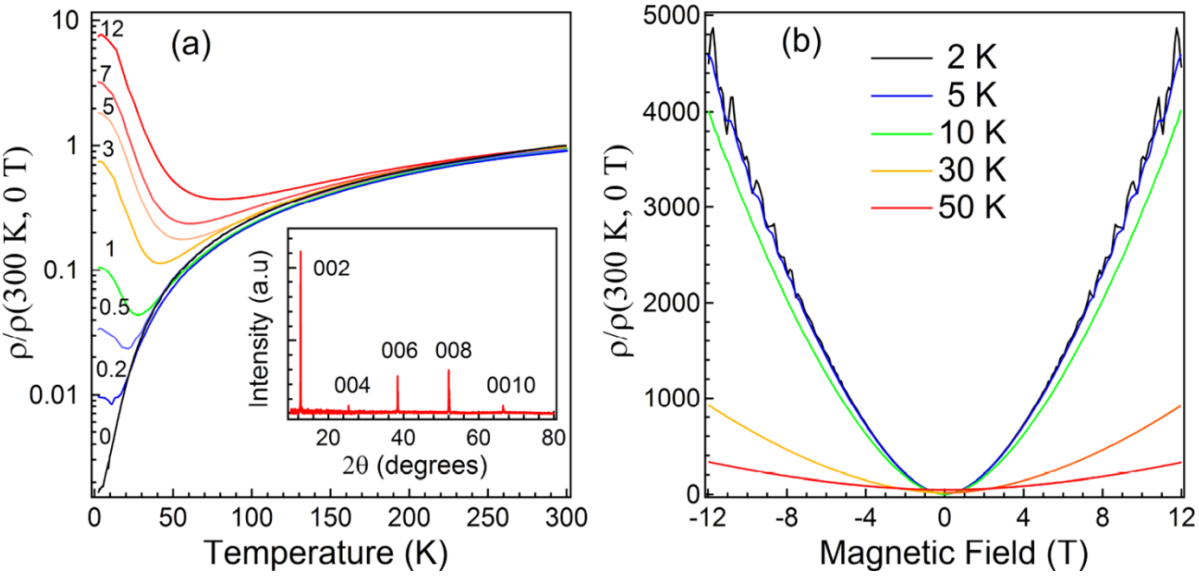

Figure 1-11. Temperature and field dependence of the MR in WTe_2, with the current along the W–W chains (a-axis) and the applied field parallel to the c-axis. (a) Normalized resistivity (at 300K and 0 T) as a function of temperature, with different magnitudes of the external magnetic field. (b) MR of WTe_2 at different temperatures[34].

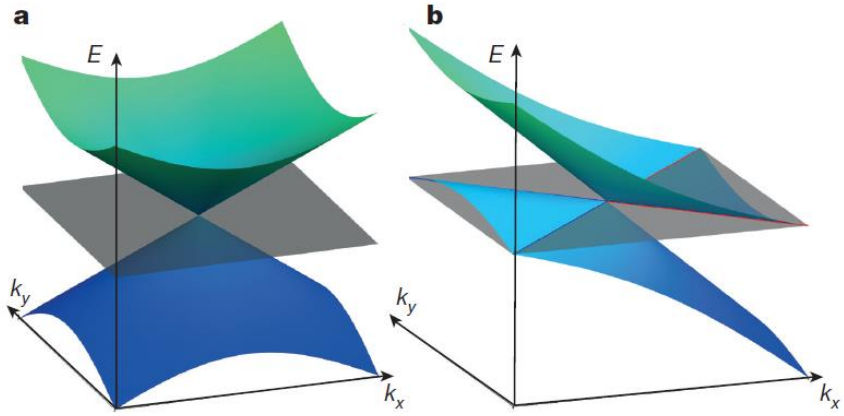

Figure 1-12. (a) Type-I Weyl point with a point-like Fermi surface, (b) A type-II Weyl point appears as the contact point between hole and electron pockets. The grey plane is the position of the Fermi levels[35].

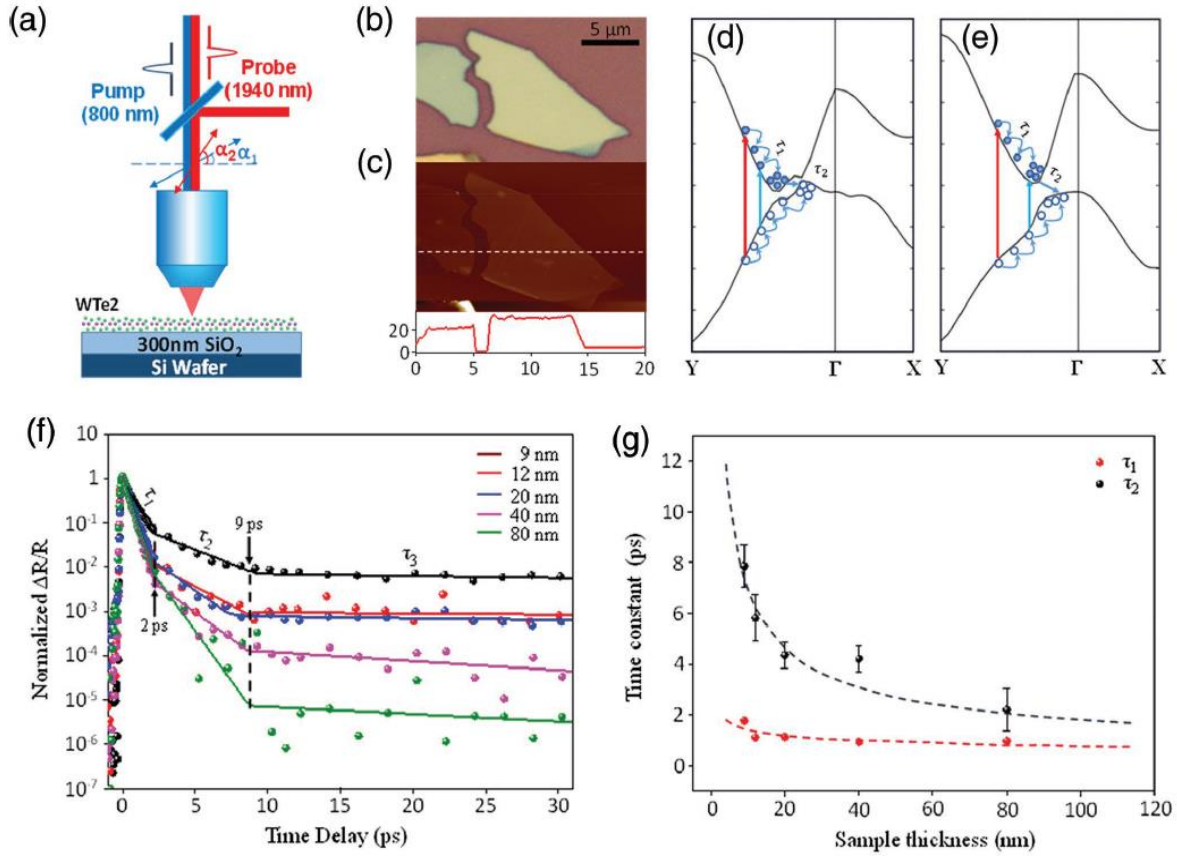

Figure 1-13. Experimental data of optical measurements of QSH nanomaterial WTe_2. (a) Schematic diagram of transient reflection experiment. (b) The OM Image and (c) AFM Image of a WTe_2 used with thickness of 20 nm. Schematic band diagram and carrier relaxation dynamics of (d) bulk and (e) monolayer 1T′-WTe_2 crystal and pump (blue) & probe (red) photon transition configuration. (f) The normalized transient reflection spectrum of 1T′-WTe_2 with different thicknesses. (g) τ_1, τ_2 as functions of the sample thickness[38].

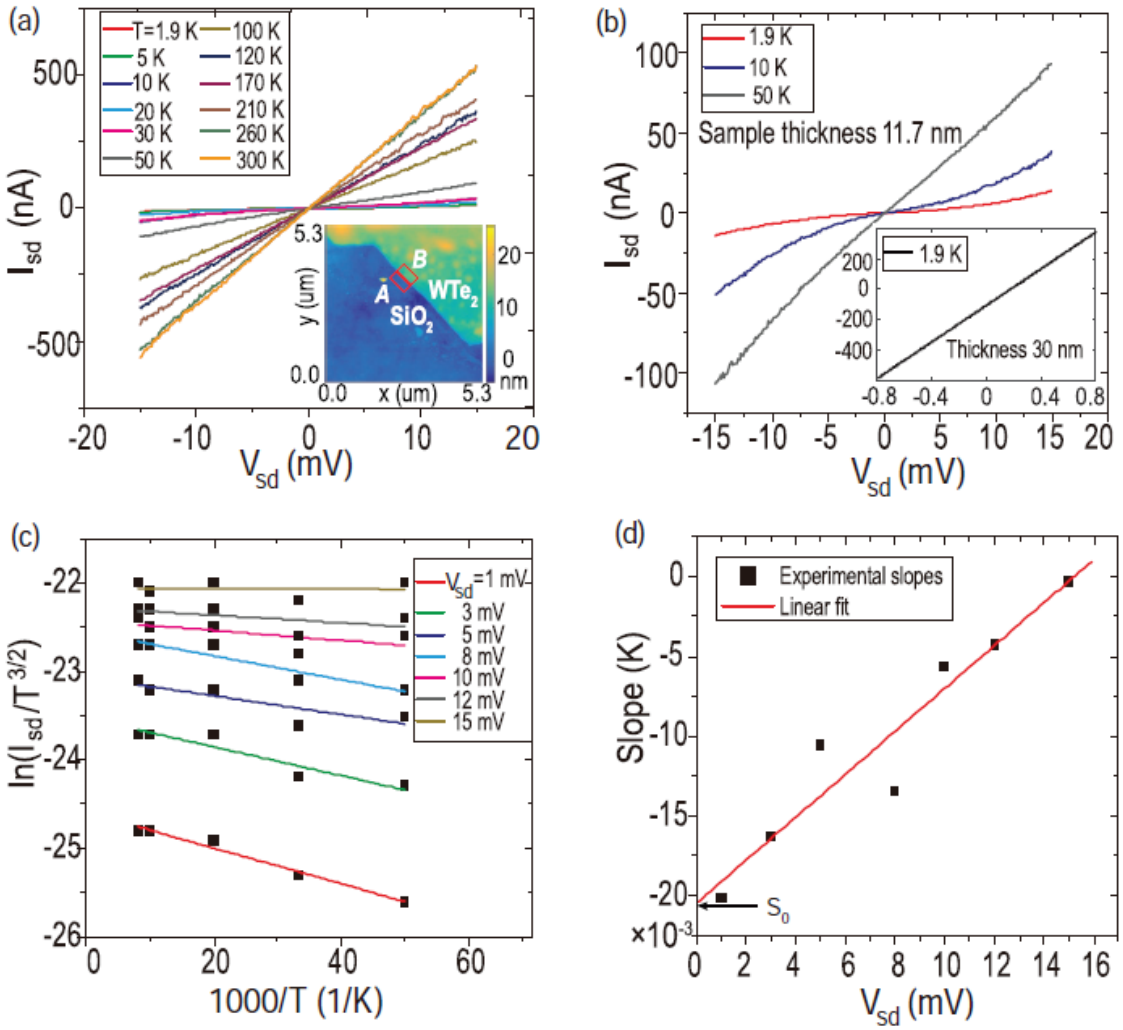

Figure 1-14. Experimental data of (a) I–V curves of an 11.7 nm thick 1T′-WTe_2 sample from 1.8 to 300 K and (b) three low temperatures (1.8, 10, 50 K). (c) Arrhenius plot of ln ($I_{sd}/T^{3/2}$) versus the inverse of temperature and linear fits. (d) Slopes of linear fits in (c), S_0 suggests the value of Schottky barrier of the 1T′-WTe_2 device[38].

1.3 Preceding Researches on Eutectic Metal Alloy Assisted Crystal Growth

Here, some previous researches for the crystal growth by means of eutectic metal alloys are introduced. In this growth mode, the reaction between gas precursors and pre-deposited metal catalyst would make liquid state eutectic alloys above its eutectic temperature. This as-reacted liquid eutectic alloy will have catalytic effect, assisting synthesis of desired nanostructures from the supersaturated liquid eutectic phase. This fundamental principle has been widely used in nanowires' fabrication via the vapor-liquid-solid (VLS) mechanism. Moreover, eutectic metal alloy assisted synthesis of WS_2 and WC nanostructure were investigated, showing the possibility of applying this growth mode to make nanostructured WTe_2. Therefore, review of the preceding researches on eutectic metal alloys assisted nano-crystal growth for low-dimensional nanostructure is very important.

1.3.1 Vapor-Liquid-Solid (VLS) Growth

Figure. 1-15 shows a schematic of the conventional VLS synthesis mechanism for 1D structured nanowire. Since the *vapor* precursor, *liquid* state alloy, and *solid* nanowires are involved in this mode, thus this growth mechanism is called as the VLS (vapor-liquid-solid) process. In this VLS growth mechanism, the pre-deposited metal catalyst forms droplets of a liquid state metal alloy by reacting with supplied vapor precursors (eutectic reaction) over the eutectic temperatures. At the elevated temperature, the vapor flux is absorbed into the catalytic liquid metal alloys to supersaturation level, holding the higher concentration of precursor elements originally from the gas source. Then, crystal growth can subsequently occurs at the vapor-liquid interface, precipitating out supersaturated solid 1D-nanowires. To be specific, the liquid state eutectic metal alloy can act as vapor flux reservoir and nucleation helper of nanowires. Nanowires can be grown only in the areas activated by the metal catalysts and the size and position of the nanowires are determined by that of the metal catalysts.

Previous researches demonstrate that metals which encounter the requirements for pre-deposited metal catalysts can be used in the VLS mechanism[41]. First, these metals must react with gas precursor and then form a liquid solution. Secondly, the equilibrium vapor pressure of the catalyst over the liquid alloy should be small, so the droplet does not vaporize during growth.

The most widely researched VLS process is a growth of Si nanowire assisted by Au particles which adsorb Si from the vapor state. Figure. 1-16 shows the phase diagram of Au-Si system. Here, the eutectic point is 364^{o}C, which means that this VLS process is conducted at elevated temperature over the eutectic temperature, resulting in the formation of supersaturated liquid alloy withheld pure solid elements that can be precipitated out. Au can form a solid-solution with Si (concentrations up to 100%) until reaching

a supersaturated state of Si in Au (the composition of liquid Au-Si alloy track the liquidus line). Consequently, Si atoms precipitate out of the supersaturated liquid state metal alloy droplet at the liquid-alloy/solid-Si interface, resulting that crystal growth can subsequently occur from the nucleated seeds.

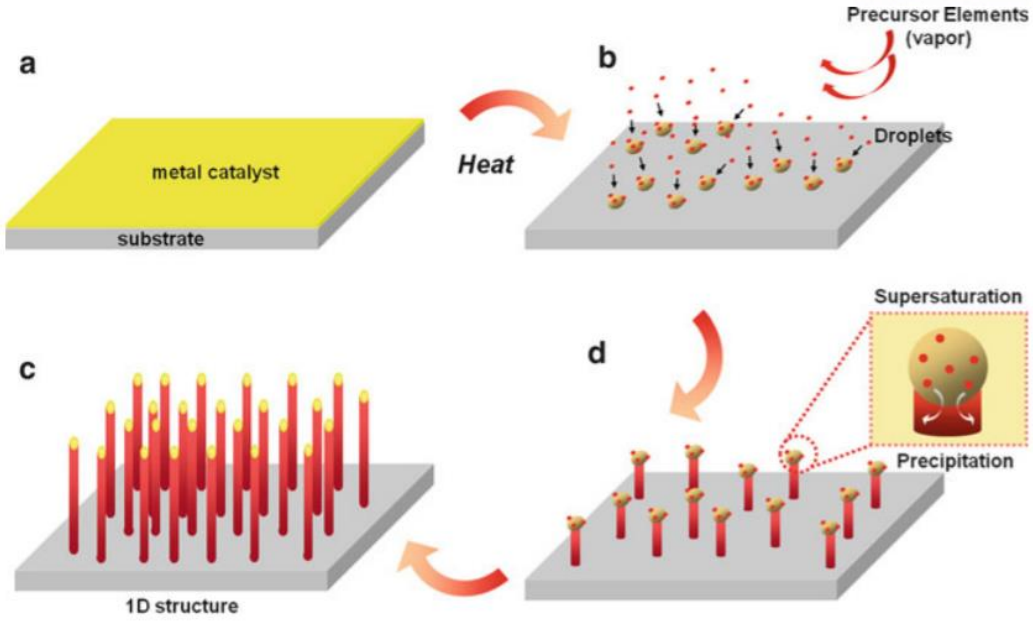

Figure 1-15. Growth of 1D nanostructures by VLS mechanism[41].

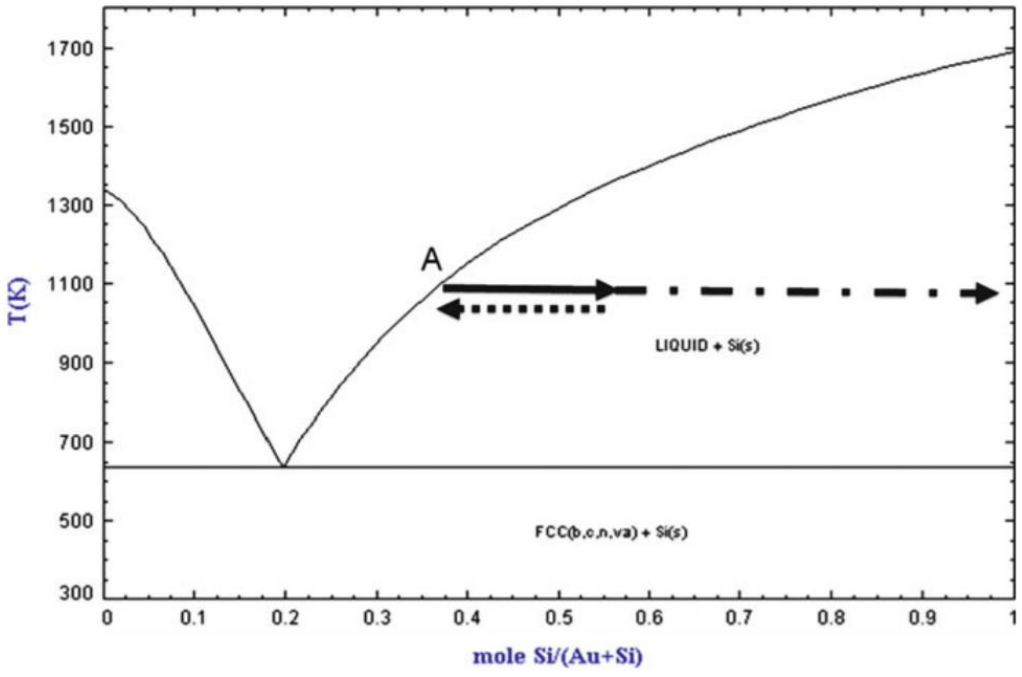

Figure 1-16. Phase diagram of Au–Si system which indicates the composition of liquid metal alloy catalyst in the course of growth of 1D nanostructures by VLS mechanism[41].

1.3.2 Rapid-Crystallization

The nickel sulfide (NiS_x) assisted crystal growth of WS_2 films has been reported[42,43]. The WS_2 films were prepared by the amorphous-solid-liquid-crystalline-solid (aSLcS) rapid-crystallization process from a Ni–S eutectic metal alloys. The mechanism was explained by the recrystallization induced by formation of liquid phase nickel sulfide droplets above the Ni-S eutectic temperature of 637˚C. The method of nickel sulfide promoter-assisted crystallization from the liquid phase could be powerful preparation technique for highly (001) textured WS_2 thin films with large crystallites (lateral dimensions of several micrometers), which are mainly oriented parallel to the substrate. This crystallization by the amorphous solid-liquid-crystalline solid rapid-crystallization process which is comparable with the vapor–liquid–solid (VLS) mechanism, displayed in figure 1-17.

First, amorphous WS_{3+x} was deposited onto Ni coated oxidized silicon substrate and then the substrate was heated. When the eutectic temperature of the Ni–S (T_{eu} = 637 °C) system is reached, the NiS_x crystallites become liquid state and dissolve tungsten or tungsten sulfide. When supersaturation is reached, the crystallization of the WS_2 starts at the bottom of the NiS_x droplets, leading to rapid lateral growth of WS_2 nanosheets. During the aSLcS process, a phase separation between WS_2 and NiS_x crystallites occurred, where the WS_2 crystallizes from the NiS_x:W melt. After cooling, the liquid NiS_x droplets crystallize and mainly float on top of the WS_2 nanosheets. This as-grown nanosheets can be clearly seen in the cross-sectional SEM image displayed in figure 1-18.

.

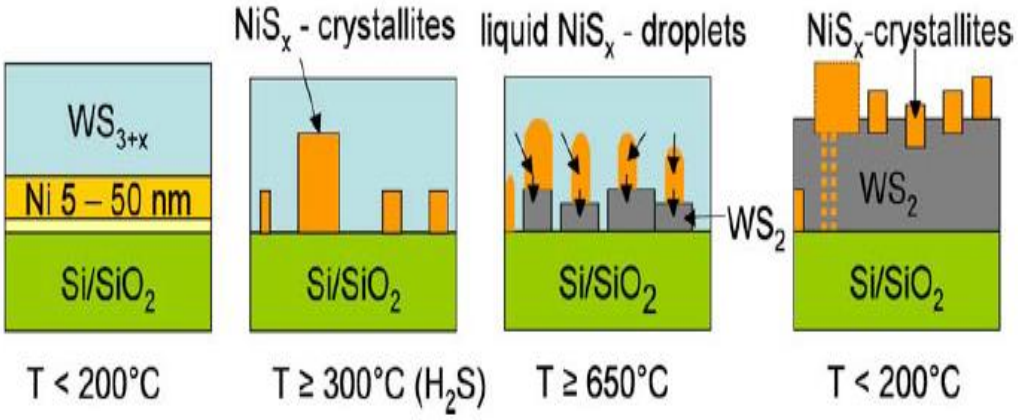

Figure 1-17. Schematic of the steps of the rapid crystallization of WS_2 by the amorphous solid-liquid-crystalline solid (aSLcS) process[42].

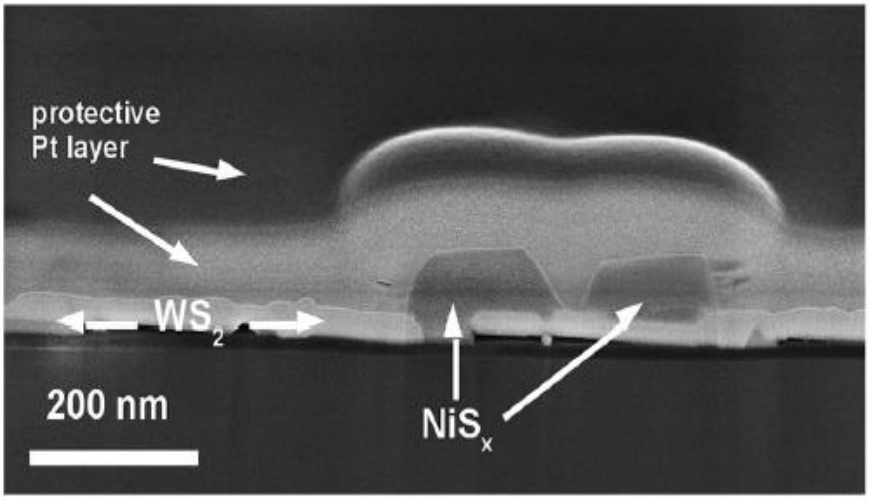

Figure 1-18. Cross-sectional SEM image of a rapidly crystallized WS_2 film. Preparation parameters: 300nm WS_{3+x}/20 nm Ni/SiO_2/Si substrate, annealed at 700˚C for 5 min[43].

1.3.3 Eutectic Solidification

A novel method to prepare low-dimensional WC nanostructure such as nanowire and nanowalls has been developed[44]. To realize the synthesis of WC nanostructure, the most serious obstacle which must be overcome is that W atoms must be provided during the growth of WC nanostructure. The key approach for supplementation of W atom is eutectic solidification in W-Al-C solution, which means a precipitation of W and C atoms in ternary W–Al–C. The active temperature of W atoms can be decreased in an W–Al environment. Transportation of C atoms through the atmosphere and W atoms enable the supplementation of W resources to be continuous through the melting liquid across the whole process. Large-scale WC nanowalls with a thickness of tens of nanometers with several micrometers in the other two dimensions were obtained through the bottom-up growth, as shown in figure 1-19. In addition, 1-D WC nanostructures can be obtained in suitable conditions.

In this work, WC nanostructures were grown on polycrystalline tungsten substrate at 1310˚C in CH_4, H_2 ambient. In detail, Al sheets were placed neared the tungsten foil. During the annealing step, Al atoms would be evaporated onto the W substrate continuously at temperature higher than 660˚C, leading to formation of eutectic metal alloys (W atoms melts in Al liquid). Continuous supplementation of Al and W atoms keeps the metal alloys in liquid state as a W-Al eutectic metal alloys. Over the temperature at 1000˚C, carbon source is introduced into the chamber from CH_4 cracking and would diffuse into the liquid, forming ternary alloys of W–Al–C. The growth of the WC nanostructures can be attributed to the eutectic precipitation in W–Al–C solution. Interestingly, there exists a solute convection area because W is supplied from bottom to top and C from top to bottom. The formation of WC nanostructure was induced by nucleation at the convection area and precipitation. The details of growth model are shown in figure 1-20.

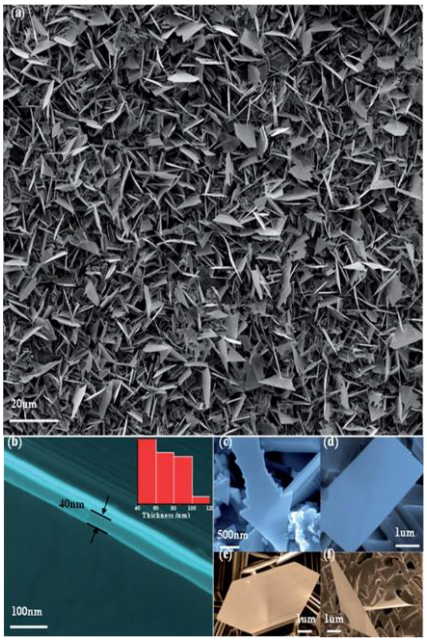

Figure 1-19. Scanning electron microscopy analysis of WC nanowalls structure. (a) Typical SEM image of as-synthesized WC nanowalls. (b) Thickness characterization of the nanowalls. (c–f) Various polygons can be found among the synthesized nanowalls but the main shape is triangle[44].

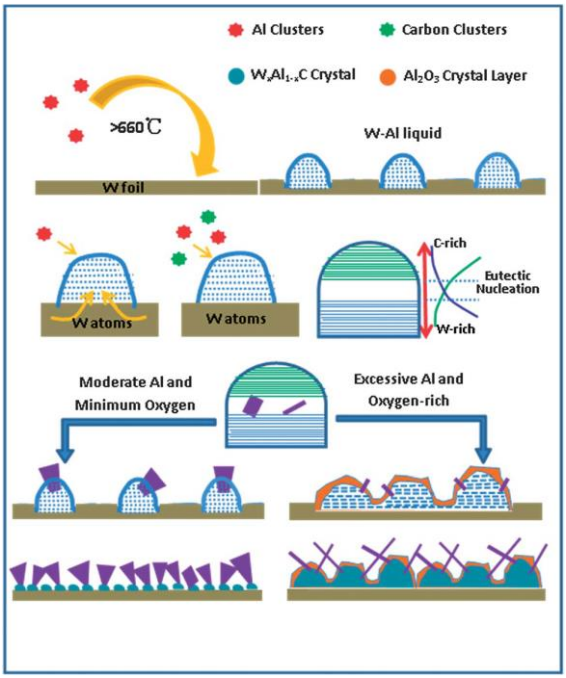

Figure 1-20. Growth model proposed for synthesis of low-dimensional WC nanostructures. The active temperature of W atoms decreased in an Al–W environment[44].

Chapter 2. Experimental Details

2.1 Deposition of Metal Films

In this study for synthesis of transition metal telluride nanostructures, we deposited 50nm-thick copper layer on a 300 nm SiO_2/Si substrate by using UHV e-beam evaporator (UEE-UHV series, ULTECH) to form eutectic metal alloys. To minimize environmental impurities and copper oxide layer on the copper film surface, the copper film was prepared in UHV main chamber, using high-purity copper solid source (99.99% Cu pellet) for deposition. Then, the tungsten layer (thickness was various depending on the experiments. e.g. 20, 100, 200, 300nm) was deposited by DC magnetron sputtering (SRN-120, SORONA) in optimized deposition condition (uniformity: less than ± 5 % within wafer). Figure. 2-1 displays the UHV e-beam evaporator and DC magnetron sputtering system used in this work.

In this work, we proposed the new type of structure of a W/Cu deposited metal layer for growth of WTe_2 nanostructures which is the inverse structure of essential structure (a Cu/W film) in previous research. In previous research, a Cu film was deposited on the pre-deposited W layer onto desired substrates (SiO_2/Si or Al_2O_3), followed by tellurization of the Cu/W/substrate at 500°C in Te atmosphere using Te powders with inert Ar gas, forming Te-rich copper telluride (Cu_xTe_y)/WTe_2/W/substrate and finally etching away Cu_xTe_y to obtain WTe_2 nanostructures on the W/substrate, as illustrated in figure 2-2.

The surface morphology of as-deposited poly-crystalline W(20nm)/Cu(50nm) was confirmed by SEM (S-4800, Hitach High-Technologies), as displayed in figure 2-3a. The size of W crystalline was confirmed by using Scherrer equation (crystalline size: ~20nm). Figure 2-3b exhibits XRD data of W(20nm)/Cu(50nm) films deposited on SiO_2/Si substrate. Moreover, feasibility of synthesis for $MoTe_2$ nanostructure as a member of the layered TMDs family was evaluated through our methods. The sample for synthesis of $MoTe_2$ nanostructure was prepared in the same way as above (Mo layer of 300nm was deposited and thickness of Cu layer was fixed).

2.2 Synthesis Methods

First of all, a W/Cu (or Mo/Cu) film deposited on SiO_2/Si was placed in a crucible containing tellurium powder (Product 264865, Aldrich). Secondly, the chamber in our furnace system (DMTF 12/150-HVAC, Daemyoung Enterprise) was evacuated to ~ 10^{-3} Torr and then filled with Ar gas to maintain atmospheric pressure and protect the system from oxygen. Figure 2-4 shows a schematic drawing of the chamber in our furnace system. The furnace was subsequently heated up to 500-600 °C and then tellurium powder

was evaporated to vapor and transported to the sample. Next, the W/Cu film is tellurized after absorption of tellurium vapor at the pre-deposited film. Here, the conversion of the pre-deposited copper films into liquid state Te-rich copper tellurides (Cu_xTe_y) droplets occurs at the atmosphere of tellurium vapors. The crystallization of nanostructures inside of Te-rich Cu_xTe_y droplets takes place at a temperature of 500 °C, above the Cu–Te eutectic temperature of 340 °C (see figure 2-5). This model describes the growth of a liquid-phase crystallization from Cu_xTe_y droplets as a role of the nucleation helper for the crystal growth of the WTe_2 and $MoTe_2$ nanostructure. Lastly, the chamber was cooled down to RT (room temperature) under atmospheric condition.

2.3 Preparation of Transition Metal Telluride Nanostructures on the Desired Substrate

First of all, in order to expose the as-synthesized transition metal telluride nanostructures in Cu_xTe_y droplets, the Cu_xTe_y droplets must be removed. For this to occur, the as-grown sample was dipped in 1M of APS (ammonium persulfates) aqueous solution for 1hr to etch the Cu_xTe_y droplet. After that, the sample was rinsed with deionized water to remove residual etchant. Through the wet etching process, we can simply get tellurides nanostructure without Cu compounds. However, the use of oxidant etchant and water induce inevitable chemical damage, leading to critical oxidation and degradation of as-synthesized products.

The as-obtained nanostructures can be easily transferred to different substrates and/or solutions by using conventional dispersion method. The nanostructures were dispersed in isopropanol (IPA) through a sonication process. Then, nanostructures were placed on the desired substrate by dispersion method and the substrate was dried at 80 °C for 10min using a hot plate. In this process, the disadvantage is that the as-synthesized nanostructures could be broken and damaged due to physical attacks during the sonication process.

To sum up, the intrinsic properties of as-synthesized nanostructures could be degraded by inevitable chemical and physical damage. In addition, fabrication of various applications has difficulties due to residue products. So-called “coffee ring effect” could be a critical problem as well, which is caused by capillary flow induced by the differential evaporation rates across the drop during the conventional dispersion methods.

To solve the problems, our approach is to mechanically peel off the Cu_xTe_y and metal layer (W and Mo layer) by using scotch tape, as shown in figure 2-6. To expose the as-synthesized nanostructures inside of the Cu_xTe_y droplets without use of chemical oxidant (APS etchant), we tried to peel off Cu_xTe_y droplets and W layer by using scotch tape. Figure 2-7a indicates the as-obtained WTe_2 nanobelts onto

desired substrate without additional chemical etching and transfer steps. This simple method of mechanical peeling off by using scotch tape can reduce the process to obtain nanostructures as well as prevent degradation of WTe_2.

2.4 Fabrication of Electronic Device

For the measurements on electrical properties of as-synthesized WTe_2 and $MoTe_2$, conventional nano-fabrication techniques (electron-beam lithography, metals evaporation and lift off) were employed to attach electrical contacts (consisting of Ti/Au bilayers, typically used 10/80 nm thick), as shown in figure 2-7b. Throughout the procedure of crystal identification and device fabrication, care was taken to minimize exposure of the material to air in order to minimize degradation. The electrical properties of WTe_2 samples with different thicknesses were investigated. The current was applied along the tungsten chains along the tungsten zigzag chains (a-axis) of WTe_2 nanostructure. Also, $MoTe_2$ was tested using two Ti/Au contacts made by a lift-off process at both edges of the synthesized $MoTe_2$ nanostructure.

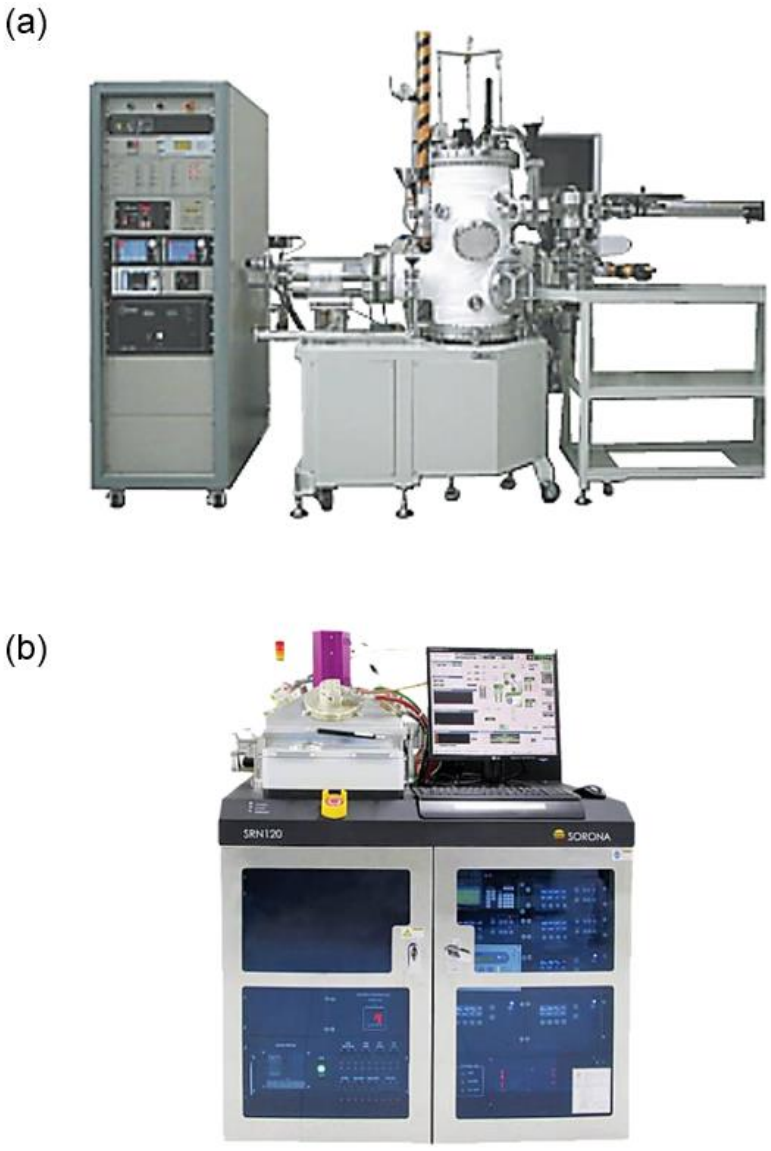

Figure 2-1. (a) A UHV e-beam evaporator system (UEE-UHV series, ULTECH) used in this work for preparation of the metal (Cu) films. (b) A DC sputter system (SRN-120, SORONA) used in this work for deposition of W (and Mo) layer.

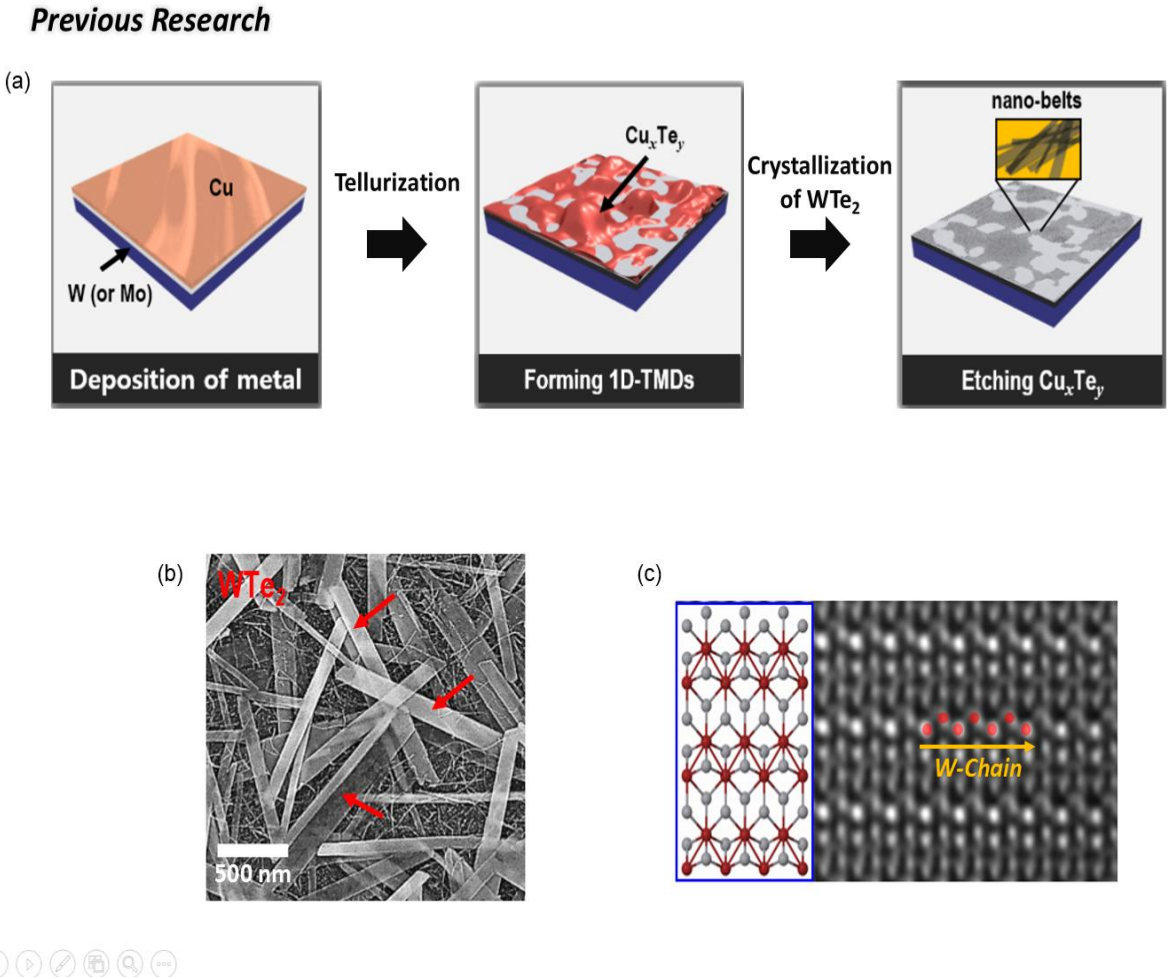

Figure 2-2. Introduction of previous research. (a) Schematic diagrams of the elementary steps for growing 1D-TMDs and obtaining WTe_2 nano-belts. In this process, a Cu film deposited on a W layer plays a key role as the Te vapor flux reservoir and promotor of improving crystallinity. Representative (b) SEM Image and (c) TEM image of the synthesized-WTe_2 nano-belts.

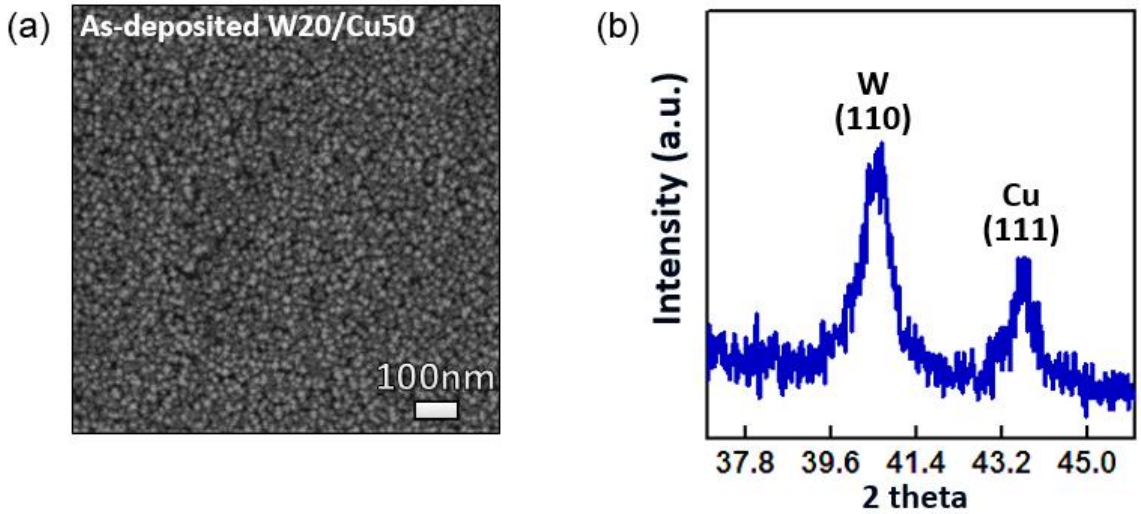

Figure 2-3. (a) Representative SEM Images of surface morphology of poly-crystalline W20/Cu50 films deposited on Sio_2/Si substrate. (b) XRD pattern for the W20/Cu50 films deposited on Sio_2/Si substrate. The size of W crystalline is within 20nm verified by using Scherrer equation.

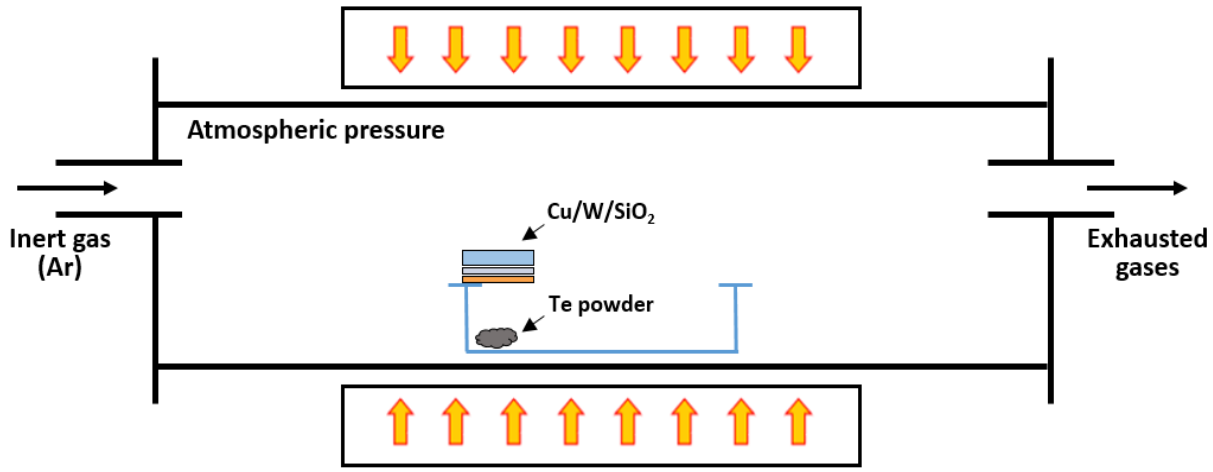

Figure 2-4. Schematic drawing of the chamber in our furnace system (DMTF 12/150-HVAC, Daemyoung Enterprise) for growth of WTe_2 nanostructures. The chamber was evacuated to ~ 10^{-3} Torr and then filled with Ar gas to maintain atmospheric pressure and protect the system from oxygen

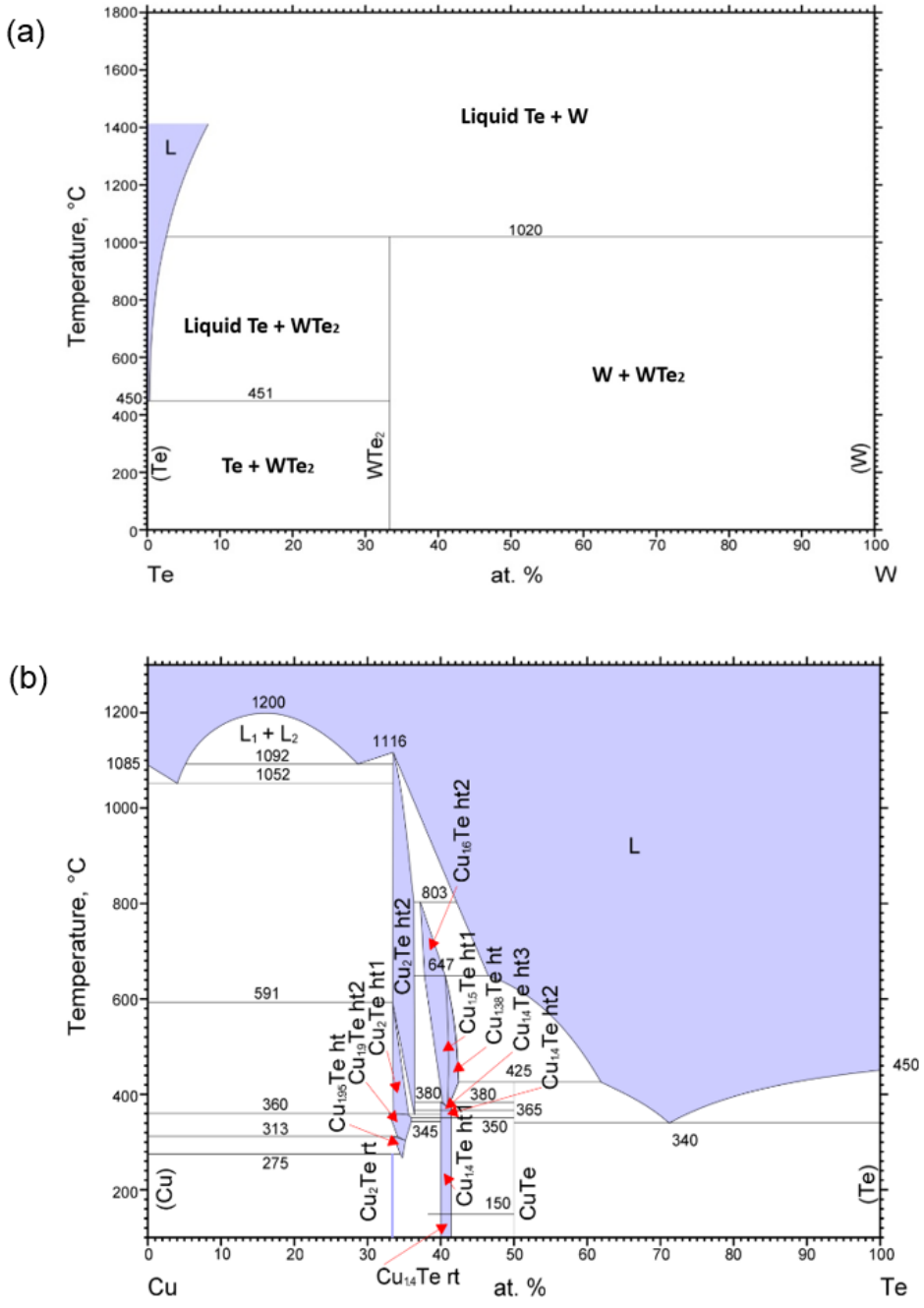

Figure 2-5. Phase diagrams of (a) the W-Te system (b) the Cu-Te system (From ASM Alloy Phase Diagram Database).

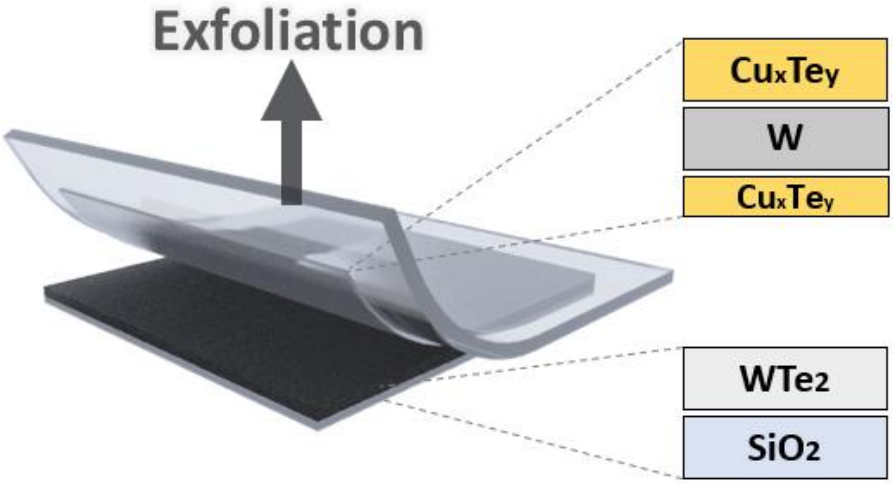

Figure 2-6. Schematic image of method of mechanical peeling off using scotch tape. The simple method of peeling off using scotch tape can reduce the whole process to form WTe_2 nanostructures on the desired substrate.

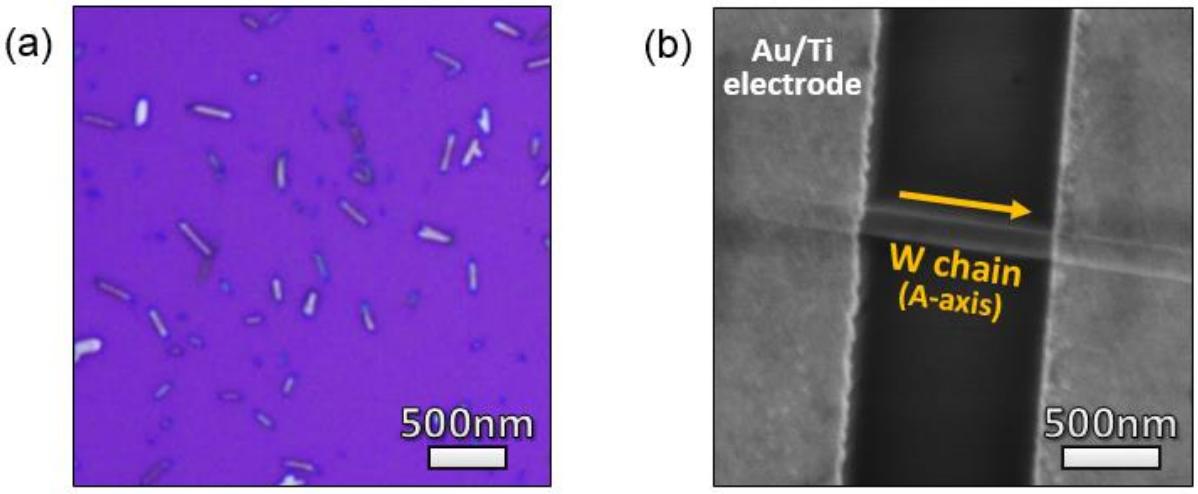

Figure 2-7. (a) Representative OM Image of as-synthesized WTe_2 nanostructures onto the desired substrate by peeling W and Cu_xTe_y droplets off using scotch tape. (b) SEM Image of fabricated WTe_2 nanostructures device, showing the channel (with current along the a-axis of W-W zigzag chains, lengths of 1μm) perpendicular to Au/Ti electrode.

Chapter 3. Results and Discussion

3.1 Role of Eutectic Metal Alloys for Synthesis of WTe_2

Previously, most of the studies on tungsten ditelluride (WTe_2) have been demonstrated in mechanically exfoliated layers from bulk crystal. Therefore, the development of direct synthesis of high quality few-layer WTe_2 is essential to study the emergent properties of nanostructured WTe_2 and for large-scale applications.

So far, a single- or few-layer WTe_2 has only been prepared by mechanical exfoliation from bulk crystals which are synthesized by chemical vapor transport method, usually conducted at high temperatures over 700˚C for several days. The products are poor-crystallinity crystals, and are limited to only large bulk-type crystals with millimeter scale. The high vapor pressure of tellurium and low chemical reaction activity of tungsten with tellurium make synthesis challenging. To obtain stoichiometric WTe_2 crystals, it needs to hinder desorption of tellurium vapor precursor and activate tungsten atoms to be reacted with tellurium atoms. To overcome these problems, we suggested a novel method for the growth of the WTe_2 nanostructure. Using our method, we can directly obtain the desired WTe_2 nanostructures with nano-scaled thickness and high quality. In comparison to conventional chemical vapor transport methods, our method requires a lower growth temperature & shorter time, which is good for mass production and novel applications.

To solve the challenge in tellurization of tungsten films and obtain stoichiometric WTe_2, our key approach is the eutectic metal alloy assisting mechanism. When above the copper-tellurium eutectic temperature, the diffused copper atoms react with tellurium vapor, resulting in the formation of Cu_xTe_y liquid state droplets holding tellurium vapor as a role of vapor flux reservoir. In addition, in liquid state Cu_xTe_y droplets, tungsten atoms from the interface between the W layer and droplets were activated to be reacted with Te. Consequently, WTe_2 crystals can be nucleated (and crystallized) in liquid-phase eutectic metal alloys. The crystal of WTe_2 grew as anisotropic nano-belts due to its intrinsic 1T'-pahse, compared to other 2H-TMDs. In short, we obtained the desired high quality single-crystalline WTe_2 nanostructures inside of the Cu_xTe_y droplet.

In this research, we proposed a method using new type of structure of deposited a W/Cu metal layer on SiO_2/Si substrate that is the inverse structure of the essential structure in our previous research (Cu/W/SiO_2/Si). We deposited the copper layer on the desired substrate (SiO_2) and then conducted the deposition of W layer. This work should be studied in terms of the different morphology of Cu_xTe_y

droplet depending on synthesis parameters as well as growth conditions.

Figure 3-1 indicates as-grown Cu_xTe_y droplet on W layer via SEM Images. The W and pre-deposited Cu layer with thickness of 100nm was used as a standard process condition. To identify the Cu_xTe_y droplet, the Raman and EDAX analysis of the droplet was carried out. The Raman spectra shows that all the measured Raman shifts indicate tellurium, at 140, 189, 224, 270 cm^{-1}. And, the Te-rich Cu_xTe_y droplet was confirmed by the EDAX analysis. We confirmed that, by introducing the pre-deposited copper layer, the Cu_xTe_y droplet was formed. Interestingly, the Cu_xTe_y droplet was observed on the surface of W layer, penetrated through the W layer, although the Cu layer was deposited under the W layer. This suggests that diffusion of copper atoms into W layer occurs through the grain boundary of the W layer. Then, diffused copper atoms would combine with the Te vapor precursor, resulting in formation of Cu_xTe_y droplets at the surface of the W layer. Another view of this phenomena is that the penetration of liquid state Cu_xTe_y through the W layer, following the formation of liquid state Cu_xTe_y over the eutectic temperature (~394°C) under the W layer, but the further study needs to be done for the mechanism confirmation. The morphology of as-grown Cu_xTe_y droplets are shown via SEM, displayed in figure 3-2. And Raman, EDAX spectra and its composition are shown in figure 3-2, corresponding the red circle in figure 3-2 (b).

The Cu_xTe_y was fully etched by dipping into Ammonium Persulfate (APS) etchant for 1hr. At the same site where the Cu_xTe_y droplet was located, we observed as-synthesized WTe_2 nanostructures on the W layer. This was confirmed by Raman analysis, and corresponds to the red circles in the figure 3-3, indicated at 163, 211 cm^{-1} of Raman shift. In addition, to check the composition and stoichiometry of the as-synthesized nanostructure which was transferred onto Al_2O_3 substrate to prevent main peak from overlapping with other signals, EDX analysis was carried out. This corresponds to the red point in the inset image. The indicated main elements of the synthesized nanostructures are tungsten and tellurium. The EDX analysis result indicates that the as-synthesized WTe_2 is highly stoichiometric with a W : Te ratio of 1:2. The use of Te-rich eutectic metal alloys eliminates the Te deficiency in the resulting products and the contamination by impurities encountered with vapor deposition process. As a result, the as-synthesized WTe_2 nanostructures are highly pure, stoichiometric, and structurally uniform.

To sum up, the growth mechanism of WTe_2 was explained by the assistance of liquid Cu_xTe_y droplets, after oversaturation with dissolved tungsten, induced a WTe_2 crystal growth.The crystallization takes place at a temperature of ~500 °C, slightly above the Cu–Te eutectic temperature of 340°C. A liquid-state eutectic metal alloy from the promoter metal (Cu) and Tellurium is formed, which dissolves tungsten up to its solubility limit. When the solubility limit is reached, the excess WTe_2 rapidly

crystallizes out of the Cu_xTe_y droplet, leading to the formation of these highly (002)-textured WTe_2 nanostructures. Particularly, the as-synthesized WTe_2 nanostructures can be easily transferred to different substrates and/or solutions for further applications. Figure. 3-3 show that the as-synthesized WTe_2 nanostructure can successfully be transferred to desired substrate using conventional dispersion method. Our optimum process condition for obtaining WTe_2 nanostructures with a thickness in few-nanometers is a tungsten layer with a thickness of 20nm and a copper layer with a thickness of 50 nm, grown at 500°C for 10min with supplement of Tellurium from Te powder of 0.1g. The thickness distribution was measured by AFM profile. The average thickness of obtained WTe_2 nanostructures was measured to be 54±15 nm, shown in figure 3-3. Figure. 3-4 clearly show the XRD pattern of highly (002)-oriented single crystalline tungsten ditelluride texture. After transfer of WTe_2 nanobelts from W surface to desired substrate (SiO_2) using conventional dispersion methods, XRD measurement was performed, displayed in figure 3-4.

.

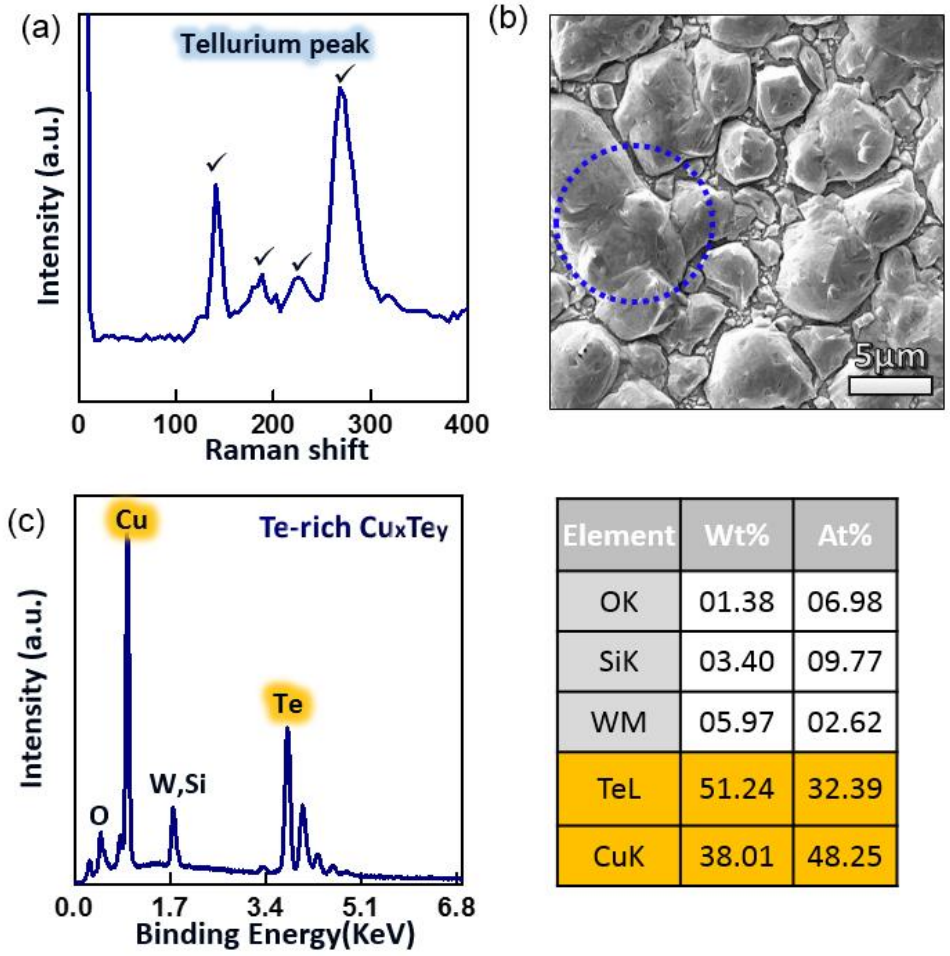

Element	Wt%	At%
OK	01.38	06.98
SiK	03.40	09.77
WM	05.97	02.62
TeL	51.24	32.39
CuK	38.01	48.25

Figure 3-1. (a) Raman spectra, corresponding to the colored blue spot in (b) image, identifying tellurium-rich Cu_xTe_y eutectic metal alloys. (b) SEM Image of tellurium-rich eutectic metal Cu_xTe_y alloys on W layer. (c) EDAX spectra, corresponding to the colored blue spot in (b) image.

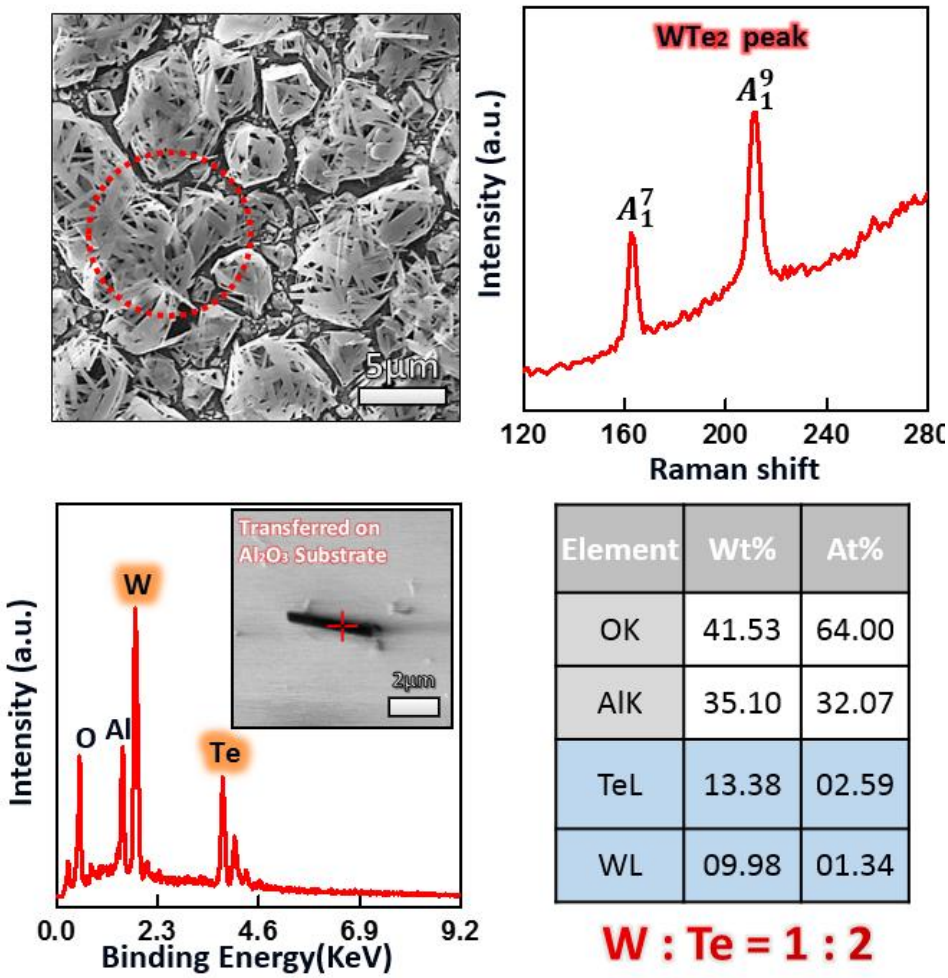

Figure 3-2. (a) Raman spectra, corresponding to the colored red spot in (b) image, identifying as synthesized-WTe_2. (b) SEM Image of as-synthesized WTe_2 nanostructures on W layer. (c) EDAX spectra, corresponding to the colored red spot in (b) image.

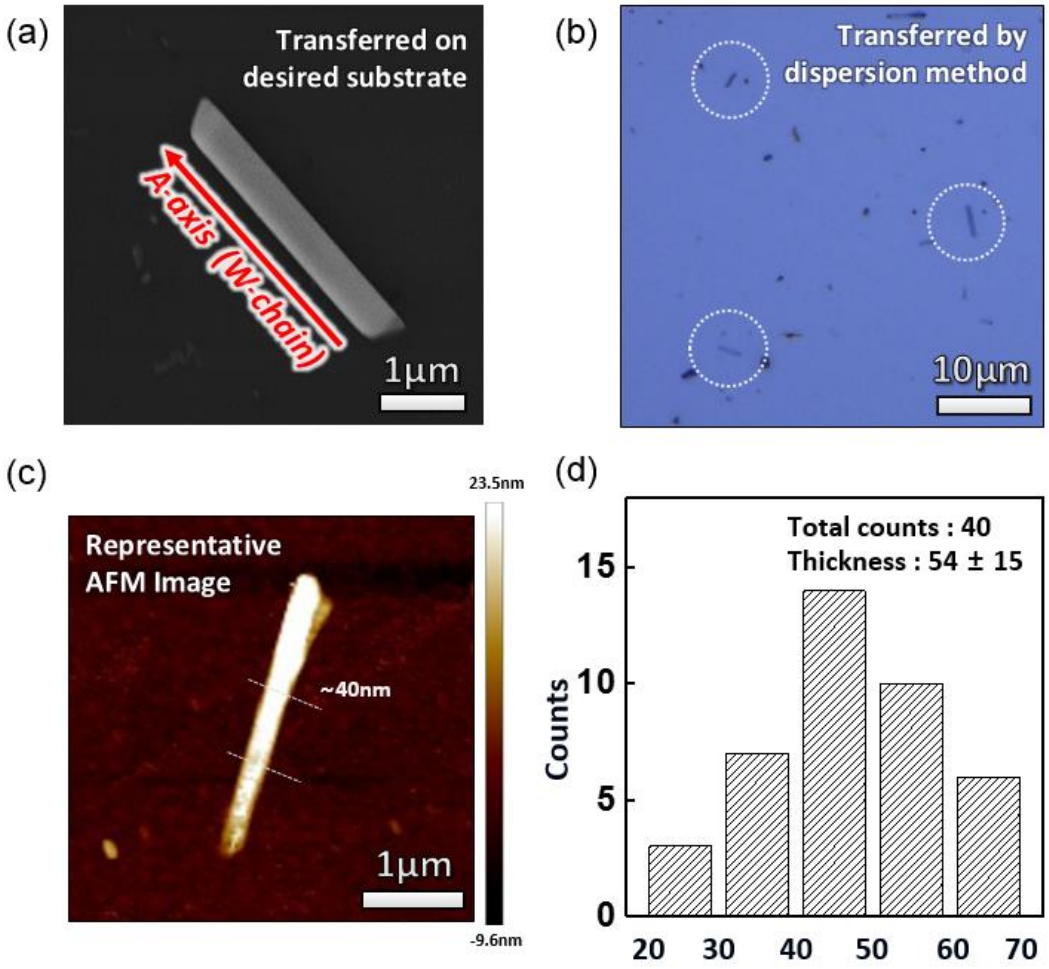

Figure 3-3. (a-c) OM, SEM and AFM images of transferred WTe_2 nanobelts on desired substrate by conventional dispersion method. (d) Diameter distribution of WTe_2 nanobelts obtained at W20/Cu50 500℃ for 10min.

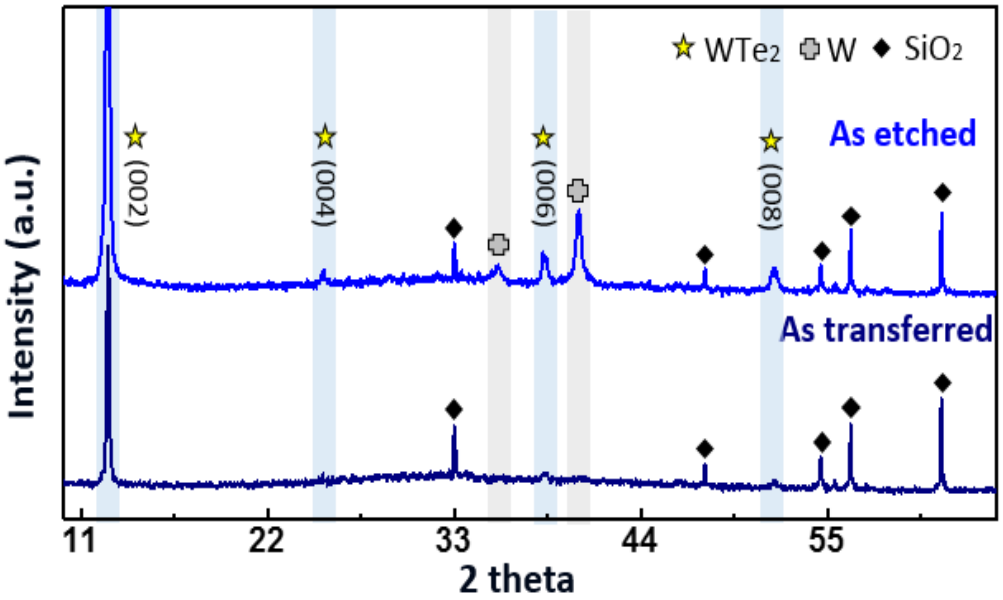

Figure 3-4. XRD data of as Cu_xTe_y etched and transferred WTe_2 nanobelts on SiO_2/Si substrate by conventional dispersion method.

3.2 Structural Morphology of Eutectic Metal Alloys on Synthesis Parameters

The role of eutectic metal and its behavior on synthesis parameters is a major factor in the synthesis of WTe_2 in our synthesis method, so studies on changes of Cu_xTe_y metal alloys on synthesis parameters were necessary. We studied the synthesis of WTe_2 by controlling the growth conditions and observing changes of Cu_xTe_y metal alloys.

3.2.1 Study on Behavior and Role of Cu_xTe_y depending on Growth Time

We examined effects of growth time first. The thickness of the sample under our optimum condition for obtaining few-nm thickness WTe_2 nanostructure (tungsten of 20nm, copper of 50nm on SiO_2/Si substrate) and growth at the temperature of 500°C with 0.1g of Te powder was fixed and only the synthesis time was adjusted. When the growth time was relatively short (2, 6 min), the Cu atoms from the copper layer below W layer did not react sufficiently with Te. As was such, Cu_xTe_y metal alloys could not form sufficiently, consequently affecting WTe_2 growth. Figure. 3-5 shows the intensities of XRD peak for Cu and Cu_xTe_y metal alloys depending on synthesis times of 2min, 6min, and 10min respectively. From the XRD analysis, the weak XRD peak of (002)-oriented Cu_xTe_y metal alloys were found at the growth time of 2 min and 6 min. The XRD peak of (002)-oriented Cu_xTe_y metal alloys is clearly shown in the case of growth time of 10min, where both Cu and Te sufficiently reacted. Correspondingly, XRD peak of the well-crystalized (002)-oriented WTe_2 is clearly identified. Figure 3-6 is the comparison of XRD intensity on as deposited, annealed w/o Te and as-grown Cu_xTe_y:W at 500°C for 10min. Compared to as deposited and annealed without Te source, our optimum condition with sufficient growth time of 10min exhibits clear XRD peaks of Cu_xTe_y metal alloys and WTe_2 nanostructure. From these results, we recognize that formation of Cu_xTe_y metal alloys from the reaction of Cu and Te has significant effects on growth of WTe_2. In figure 3-7, the Raman spectrum of as-grown Cu_xTe_y and WTe_2 shows several peaks approximately at 92, 121, 141 (tellurium peaks) and 80, 119, 134, 164, 212 (WTe_2 peaks) cm^{-1}, respectively.

Even as Cu_xTe_y metal alloys are formed, nucleation and crystallization of WTe_2 nanostructures must take place inside of eutectic metal alloys. In the case of insufficient growth time to nucleate WTe_2 nanostructure, only W nanowire can be observed. In figure 3-8, the SEM Image shows the as-obtained W nanowire at the same site where the Cu_xTe_y droplet was located. The activated W atoms induced by eutectic metal alloys did not react with Te atoms, resulting in formation of W nanowires along the [110] direction. This phenomenon is also observed in the Te deficiency region, where grown for 10min. In short, WTe_2 nanostructure can be synthesized at convection region with W atoms and Te atoms, followed by oversaturation and eventually crystallization followed by precipitation.

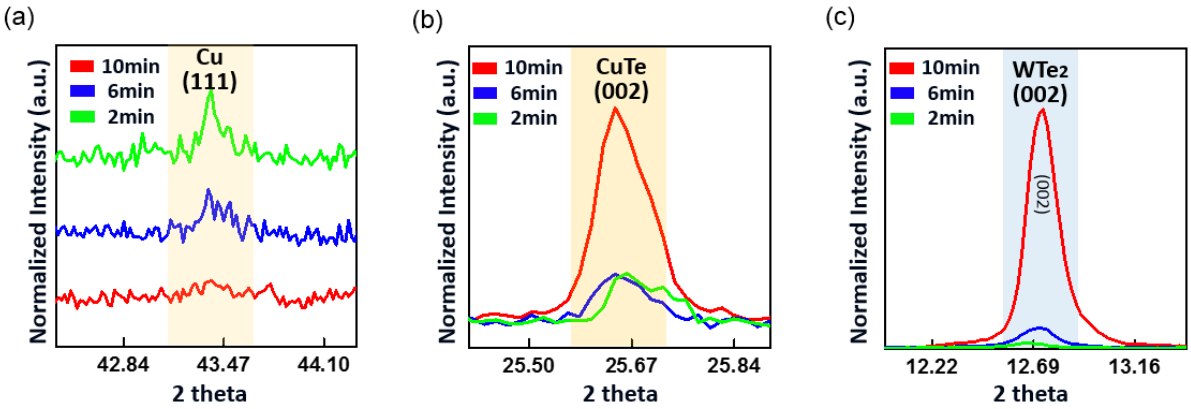

Figure 3-5. (a-c) Comparison of XRD intensity of as-grown Cu_xTe_y:W depending on growth time.

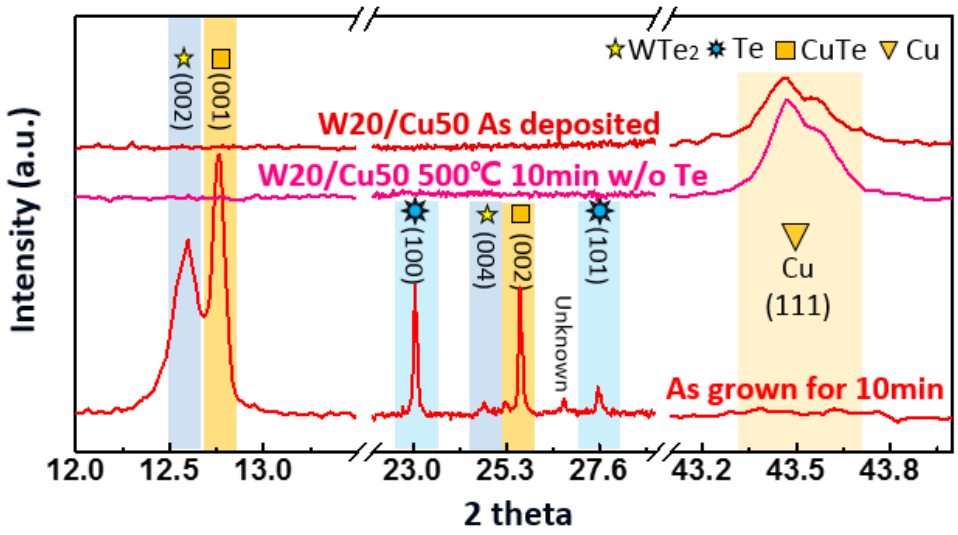

Figure 3-6. Comparison of XRD intensity of as deposited, annealed w/o Te and as-grown Cu_xTe_y:W at 500°C for 10min.

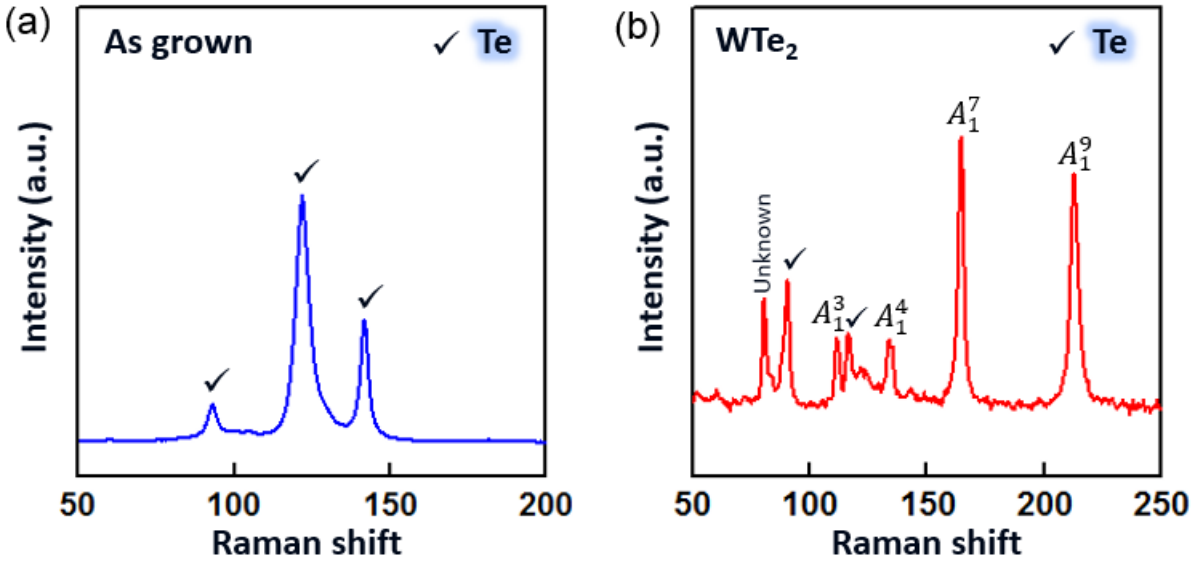

Figure 3-7. (a-b) Raman spectra of as-grown Cu_xTe_y droplet and as-synthesized WTe_2 nanostructures of a W(20 nm)/Cu(50 nm) sample at 500°C for 10min.

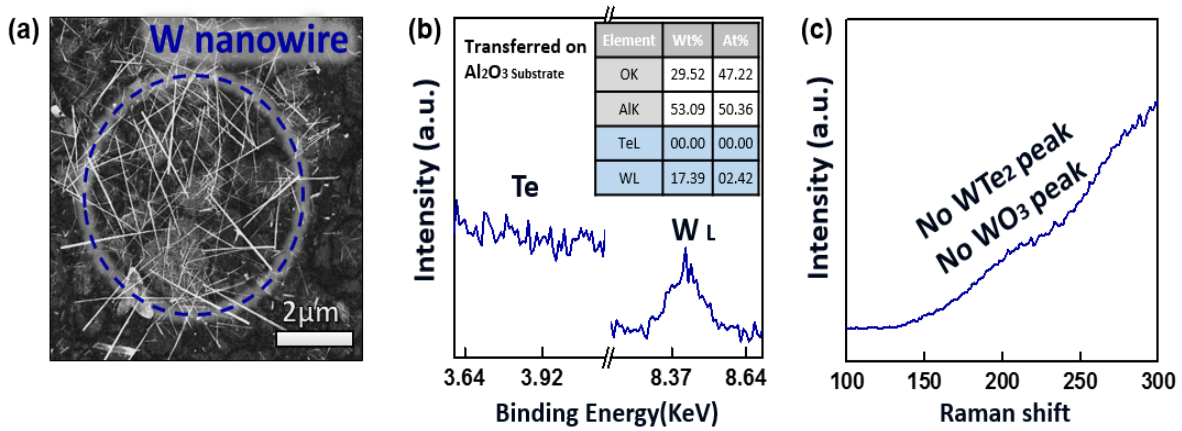

Figure 3-8. (a) SEM Image of as-synthesized W nanowires on W layer. (b-c) EDAX and Raman spectra, corresponding to the colored blue spot in (a) image.

3.2.2 Study on Behavior and Role of Cu_xTe_y depending on Growth Temperature

Next, we investigated the effect of growth temperature on formation of Cu_xTe_y droplets and synthesis of WTe_2 nanostructure. The thickness of the sample under the optimum condition for obtaining few-nm thickness WTe_2 nanostructure (tungsten of 20nm, copper of 50nm on SiO_2/Si substrate) and growth time for 10min with 0.1g of Te powder was fixed and only the synthesis temperature was adjusted. The dependency of Cu_xTe_y droplet and nanobelts structural morphology on synthesis parameters is shown in SEM images, displayed in figure 3-9. The average size of Cu_xTe_y droplet obtained from growth at 600 °C is about four times larger than Cu_xTe_y droplet grown at a temperature of 500 °C. Correspondingly, as the reaction temperature is increased, thick and long nanobelts can be obtained. The higher the temperature, the reaction of tungsten and tellurium are activated more inside of the larger Cu_xTe_y droplet, resulting in a thicker and improved crystallinity of WTe_2, as shown in figure 3-10. Figure. 3-11 indicates changes in length of nanobelts for the a-axis and b-axis and thickness of nanobelts as growth temperature is increased. From these results, we became aware that the reaction temperature of Cu and Te has significant effects on formation of Cu_xTe_y metal alloys and growth of WTe_2 nanobelts. The growth temperature affects not only the diffusion of the copper atoms from the pre-deposited copper layer into the upper layer but also activation of W atoms to be reacted with Te atoms from the W layer despite the low reactivity of W due to the high active temperature of W.

In our growth modes, the Cu_xTe_y dissolves W atoms from the W surface and forms WTe_2 nanostructures in side of Cu_xTe_y droplets. Interestingly, at a growth temperature of 600°C, an enormous amount of W nanowire grown in the (110) direction was found compared to growth temperature of 500°C. The SEM Images, as shown in figure 3-12, indicate that W nanowire have a diameter ranging from 50nm to 500nm, showing perfect straightness and grassy appearance.

Lee. Yun-Hi, et.al have reported fabrication of tungsten nanowire without use of any heterogeneous catalyst[45]. They examined X-ray diffraction (XRD) patterns that show remarkable changes of the crystallographic structure after W-nanowire formation. The XRD data for grown nanowires suggested that the interplanar distances were increased and the relative peak intensities of W (110) were increased. By HRTEM, they confirmed that the wavelength of the modulation in the HRTEM image was about 0.22 nanometers, which is the wavelength that corresponds to the inter-planar distance of (110) lattice planes of bcc W, as shown in figure 3-13.

Our results showed formation of W nanowires grown in (110) directions, and could be confirmed by XRD, indicated in figure 3-14. This figure shows that the intensity of W (100) after the growth of 600 °C

was highly increased (relatively higher than the intensity before growth). This is because the activated W atoms induced by eutectic metal alloy did not react with Te atoms, resulting in formation of W nanowires along the [110] direction. The W nanowire was dominantly observed when the temperature was increased and the amount of Te was decreased. As shown in figure 3-15, we confirmed that the size and density of the W nanowires increased significantly when the Te amount was reduced. Based on our mechanism, W atoms are dissolved in liquid state Cu_xTe_y droplets above the eutectic temperature of the Cu–Te system. These results strongly suggest that when the dissolved W atoms cannot react with Te due to deficiency of Te source, the activated W atoms grew as a nanowire shape in the (110) direction, followed by supersaturation and the crystallization from the liquid-phase. From these results, we can understand that the reaction of activated W atoms and Te precursor has a significant effects on supersaturation of WTe_2 in liquid state Cu_xTe_y droplet for growth of single-crystalline WTe_2 nanobelts.

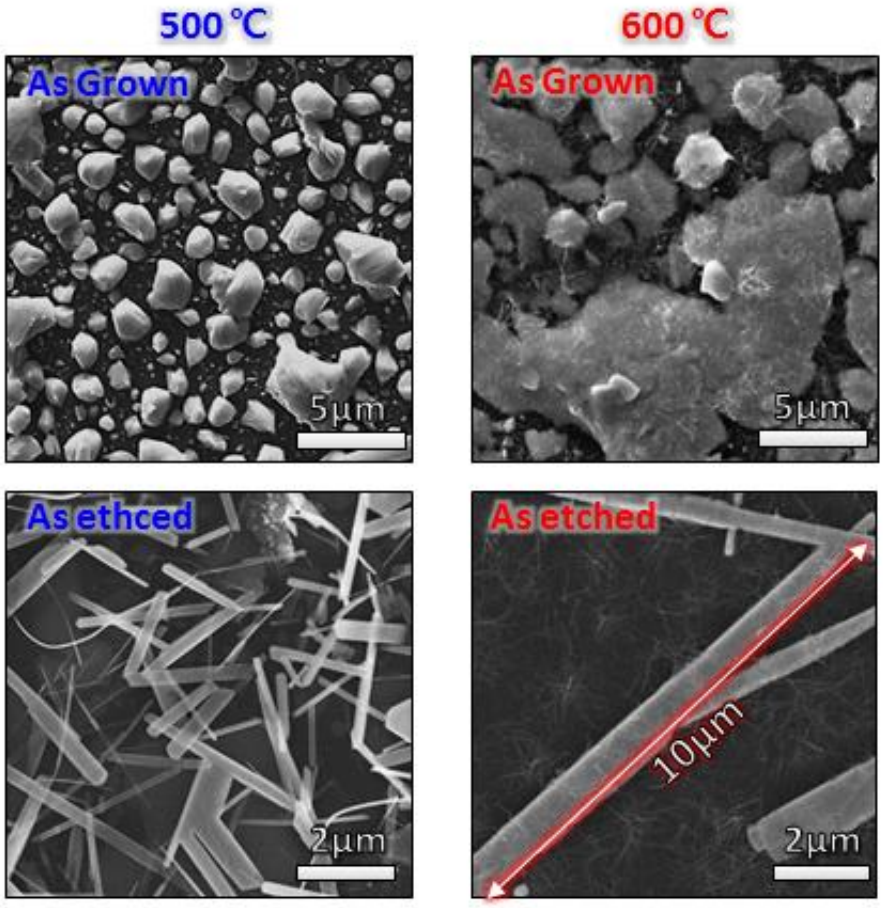

Figure 3-9. Representative SEM images of Cu_xTe_y droplet and WTe_2 nanobelts obtained at 500°C and 600°C for 10min, respectively.

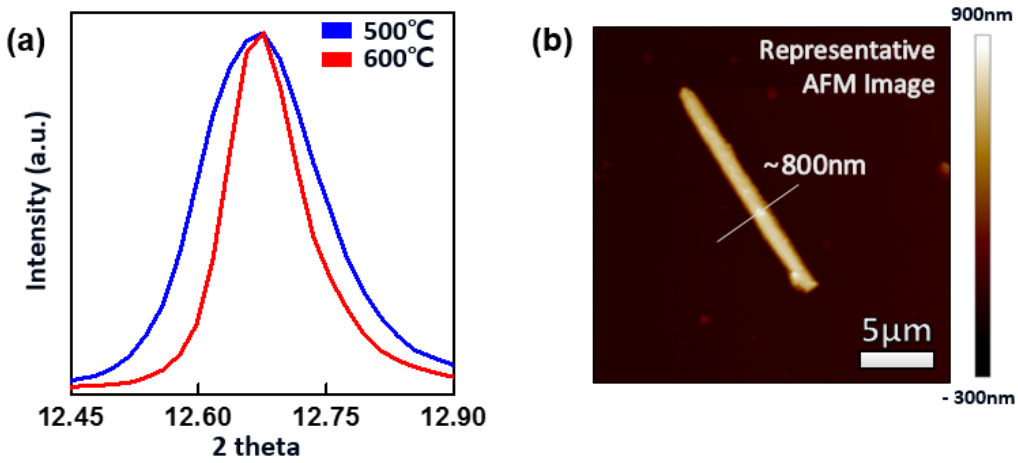

Figure 3-10. (a) XRD data of WTe_2 nanobelts obtained at 500°C and 600°C for 10min, respectively. (b) Representative AFM Image of WTe_2 nanobelts obtained at 600°C for 10min, showing highly thick nanobelts.

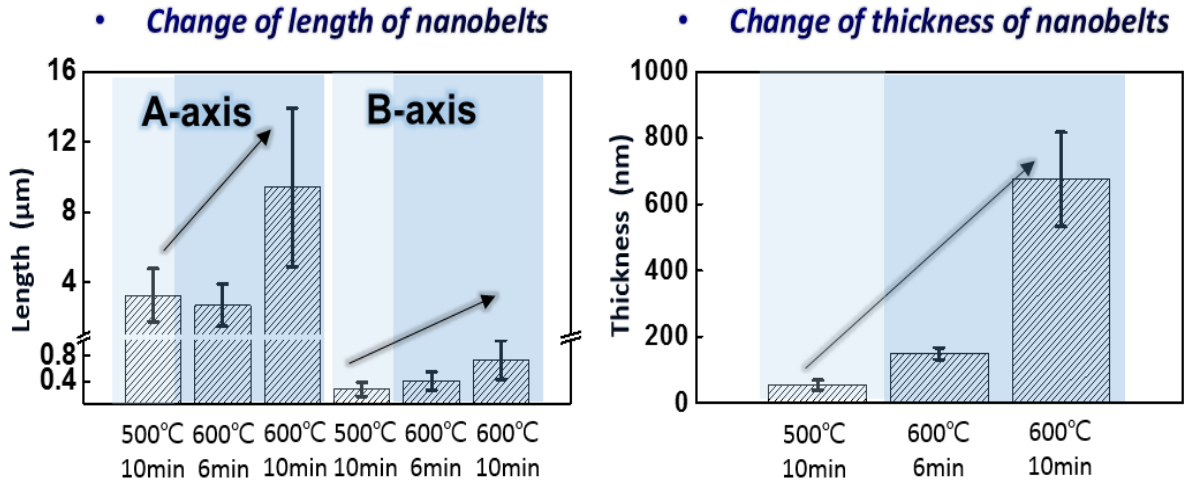

Figure 3-11. Changes of length and thickness of as-synthesized WTe_2 nanobelts as growth temperature and time increase.

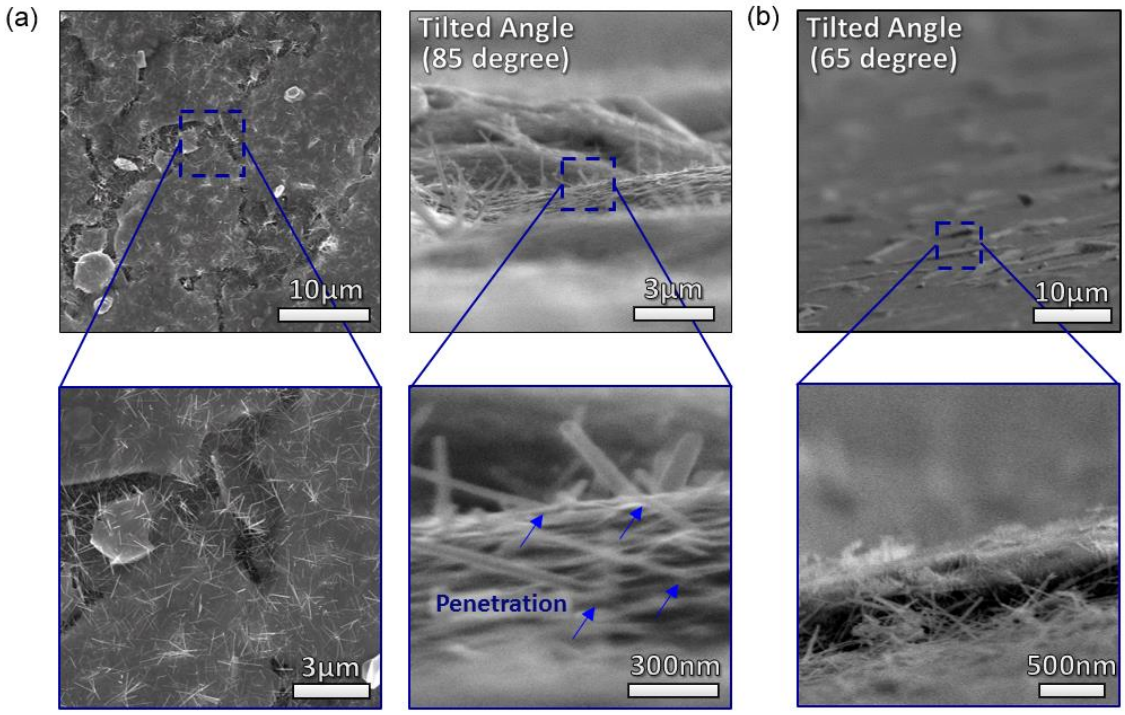

Figure 3-12. (a) Representative SEM images of Cu_xTe_y droplet & W nanowires. It is shown that the W nanowires penetrated the Cu_xTe_y droplet. (b) Cross sectional SEM Images of WTe_2 nanobelts & W nanowires.

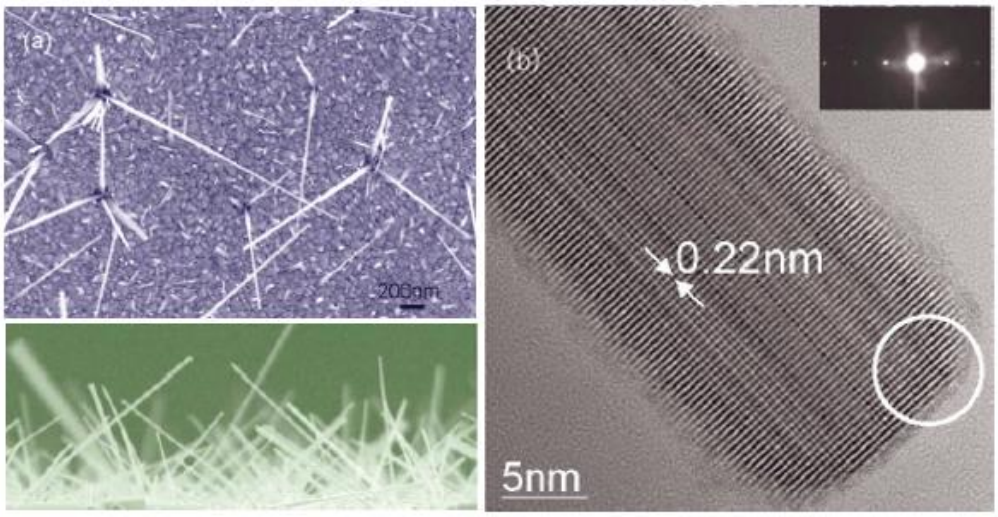

Figure 3-13. (a) SEM images of tungsten (W) nanowires at initial growth (b) The modulation phase HRTEM images of a chosen W nanowires. The inset figure is selected area electron diffraction pattern showing the growth of a well-crystallized bcc-phase W nanowire[45].

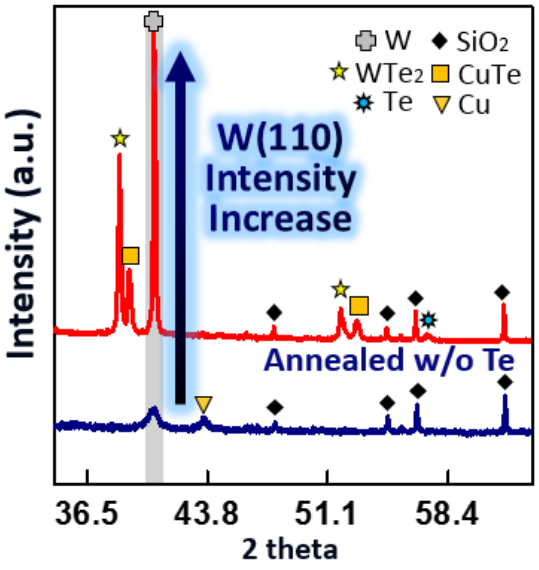

Figure 3-14. XRD data of as grown Cu_xTe_y droplet and as-annealed w/o Te at 600°C for 10min on SiO_2 substrate.

.

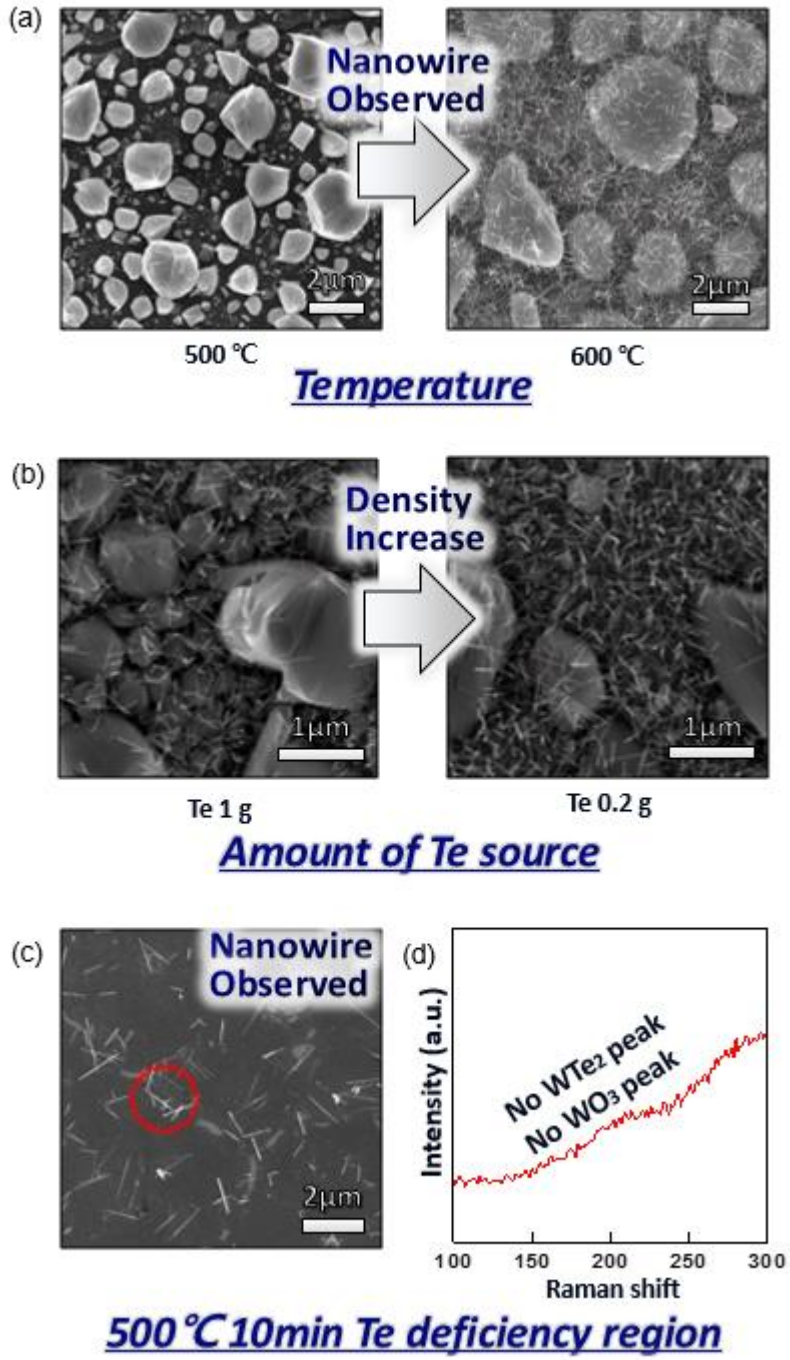

Figure 3-15. (a) Changes in the surface morphologies depending on the growth temperature. (b) Changes in the surface morphologies depending on the amount of Te source. (c) Representative SEM Images of W nanowire obtained from Te deficiency region at 500°C for 10min. (d) Raman spectra, corresponding to the colored red spot in (c) image, identifying the W nanowire.

3.2.3 Study on Behavior and Role of CuxTey depending on thickness of W layer

We have investigated the changes in the formation of Cu_xTe_y when the tungsten thickness is relatively increased. For this study, the thickness of the W layer was changed from 20 nm (optimum condition forobtaining few-nm thickness WTe_2 nanostructure) to a thickness of 100 nm. Other processes and growth conditions (copper of 50nm on Sio_2/Si substrate, growth for 10min at 500°C) were fixed and only the thickness of the W layer was changed. In this work, interestingly, as-grown Cu_xTe_y droplets couldn't be observed on W layer. This can be seen in the OM Images shown in figure 3-16a of as-grown Cu_xTe_y droplets after dipping APS etchant. However, we could not recognize any changes of the surface morphology. It is clearly shown that Cu_xTe_y droplets were formed under the W layer. We detached the W layer using a method of sonication to verify the synthesized WTe_2 underneath the W layer. At the same site where the Cu_xTe_y droplet was located, the synthesized WTe_2 was found on SiO_2/Si substrate, as shown in figure 3-16b,c. From these results, we confirm that Cu_xTe_y droplets do not penetrate the W layer as the thickness of W layer becomes relatively thick. In addition, it can be seen that WTe_2 does not grow only at the interface between W layer and Cu_xTe_y droplet. The cross sectional SEM Images (see figure 3-17) clearly exhibit the formation of WTe_2 nanostructures on the SiO_2, not on the W layer, compared to the case where the W layer is relatively thin (thickness = 20nm). Also, we investigated a change of structural morphology of synthesized WTe_2 nanobelts, as shown in figure 3-18. As we increased the thickness of W layer from 20nm to 100nm, the size of the synthesized WTe_2 increased slightly. The formation of WTe_2 nanobelts below W layer was confirmed, even at higher temperature of 600 °C, where diffusion of Cu atoms is increased, under a fixed growth and process condition. From previous experiments for studying effects of growth temperature, we found that the reaction temperature of Cu and Te has a significant effect on formation of Cu_xTe_y metal alloys. The growth temperature affects not only the diffusion of the copper atoms from the pre-deposited copper layer into the upper layer but also diffusion of Te vapor into copper layer. Compared to the case of 500°C, the larger size as-grown Cu_xTe_y metal alloys underneath W layer were exposed as they were etched by dipping APS etchant for 1hr. WTe_2 nanobelts covered with W layer and Te products can be observed in figure 3-19 and 3-20. In contrast to structural morphology of case of relatively thick W layer (t = 100nm), in the case of relatively thin W layers (t = 20nm), the Cu_xTe_y metal alloys were formed on W layer. This was clearly identified by the changes in surface morphology of Cu_xTe_y droplets depending on etching time. The Cu_xTe_y droplets on W layer were etched gradually as etching time increased, shown in figure 3-21. This shows that WTe_2 nanobelts are underneath Cu_xTe_y droplets. From these results, it was confirmed that the formation of Cu_xTe_y metal alloys and WTe_2 nanobelts are strongly dependent on the relative thickness of W layer. And we realized that the Cu_xTe_y dissolves W atoms from the W surface and helps WTe_2 to be nucleated, not just only on the W surface, but on the Sio_2/Si substrate.

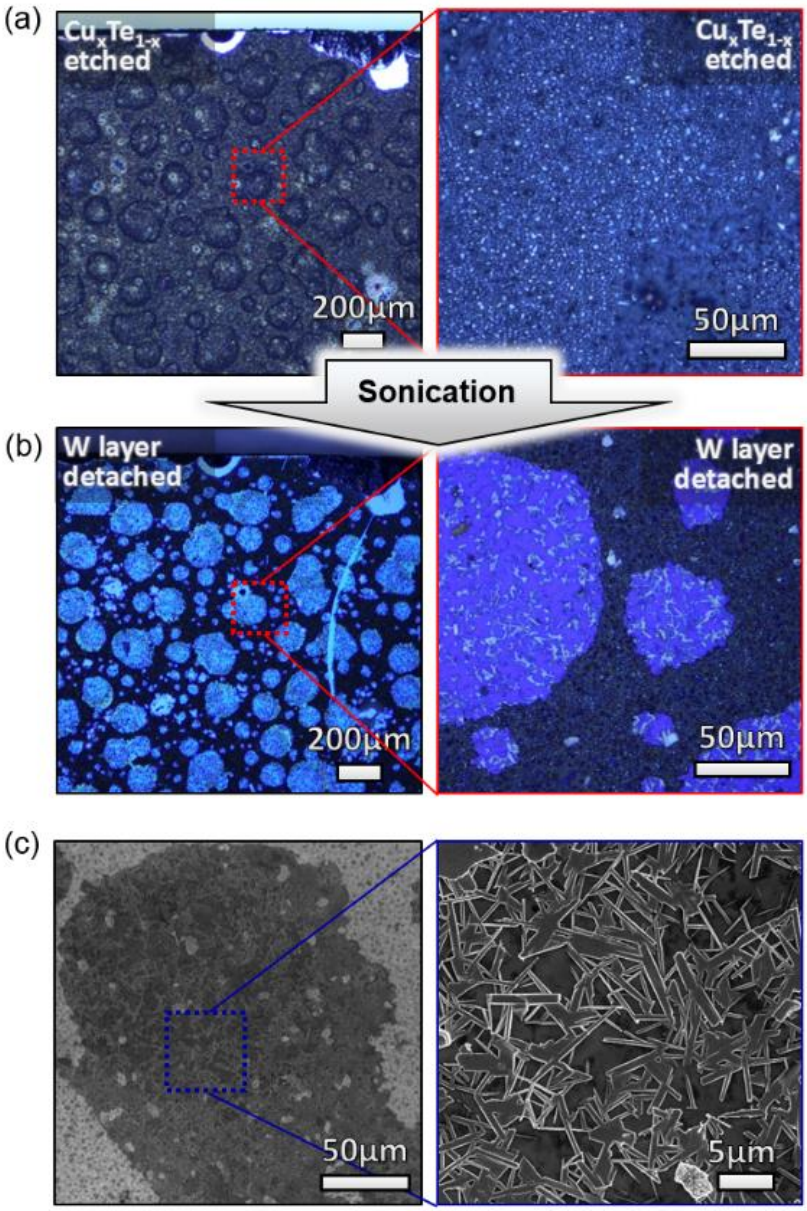

Figure 3-16. (a) OM Images of Cu_xTe_y droplets grown at W100/Cu50 at 500°C for 10min. It is shown that Cu_xTe_y droplets were formed under W layer. (b) OM Images of WTe_2 nanobelts at the same site after sonication for 1hr to detach W layer. (c) Representative SEM Images of WTe_2 nanobelts on SiO_2 substrate obtained at W100/Cu50 500°C for 10min.

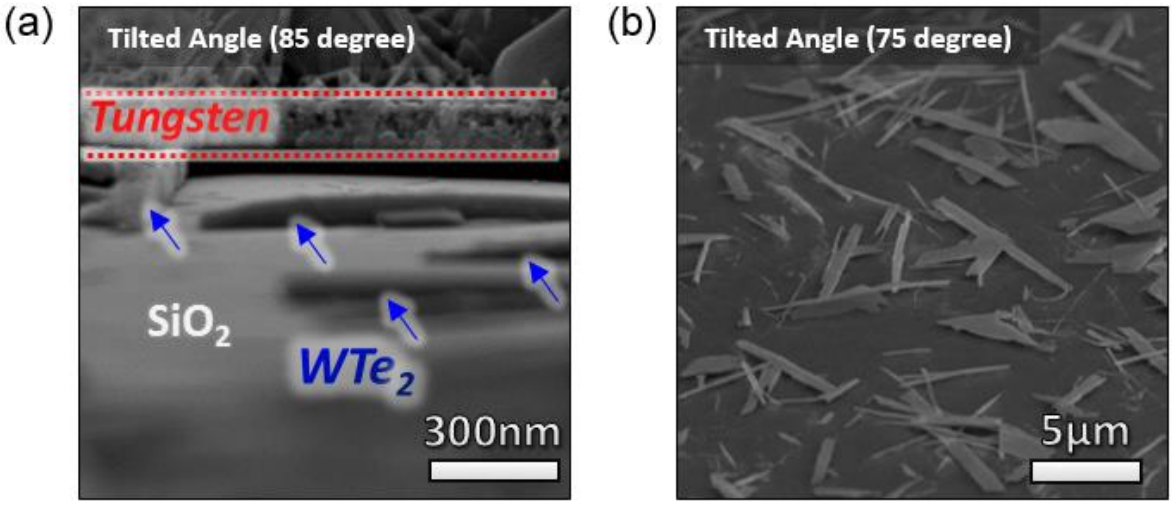

Figure 3-17. Cross sectional SEM Images of (a) WTe_2 grown on SiO_2 substrate (b) on W layer, respectively, depending on process condition of thickness of W layer.

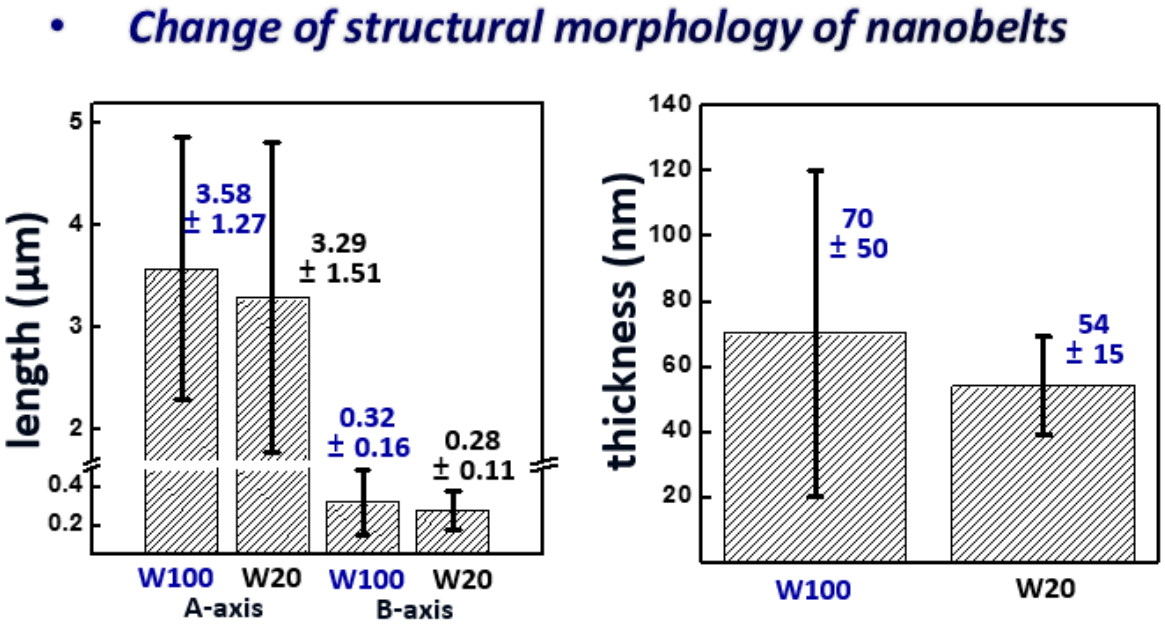

Figure 3-18. Change of structural morphology of as-synthesized WTe_2 nanobelts depending on process condition of thickness of W layer.

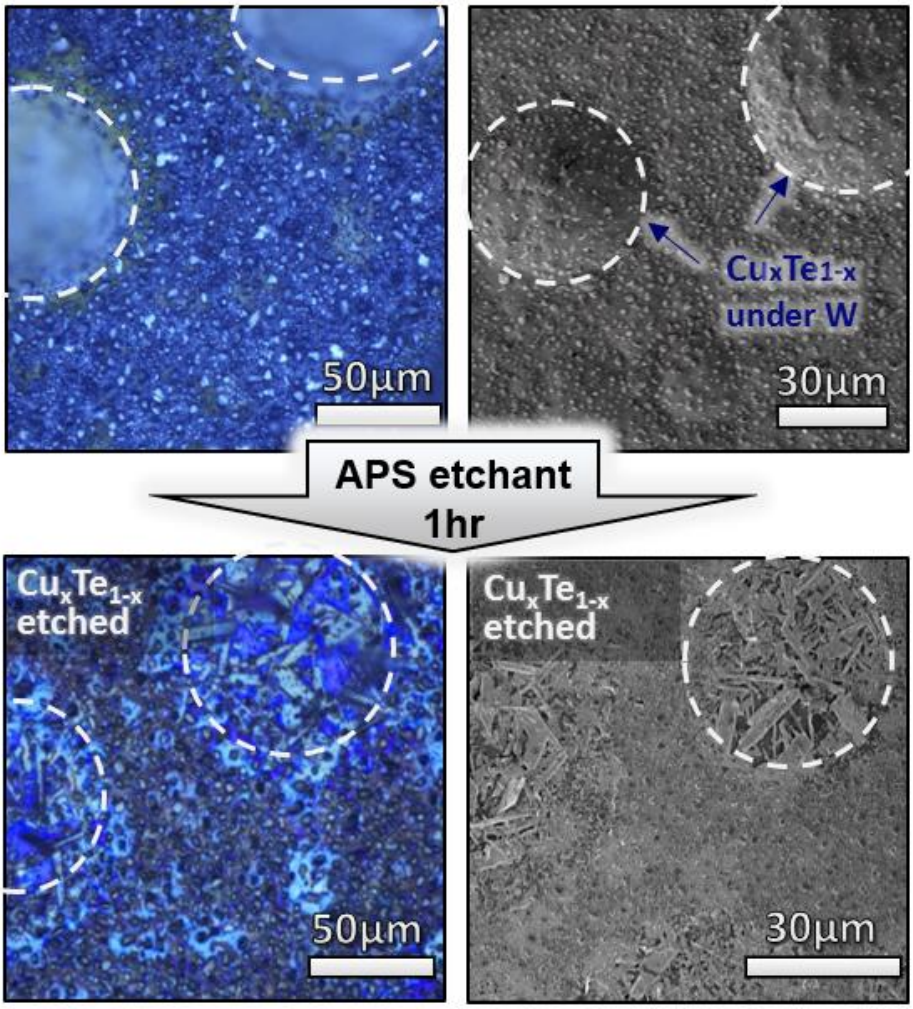

Figure 3-19. SEM Image and OM Images of Cu_xTe_y droplets grown at W100/Cu50 at 600°C for 10min. It is shown that Cu_xTe_y droplets were formed under W layer. After Cu_xTe_y etching, WTe_2 nanobelts can be observed under W layer.

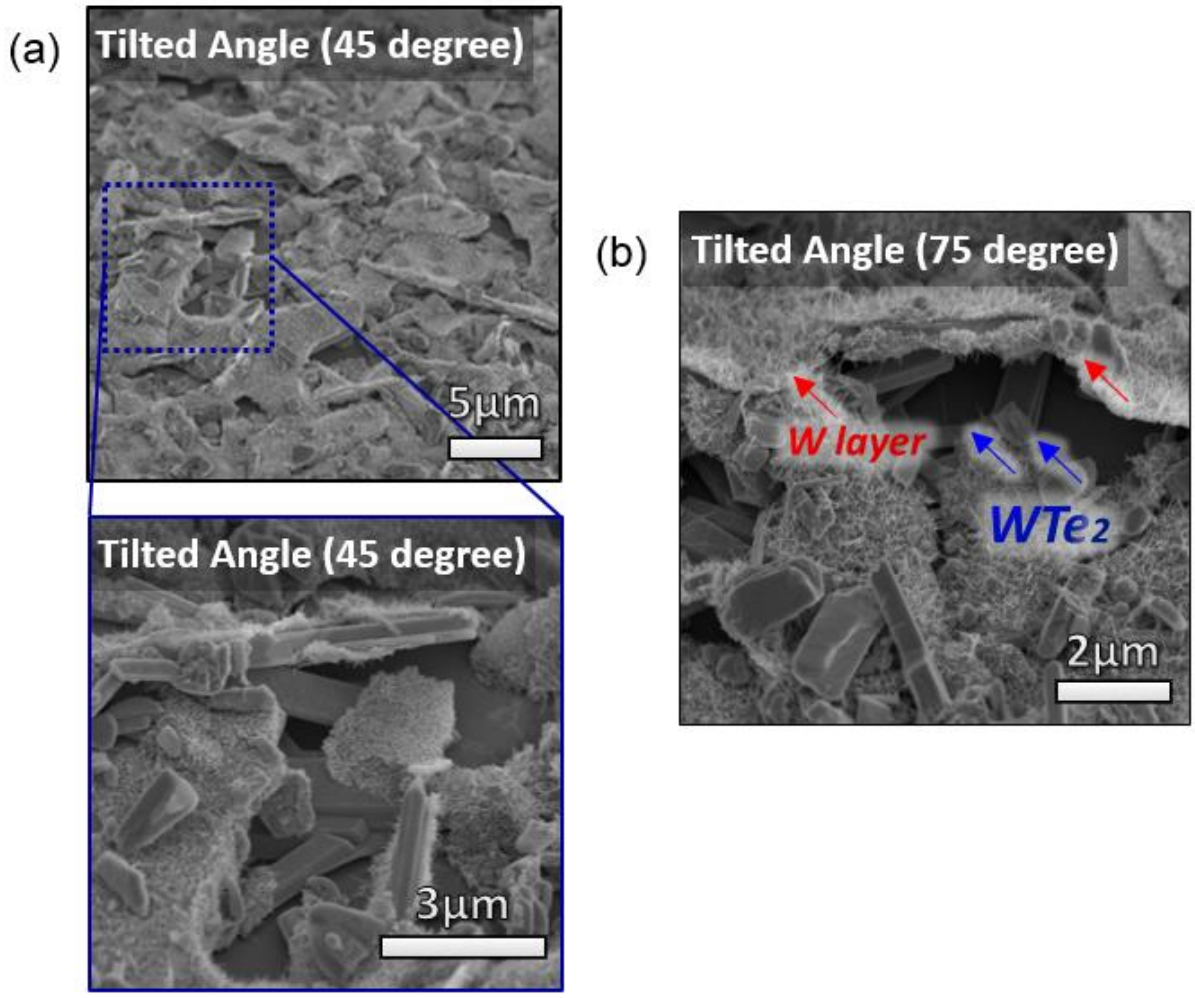

Figure. 3-20 (a-b) Cross sectional SEM images of Cu_xTe_y droplets grown at W100/Cu50 600°C for 10min. It is shown that WTe_2 nanobelts are covered with W layer and Tellurium product.

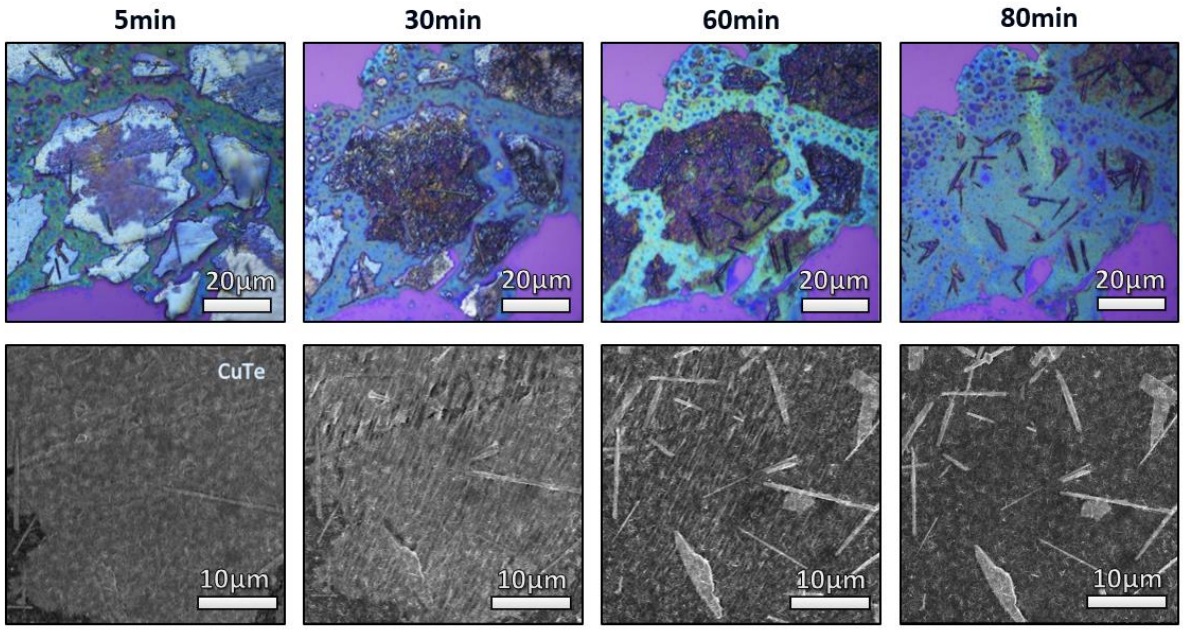

Figure 3-21. The changes in surface morphology of Cu_xTe_y droplets depending on etching time. The Cu_xTe_y droplets on SiO_2 substrate were etched gradually as etching time increased. It is found that WTe_2 nanobelts are underneath Cu_xTe_y droplets.

3.3 Transfer-Free Formation of Transition Metal Telluride Nanostructures on the Desired Substrate and Investigation of Electrical Properties

Recently, transfer-free growth of TMDs without the need for after-growth transfer process has been attracted for a fundamental research and practical applications[46]. To minimize degradation of TMDs' intrinsic properties and difficulty in fabrication of devices due to residues in process of complex transfer procedure, the development of direct formation of TMDs without necessity of an additional transfer step has been required.

In previous research, we confirmed that Cu_xTe_y metal alloys was formed on the desired substrate as the thickness of W layers became relatively thick. As shown in figure 3-22, the Cu_xTe_y was formed directly on SiO_2 /Si substrate. To expose the nanobelts inside of Cu_xTe_y droplets, we tried to mechanical peel Cu_xTe_y droplets off by using the method of peeling off using scotch tape. We confirmed that WTe_2 nanobelts were formed under the W layer and Cu_xTe_y droplet, by observing the back surface of the peeled scotch tape. As shown in figure 3-23, OM and SEM Images exhibit high density of WTe_2 nanobelts on the back surface of scotch tape. To confirm the WTe_2 nanobelts, Raman analysis was carried out, displayed in figure 3-24a.

We were able to observe as-synthesized WTe_2 nanobelts at the surface of SiO_2/Si substrate without using after-growth transfer processes. The Cu_xTe_y droplet and W layer were clearly peeled off by tape peeling off method, confirmed by EDAX and XRD analysis, indicated in figure 3-25b,c. Also, the as-obtained WTe_2 nanobelts directly on the desired substrate was confirmed by Raman spectroscopy, as shown in figure 3-24b. In short, we succeed to form WTe_2 nanobelts directly on the desired substrate without possibilities in degradation by inevitable chemical and physical damage in wet etching and transfer process.

Moreover, the feasibility of synthesis of $MoTe_2$ nanostructure as a member of the layered TMDs family was evaluated through our approaches. The formation of 2H-$MoTe_2$ and 1T'- $MoTe_2$ nanostructure on SiO_2 substrate was achieved by peeling the Cu_xTe_y droplets and Mo layer off, confirmed by Raman and Edax analysis of $MoTe_2$ nanostructure on SiO_2/Si substrate, indicated in figure 3-26.

The transfer-free formation of transition metal telluride nanostructure on desired substrate enables to investigate its electrical properties by fabricating test device directly on SiO_2/Si substrate without the needs for a further transfer process. Interestingly, we confirmed that the as-synthesized WTe_2 nanostructure by our method exhibits the similar resistivity as the exfoliated few-layer WTe_2 from the bulk crystal. The resistivity of few-layer WTe_2 nanostructure is in the range of ~ 10^{-4} to 10^{-3} Ω·cm, as shown in figure 3-7. To sum up, our approach of mechanical removal of Cu_xTe_y droplet by method of peeling off using scotch tape can reduce the whole process to obtain WTe_2 nanostructures as well as prevent degradation of WTe_2.

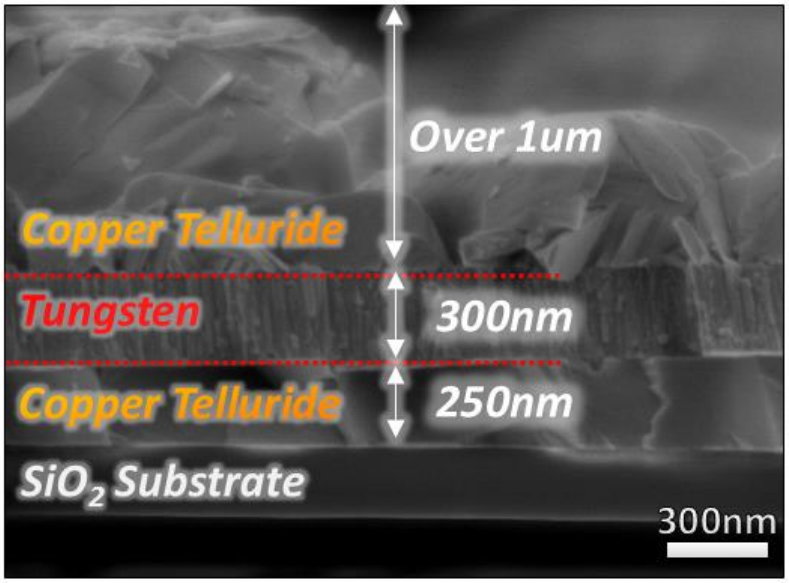

Figure 3-22. Cross sectional Image of as-grown Cu_xTe_y/W on SiO_2/Si substrate.

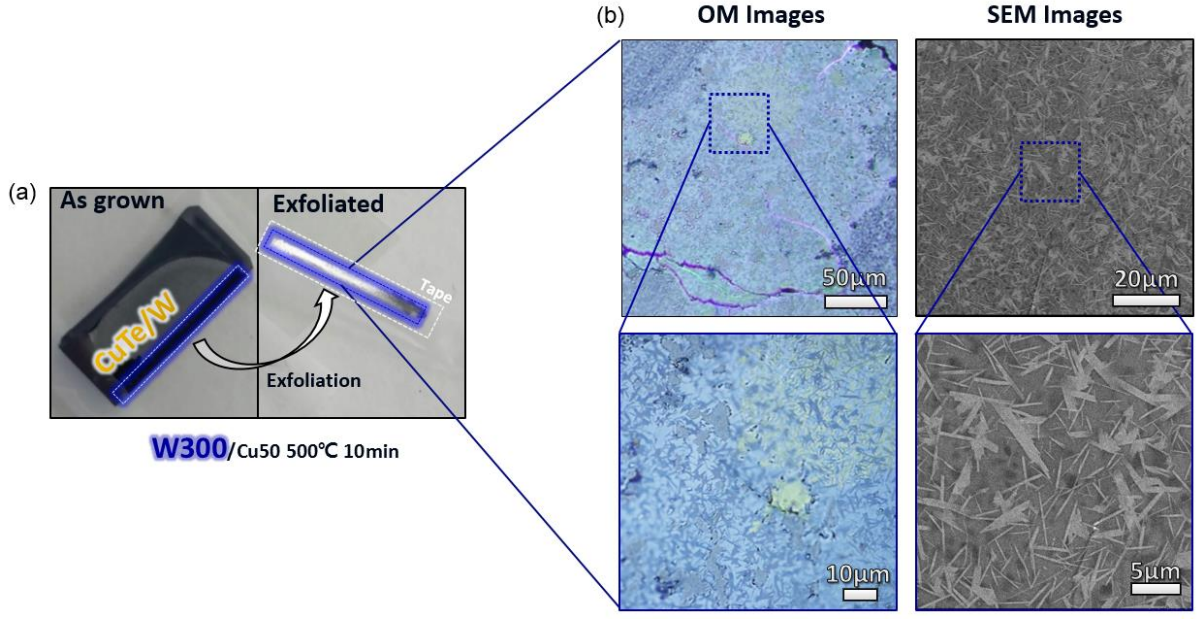

Figure 3-23. (a) Photograph of peeling off process by using scotch tape. (b) SEM and OM Images of WTe_2 nanobelts on the back side of exfoliated tape. It clearly suggests that synthesized WTe_2 nanobelts can be formed under Cu_xTe_y droplet/W layer.

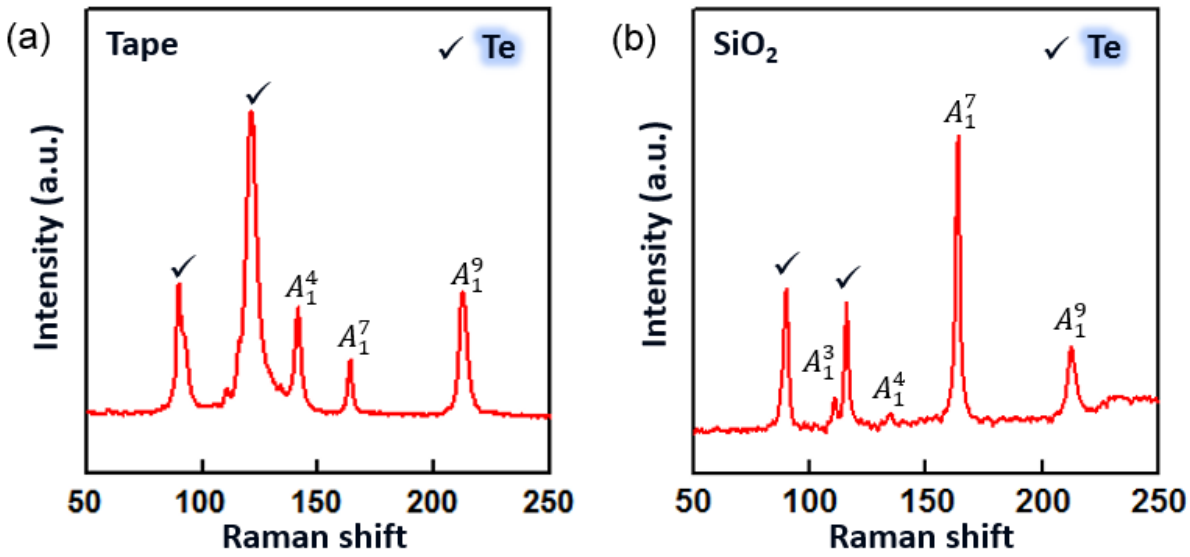

Figure 3-24. Raman spectra of WTe_2 nanobelts (a) on scotch tape and (b) on SiO_2/Si substrate, respectively.

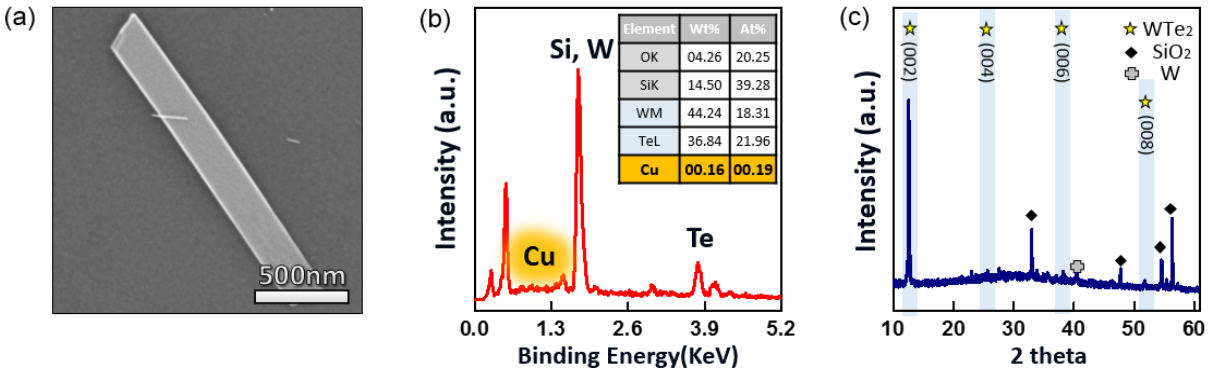

Figure 3-25. (a) Mechanical removal of Cu_xTe_y droplet by method of peeling off using scotch tape (b-c) Edax analysis and XRD data of WTe_2 nanobelts on SiO_2/Si substrate by peeling W and Cu_xTe_y droplets off, identifying that Cu_xTe_y droplets and W layer are clearly peeled off by method of peeling off using scotch tape

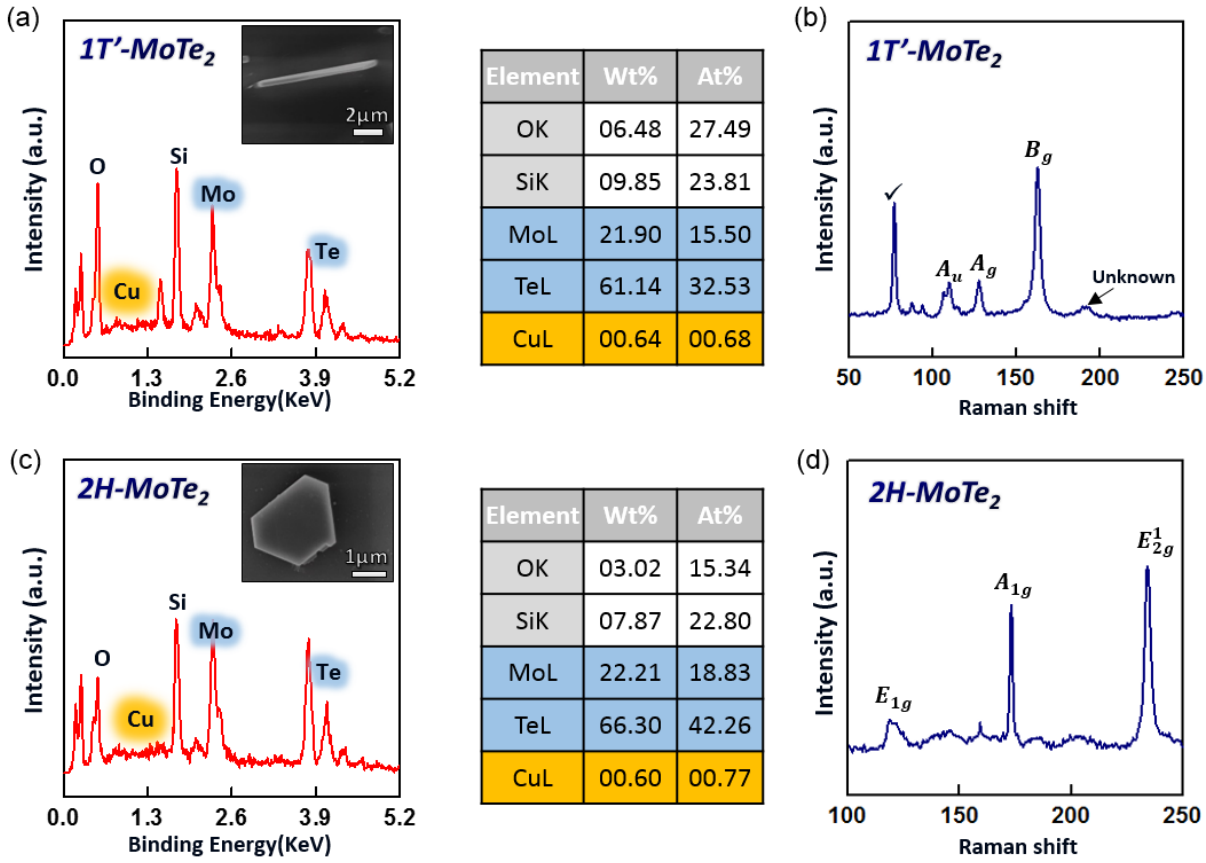

Element	Wt%	At%
OK	06.48	27.49
SiK	09.85	23.81
MoL	21.90	15.50
TeL	61.14	32.53
CuL	00.64	00.68

Element	Wt%	At%
OK	03.02	15.34
SiK	07.87	22.80
MoL	22.21	18.83
TeL	66.30	42.26
CuL	00.60	00.77

Figure 3-26. (a-d) Mechanical removal of Cu_xTe_y droplets and Mo layer by method of peeling off using scotch tape. The formation of 2H-$MoTe_2$ and 1T'-$MoTe_2$ nanostructure on SiO_2/Si substrate can be achieved by peeling Cu_xTe_y droplets and Mo layer off, confirmed in Raman and Edax spectra of $MoTe_2$ nanostructure on SiO_2/Si substrate

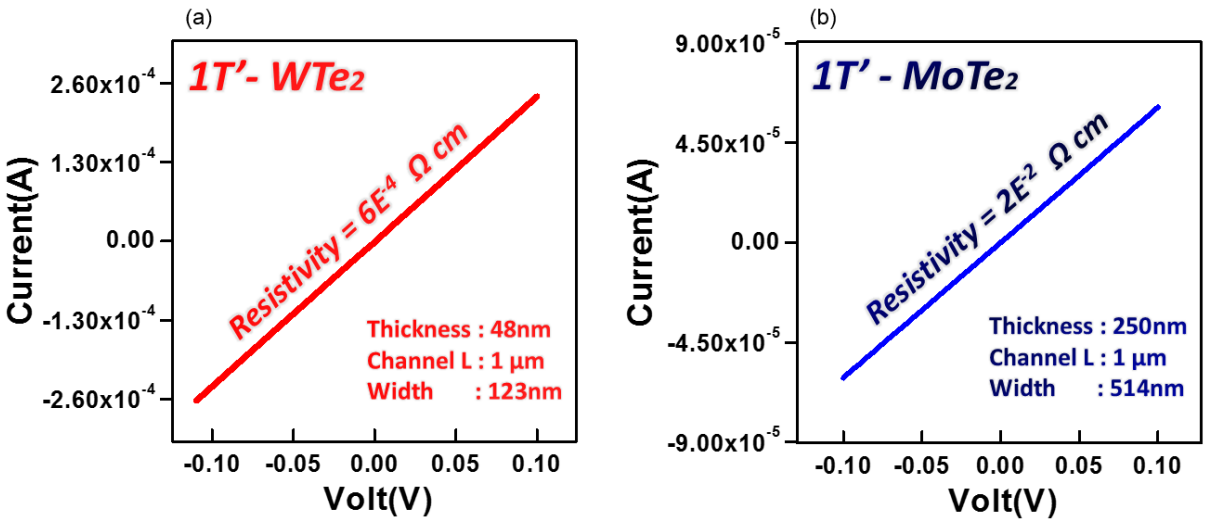

Figure 3-27. (a-b) Current vs voltage characteristics for fabricated 1T'- WTe_2 and $MoTe_2$ device, respectively. We successfully can obtain both 1T'- WTe_2 and $MoTe_2$ nanostructure directly on SiO_2/Si substrate with no needs for a further transfer process.

Chapter 4. Conclusion

Summary

In this research, the role of eutectic metal and its behavior on synthesis parameters in the synthesis of WTe_2 by using the pre-deposited films of W/Cu on SiO_2/Si substrate was studied.

First of all, the tungsten ditelluride (WTe_2) nanostructure were successfully synthesized by using eutectic metal alloys. The growth mechanism of WTe_2 was explained by the assistance of liquid Te-rich Cu_xTe_y droplets, after oversaturation with dissolved tungsten, induced a WTe_2 crystal growth. The crystallization takes place inside of Cu_xTe_y droplet at a temperature of ~500°C, above the Cu–Te eutectic temperature of 340°C. We described the crystallization of WTe_2 from solution-phase Cu_xTe_y droplets, resulting in 1-D preferential crystal growth of the single-crystalline WTe_2 nanobelts which has a stable distorted octahedral phase (1T'-WTe_2). The use of Te-rich eutectic metal alloys eliminates the Te deficiency in the resulting products and the contamination by impurities encountered with vapor deposition process. As a result, the as-synthesized WTe_2 nanostructures inside of Cu_xTe_y droplet by simple solution-phase reaction are highly pure, stoichiometric, and structurally uniform.

A different behavior of the Cu_xTe_y droplets were observed, which is strongly dependent on synthesis parameters such as growth temperature, time and process conditions of a metal film before WTe_2 growth. The structural characteristics and the formation of the products can be varied by controlling the synthesis parameters.

Particularly, we succeed to control the eutectic alloy to produce WTe_2 nanobelts where on the top of desired substrate directly. Our simple method of peeling off using scotch tape can reduce the whole process to form WTe_2 nanostructures on the desired substrate as well as prevent degradation of intrinsic properties of WTe_2, without using chemical wet etching and after-growth transfer processes. It enables to investigate its electrical properties by fabricating test device directly on SiO_2/Si substrate with no needs for a further transfer process. Moreover, the feasibility of synthesis of $MoTe_2$ nanostructure as a member of the layered TMDs family was evaluated through our approaches.

In conclusion, we develop reliable growth method of WTe_2 nanostructure using eutectic metal alloys and simple transfer-free growth method without the needs for a further transfer process. Our results provide not only a basis for optimizing WTe_2 nanostructure growth using eutectic metal alloys, but also can be adopted to research the novel properties of WTe_2 nanostructure without any degradation of the characteristics.

References

1. Butler, S. Z., *et al.* "Progress, challenges, and opportunities in two-dimensional materials beyond graphene." *ACS Nano* 7.4 (2013): 2898-2926.
2. Chhowalla, M., *et al.* "Two-dimensional semiconductors for transistors." *Nature Reviews Materials* 1 (2016): 16052.
3. Podzorov, V., *et al.* "High-mobility field-effect transistors based on transition metal dichalcogenides." *Applied Physics Letters* 84.17 (2004): 3301-3303
4. Liu, L., *et al.* "Performance limits of monolayer transition metal dichalcogenide transistors." *IEEE Transactions on Electron Devices* 58.9 (2011): 3042-3047
5. Fang, H., *et al.* "High-performance single layered WSe_2 p-FETs with chemically doped contacts." *Nano Letters* 12.7 (2012): 3788-3792.
6. Wang, Q. H., *et al.* "Electronics and optoelectronics of two-dimensional transition metal dichalcogenides." *Nature Nanotechnology* 7.11 (2012): 699-712.
7. Deng, Y., *et al.* "Black phosphorus–monolayer MoS_2 van der waals heterojunction p–n diode." *ACS Nano* 8.8 (2014): 8292-8299.
8. Furchi, M. M., *et al.* "Photovoltaic effect in an electrically tunable van der Waals heterojunction." *Nano Letters* 14.8 (2014): 4785-4791.
9. Fang, H., *et al.* "Strong interlayer coupling in van der Waals heterostructures built from single-layer chalcogenides." *Proceedings of the National Academy of Sciences* 111.17 (2014): 6198-6202.
10. Akinwande, D., *et al.* "Two-dimensional flexible nanoelectronics." *Nature Communications* 5 (2014).
11. Fiori, G., *et al.* "Electronics based on two-dimensional materials." *Nature Nanotechnology* 9.10 (2014): 768-779.
12. Chhowalla, M., *et al.* "The chemistry of two-dimensional layered transition metal dichalcogenide nanosheets." *Nature Chemistry* 5.4 (2013): 263-275.
13. Mak, K. F., *et al.* "Atomically thin MoS_2: a new direct-gap semiconductor." *Physical Review Letters* 105.13 (2010): 136805
14. Britnell, L., *et al.* "Strong light-matter interactions in heterostructures of atomically thin films." *Science* 340.6138 (2013): 1311-1314.

15. Cheiwchanchamnangij, T., *et al.* "Quasiparticle band structure calculation of monolayer, bilayer, and bulk MoS_2." *Physical Review B* 85.20 (2012): 205302.

16. Song, S., *et al.* "Room temperature semiconductor–metal transition of $MoTe_2$ thin films engineered by strain." *Nano Letters* 16.1 (2015): 188-193.

17. Ali, M. N., *et al.* "Large, non-saturating magnetoresistance in WTe_2." *Nature* 514.7521 (2014): 205-208.

18. Huang, H. H., *et al.* "Controlling phase transition for single-layer MTe_2 (M= Mo and W): modulation of the potential barrier under strain." *Physical Chemistry Chemical Physics* 18.5 (2016): 4086-4094.

19. Park, J. C., *et al.* "Phase-Engineered Synthesis of Centimeter-Scale 1T′-and 2H-Molybdenum Ditelluride Thin Films." *ACS Nano* 9.6 (2015): 6548-6554.

20. Shi, Y., *et al.* "Recent advances in controlled synthesis of two-dimensional transition metal dichalcogenides via vapour deposition techniques." *Chemical Society Reviews* 44.9 (2015): 2744-2756.

21. Novoselov, K. S., *et al.* "Two-dimensional crystals-based heterostructures: materials with tailored properties." *Physica Scripta* 2012.T146 (2012): 014006.

22. Gupta, A. *et al.* "Recent development in 2D materials beyond graphene." *Progress in Materials Science* 73 (2015): 44-126.

23. Li, J., *et al*. "Scalable Fabrication of 2D Semiconducting crystals for future electronics." *Electronics* 4.4 (2015): 1033-1061.

24. Ji, Q., *et al.* "Chemical vapour deposition of group-VIB metal dichalcogenide monolayers: engineered substrates from amorphous to single crystalline." *Chemical Society Reviews* 44.9 (2015): 2587-2602

25. Lv, H. Y., *et al.* "Perfect charge compensation in WTe_2 for the extraordinary magnetoresistance: From bulk to monolayer." *EPL (Europhysics Letters)* 110.3 (2015): 37004

26. Keum, D. H., *et al.* "Bandgap opening in few-layered monoclinic $MoTe_2$." *Nature Physics* 11.6 (2015): 482-486

27. Duerloo, K. A. N., *et al.* "Structural phase transitions in two-dimensional Mo- and W- di chalcogenide monolayers." *Nature Communications* 5 (2014).

28. Lee, C. H., *et al.* "Tungsten ditelluride: a layered semimetal." *Scientific Reports* 5 (2015).

29. Lu, N., *et al.* "Atomic and electronic structures of WTe_2 probed by high resolution electron microscopy and ab initio calculations." *The Journal of Physical Chemistry C* 120.15 (2016): 8364-8369.

30. Ali, M. N., *et al.* "Correlation of crystal quality and extreme magnetoresistance of WTe_2." *EPL (Europhysics Letters)* 110.6 (2015): 67002.

31. Kim, Y., *et al.* "Anomalous Raman scattering and lattice dynamics in mono-and few-layer WTe_2." *Nanoscale* 8.4 (2016): 2309-2316.

32. Wang, L, *et al.* "Tuning magnetotransport in a compensated semimetal at the atomic scale." *Nature Communications* 6 (2015).

33. Dai, Y. M., *et al.* "Ultrafast carrier dynamics in the large-magnetoresistance material WTe_2." *Physical Review B* 92.16 (2015): 161104.

34. Kong, W. D., *et al.* "Raman scattering investigation of large positive magnetoresistance material WTe_2." *Applied Physics Letters* 106.8 (2015): 081906.

35. Soluyanov, A. A., *et al.* "Type-II Weyl semimetals." *Nature* 527.7579 (2015): 495-498

36. Burkov, A. A., *et al.* "Weyl semimetal in a topological insulator multilayer." *Physical Review Letters* 107.12 (2011): 127205.

37. Qian, X., *et al.* "Quantum spin Hall effect in two-dimensional transition metal dichalcogenides." *Science* 346.6215 (2014): 1344-1347.

38. Zheng, F., *et al.* "On the Quantum Spin Hall Gap of Monolayer 1T′-WTe_2." *Advanced Materials* (2016).

39. Zhao, Y., *et al.* "Anisotropic magnetotransport and exotic longitudinal linear magnetoresistance in WTe_2 crystals." *Physical Review B* 92.4 (2015): 041104.

40. Kang, D., *et al.* "Superconductivity emerging from a suppressed large magnetoresistance state in tungsten ditelluride." *Nature Communications 6* (2015).

41. Choi, H. J., *et al.* "Vapor–liquid–solid growth of semiconductor nanowires." *Semiconductor Nanostructures for Optoelectronic Devices.* Springer Berlin Heidelberg, 2012. 1-36

42. Ellmer, K. *et al.* "Preparation routes based on magnetron sputtering for tungsten disulfide (WS_2) films for thin-film solar cells." *Physica Status Solidi (b)* 245.9 (2008): 1745-1760.

43. Brunken, S., *et al.* "Analysis of the early stages of the rapid, nickel-assisted crystallization of WS_2 films." *Journal of Applied Physics* 120.16 (2016): 165307.

44. Sun, Y., *et al.* "Eutectic solidification applied to nanofabrication: a strategy to prepare large-scale tungsten carbide nanowalls." *Journal of Materials Chemistry* 22.32 (2012): 16566-16571.

45. Lee, Y. H., *et al.* "Tungsten nanowires and their field electron emission properties." *Applied Physics Letters* 81.4 (2002): 745-747.

46. Huang, C. C., *et al.* "Transfer-free growth of atomically thin transition metal disulfides using a solution precursor by a laser irradiation process and their application in low-power photodetectors." *Nano Letters* 16.4 (2016): 2463-2470.